

**THEORY AND MODELING
IN SUPPORT OF TETHER**

Final Report

NASA Contract No. NAS8-36811

Contract Period: December 19, 1985 to September 31, 1999

SAIC Project Number 01-0157-00-0919-000

Submitted to:

**Mr. Murray Castleman
NASA/MSFC - FD11
Huntsville, Alabama 35812**

Prepared by:

**C.L. Chang, G. Bergeron, A.D. Drobot, K. Papadopoulos,
S. Riyopoulos, E. Szuszczewicz**

**Science Applications International Corporation
1710 Goodridge Drive, McLean Virginia 22102**

September 30, 1999

Introduction

This final report summarizes the work performed by SAIC's Applied Physics Operation on the modeling and support of Tethered Satellite System missions (TSS-1 and TSS-1R) for NASA under Contract No. NAS8-36811. The SAIC team, known to be Theory and Modeling in Support of Tether (TMST) investigation, was one of the original twelve teams selected in July, 1985 for the first TSS mission. The accomplishments described in this report cover the period December 19, 1985 to September 31, 1999 and are the result of a continuous effort aimed at supporting the TSS missions in the following major areas. During the contract period, the SAIC's TMST investigation acted to:

- Participate in the planning and the execution on both of the TSS missions;
- Provide scientific understanding on the issues involved in the electrodynamic tether system operation prior to the TSS missions;
- Predict ionospheric conditions encountered during the re-flight mission (TSS-1R) based on realtime global ionosonde data;
- Perform post mission analyses to enhance our understanding on the TSS results. Specifically, we have 1) constructed and improved current collection models and enhance our understanding on the current-voltage data; 2) investigated the effects of neutral gas in the current collection processes; 3) conducted laboratory experiments to study the discharge phenomena during and after tether-break; and 4) perform numerical simulations to understand data collected by plasma instruments SPES onboard TSS satellite.
- Design and produce multi-media CD that highlights TSS mission achievements and convey the knowledge of the tether technology to the general public.

Overview on the SAIC's TMST investigation is presented in next section. It consists a brief description of the TMST roles in the TSS missions since the beginning. This is followed by the major investigation results on TSS engineering, which contains a critical evaluation of the TSS performance in terms of efficiency in power generation and comparison with the known analytic models. One of the surprises in the TSS missions, namely high current collection after tether break in TSS-1R, is also addressed. Next is the summarized description on major scientific results by the TMST team (Appendices 6, 11, 13). Science research is focused on another major surprise in the TSS mission - high current collection during nominal operation. A number of physical processes that may contribute to the elevated level of current flow have been investigated, which include motional effects of the satellite (Appendices 17, 19), the presence of thermal ambient electrons, neutral gas surrounding (Appendices 8, 12), and ion reflection (Appendix 16). Finally, lessons learned from the TSS-1R mission is discussed. In particular, the need for free flyers in the vicinity of the satellite for the future tether investigations is emphasized.

Part of the overall effort to support TSS mission went into providing realtime forecast of the ionospheric conditions along the TSS orbit during the reflight mission. The purpose of this effort was to enhance scientific productivity during interactive on-orbit experimentation. Prediction of F-region heights and densities were made around-the-clock based on realtime reports from a global network of ionosonde stations. Detailed report of such effort is described in a published paper (Appendices 5, 15).

Post mission laboratory experiments were conducted to investigate the possible cause of tether breakdown (Appendix 22). The laboratory investigation was focus on the discharge properties of a section of tether under low pressure and high voltage conditions. Experimental results

indicated that breakdown could occur at low pressure (m Torr) and high voltage (10 kV), presumably due to the release of the trapped gas in tether. However, the experimental results cannot offer definitive proof that the root cause of the tether break was plasma breakdown.

Post mission analyses also include the effort on numerical simulation of onboard instruments (SPES) measuring ambient electron energy. These tasks were performed to resolve the unexplained origin of "hot" electrons (~ 200 eV) around the TSS satellite as shown in SPES data. Using simulation as a tool, a number of plausible mechanisms that may contribute to "hot" electrons inside the SPES instrument were examined. No evidence was found to be the cause of "hot" electron readings. Detailed report of such simulation effort is given in Appendix 18.

In this final report, a list of publications and presentations derived from the TMST investigation span over the performance period is compiled. Copy of these publications and presentations is included in the Appendices section of this final report. Citations to some of these publications have been made at various places in this final report.

Copies of the multi-media tether CD (500 copies plus original sound track) were delivered to NASA/MSFC via FEDEX on September 28, 1999.

Overview on the TMST Investigation

1. The TMST Investigation:

The TMST investigation had two major roles in the TSS-1R mission.

- The formulation, within the limits of the payload configuration, instrumentation, and mission orbital constraints, the experimental functional objectives (FO's) required to collect the data set required for completion of the major scientific and technological objectives of the TSS-1R investigation.
- The usage of the data set with the pre-mission models to furnish answers to the critical issues of the investigation and guidance as to future mission planning.

To accomplish its mission role the TMST investigation developed a large number of theoretical and computational models (Appendices 2, 3, 4, 7, 10), used them to analyze particular investigations and functional objectives (Appendices 11, 13, 14), actively participated in the mission planning IWG's and the mission conduct, and provided a ground set of ionosonde measurements and models required to predict and model the ambient ionospheric conditions during the mission (Appendix 5, 15).

2. Major Engineering Results:

Despite the shortened mission, caused by the faulty engineering design of the tether by the mission's prime contractor, the anticipatory staging of the functional objectives allowed the team to accomplish major objectives and demonstrate breakthrough-engineering performance by the TSS.

The most significant result was the surprisingly high collection efficiency of the TSS system, which exceeded by far all pre-mission models and upper limits (Appendix 6, 13). This was demonstrated by our analysis of the mission data illustrated in Figure 1. The figure shows the maximum available power, $P = I(E - \Phi_s - \Phi_o)$, computed using the values of the current I , the electromotive force (emf) E , the satellite potential Φ_s , and the orbiter potential Φ_o measured during the flight vs. the current collected by the TSS satellite. The value of P is the difference between the maximum available power $I-E$ and the power $I-(\Phi_s - \Phi_o)$ lost in collecting the current. It represents a figure of merit of the system in the ideal case that resistive losses in the tether itself are small. The experimental results are compared to the leading pre-mission models, the *Parker-Murphy* (PM) and the *Beard-Johnson* (BJ) models. The latter (BJ) model ignores limitations in the current collection imposed by the effect of the geomagnetic field on the electron orbits and it has been considered as a theoretical upper limit for current collection. The former (PM) model was the consensus pre-mission model, validated by rocket and laboratory experiments. Figure 2 is complementary to Figure 1 and shows the relative efficiency as a function of input power. It is clear that the efficiency stays above 80% even at powers exceeding 1.5 kW contrary to the pre-mission expectations. The voltage-current characteristic implied by the TSS measurements is shown in Figure 3, along with ones expected by the PM and BJ models. From the results of Figs. 1, 2 and 3 we conclude that

- Contrary to the expectations of the PM theory, which predicted a maximum effective power of 600 W, the TSS-1R produced effective power approaching 2 kW.
- The 2 kW effective power was larger than the upper limit imposed by the isotropic space charged limited collection imposed by the BJ model, implying an additional free energy source.

- There was no saturation in the effective power scaling with current up to the maximum current allowed in the system.

The second major mission surprise came following the tether break. When the failure point of the tether entered into the ambient plasma, the current conducted through the tether reached 1.1 Amperes and was maintained for approximately 75 seconds after the break. According to the PM model, collection of such a current would have required potentials in excess of 15 kV. It should be noted that this was achieved with a downward tether configuration. The TMST analysis attributes the new and efficient current collection on a process similar to the vacuum arc, with “vacuum” implying that the arc starts in vacuum, but is burning in the cathode vapor. In addition to this surprise we should add another mission finding related to the presence of neutral gas in the vicinity of the collector (Appendices 8, 12, 21). Gas was released from the yaw thrusters of the satellite during a current collection cycle. It reduced the voltage required for collection of 500 mA of current from in excess of 1 kV to less than 100 V – an order of magnitude increase in the collection efficiency. Figure 4 compares the collection efficiency during the two events described above with one found during regular operation. These discoveries open up new avenues in the design and utilization of compact but efficient tether systems.

Both findings have profound implications on the utility and design of electrodynamic tethers for space power or propulsion.

3. Major Scientific Results:

While key objectives of the mission were accomplished despite its abbreviated nature, the limited data set obtained did not allow for definitive understanding of the details of the physical processes responsible for the high current collection efficiency. It was clear from the results that the

various models developed over the last 50 years did not include the physics required to describe current collection in space by probes moving at supersonic speeds (Appendices 17, 19). It was found that:

- The Voltage-Current characteristics recorded differed significantly, both quantitatively and qualitatively, from the laminar, space charge limited, magnetically insulated models that described collection in the laboratory and by subsonically moving space probes (Appendix 11).
- A large number of physical effects associated with collective interactions, such as plasma waves, suprathermal particles, and anomalous magnetic perturbations seemed to affect significantly the collection process.
- An unexpected abrupt transition in the collection physics appeared for potentials exceeding +5 Volts – which corresponds to the ram energy of the ambient oxygen ions.

Several of these issues were addressed theoretically by the TMST team, although often the answers were not conclusive due to the lack of a comprehensive as well as systematic data set. Our team identified ion reflection from the charged satellite when the potential exceeded the ram energy of the oxygen ions as supplying a new free energy source in addition to the electrostatic energy surrounding a stationary charged sphere (Appendix 16). This new free energy source drove a number of collective interactions ahead of the satellite, which were responsible for the unexpectedly large current collection efficiency. The same concept could account for many of the wave and particle spectra measured in the vicinity of the satellite. The high efficiency of current collection observed during the tether break and during the neutral gas release were also analyzed by the

TMST team (Appendices 21, 22). The severely limited data base related to these events did not permit us to develop a comprehensive quantitative understanding of the underlying physics and the scaling laws controlling it. Nevertheless our analysis of the tether break event appears consistent with a “vacuum arc” discharge process fueled by vapor from the burning tether wire tip. On the other hand the physics of the neutral gas event seems discharge dominated, although with unexpectedly high efficiency.

4. Lessons Learned:

Besides the engineering and science lessons, the TSS-1R mission clearly demonstrated the need for flyers in the vicinity of the satellite for future investigations. It is clear that ram as well as side effects extending 100's of meters from the satellite control the collection process. In situ measurements at these locations are necessary to resolve the controversies on the collection physics and its scaling. Furthermore the presence of booms in the vicinity of the satellite and instruments near the sheaths aliased the data and resulted in measurements of questionable validity. It is imperative that future tether investigations minimize instrumentation in satellite booms and rely, if possible, completely on free flying instruments.

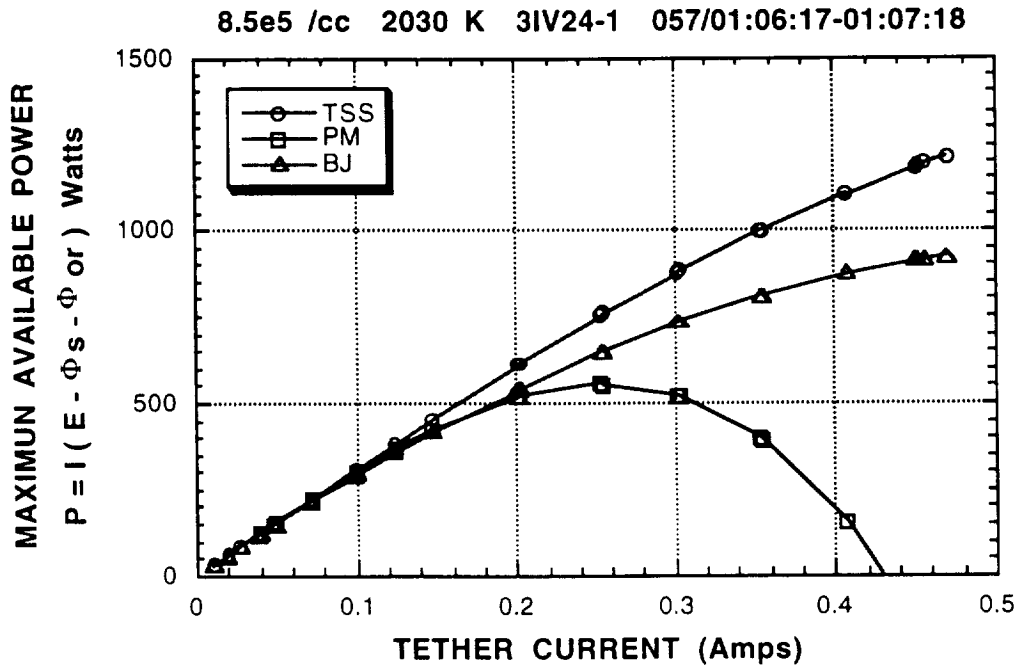


Figure 1. Maximum available power, $P = I(E - F_s - F_o)$, computed using the values of the current I , the electromotive force (emf) E , the satellite potential F_s , and the orbiter potential F_o measured during the TSS flight is plotted vs. the current.

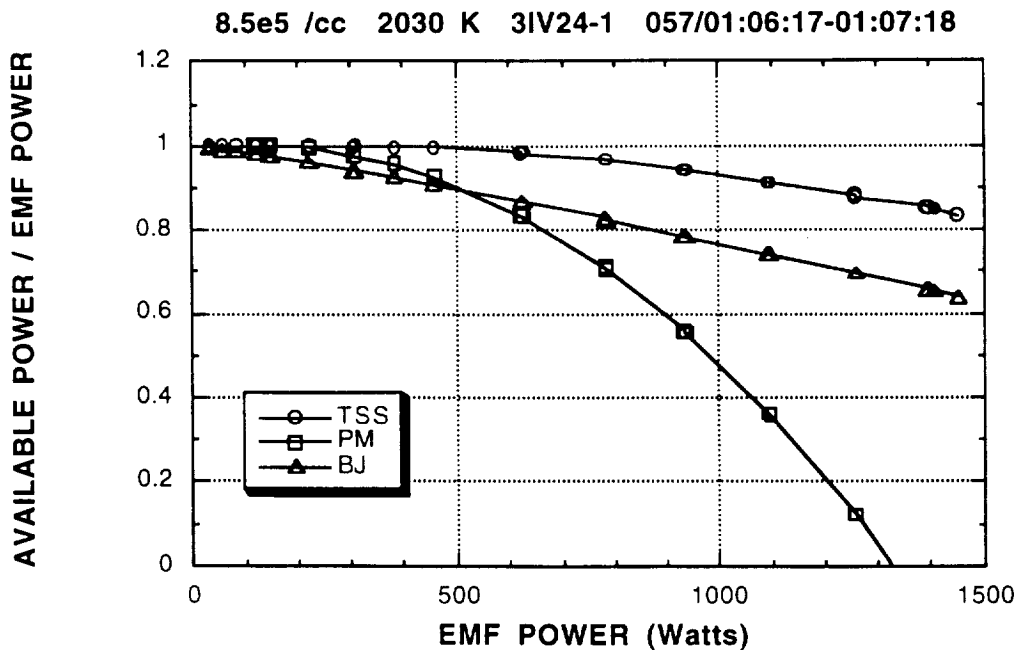


Figure 2. The relative efficiency is plotted as a function of the input EMF power. It is clear that the efficiency stays above 80% even at powers exceeding 1.5 kW contrary to the pre-mission expectations.

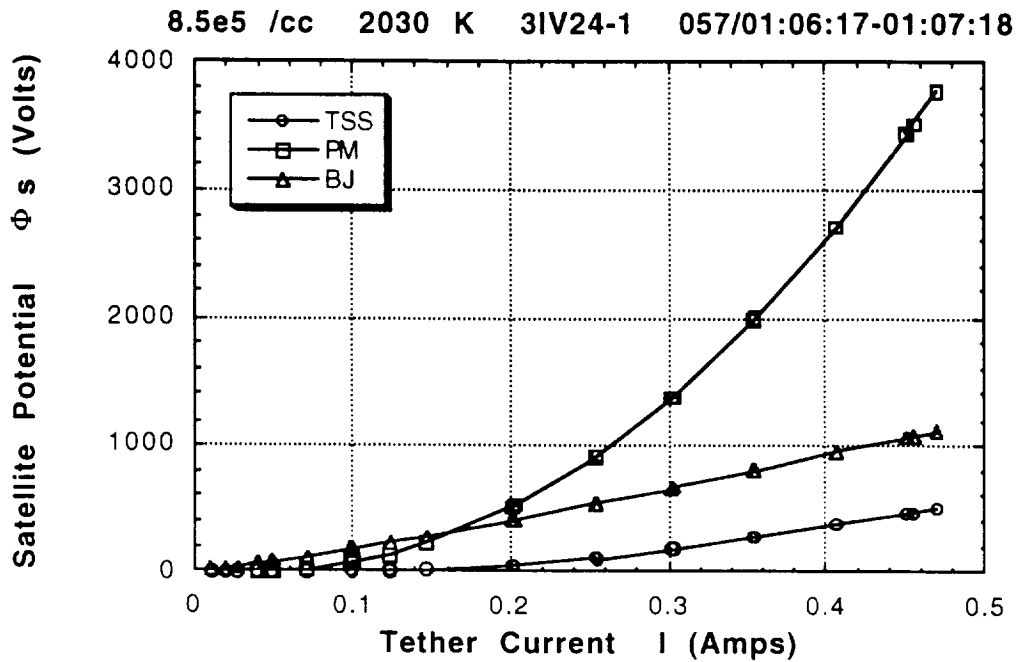


Figure 3. The voltage-current characteristic implied by the TSS measurements is shown along with ones expected by the PM and BJ models.

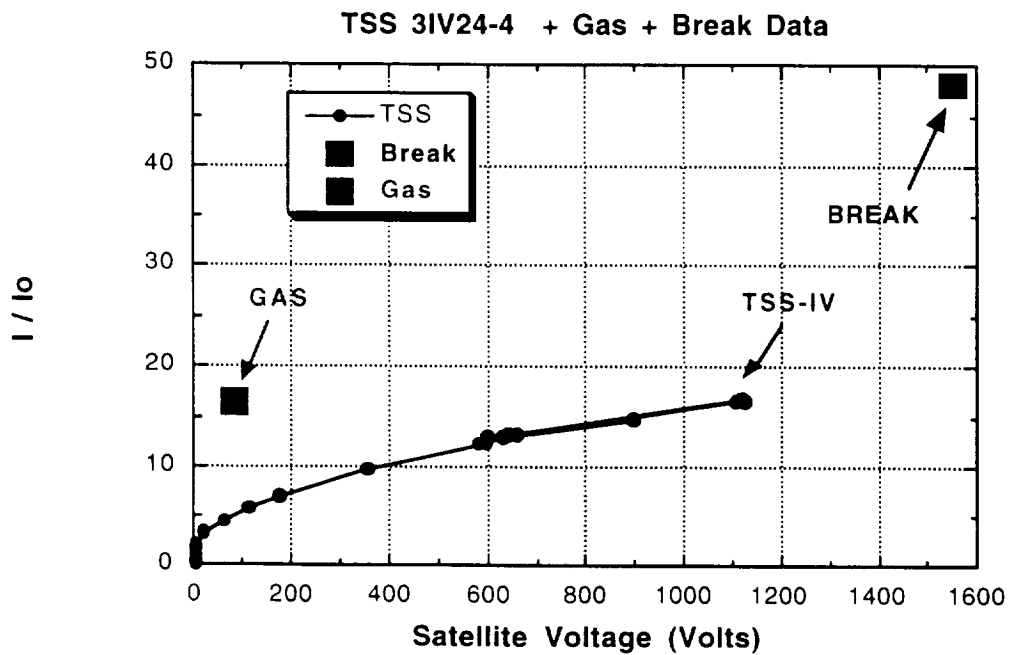


Figure 4. Comparison of the collection efficiencies during the gas and break events with ones found during regular TSS operation.

List of Publications and Presentations

- Appendix 1. The Flight of the Tethered Satellite System, EOS, Vol. 73, No. 30, p. 321-323, July 28, 1992.
- Appendix 2. Hybrid Simulation of Whistler Waves Generation and Current Closure by a Pulsed Tether in the Ionosphere, Geophys. Res. Lett., Vol. 31, No. 11, p. 1015, 1994.
- Appendix 3. Current Closure for a Tethered Satellite System, 4th International Conference on Tethers in Space, Vol. II, p. 935, Washington DC, April 10, 1995.
- Appendix 4. Basic Physics of Current Collection, TSS IWG Meeting, Johnson Space Center, May 10, 1995.
- Appendix 5. Causality and Characteristics of the Ionospheric-Thermospheric Environment, TSS IWG Meeting, Johnson Space Center, May 10, 1995.
- Appendix 6. TSS-1R Quick-Look Science Assessment, NASA HQ, March 28, 1996.
- Appendix 7. Electron Collection by the TSS Satellite, Spring AGU, Baltimore 1996.
- Appendix 8. Neutral Environment of the TSS Satellite and Its Effects on Current Collection, Fall AGU, San Francisco, December 15, 1996.

- Appendix 9. Temperature Dependent Tether Resistance and Its Effects on the IV Characteristics of the TSS System, Fall AGU, San Francisco, December 19, 1996.
- Appendix 10. An Expedient Model of Electron Sheath Around Charged Conductor and Its Applications to the Current Collection by the TSS Satellite, SAIC Report, January 1997.
- Appendix 11. I-V Characteristics of the Tethered Satellite System, 35th Aerospace Sciences Meeting & Exhibit, Reno Nevada, January 8, 1997.
- Appendix 12. Neutral Environment of the Tethered Satellite System (TSS), 35th Aerospace Sciences Meeting & Exhibit, Reno Nevada, January 8, 1997.
- Appendix 13. The Tethered Satellite Mission - Surprises and Puzzles, SAIC Report, February 1997.
- Appendix 14. Current-Voltage Characteristics of the Tethered Satellite System: Measurements and Uncertainties due to Temperature Variations, Geophys. Res. Lett., Vol. 25, No. 5, p. 713, March 1, 1998.
- Appendix 15. The First Realtime Worldwide Ionospheric Predictions Network: An Advance in Support of Spaceborne Experimentation, On-Line Model Validation, and Space Weather, Geophys. Res. Lett., Vol. 25, No. 5, p. 449, March 1, 1998.

Appendix 16. Ion Reflection by the TSS-1R Satellite, Geophys. Res. Lett., Vol. 25, No. 5, p. 745, March 1, 1998.

Appendix 17. Satellite Motion Effects on Current Collection in LEO Space, TSS IWG Meeting, Annapolis Maryland March 1998.

Appendix 18. Numerical Simulation of the SPES Instrument Operation Aboard TSS-1R - A Progress Report, SAIC Report , April 1998.

Appendix 19. Satellite Motion Effects on Current Collection in LEO Space, Spring AGU, Boston MA, May 26, 1998.

Appendix 20. Electron Collection by the High Voltage TSS Satellite, Spring AGU, Boston MA, May 26, 1998.

Appendix 21. Neutral Gas Release from High Voltage TSS Satellite and Its Effects on the Current Collection, Spring AGU, Boston MA, May 26, 1998.

Appendix 22. Post Mission Laboratory Tests, SAIC Report, October 1998.

APPENDIX 1

EOS

VOLUME 73, NUMBER 30

July 28, 1992

PAGES 321-328

The Flight of the Tethered Satellite System

PAGES 321, 323

Dennis Papadopoulos, Adam T. Drobot, and Nobie Stone

The first Tethered Satellite System (TSS-1) Electrodynamics Mission is scheduled for launch aboard the space shuttle ST-46 on July 31, 1992, as a joint mission between the United States and Italy. A 500-kg, 1.6-m-diameter satellite, attached to the shuttle by a thin (.24 cm), conducting, insulated wire (tether), will be reeled upwards from the orbiter payload to a distance of 20 km when the shuttle is at a projected altitude of 300 km.

TSS-1 is an extremely ambitious mission with high-risk payoff potential. This is the type of pioneering mission NASA and the United States should be encouraging, with the risk in the achievement of the mission objectives rather than in safety. The mission has been likened to the maiden flight of a new airplane. We expect surprises and hope to set the stage for the next mission, the TSS-reflight.

The TSS-1 mission will score many "firsts" for space experiments in general and shuttle experiments in particular.

- It is the first flight in which the shuttle will be used not only as a launching or observing platform, but actually as part of the experiment. The shuttle is the pivot of the inverted mechanical pendulum and one of the poles of the electrodynamic circuit.

- It is the first mission with an integrated approach to science, with the instrumentation, particular experiments, and mode of operation selected to characterize the dynamic and electric properties of TSS.

- It is the first attempt to resolve the problem postulated in the 1920s by Langmuir that led to the beginnings of plasma physics as a discipline: the determination of the dynamic, current-voltage characteristics for a body charged to high potential, located in a magnetized plasma in the absence of physical boundaries.

- It is unique in combining the potential for resolving a fundamental physics problem (the Langmuir problem), with the exploitation of a technological capability of critical importance to space power and propulsion.

- Finally, it is the first time such a complex, large, gravity-gradient stabilized, electrodynamic tether-system has been flown. The mission has all the uncertainties and excitement of a first experiment that stresses the limits of the system and the interplay of dynamics and electromagnetics.

During TSS-1, when the satellite is in the shuttle cargo bay, the force of gravity will be balanced by the centrifugal force at the orbital velocity of ~ 8 km/sec. At an outward distance Δ from the orbiter, the centrifugal force will exceed that of gravity and the satellite will feel an effective gravitational acceleration $g_{eff} = g \cdot \Delta / R_E$, where g is the gravitational constant and R_E is the Earth's radius (~ 6000 km). The tension on the tether due to this force would be too small to accelerate the satellite away from the tether for separation distances less than 1 km, and the satellite in-line thrusters will be used to achieve the initial separation. Subsequently, the excess centrifugal force, acting as inverse gravity, will induce sufficient tension on the tether to lift the satellite to its projected orbit 20 km away from the shuttle. This configuration is referred to as gravity-gradient-balanced tether equilibrium.

Moving through the ionosphere, the satellite-tether-shuttle system will intersect the Earth's magnetic field, creating an electromotive force (emf) between the satellite and the shuttle, whose value is given by $\Delta\phi = \mathbf{u} \times \mathbf{B} \cdot \mathbf{L}$, where \mathbf{u} is the shuttle velocity (8 km/sec), \mathbf{B} the Earth's magnetic field ($\sim 1/3$ Gauss), and \mathbf{L} the tether length. The maximum emf produced by the TSS is about .25 volts per tether meter, or about 5 kV at the 20-km deployment distance. For the eastward-moving shuttle, the satellite will charge positive, while the shuttle will be negative with respect to the ambient ionospheric plasma. The induced emf will lead to collection of electrons at the satellite and electron emission at the orbiter, using one of the two sets of electron guns in the shuttle bay. In-



The Tethered Satellite System (TSS-1) Electrodynamics Mission, attached to the space shuttle. Scheduled for launch on July 31, 1992, TSS-1 targets a fundamental problem in plasma physics, with a major impact on space engineering as well.

vestigating how TSS can draw current from the ionosphere, and thus generate power, is a primary objective of the mission.

The dominant objective of the electrodynamic mission is the development of a cause-and-effect understanding of the capabilities and limitations of electrodynamic tethers to draw current from the ionospheric plasma. In engineering terms, this translates to the determination of the current-voltage (I/V) characteristics of the circuit composed of the TSS and the ionosphere. The tether voltage will be varied by controlling the current, using the electron guns located in the orbiter bay, and monitored by the scientific instruments. One set of electron guns can eject up to 0.75 amp of current. The guns are powered by the tether to which they are connected via a master switch. A voltmeter measures the tether potential with respect to the shuttle structure. A second set of electron guns has its own independent power supply and provides the means for investi-

Dennis Papadopoulos, Science Applications International Corporation and the University of Maryland, Dept. of Physics, College Park, MD 20742; Adam Drobot, Science Applications International Corporation, 1710 Goodridge Drive, McLean, VA; Nobie Stone, NASA Marshall Space Flight Center, Huntsville, AL

gating control of the tether current by electron emission at the shuttle end of the TSS circuit. The emitted electron beam has an energy of 1 keV and its current can be set at .05 or .1 amp. This gun can be pulsed with on/off times of about 100 nanoseconds and used to determine transient characteristics of the circuit.

The circuit properties and power-generating capabilities of the TSS critically depend on the nature and structure of the sheaths surrounding the satellite and the orbiter. In the pioneering experiments that provided the foundations of plasma physics in the 1920s, Langmuir developed the steady state I/V characteristics of a sphere charged to high voltage inside an unmagnetized plasma. This led to the concept of space-charge limited flow and the famous Langmuir-Blodgett $I \sim V^{3/2}$ relationship. For TSS the situation is significantly more complex. First, the ionospheric plasma is magnetized, thus breaking the isotropy of the configuration and preventing effective electron collection across the magnetic field (the physics of magnetic insulation). The steady state I/V characteristics in a magnetized plasma were studied theoretically by Parker and Murphy. Corresponding laboratory experiments have been inconclusive because of the presence of walls. Second, the supersonic motion of the satellite perturbs its environment by developing wake and front structures with significant local plasma density and kinetic gradients. Third, variations in the ambient plasma conditions and the angle of attack to the magnetic field as the TSS travels through the ionosphere make the situation a dynamic one, to which applicability of steady-state theories is in doubt. Fourth, the presence of neutral gas in the vicinity of the satellite and the orbiter (outgassing, thruster operation, and water dumps) can lead to localized discharges significantly altering the current-collecting properties of the TSS.

While several rigorous and speculative models, both analytic and numerical, have been developed to address the basic physics of current collection, the TSS measurements will be the first to address these issues experimentally. The satellite and the shuttle are equipped with many diagnostic instruments that will characterize the sheaths in engineering terms and elucidate the dominant physical processes.

An important science issue that could potentially be resolved by the TSS is the closure path of the induced current through the ionospheric plasma. Current closure across magnetic-field lines and the development of field-aligned anomalous resistivity is a problem of critical importance to space physics in general and to auroral physics in particular. Early models of TSS-like configurations speculated that the currents will flow along magnetic field lines to the lower ionosphere in the form of Alfvén waves, where they will close across the magnetic field due to the high electron-neutral-collision frequency. If this is the case, a series of phantom current loops, each with a circumference over 500 km in extent, will follow the motion of TSS, forming a long solenoid. More recent think-

ing stimulated by Stenzel's laboratory experiments at UCLA indicate that the current closure will be local for TSS-1, through intersecting, current-carrying whistler waves rather than Alfvén waves. Although the absence of a free flyer with diagnostic instrumentation makes direct observations of the current path impossible, combining measurements of low-frequency magnetic fields, observations of emissions using the orbiter camera, and radar diagnostics during the overflight above Arecibo will improve understanding of this important topic.

The global current closure mechanism already discussed indicates that TSS can act as a large antenna for ULF (~ 1 Hz) waves through modulation of the tether current at a low frequency. This concept will be tested during the TSS-1 mission by low-frequency-wave ground measurements from stations in Puerto Rico, Australia, the Canary Islands, and Kenya. It should be stressed that if the current closure is local, by intersecting whistlers, there will be two antiphased current loops produced in the tether vicinity and the radiation efficiency at ULF may be undetectable. On the other hand, whistler waves in the kHz range will be produced and should be observed on the field-line footprints.

The TSS-1 is the first step toward utilizing tethers for space power propulsion and as a unique space laboratory. The maximum power that can be demonstrated by TSS-1 is approximately 2.5 kW and is limited by the tether resistance and the maximum current from the electron guns. Whether the ionosphere can stably support such a high current is to be determined. Preliminary estimates indicate that gas from thruster operation can sustain currents in excess of 1 amp. The projection is that long tethers will generate tens of kW of space power. It should be noted that the tether operation is reversible. If the current direction is reversed using on-board power, thrust can be generated for spacecraft maneuvering without the use of propellant. This reversible tether operation, which is a form of energy storage, is an attractive engineering feature for future space applications.

A primary engineering objective of TSS-1 is to demonstrate deployment of the satellite to a distance of 20 km, and subsequent retrieval. Since this is the first such experiment, there are several unknowns. Viewed superficially, the TSS system resembles an inverted pendulum; it is actually a regular pendulum, since the direction of the effective gravity force is upwards. Similar to a pendulum, it is subject to various oscillation modes. The oscillations can be longitudinal, transverse, and pendulous. The oscillation frequencies vary with tether length and tension. The period of the oscillations is typically on the order of a few minutes. Mode couplings and resonances can cause circularization of the transverse oscillations, leading to an oscillation resembling "skip-rope" motion. Oscillations can be driven or damped by movements of the satellite and shuttle. Furthermore, the $\mathbf{J} \times \mathbf{B}$ force on the tether can drive or damp oscillations. When the satellite is retrieved, the excited modes

can be amplified and coupled. A series of dynamic experiments planned by the dynamics group will study the oscillations of the TSS system and aim to learn how to control them.

Scientific and other advisory committees realized the importance of the quick reflight of a first mission, and incorporated it as part of the original selection plan. For this reason, satellite recovery has been raised from a secondary to primary mission objective. We look forward to this shuttle mission as a major scientific and engineering milestone in the space sciences and in spacecraft performance.

Scientific Investigations and Diagnostic Instrumentation

- Mission Scientists:* Nobie Stone, Mike Chandler (Asst.), NASA/MSFC; M. Candidi, J. Sabbagh (Asst.), ASI, Rome, Italy
 DCORE: Core electron gun, vacuum gauge, accelerometer (shuttle bay) satellite arm-meter—C. Bonifazi, ASI, Rome, Italy
 SETS: Fast pulse electron gun, retarding potential analyzer, Langmuir probe, fluxgate magnetometer (shuttle bay)—P. Banks and B. Gilchrist (Univ. of Michigan), J. Raitt (Utah State)
 SPREE: Electrostatic analyzers, measure orbiter potential and particle distributions above 10 eV (shuttle bay)—M. Oberhardt (Phillips Lab/GL, Hanscom Field, MA), D. Hardy (Phillips Lab/GL, Hanscom Field, MA)
 TOP: Imaging system, crew operated camera (shuttle)—S. Mende (Lockheed, Palo Alto, CA)
 RETE: Electric and magnetic field probes, Langmuir probe (on extendable satellite booms)—M. Dobrowolny (IFSI, Frascati, Italy), C. Harvey (Meudon Observatory, France)
 ROPE: Differential ion and flux probe, soft particle electron spectrometer (on satellite and fixed boom)—N. Stone, K. Wright (NASA/MSFC), D. Winningham (SWRI, San Antonio, TX)
 TMAG: Triaxial fluxgate magnetometers, measure magnetic field in satellite region (tip and middle of retractable boom)—F. Manarini (Second University of Rome, Italy)
 EMET: Generation and ground observation of low frequency waves—R. Estes (SAO, Cambridge, MA)
 OESEE: Generation and ground observation of low frequency waves—G. Taconi (University of Genoa, Italy)
 IMDN: Investigation of TSS dynamics using satellite accelerometers and gyros—G. Gullahorn (SAO, Cambridge, MA)
 TEID: Investigation of TSS dynamics using satellite accelerometers and gyros—S. Bergamaschi (Institute of Applied Mech., Padua, Italy)
 TMST: Develop overall mission models including I/V characteristics, current closure, sheath structure, current collection capability, and wave efficiency generation—A. Drobot (SAIC, McLean, VA), K. Papadopoulos (Univ. of Maryland, College Park)

TSS Management

Program Managers: T. Stuart, NASA HQ, Code M; J. F. Manarini, ASI, Rome, Italy
TSS-1 Science Program Manager: R. Howard, NASA HQ, Code SE
Mission Manager, TSS-1 Project Manager: W. Nunley, NASA/MSFC
Flight Director: C. Shaw, NASA/JSFC

System Components for TSS

Shuttle: Mission Platform—Orbiter Crew: L. J. Shriver (USAF), A. M. Allen (USMC), M. S. Ivins (NASA); Science Crew: J. A. Hoffman (NASA), F. R. Chang-Diaz (NASA), C. Nicollier (ESA), F. Malerba (ASI), U. Guidoni (ASI)
Deployer: Equipment for release, deployment control, and retrieval of the tethered satellite—R. Schwindt, Mgr. (Martin Marietta Astronautics Group, Denver, CO)
Satellite: Satellite structure and instrumentation—B. Strim, Mgr. (Alenia Space Group, Turin, Italy)

Hill Takes Action on NOAA Funding

PAGES 321-322

Action was taken recently in both the House and Senate on fiscal year 1993 appropriation bills that fund the National Oceanic and Atmospheric Administration.

The House Commerce, Justice, and State, the Judiciary and Related Agencies Subcommittee voted on its funding bill on June 30. The Senate, the Commerce, Justice, and State, the Judiciary and Related Agencies Appropriations Subcommittee marked up its bill on July 22.

The House bill proposed that Climate and Global Change receive \$43.9 million, a decrease from this year's level of \$46.9 million. The president requested \$78.2 million for this program. For the Coastal Ocean program, spending is set at \$12 million, a decrease from the president's request of \$17 million, but up from the fiscal 1992 level of \$11.5 million. Weather research, which includes PROFS/Advanced Forecasting Applications, the wind profiler, and federal and state weather modernization grants, would receive \$37.6 million, a decrease from the 1992 \$38.9 million level. The president requested \$35.1 million for weather research. The House would fund Solar-Terrestrial Services and Research at \$5 million, a slight increase from 1992, but down from the president's proposed level of \$5.6 million.

Funding was restored to both VENTS, NOAA's ocean vent exploration program, and NURP, NOAA's Undersea Research Program. VENTS would receive \$2.4 million, a slight decrease from the 1992 level of \$2.6 million, while NURP would receive \$15.9 million, an

increase from the 1992 level of \$15.2 million. The president eliminated both programs in his budget request.

Spending for operations and research in the National Weather Service, which is undergoing a modernization, would increase from the 1992 level of \$311.5 million to \$341.6 million. The president requested \$371 million for the modernization. NEXRAD (next generation radar) would receive \$79.3 million in the House bill. Spending for 1992 was \$83.4 million, and the president requested \$84.5 million.

Funding for National Environmental and Satellite, Data, and Information Service (NESDIS), which manages NOAA's environmental data and the weather satellites, was set at \$349.2 million, a drop of \$88.7 million from the president's request. Spending for 1992 was \$338.4 million.

NOAA's fleet modernization of its research vessels would receive the requested \$2 million, which was a sharp drop from the 1992 level of \$33 million.

While Senate action does not usually proceed until House action is complete, subcommittee chairman Ernest Hollings (D-S.C.) felt it necessary to get the Senate process moving quickly this year. "I intend to move this bill forward, and with any luck, bring back a conference report before the Republican convention [in August]," he said. The House action was delayed for over a month because of necessary reductions under this year's low budget allocations, he explained. During the Senate mark up, Hollings noted that "This has been a tough year. . . . A lot of domestic agencies will be provided funding below the fiscal 1992 enacted level."

Hollings said that he rejected the "fair share" approach and instead assigned priorities to five areas under this broad Senate appropriations bill. Maintaining and modernizing the National Weather Service in support of its mission to protect the life and safety of Americans ranked third among justice, trade, and economic issues.

The Senate bill proposes \$401.8 million for the operation and staffing of the NWS, an increase of \$54.6 million from fiscal 1992. More funding will enable the NWS to maintain stations across the country at current operations and staffing, said Hollings. The bill also proposes \$177 million for acquisition of NEXRAD "tomado detecting" Doppler radar, facilities, and other technologies needed to upgrade the NWS's capabilities of issuing warnings and to protect Americans from severe weather.

The spending bill would cut \$62.6 million from what Hollings called the "ill-conceived polar next-satellite program." The five geostationary satellites of GOES-NEXT were to replace the GOES (Geostationary Operational Environment Satellites) series, the last of which is due to expire soon.

The NOAA fleet modernization program would receive \$37 million, an increase of \$35 million from fiscal 1992. This includes \$22 million to convert a Navy oceanographic ship for use by NOAA.—Susan Bush

Watkins Offers View of Future DOE Mission

PAGE 322

The fifth plenary meeting of the Secretary of Energy Advisory Board (SEAB) was held in Washington on July 10. Opening comments by Admiral James Watkins, Secretary of the Department of Energy, provided insights into his vision of the agency's future direction.

These are exciting times, Watkins said, declaring that the "evil empire has disappeared." He hailed Boris Yeltsin's recent declaration to Congress that communism is dead. Watkins spoke of the opportunities of the "new world order," but also said that DOE is facing a management challenge of great proportions.

Among these challenges will be cleaning up 40 years of environmental problems at weapons production facilities, turning "swords into plowshares," and defining a role for DOE in a new strategy for national economic competitiveness. Watkins discussed at some length the role DOE could play in America's economic future.

After an extensive task force presentation calling for a new DOE unit to perform economic analysis and modeling relating to energy, Watkins spoke somewhat emotionally about the difficulties he will encounter in attempting to carry this out. DOE will be criticized, he said, for excessive headquarters growth and will be told that this is not any of DOE's business. This will, Watkins said, require "a lot of push," both in Congress and within the executive branch.

Watkins is frustrated with Congress. He cited problems in getting a final version of the massive energy bill, HR776, passed by the House and Senate. Even more frustrating to him are the delays in opening up the New Mexico nuclear waste facility. Watkins charged critics of this facility with distorting science, misleading the public, and retarding national economic progress. He conceded, though, that DOE has had a credibility problem, saying that the agency has to make up for 10 lost years of eroded public confidence.

"The jewels in our crown" are the national labs, Watkins said, praising them for having the "finest technology in the world." On-going efforts to provide industry with some of the technical knowledge of the labs are paying dividends, he declared, calling for increased efforts in this area. Comparing these efforts to the Manhattan Project, he spoke of this being DOE's challenge for the next 10 years. Yet these efforts have been frustrated, he said, by a Congress that has not yet given its approval for the reprogramming of \$160 million for domestic purposes.

It is somewhat telling that during the entire day-long presentation, only one mention was made of the recent House vote to terminate the superconducting super collider. Watkins, toward the end of the meeting, wondered what facility or instrument might be eliminated next.—Richard M. Jones, American Institute of Physics

UA
Of
PAC
mos
bro
cor
for
troll
F
TI
PAC
tute
lav
long
take
Jian
a re.
Ur
En
Gre
Vol
and
Har
abo
sior
calc
emi
stat
CO₂
sion
ties
plex
that
and
glot
that
aim
sion
men
and
year
silio
emr
"but
al.
IPCC
moc
of th
lion
nari
clud
mos
(
falls

APPENDIX 2

Hybrid simulations of whistler waves generation and current closure by a pulsed tether in the ionosphere

C.L. Chang, A.S. Lipatov, A.T. Drobot, K. Papadopoulos, and P. Satya-Narayana

Science Applications International Corporation, McLean, Virginia

Abstract. The dynamic response of a magnetized collisionless plasma to an externally driven, finite size, sudden switch-on current source across the magnetic field has been studied using a two dimensional hybrid code. It was found that the predominant plasma response was the excitation of whistler waves and the formation of current closure by induced currents in the plasma. The results show that the current closure path consists of: a) two antiparallel field-aligned current channels at the end of the imposed current sheet; and b) a cross-field current region connecting these channels. The formation of the current closure path occurred in the whistler timescale much shorter than that of MHD and the closure region expanded continuously in time. The current closure process was accompanied by significant energy loss due to whistler radiation.

Introduction

Determination of the dynamic response of a magnetized collisionless plasma to an "externally imposed" cross-field current or current source driven by an electromotive force (emf), is of paramount importance in space plasma physics. Of particular interest is the formation of the closure path of the induced current flow through the magnetoplasma. A quantitative description of the current closure is required to address a diverse range of space plasma physics problems, such as, the operational characteristics of emf inducing tethered systems [Colombo et al., 1974], the efficiency of generation of ELF waves by ionospheric heating [Papadopoulos et al., 1990], the structure of tangential discontinuities in the magnetosphere [Chapman and Ferraro, 1931], and the effect of whistler waves in the magnetotail equilibrium [Kokubun et al., 1992].

Previous theoretical studies on the subject of current closure assumed steady state conditions and used the MHD equations [Drell et al., 1965; Dobrowolny and Veltri, 1986]. When the steady state MHD theory is applied to the closure problem of a tethered satellite system (TSS) carrying a motionally induced emf current, it predicts a global closure path through the conducting lower ionosphere mediated by the propagation of low frequency Alfvén waves [Banks et al. 1981]. Implicit in such formulations is the assumption that the ion polarization current is the dominant cross-field current. For this to happen the timescale must be longer than the ion cyclotron period ($t > 1/f_{ci}$), so that the ions are magnetized and the electron Hall current is balanced by an opposite ion Hall current. However, processes with timescales shorter than ion cyclotron period can also contribute significantly to the current closure around TSS. For instance, there are whistler waves supported by the electron Hall current [Stenzel and Urrutia, 1990]. Distinction in timescales between the whistler and the Alfvén processes can be made analytically by considering the magnetic equation

$$\partial^2 B/\partial t^2 + \nabla \times [\nabla \times (\partial B/\partial t) \times (cB_0/4\pi en_0)] - v_a^2 \nabla \times [b_0 \times (b_0 \times (\nabla \times B))] = 0 ; \quad (1)$$

where v_a is the Alfvén velocity, n_0 is the plasma density, and b_0 is the unit direction along B_0 . From this equation, we can see that the second term corresponds to whistler waves and the third term corresponds to Alfvén waves. If we were to normalize Eq. (1) in such a way that $T = f_{ci}t$ and $X = x f_{ci}/v_a$, then the equation depends only on dimensionless variables X and T and has no numerical coefficients. The characteristic distinction between the Alfvén and the whistler terms is determined by the timescale T . Consequently, for $T > 1$ (or $t > 1/f_{ci}$), the Alfvén wave dominates. For $T < 1$ (or $t < 1/f_{ci}$), the whistler wave dominates. In situations when the tether current is pulsed with timescale shorter than $1/f_{ci}$, or the transit time of the tether is of the order of msec in the Low Earth Orbit (LEO), one would expect that "local" current closure by whistler waves around TSS precedes Alfvén closure. Recent laboratory experiments indicate that this is the case. Briefly, the experiments of Stenzel and Urrutia [1990, see also Urrutia and Stenzel, 1990] studied the generation and the propagation of electromagnetic disturbances induced by a pulsed current wire in a plasma chamber with a dc magnetic field. The timescale of the current pulse favored whistler excitation. Probe measurements showed that current carrying disturbances were emitted from the current wire at approximately the group speed of a "whistler" wave packet. The dispersion characteristics and the polarization of the generated waves were those of whistlers. The propagation front carried a cross-field "polarization" current which is opposite to the imposed current in the tether wire. And most notably, the current closure was local rather than global.

These results indicate that a proper theoretical analysis of the current closure problem requires the solution of an initial value, rather than a steady state, problem, and a plasma model that includes the electron dynamic response. It is the objective of this letter to present the results of a study of the dynamic response of a two dimensional (2D) magnetoplasma to an externally imposed current source of the form

$$J_x(x,t) = I_0 \delta(z) [1 - \eta(|x| - L_s/2)] \eta(t) \hat{e}_x \quad (2)$$

where z is the direction of the magnetic field, x is the direction of the current flow, I_0 is the current strength, L_s is the length of current source along x , δ is the Kronecker-delta function, and η is the step function.

Two Dimensional Hybrid Simulations

The study has been conducted using a 2D hybrid simulation code [Mankofsky et al., 1987]. Particular emphasis is placed upon the determination of the dynamics, the asymptotic state, and the establishment timescale of the resultant current path. It is worthwhile to discuss the validity of two commonly adopted assumptions in the hybrid simulation technique. The assumption of massless electrons implies timescales longer than the electron gyrotime $1/f_{ce}$, and is valid for wavelenghts longer than c/f_{pe} , where f_{ce} and f_{pe} are electron gyrofrequency and plasma frequency in Hz, respectively. For parallel whistler propagation, the difference between a massless electron dispersion $k_z =$

Copyright 1994 by the American Geophysical Union.

Paper number 94GL00700
0094-8534/94/94GL-00700\$03.00

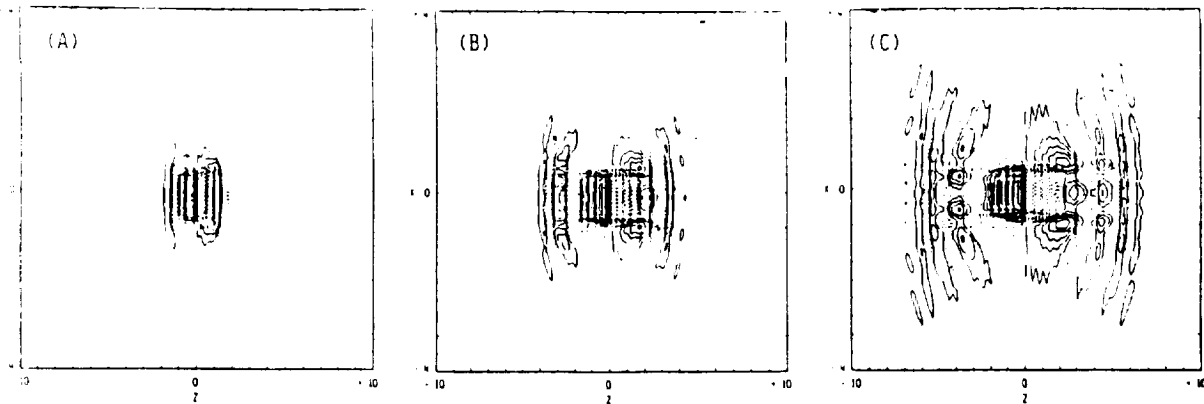


Figure 1. Contour of B_y at times: (a) 0.1 msec. (b) 0.25 msec. and (c) 0.4 msec after tether current switch-on.

$2\pi(f_{pe}/c)(f/f_{ce})^{1/2}$, where k_z is the parallel wavenumber and f is the wave frequency in Hz, and a dispersion with finite electron mass $k_z = 2\pi(f_{pe}/c)(f/(f_{ce}-f))^{1/2}$ becomes significant only when the wave frequency approaches the electron gyrofrequency [Helliwell, 1965]. Another assumption is the neglect of the displacement current in Ampere's law. This too, can be justified by the fact that the displacement current term does not contribute significantly to the whistler dispersion as long as $f \ll f_{ce}$.

The simulation was conducted for parameters relevant to TSS experiments in the F-region of the magnetosphere. The ambient magnetic field B_0 and the plasma density n_0 were uniform, with values equal 0.3 gauss and 10^{23} /c.c., respectively, corresponding to an electron gyrofrequency $f_{ce} = 0.84$ MHz and a plasma frequency $f_{pe} = 2.84$ MHz. The ambient plasma consisted of cold oxygen ions (with realistic mass) and warm electrons at a temperature of $T_e = 0.1$ eV. The simulation box was in the x - z plane and covered a region of $L_x = 8$ km by $L_z = 20$ km in size. The grid resolution was 80 (in x) by 200 (in z) cells, which corresponds to spatial resolution of 0.1 Km in both the x and z directions. Periodic boundary conditions were imposed in both the x and z directions. The simulations run at a fixed time step of

$\Delta t = 5 \times 10^{-7}$ sec. and were terminated before the disturbances reach the simulation boundary. The grid resolution was selected to filter out the effect of whistler waves of frequencies above 100 kHz, consistent with the neglect of the electron mass and the displacement current.

In the simulations, a source current J_s with the form given by Eq. (2) was introduced into a spatial region filled with stationary plasma and uniform magnetic field $B_0 = B_0 \hat{e}_z$. This current source was located at the center of the simulation region, had a finite extent ($L_s = 1$ Km) in x , and $I_0 = 1$ mAmp/m. An equivalent three dimensional view of the source current is a thin current slab extending infinitely in the y direction. In the following, the current source will be simply referred to as the tether. Before presenting the results we make the following comments. First, the tether is introduced into the plasma region initially. This is equivalent to a current switch-on at time zero, with a rise time of one time step. Therefore, the timescale involved in the hybrid simulation favors the whistler excitation. Second, the assumption of quasi-neutrality in the hybrid code requires that there is no net charge accumulation in the simulation region. Therefore, the sheath phenomena around plasma contactors at the tether ends are not included. This is in consistent with the aim of this study which focuses on the current closure through magnetoplasma away from the sheath regions.

Current Closure

Figure 1 shows the isomagnetic contours of the B_y field in the x - z plane at times 0.1, 0.25, and 0.4 msec. Two dominant features can be distinguished. First, an oscillatory radiative structure propagates away from the tether in a characteristic whistler wavepacket with group velocity of $v_g = 10^9$ cm/sec. Its wavefront spreads in a $15 - 25^\circ$ cone with respect to B_0 . This is followed by a region containing the bulk of magnetic field on either side of the tether. The bulk region is a localized magnetic field profile of the form $\pm B_y(z \pm vt) \eta(|x| - L_s/2)$. It expands spatially along B_0 at a speed of $v = v_g/2$ at early time, but the expansion slows down to $v \ll v_g$ at late times. Dynamics of the bulk region is governed by the whistler portion of Eq. (1), which has the form of a diffusion equation

$$\partial B/\partial t + \nabla \cdot [(\nabla \times B) \times (cB_y/4\pi en_0)] = 0. \quad (3)$$

Thus, we can view the expansion as an analogous diffusion process which has a decreasing speed that asymptotes to zero as $t \rightarrow \infty$. The significance of the bulk of magnetic field around tether is that it embraces a region of substantial closure current. Since $\nabla \times B = (4\pi/c) J$, there is a cross-field current component J_x associated with the bulk region. As will be shown later, J_x is an essential component in the current closure path.

Figure 2 displays plots of B_x and B_y as functions of z along the line $x = 0$, at times 0.1, 0.25, and 0.4 msec. Notice that the early pulses of B_x and B_y exhibit typical characteristics of whistler waves. They are right-hand circularly polarized (B_x, B_y

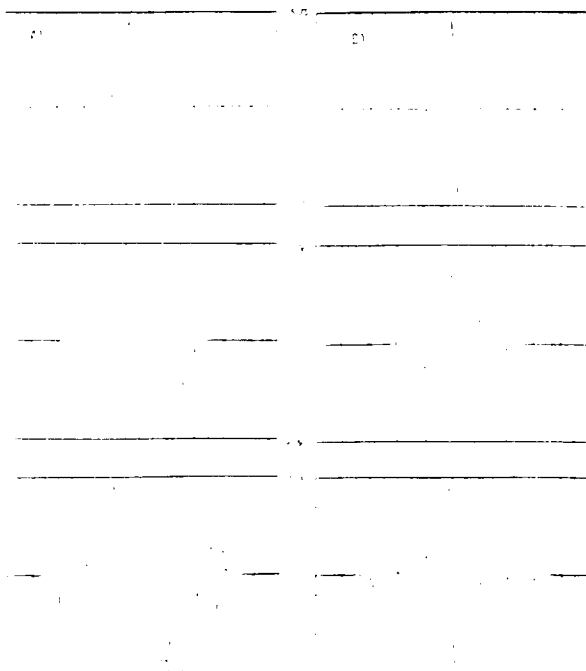


Figure 2. Cross section plots of field amplitude for (a) $B_x(z)$, and (b) $B_y(z)$ along the midplane cutting across the center of the current source at $x = 0$ and at times $t = 0.1, 0.25,$ and 0.4 msec.

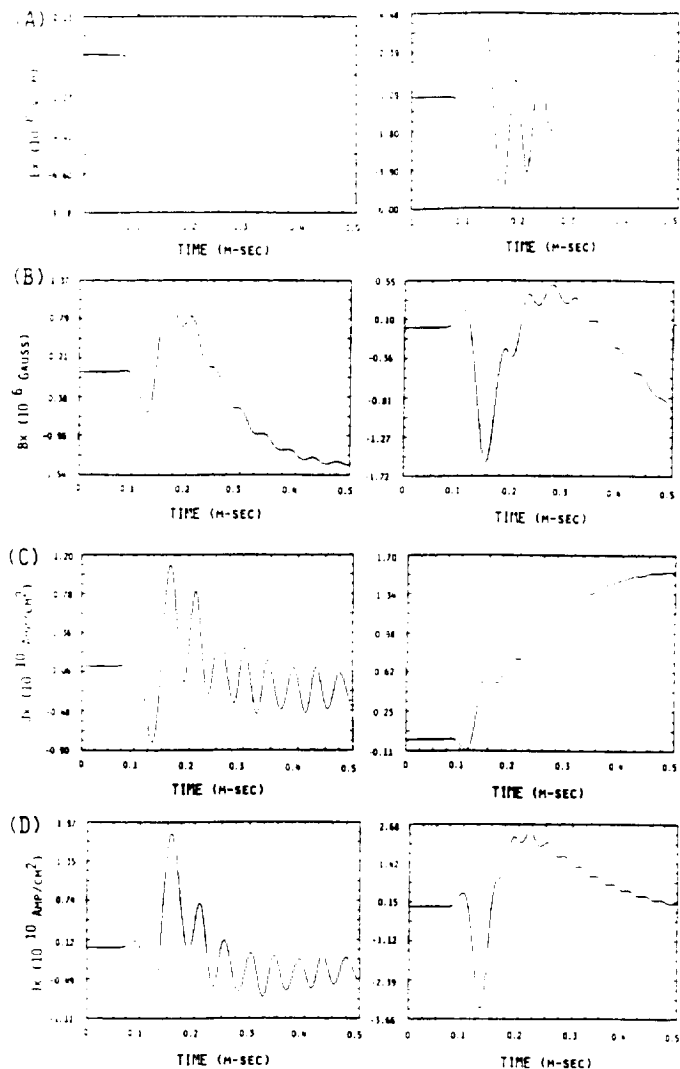


Figure 3. Field and current data at probe 1 & 2 as functions of time from $t = 0$ to $t = 0.5$ msec. Probe 1: row (a) electric fields E_x and E_y ; row (b) magnetic fields B_x and B_y ; and row (c) total plasma currents J_x and J_z . J_x and J_z at Probe 2 is in row (d).

90° out of the phase) and are highly dispersive, with shorter wavelengths running ahead of the longer ones. The wave amplitude approaches 7×10^{-6} G at the peak of the bulk, corresponding to a current strength of $I_0 = 1$ mAmp/m in tether. Size of the bulk region, as is measured by the first node of B_y , increases incrementally from 1 km, 1.7 km, to 2.2 km at times 0.1, 0.25, and 0.4 msec, respectively. Therefore, the expansion of the bulk region is continuing during the simulation run and no steady state is yet reached.

To visualize the results two probes were introduced to monitor the temporal behavior of the current and of the fields. Probe 1 was located at (0.5 km, 2 km), on the magnetic field line passing through the end of the current source. Probe 2 was located at (0, 2 km), on the midplane bisecting the current source. Time series data collected by probe 1 are shown in Figure 3. These data include the field components E_x , E_y , B_x , B_y , and total current density components J_x and J_z . All the quantities are plotted as functions of time, from $t = 0$ up to $t = 0.5$ msec. The electric field plots in Figure 3(a) show an amplitude oscillation in time long after the pulse front caused by switch-on passes through the probe location. This indicates a continuous excitation and emission of whistler waves during the expansion of the current closure loop, even though the tether current is maintained at a steady value. The oscillation period is approximately 0.045

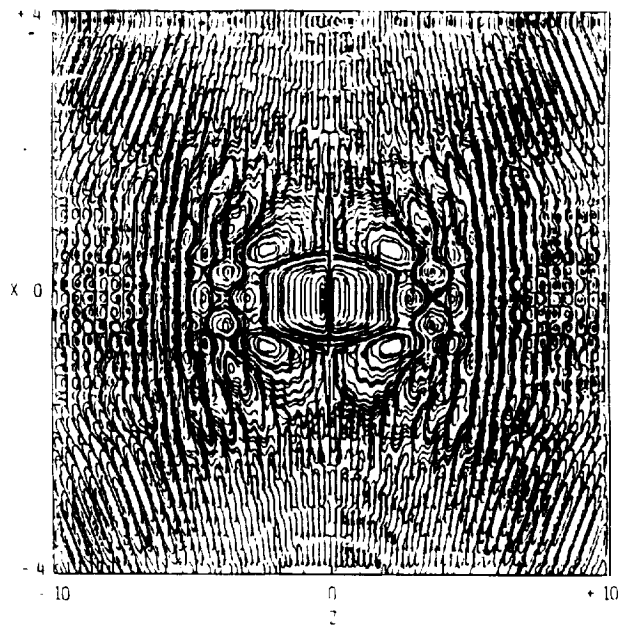


Figure 4. Streamline plot of the J_x versus J_z flow in the $x-z$ plane at a time $t = 0.4$ msec.

msec, which corresponds to a wave frequency of 22 kHz. The oscillation phases of E_x and E_y are offset by one quarter of a time cycle (i.e. 90 degrees out of phase), again indicating that the emitted wave is indeed a right hand circularly polarized whistler wave. The magnetic field plots in Figure 3(b) show similar oscillations superimposed on a steadily growing amplitude in time after the pulse front passes through. Since the magnetic field is related to the plasma current through Ampere's law, the growing amplitude in B implies an increase in the plasma current around probe 1. The current components J_x and J_z are given in Figure 3(c). The J_z plot at the lower panel shows an initial jump as the pulse front arrives. This is followed by a monotonic amplitude increase that approaches a steady value at later time. Physically, this means that a field-aligned current starts to flow from the tip of the current source after switch-on. The current strength increases in time as the closure loop expands and asymptotes to a steady value. Accompanied with the formation of a field-aligned current J_z is the emergence of a cross-field current J_x . The left panel of Figure 3(c) shows an oscillatory behavior of J_x at early time and, by taking a time average over the oscillation period, the emergence of a net J_x component after

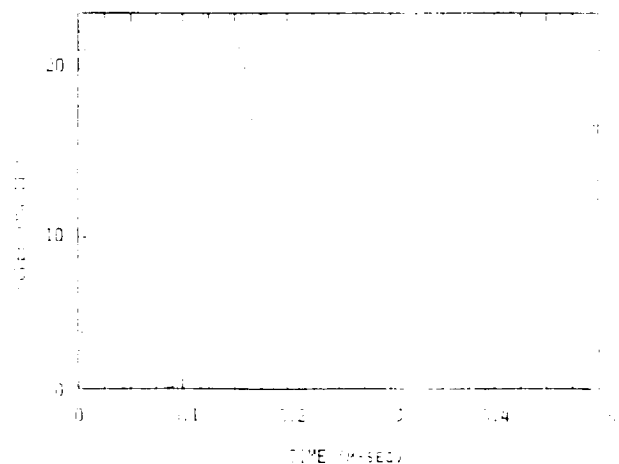


Figure 5 Power loss due to whistler radiation along magnetic field line in the unit of mWatts/m, as a function of time.

0.3 msec. The amplitude of the net J_x current lies below the initial zero level, indicating that it flows in the -x direction.

Time series data collected by probe 2 show similar whistler emission characteristics as those in probe 1. However, probe 2 registers a net cross-field J_x current at late time as shown by Figure 3(d). The field-aligned current J_z behaves quite differently at late times also. Figure 3(d) shows that the J_z amplitude reaches a high level at the pulse front and falls toward zero afterward. This suggests that, as the closure loop expands way beyond probe 2, the only significant current component observed at mid-plane is the cross-field current J_x . The magnitude of the steady J_x is approximately the same as that at probe 1. Thus, the time-averaged J_x component constitutes the essential part of the current closure path through which the source current closes upon itself.

To complete the picture of current closure a 2D streamline plot of J_x versus J_z is provided in Figure 4. This is a snapshot taken at time $t = 0.4$ msec, which shows that there is a region around the tether where streamlines connect to both ends of the current source. This region coincides with the bulk of the B_y region described in Figures 1-2 and can be viewed as the region for current closure since the tether current and the plasma currents form a closed loop. To be more exact, the complete current closure path consists of: (1) The outgoing portion of the closure current, as represented by the streamlines originating from the top of the tether along magnetic field lines connecting the top; (2) The cross-field portion of the closure current, as represented by the streamlines cutting across the magnetic field and the midplane on both sides of tether; and (3) The return portion of the closure current, as represented by the streamlines terminated at the bottom of the tether extending along magnetic field lines connecting the bottom. The transverse size of the closure region is estimated to be 2.2 km on either side of the tether at time $t = 0.4$ msec. Taking the expansion into account, the eventual closure circuit formed by the whistler pulses would be very localized.

Radiation Loss

As noted above, continuous emission of whistler waves from the tether is observed while the current closure path forms and expands. This is most evident in Figure 3(a) and Figure 4(a), which show persistent oscillations in electric field amplitudes after the pulse front passes through the observation points. Power loss due to whistler radiation along a magnetic field line is estimated by integrating the Poynting flux across a constant z line passing through the diagnostic probes. Figure 5 shows the integrated Poynting flux, in units of mWatts/m, as a function of time. Total power loss due to whistler radiation asymptotes to a value of $P = 32$ mWatts/m at late time. Note that this value is twice that given in the figure because whistler waves propagate in both directions of z . A set of simulations was conducted to find the scaling of radiation power as a function of the current strength I_0 . It was found that electric field, magnetic field, electron flow speed, and density perturbation scale linearly with I_0 , while the field energy densities and radiation power is proportional to the square of I_0 . Therefore, a source current at ten times the present strength radiates at one hundred times the present power.

The radiation resistance R of the whistler circuit can be evaluated using the relation $P = R I_0^2$. Based on the values of P and I_0 in unit length, the radiation resistance is estimated to be $R = 3.2 \times 10^{-4}$ Ohm/m. This numerical radiation resistance is two orders of magnitude larger than the analytic radiation resistance for the Alfvén waves [Dobrowolny and Veltri, 1986] based on a tether wire of 1 cm thick. Therefore, power loss due to whistler radiation is expected to be an important factor in determining the overall efficiency of the TSS. This agrees with an earlier analytical estimate by Barnett and Olbert [1986] who, using a constant-current moving-tether model, concluded that the radiation resistance from the lower hybrid band is much larger than that of the low frequency band.

Discussion

The issues of the plasma response to an imposed cross-field current and its application to the TSS current closure have been addressed in this letter. Previous MHD studies [Drell et al., 1965; Dobrowolny and Veltri, 1986] indicate that current closure is established by the Alfvénic pulse reaching the highly conducting lower ionosphere. In this scenario, a global current closure loop is envisioned and the timescale in forming such loop is expected to be longer than the ion cyclotron period [Goertz and Boswell, 1979]. Our simulation results augment previous understanding by focusing on closure processes of timescales shorter than the ion cyclotron period. Specifically, we consider the current closure being conducted by whistler-like processes in the magnetoplasma. In contrast to the Alfvénic picture, the whistler closure is highly localized around TSS and can be the dominant feature at early time. The Alfvénic processes can contribute to the current closure of the TSS only after the formation of the whistler loop. The details of the transition from the whistler closure to the Alfvénic one will be reported later.

Acknowledgment. This research was supported in part by NASA under contract NAS8-36811.

References

- Banks, P. M., P. R. Williamson, and K.-I. Oyama, Electrical behavior of a shuttle electrodynamic tether system (SETS), *Planet. Space Sci.*, **29**, 139-147, 1981.
- Barnett, A., and S. Olbert, Radiation and waves by a conducting body moving through a magnetized plasma, *J. Geophys. Res.*, **91**, 10117-10135, 1986.
- Chapman, S., and V. C. A. Ferraro, A new theory of magnetic storm, *Terr. Mag.*, **36**, 77, 1931.
- Colombo, G., E. M. Gaponchkin, M. D. Grossi, and G. C. Weiffenbach, Shuttle-borne <<Sky-hook>>: a new tool for low orbital altitude research, Report Geoastronomy No. 1, Smithsonian Astrophysical Observatory, 1974.
- Dobrowolny, M., and P. Veltri, MHD power radiated by a large conductor in motion through a magnetoplasma, *Nuovo Cimento C*, **2**, 27-38, 1986.
- Drell, S. P., H. M. Foley, and M. A. Ruderman, Drag and propulsion of large satellites in the ionosphere: an Alfvén engine in space, *J. Geophys. Res.*, **70**, 3131-3145, 1965.
- Goertz, C.K., and R.W. Boswell, Magnetosphere-Ionosphere Coupling, *J. Geophys. Res.*, **84**, 7239-7246, 1979.
- Helliwell, R.A., *Whistlers and Related Ionospheric Phenomena*, p. 30, Stanford Univ. Press, 1965.
- Kokubun, S., K. Hayashi, H. Kawano, T. Yamamoto, A. Nishida, K. Shiokawa, Y. Tonegawa, F. Tohyama, and T. Kamei, Magnetic field measurements on GEOTAIL, AGU fall meeting, SM51C-9, 1992.
- Mankotsky, A., R. N. Sudan, and J. Denavit, Hybrid simulation of ion beams in background plasma, *J. Comp. Phys.*, **70**, 89-116, 1987.
- Papadopoulos, K., C. L. Chang, P. Virello, and A. Drobot, On the efficiency of ionospheric ELF generation, *Radio Science*, **25**, 1311-1320, 1990.
- Stenzel, R.L., and J.M. Urrutia, Currents between tethered electrodes in a magnetized laboratory plasma, *J. Geophys. Res.*, **95**, 6209-6226, 1990.
- Urrutia, J.M., and R.L. Stenzel, Modeling of induced currents from electrodynamic tethers in a laboratory plasma, *Geophys. Res. Lett.*, **17**, 1589-1592, 1990.
- Chang, C. L., A. T. Drobot, and P. Satya-Narayana, Science Applications International Corporation, 1710 Goodridge Drive, McLean, Virginia 22102.
- A. S. Lipatov, Institute of Space Physics, Moscow, Russia.
- K. Papadopoulos, Department of Physics and Astronomy, University of Maryland, College Park, Maryland 20770.

Received: October 1, 1993; Revised: December 29, 1993; Accepted: February 28, 1994

APPENDIX 3

PROCEEDINGS
of the

Fourth International Conference
on
Tethers In Space

Smithsonian Institution • Washington, D.C.

10 - 14 April 1995

Sponsored By:

- **National Aeronautics and Space Administration**
 - **Smithsonian Astrophysical Observatory**
 - **Agenzia Spaziale Italiana**
 - **Lockheed Martin**
 - **Alenia Spazio S.p.A.**
 - **Science Applications International Corporation**
-

Volume II

CURRENT CLOSURE FOR A TETHERED SATELLITE SYSTEM

Chia-Lie Chang and Adam T. Drobot
Applied Physics Operation
Science Applications International Corporation
1710 Goodridge Drive, McLean, Virginia 22102

Konstantinos Papadopoulos
Department of Physics, University of Maryland
College Park, Maryland 20742

Abstract

Physical processes of current closure for a moving tethered satellite system (TSS) subject to a sudden switch-on electric current have been studied analytically based on a three dimensional linear model that included both the electron and the ion responses. It was found that the current closure loops were formed at early time as the whistler pulse excited by the surge of the tether current propagated away. The formation of the current closure path occurred in the whistler timescale, which is much shorter than that of the Alfvénic time. The closure loops expanded rapidly along the magnetic field lines at the whistler speed. However, these loops could be highly localized around the TSS if the magnetic field is not perpendicular to the tether orientation.

Introduction

A fundamental problem associated with the operation of electrodynamic tethers in space is the current closure through the magnetoplasma. Owing to the motion of the tethered satellite system (TSS) relative to the stationary geomagnetic field, an emf is induced across the conducting tether. If electrical contact is established with the ionospheric plasma at both ends of the tether, current can be drawn through the tether with a variety of interesting applications [1-2]. However, as the TSS moves through the ambient plasma at a speed V_0 , disturbances will be generated in the ionosphere at a typical time scale of l/V_0 , which is the transit time of the plasma contactors having a characteristic size l in the direction of the motion. As a result, the current collection and emission processes associated with the TSS are strongly influenced by this transit time effect. Moreover, the description of TSS as an electric circuit will not be completed unless the dynamic and transient nature of the current closure processes occurred in the surrounding plasma is included. The feasibility for the ionospheric plasma to react and to form a closure path within the transit time is the main focus of this study.

In the past, theories describing waves generated by the motion of a conducting body through a magnetized plasma have assumed steady state conditions under MHD approximation [3-5]. When the steady state MHD theory is applied to the closure aspect of TSS, it predicts a global current closure path through the conducting lower ionosphere mediated by the propagation of Alfvén waves. The implicit assumption in this approach is that the time scale involved in the

closure processes is longer than the ion cyclotron period. However, by considering the realistic TSS parameters, $V_o \approx 8$ km/sec and the satellite size $l \approx$ few meters, the transit time is of the order of \sim msec, which is more than an order of magnitude below the ion cyclotron period ($1/f_{ci} \approx 30$ msec). Thus the viable waves involved in the closure process are likely to have higher frequency than those of the Alfvén waves. This suggests that the whistler waves in the frequency range of kHz and above are more likely to contribute to the current closure processes around the TSS. Recent laboratory experiments [6-13] and hybrid simulations [14] have yielded similar conclusion, namely, whistler dynamics may be the most prominent physical effect at Low Earth Orbit (LEO) during the TSS mission.

In view of the deficiency in the understanding of current closure processes in the magnetoplasma, we performed a comprehensive study of the current closure problem in space that includes low frequency Alfvén and ion acoustic waves, as well as high frequency whistler waves. Our analytic approach is to solve a three dimensional, initial value problem of a moving tether with a sudden switch-on of its current. Specifically, we have formulated and solved the linearized Maxwell's equations in Fourier space. Contributions from individual plasma waves were summed over to yield a combined spectral amplitude. Subsequently, we have performed inverse Fast Fourier Transform (IFFT) to obtain numerical solutions in real space and time. The plasma currents involved in the formation of current closure path were derived from the field solutions. This approach provides detailed dynamic description of the closure processes as well as the topological information of the current closure path in space. Moreover, relative weighting of the contributing waves in the closure processes can be assessed. Numerical examples shown in the following sections are based on realistic ionospheric parameters relevant to the TSS mission.

Theory

A schematic view of the three dimensional model used in the ensuing analysis is shown in Figure 1. Specifically, a tether of length L is oriented in the z direction and is located at the center of the computation domain as prescribed by the box. The tether moves in the x direction at a speed V_o . The ambient magnetic field, as represented by B_o , is uniform in space and can have arbitrary orientation. In Figure 1, it is drawn to point in the y direction for illustrative purpose. The tether current density, in its analytic form, can be expressed as

$$J_z = I_o \delta(x - V_o t - L_x / 2) \delta(y - L_y / 2) H\left(\frac{z - L_z / 2}{L / 2}\right) \eta(t) \hat{e}_z \quad (1)$$

where I_o is the current strength, $\eta(t)$ is a switch-on function at time $t = 0$, $H(z)$ is a top-hat function representing finite length of the tether in the z direction, L_x , L_y , and L_z are the sizes of the computation region (the box) in the x , y , and z directions, respectively. There are two important time scales introduced by the current expression in (1). For instance, tether motion is represented by the first delta function on the RHS of (1), which indicates that the tether location in x changes with time t , at a speed V_o . As was discussed in the Introduction section, the motion of tether will induce transient plasma responses due to the transit time effects of the tethered satellite. In the case of TSS, this time scale falls in the whistler regime. Therefore, this is the first important time scale in the closure problem. The second time scale is embedded in the switch-on function $\eta(t)$. In the current analytic model it is taken as a step function in time. Thus it contains predominantly very short time scales. In reality, the switch-on time is determined by various factors, such as the switches in the electric circuit of the TSS, and the charge collection and emission processes at the satellite and the orbiter end, respectively. A more practical switch-on factor should be constructed based on systemic consideration of the TSS. Such factors will be introduced in the future studies of the current closure problem.

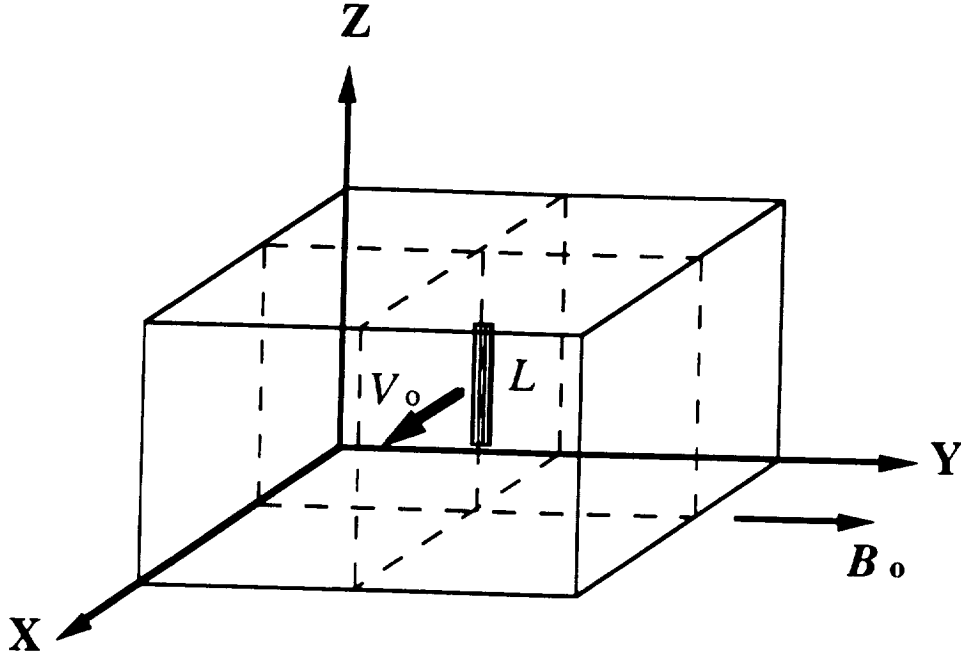


Figure 1. Coordinate system of analytic model of a tethered satellite system (TSS) moving in the ionosphere in three dimensions.

A linearization procedure is used to derive the governing wave equations. The field disturbances E , B in the magnetoplasma surrounding the tether current J_s are taken as the first order quantities. From Maxwell's equations, we have

$$\nabla \times E = -\frac{1}{c} \frac{\partial B}{\partial t} \quad (2)$$

$$\nabla \times B = \frac{4\pi}{c} [J_s + n_o e (V_i - V_e)] \quad (3)$$

where the displacement current term is neglected. This approximation is justified at frequencies about or below the whistler regime. The plasma currents V_i and V_e are derived from warm fluid equations given by

$$\frac{\partial n_{i,e}}{\partial t} + n_o \nabla \cdot V_{i,e} = 0 \quad (4)$$

$$n_o \frac{\partial V_i}{\partial t} = \frac{n_o e}{m_i} \left(E + \frac{V_i \times B_o}{c} \right) - \frac{\nabla(n_i T_{io})}{m_i} \quad (5)$$

$$n_o \frac{\partial V_e}{\partial t} = -\frac{n_o e}{m_e} \left(E + \frac{V_e \times B_o}{c} \right) - \frac{\nabla(n_e T_{eo})}{m_e} \quad (6)$$

Both V_i and V_e are first order quantities. Note that the electron and the ion temperatures are included in the fluid formulation so that the ion acoustic waves can be retained in this representation. In order to simplify the above equations, we invoke the quasi-neutrality condition

$$n_e \approx n_i \quad (7)$$

This condition implies that there is no net charge accumulation in the current closure region. Therefore, the sheath regions around plasma contactors at both ends of the TSS are not included in this analysis. This is consistent with the fact that the current closure path under this study locates away from the sheath regions.

To carry out the analysis further, we replace the first order quantities such as the perturbed electric and magnetic fields by their Fourier representations

$$E, B \propto \exp(ik \cdot x - \omega t) \quad (8)$$

This corresponds to switching the spatial and the temporal operators by their Fourier equivalents

$$\nabla \rightarrow ik ; \quad \frac{\partial}{\partial t} \rightarrow -\omega \quad (9)$$

After some lengthy algebra, equations (2) to (7) can be combined to yield the following simplified equation for the B field

$$\begin{aligned} -\lambda \omega^2 B &+ \omega^2 (\lambda - 1) [k \times (k \times B)] \\ &- k \times \{ [(k \times B) \times \hat{b}] \times \hat{b} \} \\ &- \omega (2 - \lambda) k \times [(k \times B) \times \hat{b}] \\ &+ \frac{\beta}{\lambda \omega^2 + \beta k^2} [k \times (k \times \hat{b})] \{ k \cdot [(k \times B) \times \hat{b}] \} \\ \equiv &- i \omega^2 (\lambda - 1) (k \times J_s) \\ &+ i k \times [(J_s \times \hat{b}) \times \hat{b}] \\ &+ i \omega (2 - \lambda) k \times (J_s \times \hat{b}) \\ &- i \frac{\beta}{\lambda \omega^2 + \beta k^2} [k \times (k \times \hat{b})] [k \cdot (J_s \times \hat{b})] \end{aligned} \quad (10)$$

where

$$\lambda = 1 + (m_e / m_i); \quad \hat{b} = B_0 / |B_0|$$

In deriving (10), the following normalizations are adopted:

$$B \Leftrightarrow B / |B_0|; \quad k \Leftrightarrow k c / \omega_{pi}$$

$$w \Leftrightarrow w / \Omega_i ; \quad J_s \Leftrightarrow \left(4\pi / |B_o| \omega_{pi} \right) J_s \quad (11)$$

Although complicated in form, equation (10) is arranged in a physical way so that each term represents a physical process occurred in the plasma. For instance, the second term on the LHS is due to finite electron mass effect. The third term on the LHS is from the Alfvén responses. The fourth term on the LHS is from the whistler reaction of electrons, and the fifth term represents the ion acoustic responses. Corresponding terms on the RHS of Eq. (10) represent excitations of similar nature by the switch-on of tether current. It is important to remark that the only approximations used in deriving Eq. (10) are the exclusion of displacement current term in (3) and the utilization of quasi-neutrality condition. Both approximations are valid in dealing with the whistler, the Alfvén, and the ion acoustic waves. In addition, Eq. (10) includes the effect of finite electron mass, which is a more advanced treatment than that of the hybrid simulation [14].

Based on the analytic tether current given in (1), magnetic perturbation B as a function of Fourier components k and w can be solved by inverting Eq. (10). The inversion process involves the evaluation of the 'poles' of the plasma dispersion as the representative contribution from various wave components. The first order B field can then be estimated by summing over the contributions from all these poles. Since the tether motion introduces a relation $w = k \cdot V_o$ in the Fourier space, perturbed magnetic field B is a function of k only. Knowing B , the plasma current J can be obtained by

$$J = \frac{ic}{4\pi} k \times B \quad (12)$$

Both J and B in the above equation are under Fourier representations. Inverse Fast Fourier Transform (FFT) can be applied numerically to transform these components back into the real space and time.

Numerical Results

Numerical examples to be shown in the following correspond to a source current J_s of unit strength. Since equation (10) is linear, the results can be scaled proportionately with the source current strength. The computation is conducted for parameters relevant to the TSS in the F-region of the ionosphere. The ambient environment consists a stationary plasma (with O^+ ions) and a uniform magnetic field B_o . The background magnetic field strength B_o and the plasma density n_o are 0.35 gauss and 10^{16} /c.c., respectively. The tether length $L = 1$ km, which is located at the center of the box, and travels at a speed of $V_o = 8$ km/sec in x . The computation box contains $64 \times 128 \times 64$ rectangular grids with a spatial resolution of 0.1 km in each direction. Thus the box covers a geospace of the size 6.4 km \times 12.8 km \times 6.4 km. In the first set of examples the magnetic field is in the y direction. In the second example the magnetic field is in the y - z plane and has an angle of 30 degrees with respect to the y axis.

There are a number of important issues to be addressed after the initial switch-on of the tether current. Specifically, the key questions to ask are:

- (a) What are the dominant mechanisms in the ionospheric plasma for current closure ?
- (b) What is the timescale for current loops to form ?
- (c) What is the size and shape of these current loops ?

Figure 2 shows the contour plot of field-aligned current density perturbation J_y at a fixed time of $t = 0.3$ msec after the initial switch-on. The computation domain is encircled by the box of white border lines. Horizontal lines are in the y direction and vertical lines are in the z direction. The contours of J_y in a y - z plane passing through the tether are plotted in gray scales from minus (light) to plus (dark) in normalized unit. The ambient magnetic field is directed in the y direction. As we can see from this plot, the amplitude of field-aligned current density is peaked along the magnetic field lines passing through both ends of the tether. Thus two field-aligned current channels linking

to the top and the bottom of the tether are identified. Along these channels, J_y amplitude changes sign as one passes through the end point of the tether, signifying that the field-aligned current flows either toward the end point (the upper channel) or away from the end point (the lower channel). This picture is consistent with that of the 2D hybrid simulation results [14], which show similar field-aligned current channels as part of the current closure loops.

Figure 3 shows the contour plot of the corresponding cross-field current density J_z in the same settings as those in Figure 2. The tether current can be seen as the bright line at the center of the y-z plane and is directed toward the negative z direction. The gray shaded areas in between the upper and the lower field-aligned current channels contain the closure currents flowing in the positive z direction. Since these closure currents are distributed over a large volume in space, their amplitudes are more than an order of magnitude lower than that of the tether current. Therefore, their presence are not as noticeable as the tether current in gray scales. However, by completing the return paths between two field-aligned current channels they are an integral part of the closure loop. As will be evident later, these closure currents are in fact the cross-field electron Hall currents associated with the whistler waves.

Figure 4 shows the contours of the field-aligned current density J_y at three different times 0.1, 0.3, and 1.0 msec after the switch-on. As we can see from this plot, the current channels expand rapidly in time. The expansion along the field lines has a speed of roughly 10^4 km/sec, which corresponds to the group velocity of whistler propagation at a frequency of 10 kHz. It is important to realize that this speed is two orders of magnitude faster than the typical Alfvén velocity in the region ($V_A \sim 200$ km/sec). Therefore, this observation implies that (a) the dominant physical process for current closure is the whistler waves, and (b) the current loop is formed in whistler timescale. Further confirmation of the whistler loop is given by Figure 5. In this Figure, the B vectors at various y points along one of the current channels are plotted. The time for this plot is at $t = 1$ msec. As we can see, orientation of the B field rotates continuously along the current channel (or equivalently along the field line), thus agreeing with the characteristics polarization of a right-hand circularly polarized whistler wave rather than to the Alfvén waves of linear polarization.

Our numerical computation can provide quantitative estimates of the relative contributions from various wave modes. Assuming that the whistler contribution at $t = 1$ msec is of the order 1, relative weightings from other wave modes are arranged in descending order: magnetosonic waves (compressional Alfvén waves perpendicular to B_0) $\sim 10^{-1}$; compressional Alfvén waves parallel to B_0 $\sim 10^{-2}$; shear Alfvén waves and ion acoustic modes are below the level of $\sim 10^{-4}$. Thus at early time (≤ 1 msec) the predominant plasma response is the whistler waves. However, the compressional Alfvén waves may have significant contributions at later time. To estimate its effects, the computational domain has to be extended to provide proper resolution for the long wavelength Alfvén modes at low frequency. Such work is currently in progress.

In order to address (c), we now show in Figure 6 the streamline plots of the current density J vector in three dimensions at times 0.1, 0.3, and 1.0 msec. The J streamlines are constructed in a sub-region within the computation box, which consists of a stack of half y-z planes extending from near the tether (on the right at $y = L_w/2$) to the open space (on the left at $y = 0$). The half y-z planes to be included in the sub-region are the left half of the mid y-z plane that contains the tether, and two additional half y-z planes on either side. As can be seen from these plots, the current loops are represented by tangled streamlines in space. Initially, they are concentrated near the tether at 0.1 msec, and later expanded into a more familiar form of current channels plus cross-field currents at 1 msec. In response to the sudden switch-on, the current loops are formed by and expand with the whistler pulse. Main portion of the cross-field currents can be seen located near the pulse front. These currents are part of the electron Hall currents associated with the whistler waves. From the side view of the sub-regions (not shown in this paper), we can see that the current loops are narrowly confined in x, with a typical width of $\Delta x \sim 0.2$ km. Since the current loops expand at a much higher speed than the tether motion, there is no discernible whistler wing pattern.

The above numerical examples have a B_0 oriented in perpendicular to tether. A more realistic situation is to have an inclined ambient magnetic field with respect to the tether at angles other than 90 degrees. We have investigated a case of B_0 at 60 degrees angle with respect to the tether (or 30 degrees to the y axis). Preliminary results indicate that the topology of current closure loops

differs substantially from that of the perpendicular case. Figure 7 shows the J streamlines of such example at $t = 1$ msec. The magnetic field is directed from the lower left corner to the upper right corner of the small box. It is interesting to observe that the current loops are skewed to one side of the tether. A possible explanation is that the current loops favor the side that has shorter closure path. These current loops are formed close to tether at early times and remain stable after the whistler pulse clears the region. The details of this investigation will be reported later.

CONCLUSIONS

We have performed analytic study of the current closure problem for the tethered satellite system in the Low Earth Orbit (LEO). Our results show that, at early time, the dominant physical mechanism responsible for the formation of current closure loops is the whistler waves excited by the switch-on of tether current. Thus the time scale for the formation of closure loops is the whistler period, which is much shorter than the Alfvénic time. The resulting current closure loops consist field-aligned current channels as well as cross-field current regions connecting these channels. These current loops are localized around TSS instead of reaching far into the lower ionospheric E-region. The localization improves as the angle between the ambient magnetic field and the tether orientation deviates from 90 degrees.

ACKNOWLEDGEMENTS

This work was supported in part by NASA under Contract Number NAS8-36811.

REFERENCES

- [1] Colombo, G., Gaposchkin, E.M., Grossi, M.D., and Weiffenbach, G.C., "Shuttle-borne 'Skyhook'; A new tool for low-orbital altitude research", *Smith. Astrophys. Res. Rep.* in *Geoastromy* No. 1, 1974.
- [2] Williamson, P.R., and P.M. Banks, "The tethered balloon current generator - a space-tethered subsatellite for plasma studies and power generation", A final report submitted to NOAA, Environmental Research Laboratories, Boulder, Colorado, 80302, 1976.
- [3] Drell, S.P., H.M. Foley, and M.A., Ruderman, "Drag and propulsion of large satellites in the ionosphere: an Alfvén engine in space", *J. Geophys. Res.*, **70**, p. 3131-3145, 1965.
- [4] Dobrowolny, M., and P. Veltri, "MHD power radiated by a large conductor in motion through a magnetoplasma", *Nuovo Cimento C*, **2**, p. 27-38, 1986.
- [5] Estes, R.D., "Alfvén waves from an electrodynamic tethered satellite system", *J. Geophys. Res.*, **93**, p. 945-956, 1988.
- [6] Stenzel, R.L., and J.M. Urrutia, "Currents between tethered electrodes in a magnetized laboratory plasma", *J. Geophys. Res.*, **95**, p. 6209-6226, 1990.
- [7] Urrutia, J.M., and R.L. Stenzel, "Modeling of induced currents from electrodynamic tethers in a laboratory plasma", *Geophys. Res. Lett.*, **17**, p. 1589-1592, 1990.
- [8] Stenzel, R.L., J.M. Urrutia, and C.L. Rousculp, "Pulsed currents carried by whistlers. Part I: Excitation by magnetic antennas", *Phys. Fluids B*, **5**, p. 325-338, 1993.
- [9] Urrutia, J.M., R.L. Stenzel, and C.L. Rousculp, "Pulsed currents carried by whistlers. II. Excitation by biased electrodes", *Phys. Plasmas*, **1**, p. 1432-1438, 1994.
- [10] Rousculp, C.L., R.L. Stenzel, and J.M. Urrutia, "Inductive and space charge electric fields in a whistler wave packet", *Phys. Rev. Lett.*, **72**, p. 1658-1661, 1994.
- [11] Urrutia, J.M., R.L. Stenzel, and C.L. Rousculp, "Three-dimensional currents of electrodynamic tethers obtained from laboratory models", *Geophys. Res. Lett.*, **21**, p. 413-416, 1994.

- [12] Urrutia, J.M., R.L. Stenzel, and C.L. Rousculp, "Pulsed currents carried by whistlers. III. Magnetic fields and currents excited by an electrode", *Phys. Plasmas*, 2, p. 1100-1113, 1995.
- [13] Stenzel, R.L., J.M. Urrutia, and C.L. Rousculp, "Pulsed currents carried by whistlers. IV. Electric fields and radiation excited by an electrode", *Phys. Plasmas*, 2, p. 1114-1128, 1995.
- [14] Chang, C.L., A.S. Lipatov, A.T. Drobot, K. Papadopoulos, and P. Satya-Narayana, "Hybrid simulations of whistler waves generation and current closure by a pulsed tether in the ionosphere", *Geophys. Res. Lett.*, 21, p. 1015-1018, 1994.

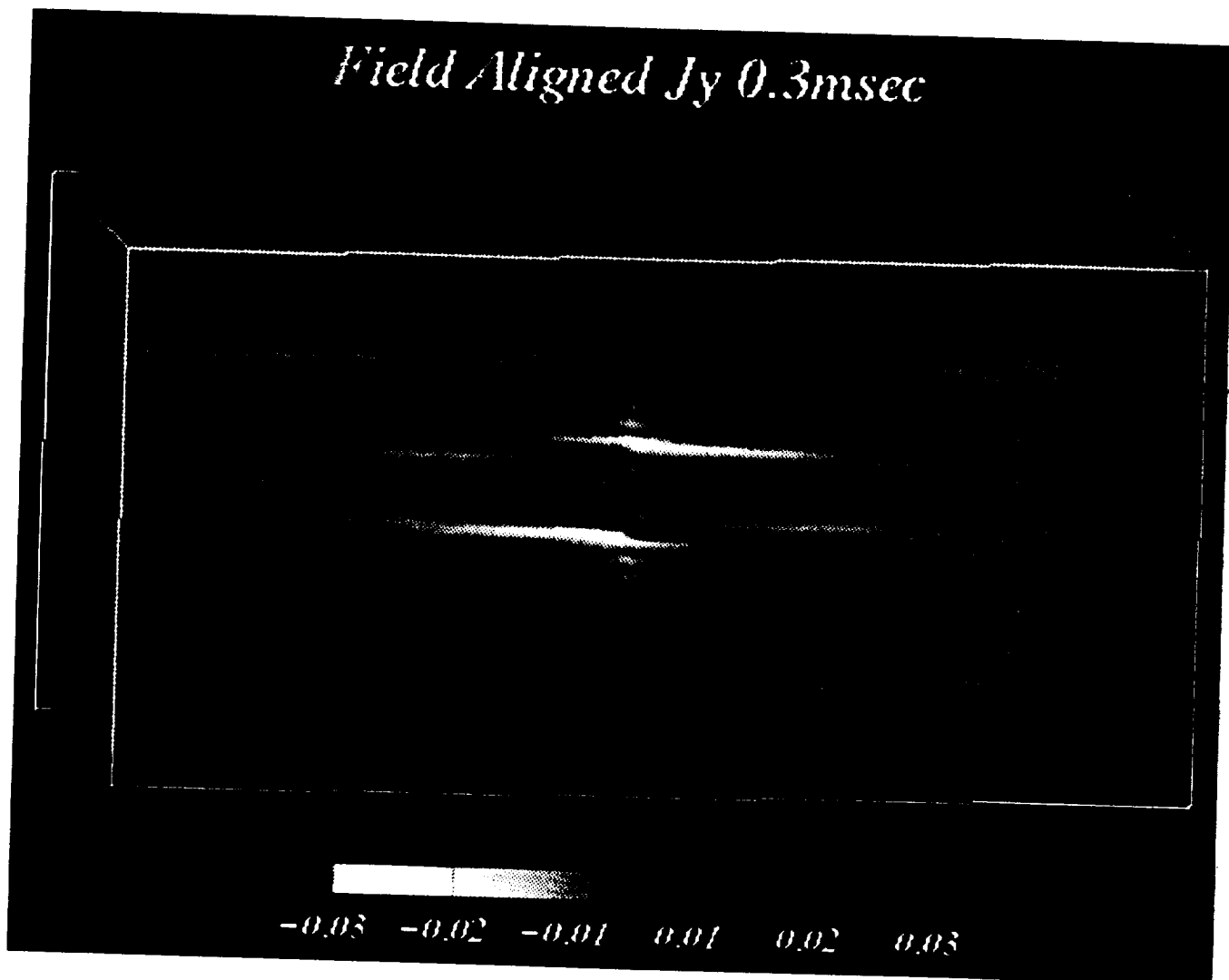


Figure 2. Coontours of J_y current in the y - z plane that contains a vertical tether at center. Two field-aligned current channels can be identified as the black/white horizontal strips passin through both ends of the tether.

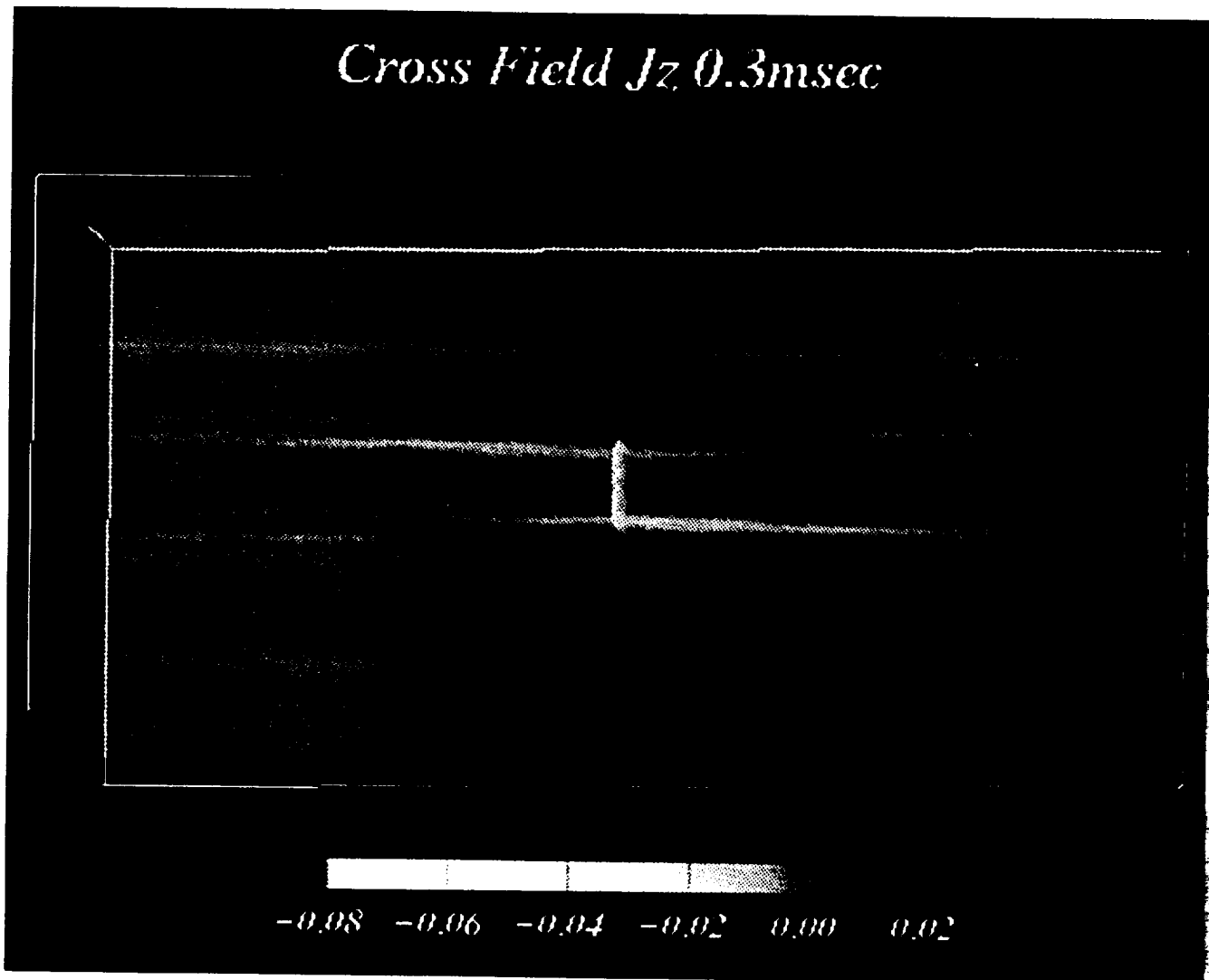


Figure 3. Coontours of J_z current in the y-z plane. Tether current is the white vertical line at the center of the plane. Closure currents that connect two field-aligned current channels are contained in the gray areas in between the current channels.

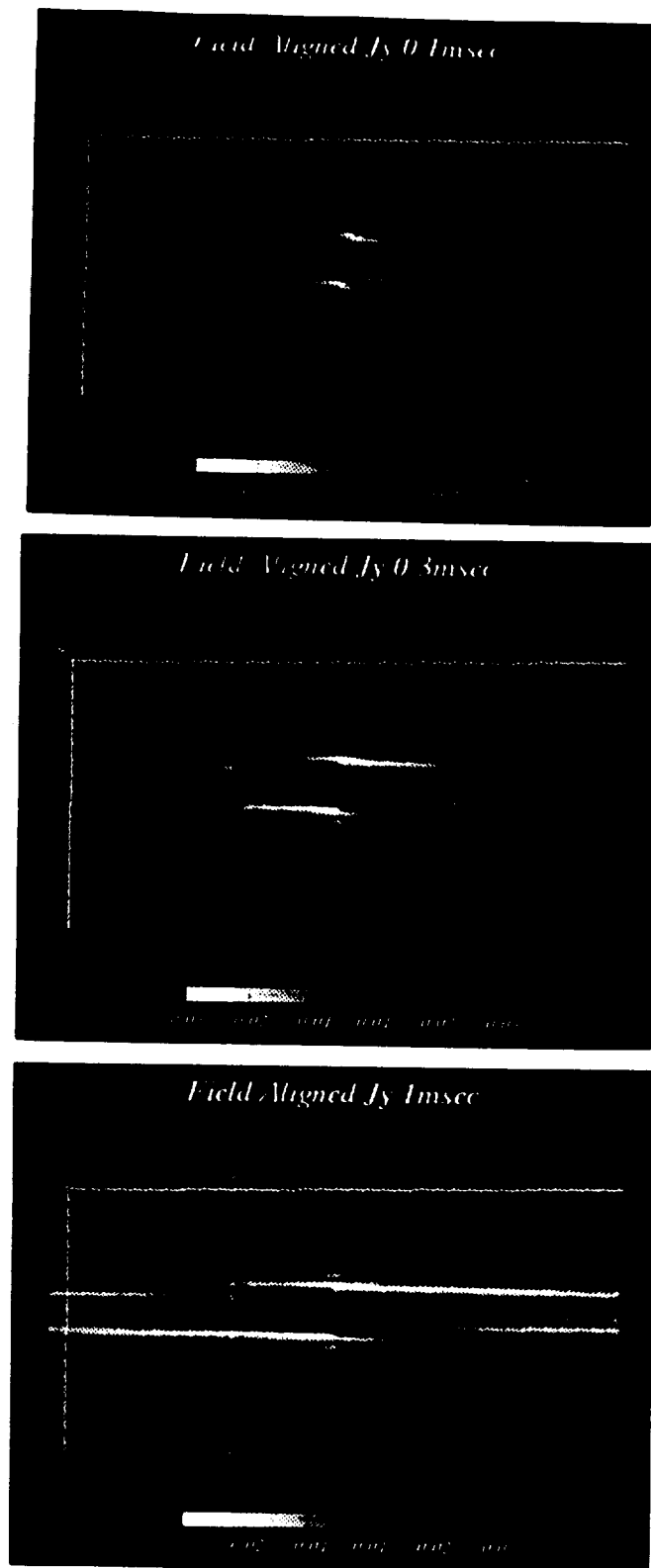


Figure 4. Coontours of J_y current at time 0.1, 0.3, and 1 msec after switch-on. The field-aligned current channels expand along the field line at the whistler speed. This is a clear indication that the current closure process at early time is dominated by the whistler dynamics.

B Vector Along Field Line 1msec

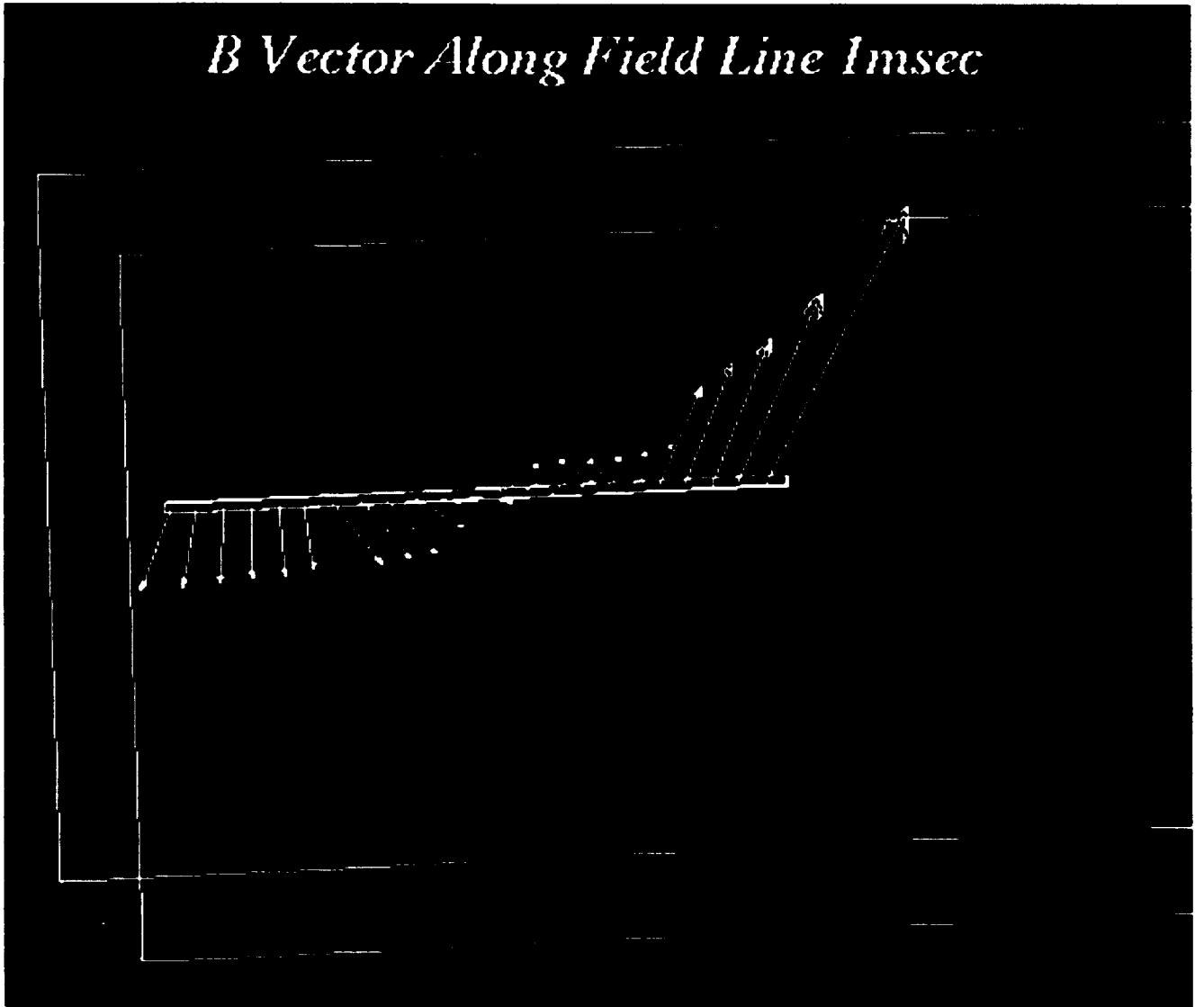


Figure 5. Vector plot of B field along one of the current channel. Rotation of the B vectors along the field lines is observed, which is a typical characteristics of the whistler waves.

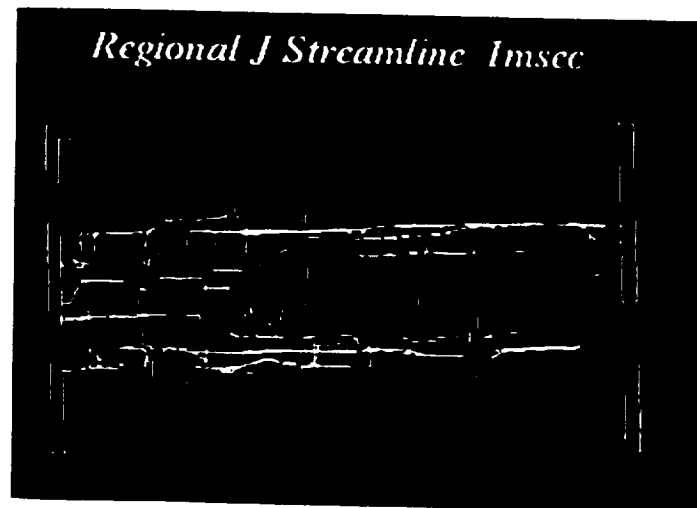
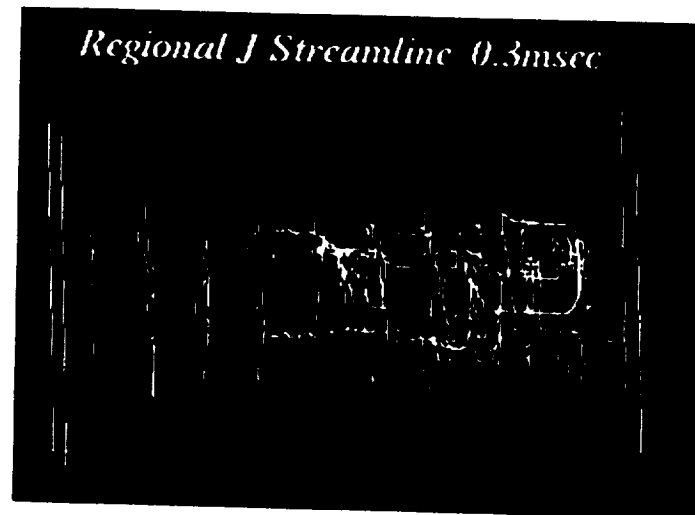
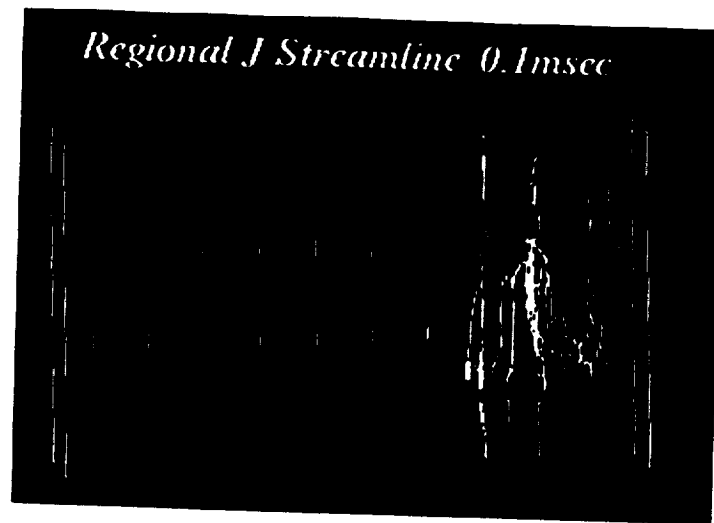


Figure 6. Three dimensional streamlines of the current density vector J at times, 0.1, 0.3, and 1 msec. These streamline plots show substantial amount of cross-field currents in the whistler pulse, especially at the pulse front. Field-aligned current channels are formed as the pulse front passes through.



Figure 7. Example of J streamlines in a B_0 field that is at 60 degree angle with respect to the tether . Direction of the magnetic field is pointed from lower left corner to upper right corner. Current closure loops are found to be skewed to the left side of the tether.

APPENDIX 4

Basic Physics of Current Closure

presented

by

Chia-Lie Chang

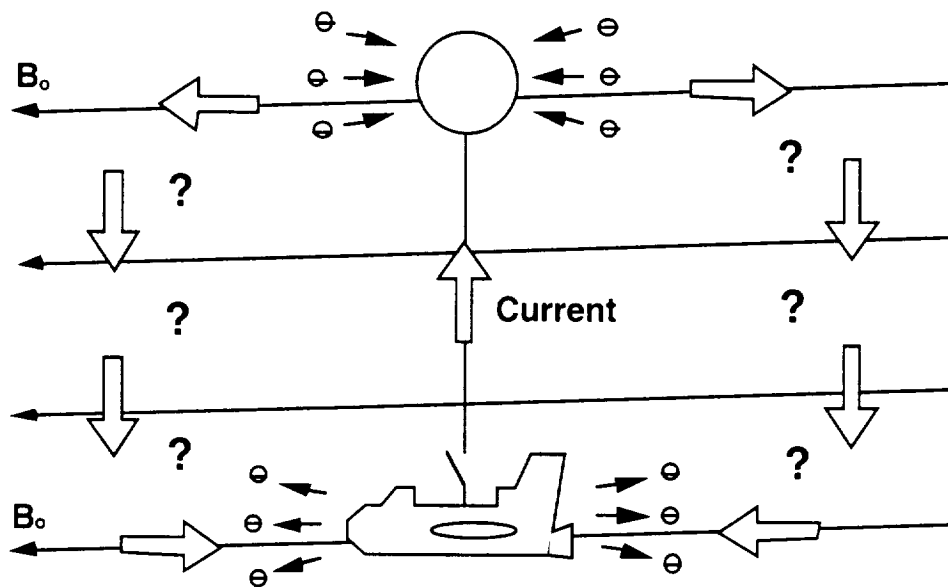
**Science Applications International Corporation
McLean, Virginia**

May 10, 1995

BASIC CONCEPT OF CURRENT CLOSURE

AFTER THE MAIN SWITCH IS CLOSED, CURRENT STARTS TO FLOW

CIRCUIT COMPONENTS: TSS + IONOSPHERE



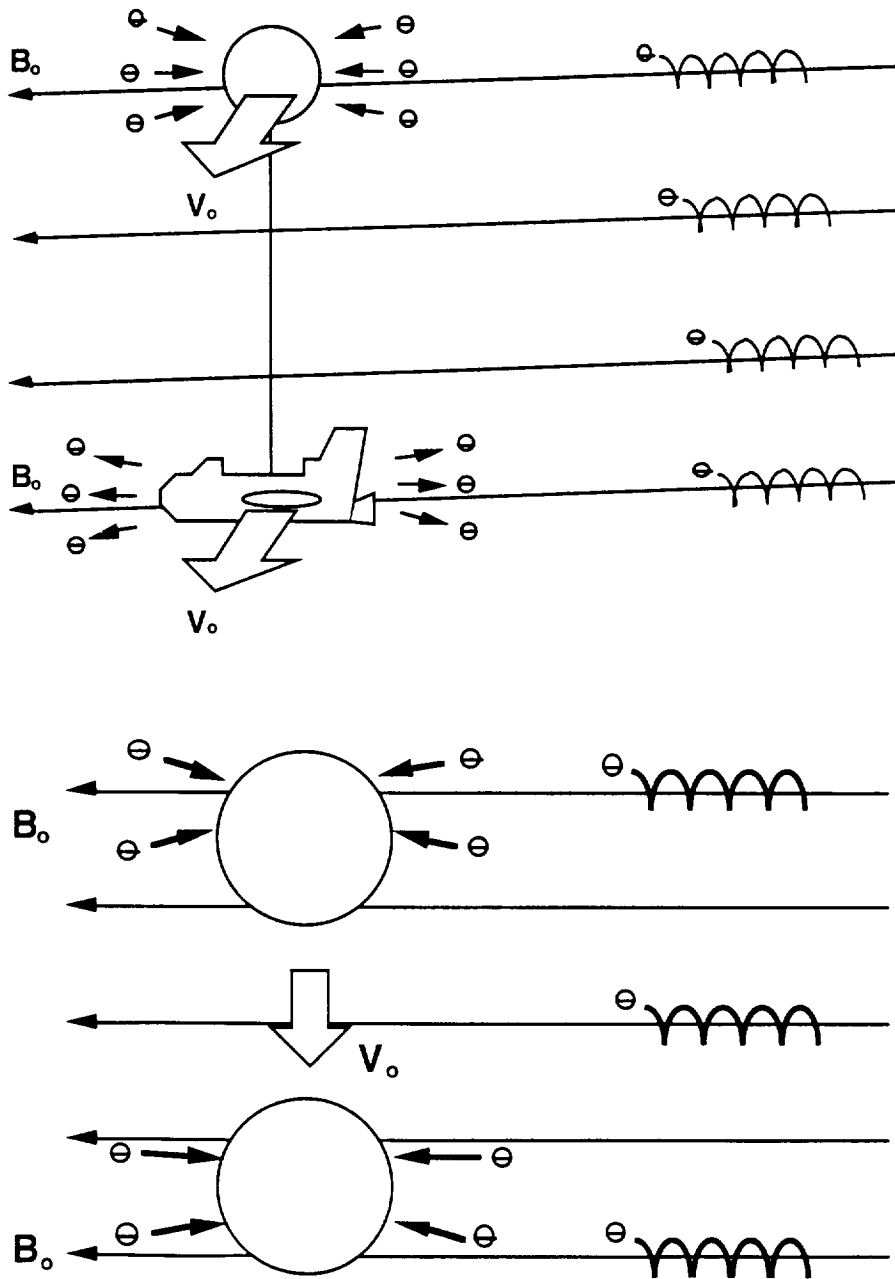
THE KEY QUESTION IS:

HOW DOES THE CURRENT FLOW THROUGH IONOSPHERE ??

CURRENT CLOSURE FOR THE TSS

ELECTRONS ARE **TIED** TO THE MAGNETIC FIELD LINES

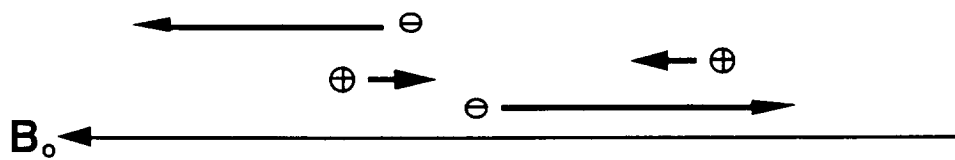
SATELLITE IS MOVING **ACROSS** THE FIELD LINE AT ~ 8 Km/Sec



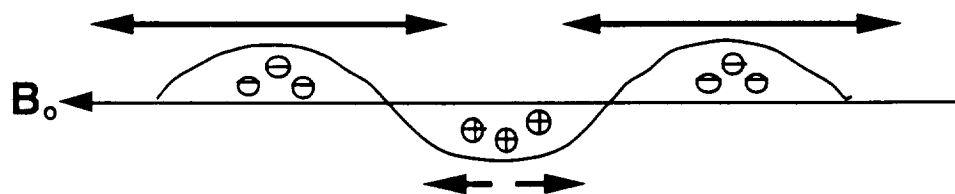
MOTION OF THE CHARGE PARTICLES

ALONG THE MAGNETIC FIELD

RANDOM THERMAL MOTION

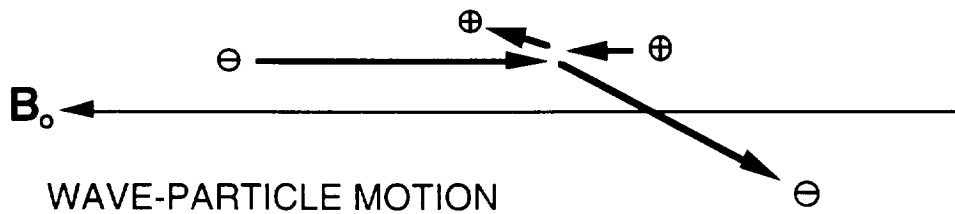


ORDERLY WAVE MOTION

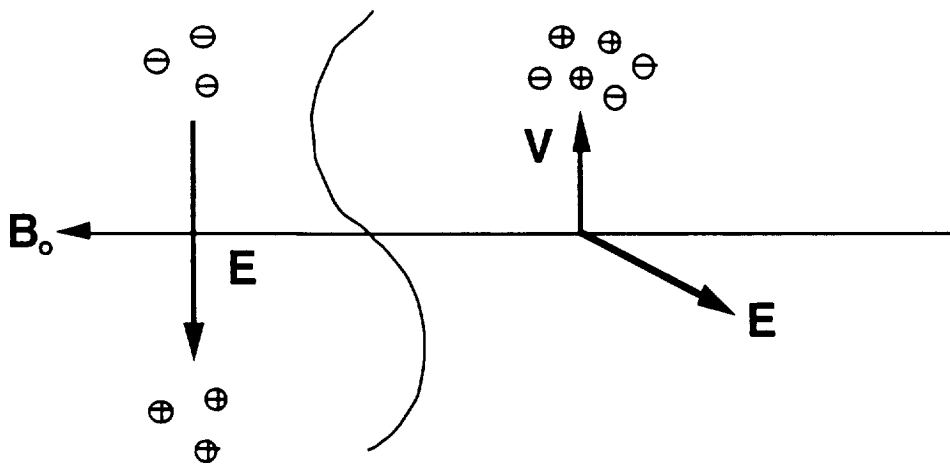


ACROSS THE MAGNETIC FIELD

PARTICLE COLLISIONS

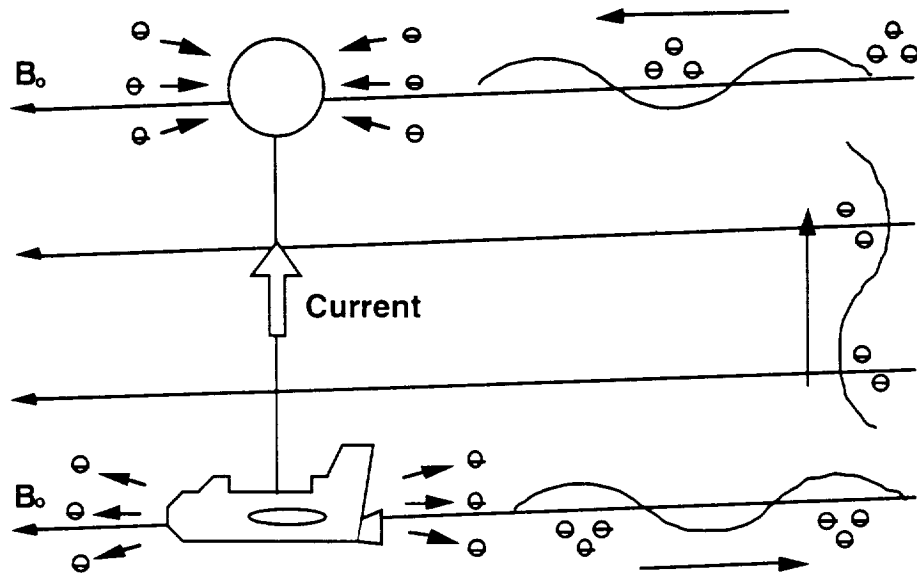


WAVE-PARTICLE MOTION



CURRENT CLOSURE AND PLASMA WAVES

TRANSPORT OF CHARGES (& CHARGE DISTURBANCES) OCCURS IN THE FORM OF PLASMA WAVES



TWO POSSIBLE PLASMA WAVES THAT CAN CARRY CURRENT AT THE TSS-1R ORBIT DURING THE MISSION

ALFVEN WAVES
WHISTLER WAVES

CHARACTERISTICS OF ALFVEN WAVES

WAVE MOTION: INVOLVE BOTH O⁺ IONS AND ELECTRONS

DISPERSION: $\lambda f = V_A$

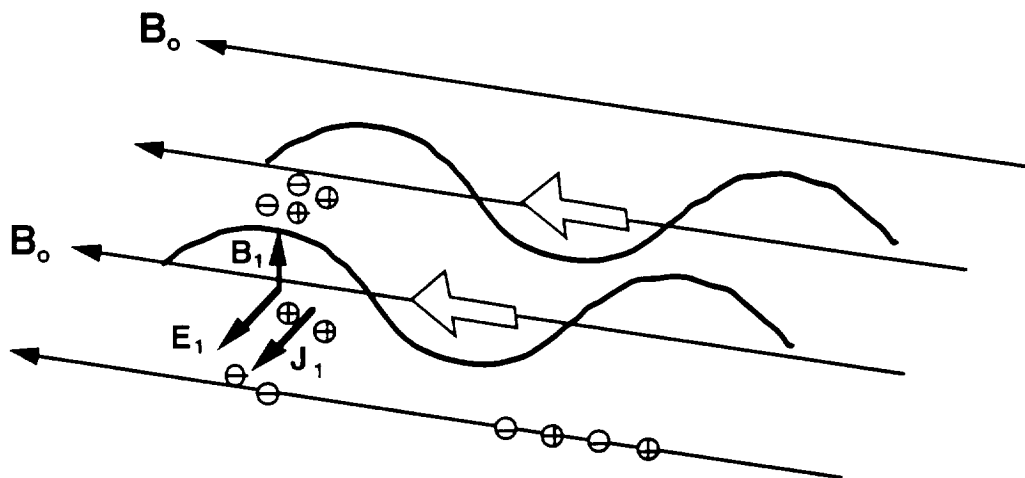
FREQUENCY(f): BELOW CYCLOTRON FREQUENCY OF O⁺ (< 33 HZ)

WAVE SPEED: $V_A \sim B_0 / \sqrt{N_0}$, 190 Km/Sec -> 1900 Km/Sec

WAVELENGTH: $\lambda = V_A / f$, LOONGER THAN 6 Km -> 60 Km

DIRECTION: MAINLY PARALLEL TO THE MAGNETIC FIELD

POLARIZATION: LINEARLY POLARIZED

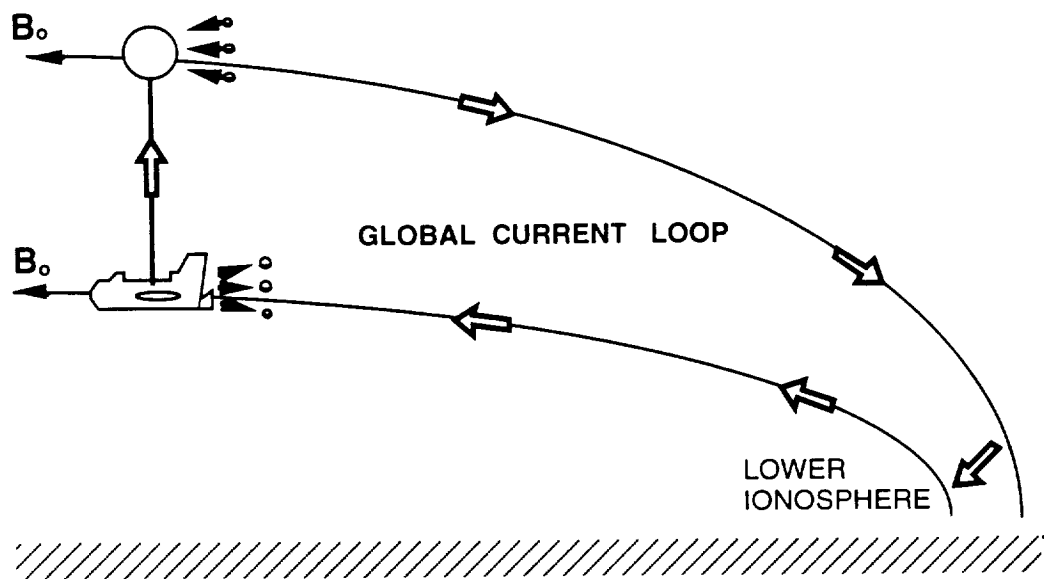


ALFVENIC CIRCUIT FOR CURRENT CLOSURE

ENVISION **LARGE PHANTOM LOOPS** EXTENDING FROM TSS ALL THE WAY INTO **LOWER IONOSPHERE**

ELECTRONS MOVE **ALONG** MAGNETIC FIELD LINES AT **HIGH ALTITUDE**

ELECTRONS MOVE **ACROSS** MAGNETIC FIELD LINES VIA **COLLISIONS** AT THE LOWER IONOSPHERE.



CHARACTERISTICS OF WHISTLER WAVES

WAVE MOTION: INVOLVE ELECTRONS ONLY

DISPERSION: $\lambda f = (c f / f_{pe}) (f_{ce} / f - 1)^{1/2}$

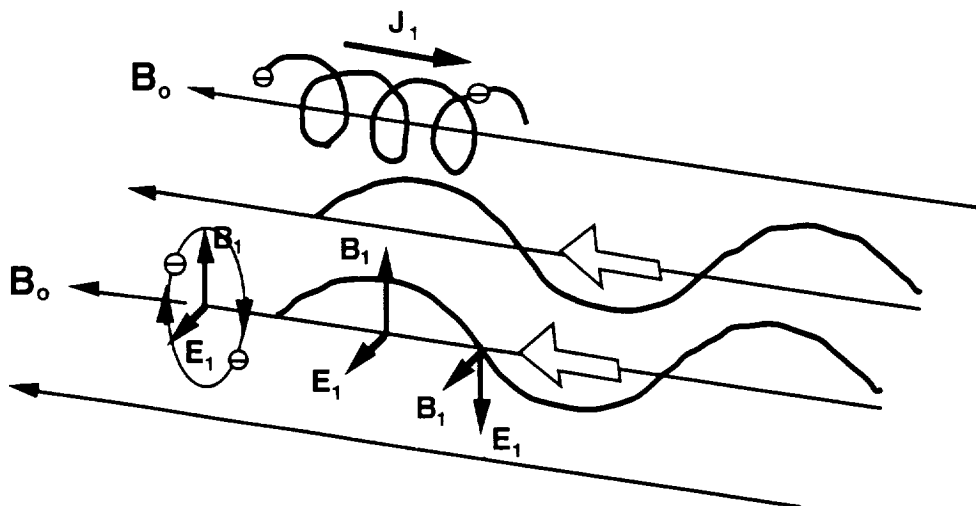
FREQUENCY(f): ABOVE CYCLOTRON FREQUENCY OF O+ (> 33 HZ)
BUT BELOW CYCLOTRON FREQUENCY OF THE
ELECTRONS (< 1 MHz)

WAVE SPEED: $V_w \sim B_0 / N_0$, 200 Km/Sec -> 10000 Km/Sec
FOR $N_0 \sim 10^6 / \text{c.c.}$

WAVELENGTH: $\lambda = V_w / f$, SHORTER THAN 3 Km

DIRECTION: MAINLY PARALLEL TO THE MAGNETIC FIELD UP TO AN
ANGLE OF 19°

POLARIZATION: CIRCULARLY POLARIZED

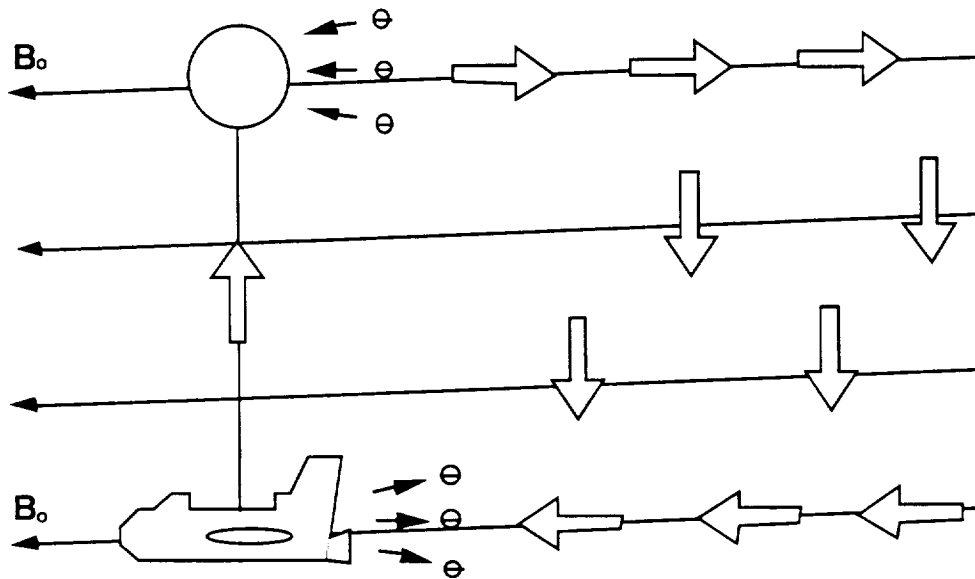


WHISTLER CIRCUIT FOR CURRENT CLOSURE

LOCAL CURRENT LOOPS EXPANDING FROM TSS ALONG THE
MAGNETIC FIELD LINES

CURRENT MOVE **ALONG** MAGNETIC FIELD LINES AT **WHISTLER** SPEED

ELECTRONS MOVE **ACROSS** MAGNETIC FIELD LINES VIA **$E \times B$** MOTION
(HALL CURRENT) TO PROVIDE LOCAL CURRENT CLOSURE



TRANSIT TIME EFFECT

SINCE THE TSS IS IN MOTION ALL THE TIME, AMBIENT PLASMA SENSES A TRANSIENT PULSE AT THE TIME INTERVAL

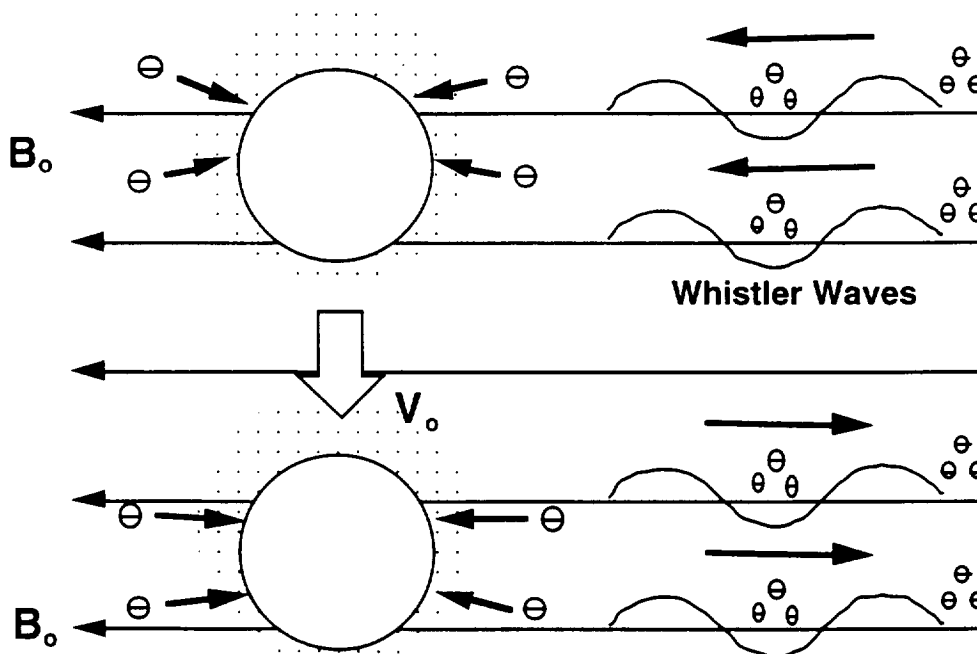
$$\Delta T \sim L/V_0$$

L: SIZE OF THE SATELLITE + SHEATH ~ FEW METERS

V_0 : SPEED OF TSS ~ 8 Km/Sec

THIS CORRESPONDS TO A TRANSIT TIME OF $\Delta T \sim 10^{-4}$ Sec
OR A TRANSIT FREQUENCY OF $1/\Delta T \sim 10$ KHz
WHICH IS IN THE WHISTLER FREQUENCY REGIME

TSS IS MORE LIKELY TO HAVE WHISTLER CLOSURE



APPENDIX 5

CAUSALITY AND CHARACTERISTICS OF THE IONOSPHERIC-THERMOSPHERIC ENVIRONMENT

(A Briefing in Preparation for the Tether Mission of March 1996)

Presented by

E.P. Szuszczewicz

May 10, 1995

Theory, Modeling and Support of Tether

Johnson Space Center



An Employee Owned Company

Applied Physics Operation
McLean, VA 22102

OUTLINE

- **FUNDAMENTAL CONCEPTS AND CAUSALITY**
 - The Sun-Earth System and Plasma Production
- **DENSITY DISTRIBUTIONS AND MORPHOLOGIES**
 - E and F-Region Characteristics
 - Day/Night and Latitudinal Controls
 - Quiet-Time vs Storm-Time Conditions
 - Current Research Thrusts
- **MISSION EXPECTATIONS: THE PREVAILING ENVIRONMENT**
 - TSS-1 vs TSS-R
 - Scale Heights and Projected Observations



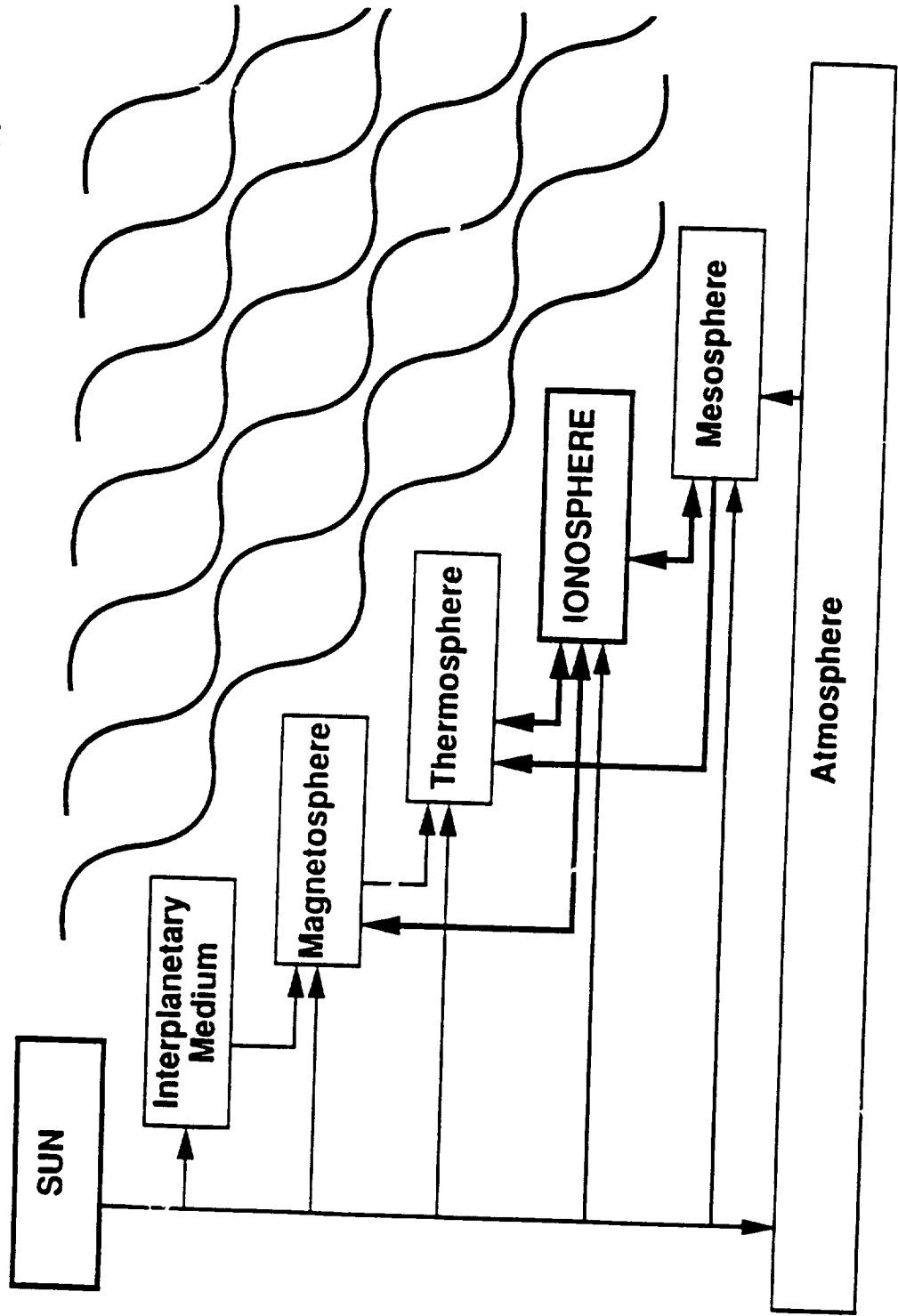
An Employee Owned Company

Applied Physics Operation
McLean, VA 22102

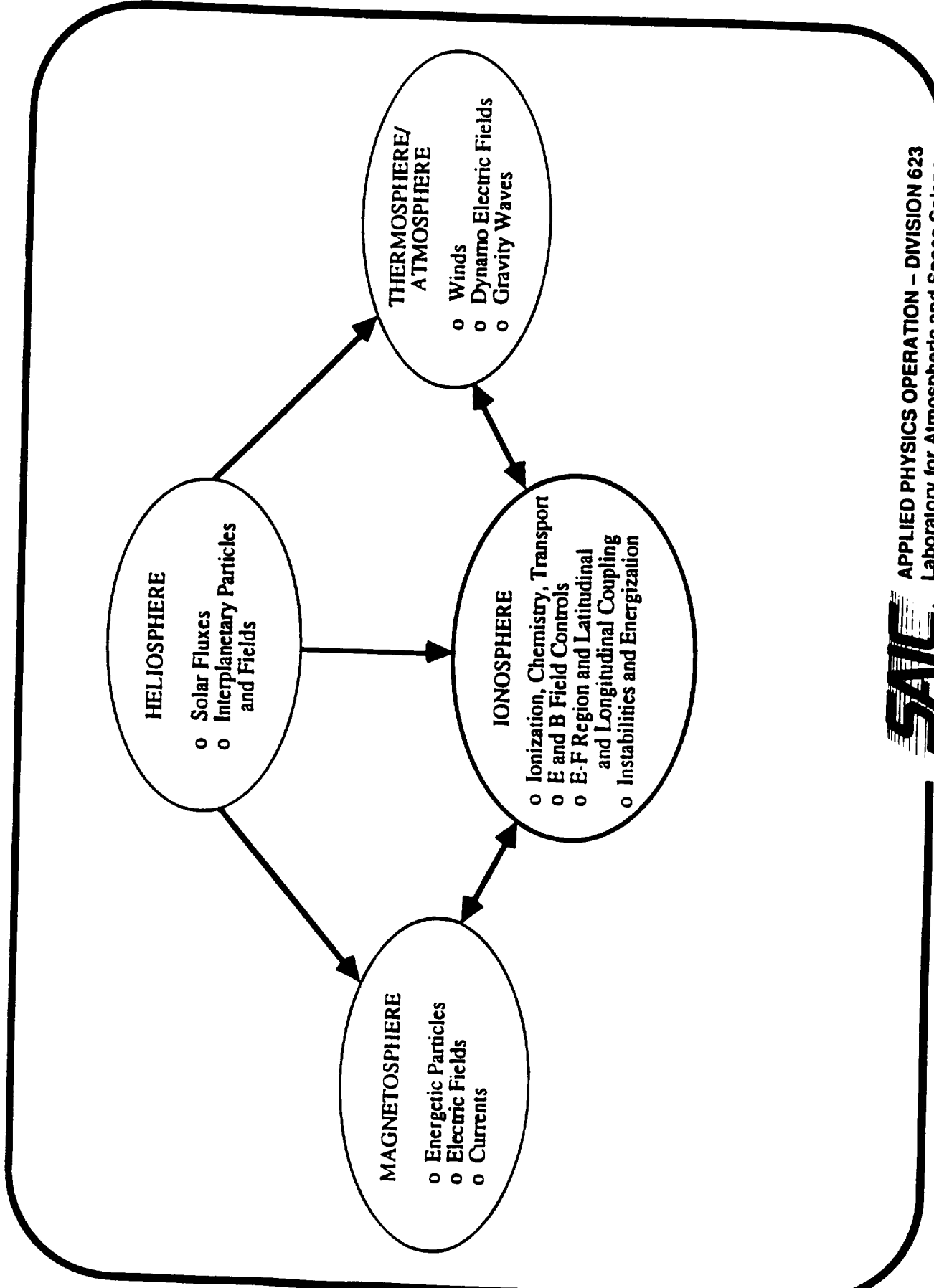
30-42

30.10

Coupling and Dynamics in the Cascading of Particles, Fields, and Waves in the Solar-Terrestrial Environment



ITMP - SIS
Ionospheric - Thermospheric - Mesospheric - Physics
Strateau Implementation C...



24.79 ad

ZERO-ORDER CONTROLS

Solar Electromagnetic Radiation
 From "Solar-Terrestrial-Physics" (Oxford 1972)

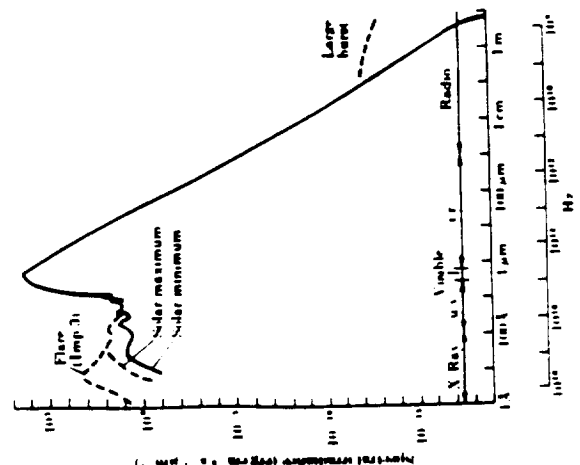


Fig. 1.6. The solar spectrum from \AA to 10 m from different solar conditions. After Malitson (1965, modified)

Solar Wind-Magnetosphere-Ionosphere Interactions (Particles and Fields)
 From "Solar Terrestrial Programs" (NASA/OSSA 1977)

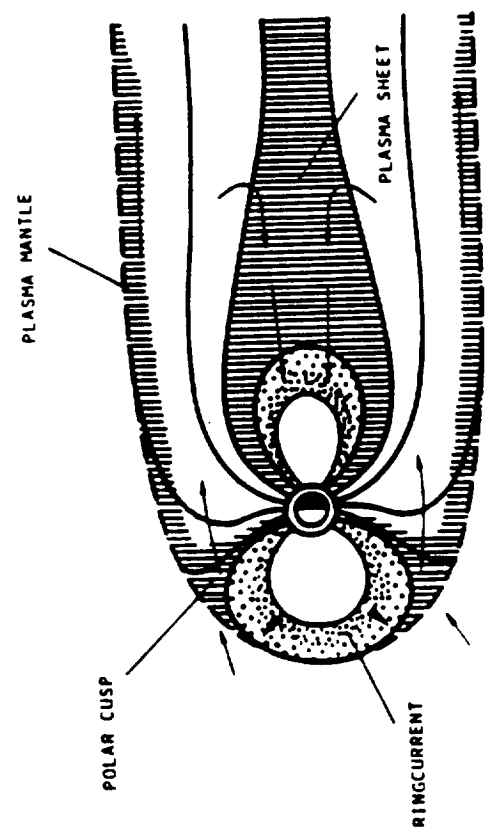


Fig. 10. Convective flow of hot plasma through magnetosphere. The convection, or magnetospheric electric field is produced mainly as a result of stresses exerted at the magnetopause by the solar wind.

from

HIGHER-ORDER CONTROLS

- Neutral Densities, Composition and Winds
(Thermospheric Controls)
- Magnetic Fields
- High-Latitude Convection Electric Fields and Energetic Particle Precipitation Patterns
- Global-Scale Electric Fields
- Energetic Man-Made Events



APPLIED PHYSICS OPERATION
Laboratory for Atmospheric and Space Sciences
McLean, Virginia 22102

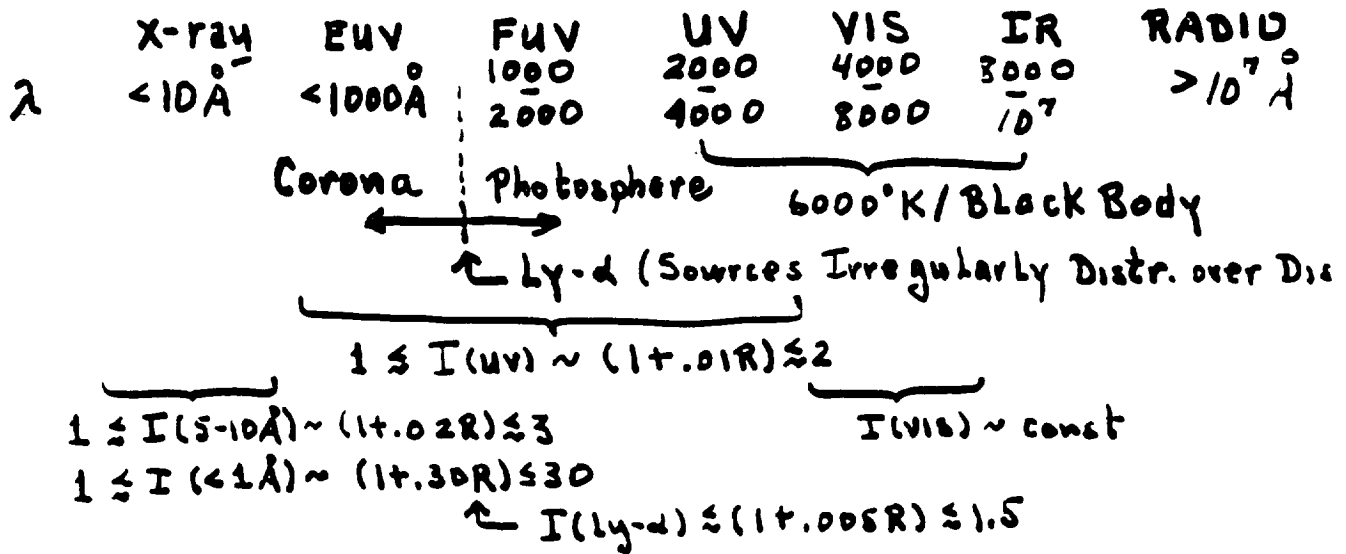
An Employee-Owned Company

SOME FUNDAMENTAL CONCEPTS

1) DIFFUSIVE EQUILIBRIUM

$$n = n_0 \exp \left\{ -z / (kT/mg) \right\}$$

2) SOLAR RADIATION



3) CHAPMAN LAYER (Production Layer) ... $N_0 \equiv 1$

$$q = q_0 \exp \left\{ 1 - z - \sec(\chi) \exp(-z) \right\}$$

$$q_0 = c I_0 / e H \quad z = (h - h_0) / H \quad H = kT/mg$$

4) FINAL EQUILIBRIUM DISTRIBUTION ← Production + Loss

$$\frac{dn}{dt} = q - L - \frac{d(nv)}{dz}$$

Production ←
↘ chemical losses (recombination) → $\alpha n_i n_e = \alpha n_e^2$
↗ diffusion, transport (e.g. $\vec{E} \times \vec{B}$, winds)

If $L, v = 0$ $\frac{dn}{dt} = -(\alpha n) n \rightarrow \frac{1}{n} - \frac{1}{n_0} = \alpha t$

↘ "effective time const." $\tau \equiv 1/\alpha n$

Radiative Recombination: $O^+ + e \rightarrow O + h\nu$ $\frac{1}{\alpha n} \sim \frac{1}{10^{14} 10^6} = 10^6 \text{ s (12 d)}$

Dissociative Recombination: $NO^+ + e \rightarrow N + O$ $\frac{1}{\alpha n} \sim \frac{1}{10^{17} 10^6} = 10^2 \text{ s (2 m)}$

5) "FROZEN-IN" FIELDS

$$\frac{1}{2} m v_{sw}^2 > B^2 / 2\mu_0$$

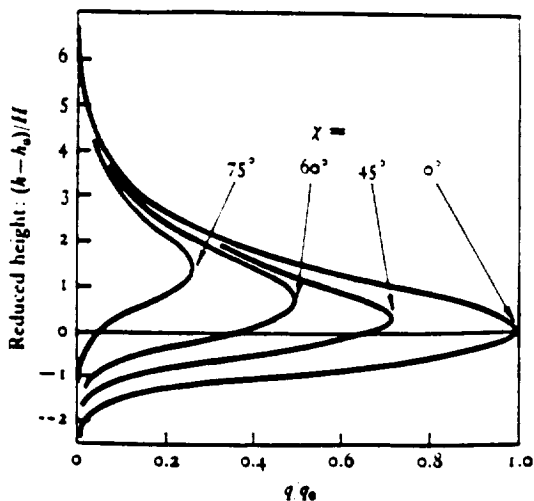


Fig. 1.6. 'Chapman' type production curves for different solar zenith angles (χ). Heights are measured in units of scale height H from the level of the peak when $\chi = 0$. Rates (q) of production are measured in units of q_0 , the rate at the peak when $\chi = 0$. If any one of these curves is replotted with normalized co-ordinates described in the text it takes the form of the curve for $\chi = 0$ (after reference 5).

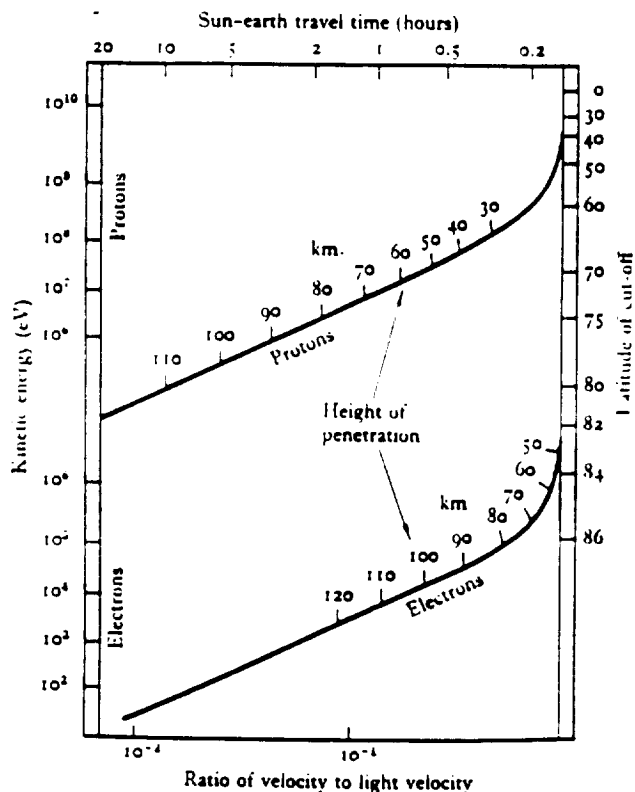
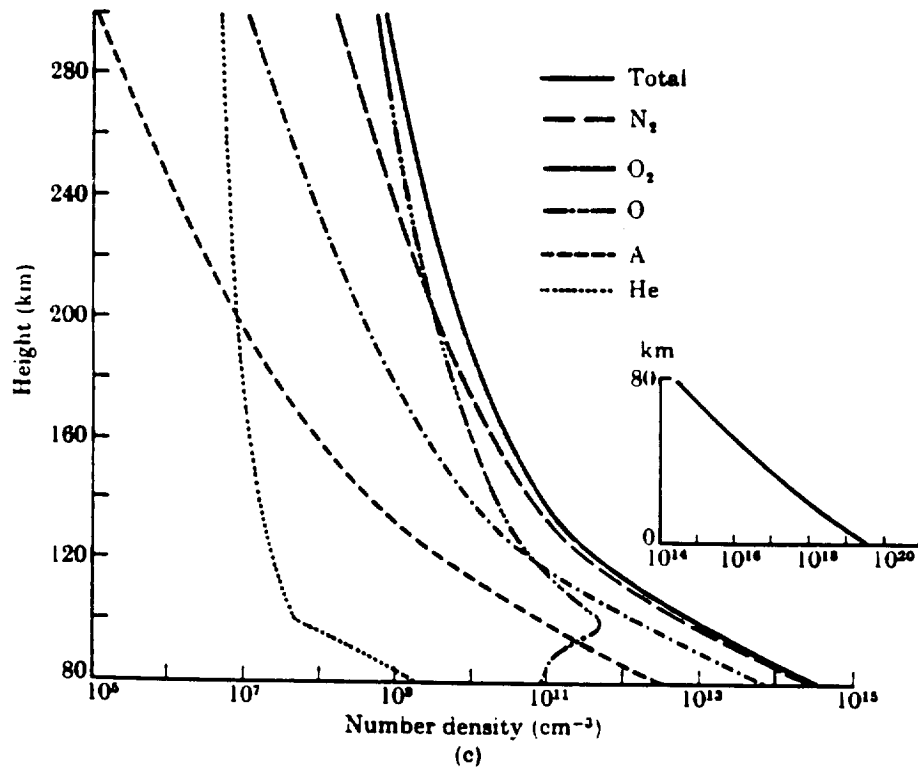
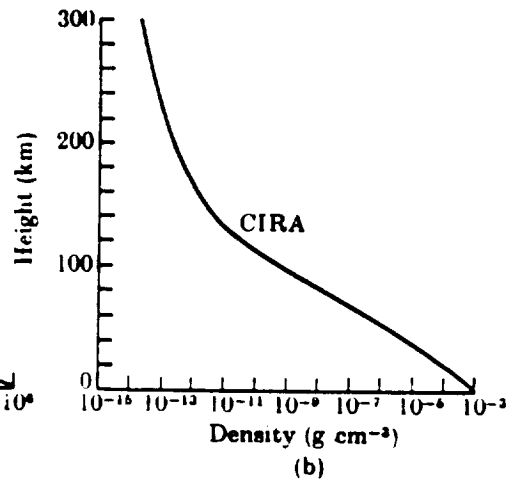
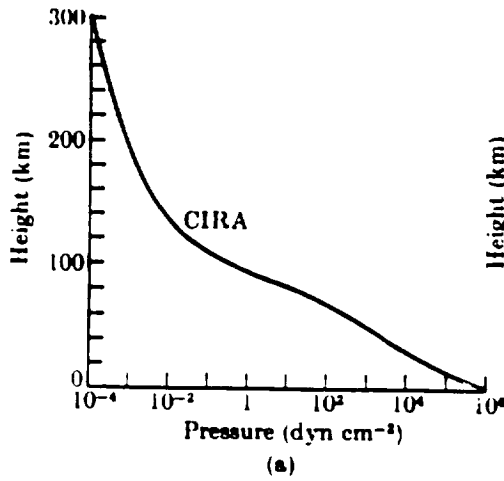


Fig. 1.7. The two curves refer to electrons and protons travelling with velocities as indicated on the bottom horizontal scale. The depths of penetration into the atmosphere are marked on the curves. Reference to the other scales shows (a) the travel times from sun to earth, (b) the kinetic energy, (c) the latitude of 'geomagnetic cut-off' below which the particle cannot reach the earth (after reference 43).

THERMOSPHERIC DENSITIES, PRESSURES AND COMPOSITION

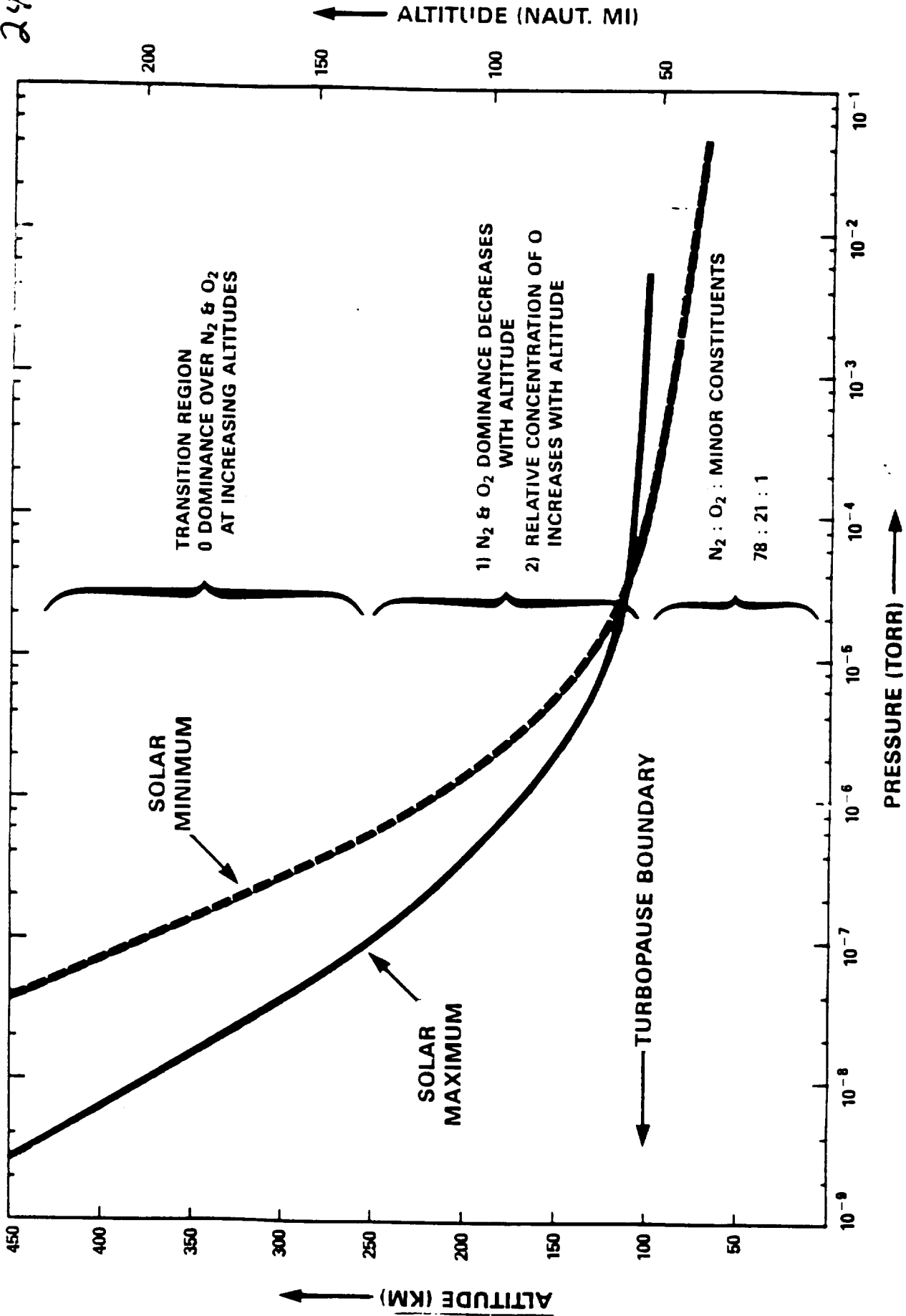


An Employee Owned Company

Applied Physics Operation
McLean, VA 22102

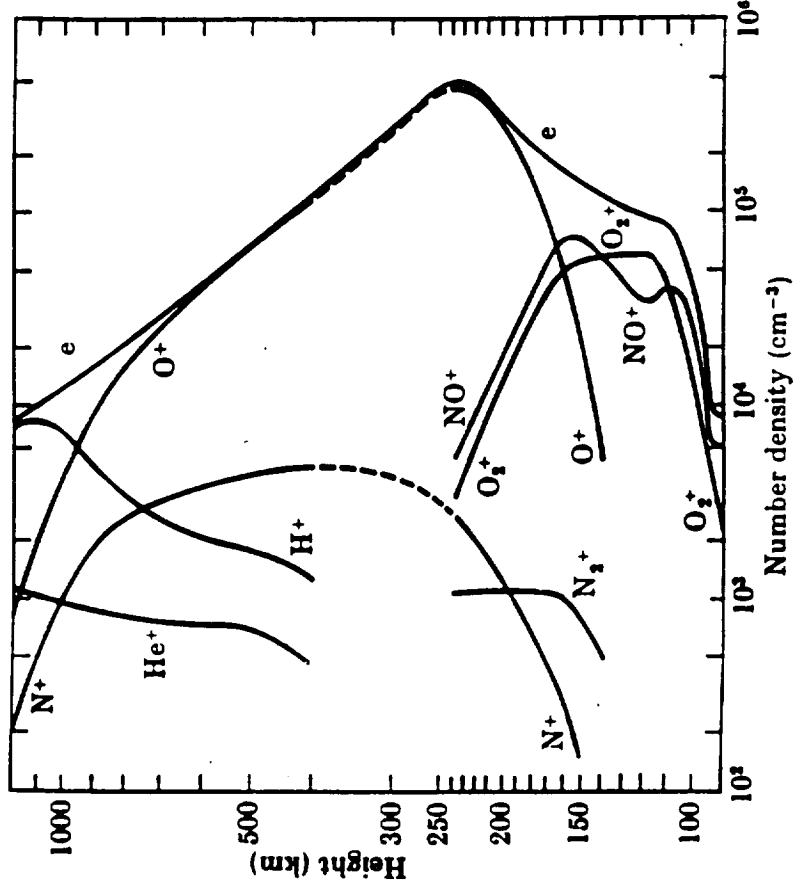
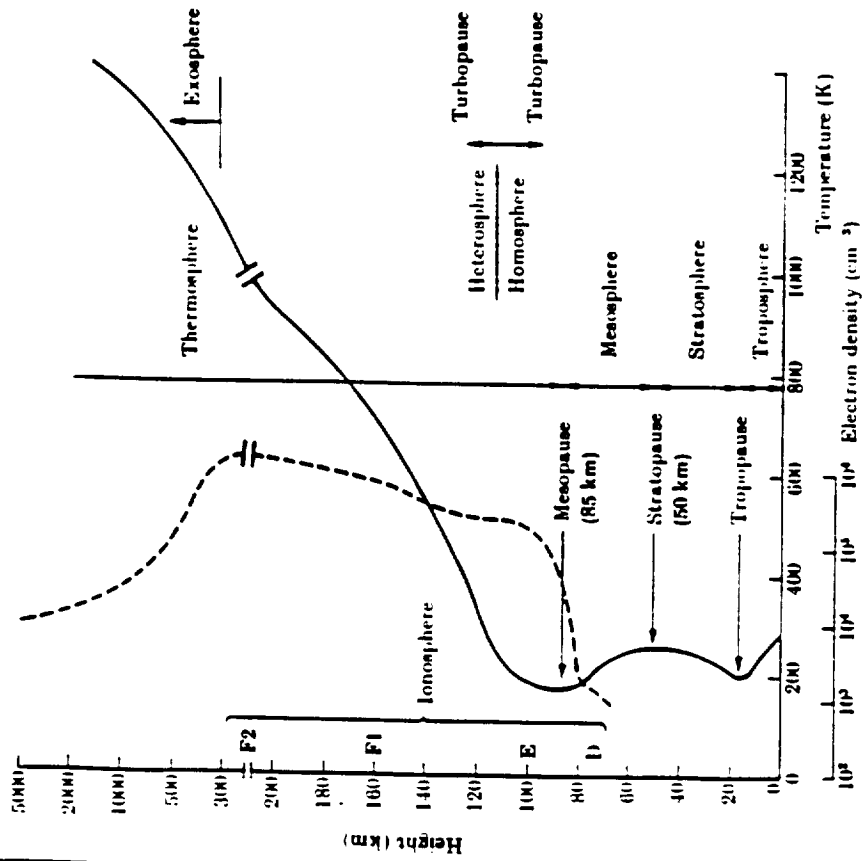
BR 24-20

24-20



NOMINAL SPECIFICATION OF HIGH ALTITUDE NEUTRAL GAS ENVIRONMENT

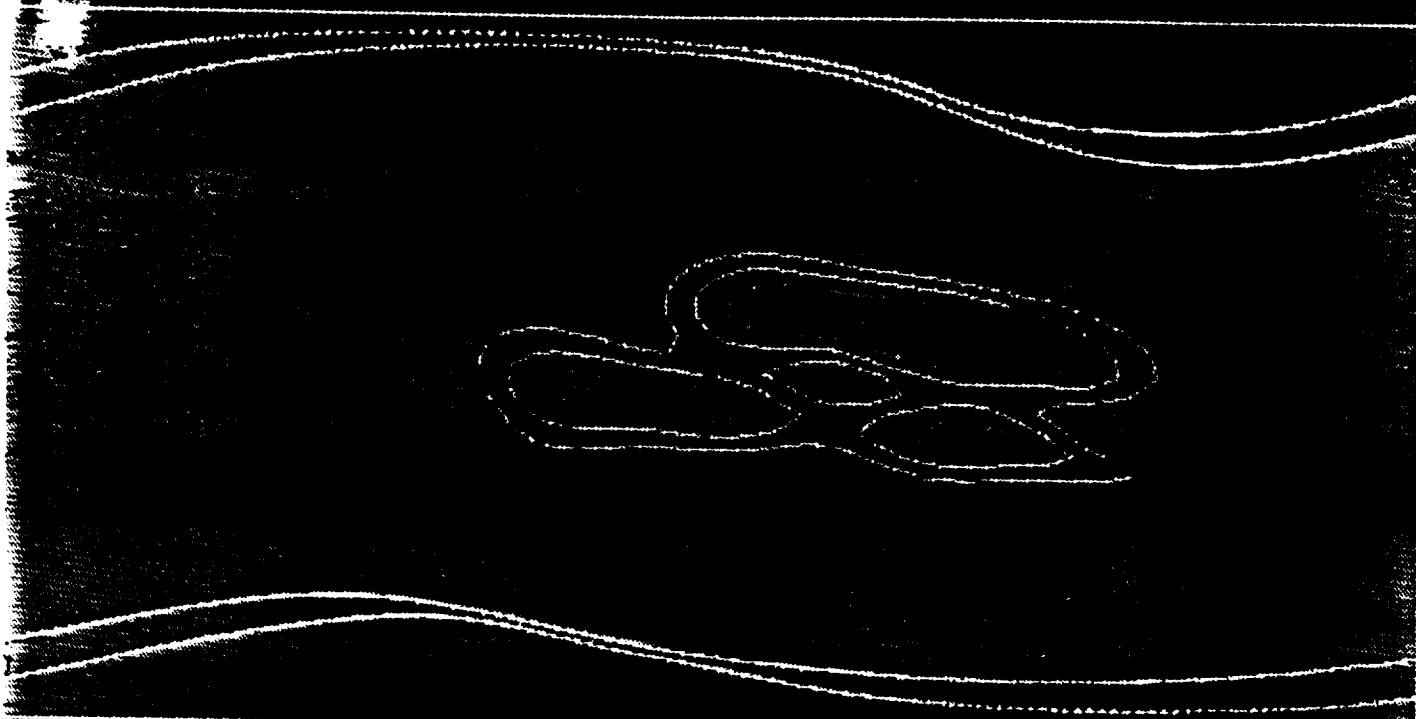
A NOMINAL MID-LATITUDE IONOSPHERE



An Employee Owned Company

Applied Physics Operation
McLean, VA 22102

August '92 UT=0
IRI: R=80
Feldstein Oval: Q=4



foF2 (MHz)

1.7

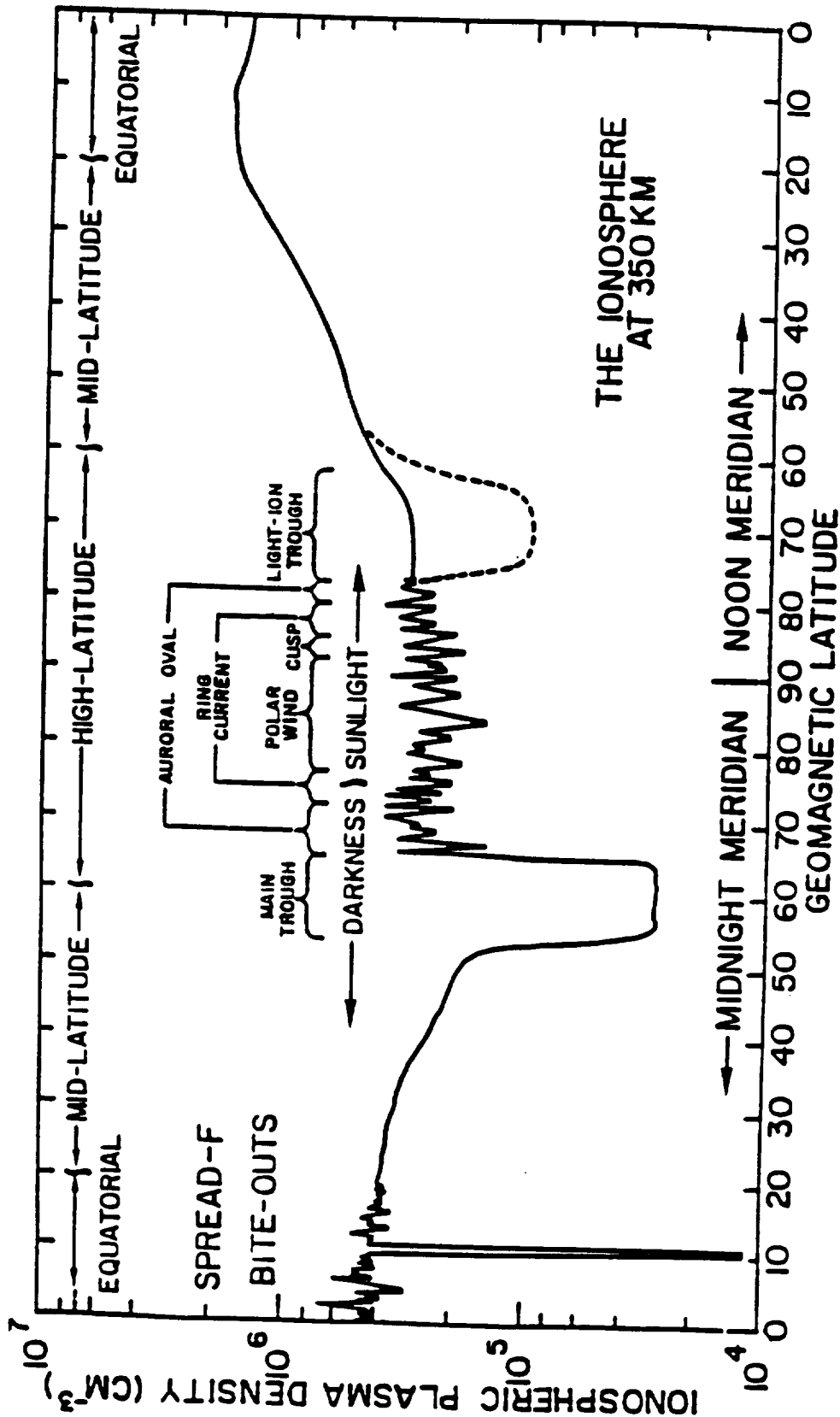
4.4

7.1

9.8

12.5

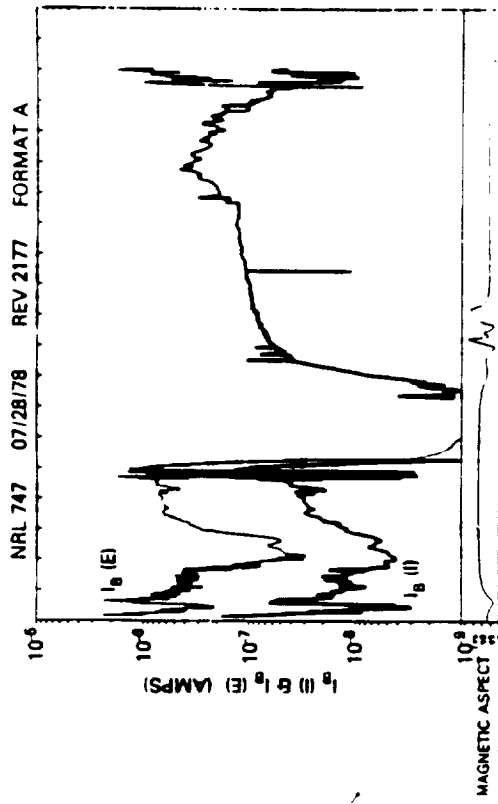




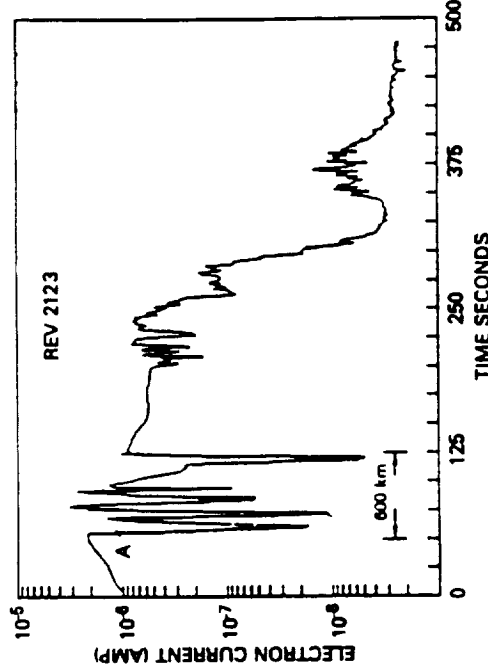
24.77j

NATURALLY-OCCURRING IRREGULARITIES IN THE F-REGION

THE S3-4 IONOSPHERIC IRREGULARITIES SATELLITE EXPERIMENT



THE S3-4 IONOSPHERIC IRREGULARITIES SATELLITE EXPERIMENT



Relative electron density as measured on one complete orbit by the pulsed-plasma-probe experiment on the S3-4 satellite.

An expanded view of relative electron density encountered during the nighttime equatorial crossing on S3-4 rev 2123. The relative electron density is presented by baseline electron saturation current.



APPLIED PHYSICS OPERATION
 Laboratory for Atmospheric and Space Sciences
 McLean, Virginia 22102

24-64K

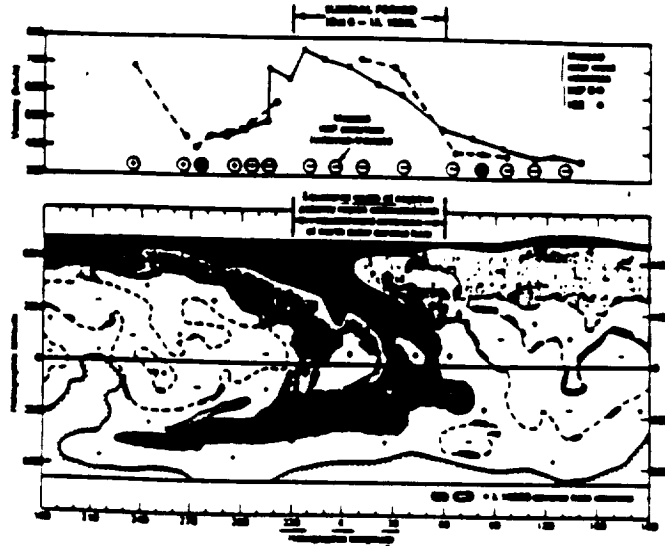


FIG. II.C-10 Presentation of Coronal Hole Morphology and Solar Wind Conditions during SUNDIAL Period (prepared by E. Roelof, in SUNDIAL Interim Report, Szuszczewicz, 1985).

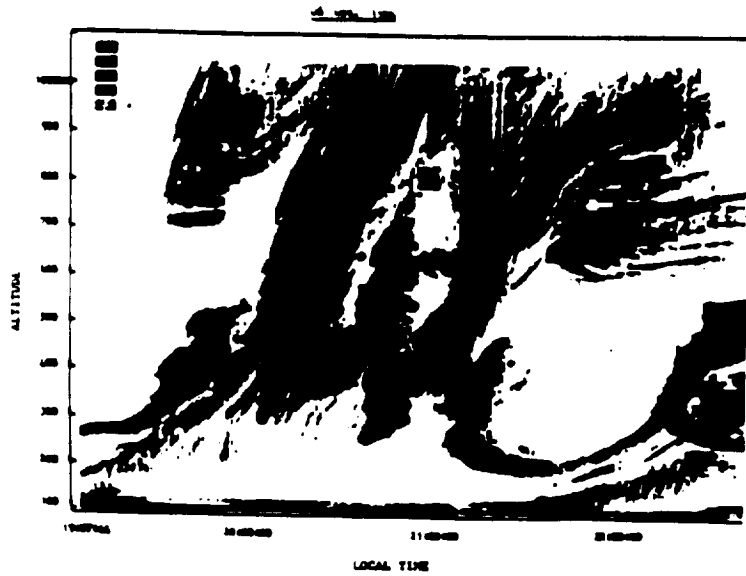
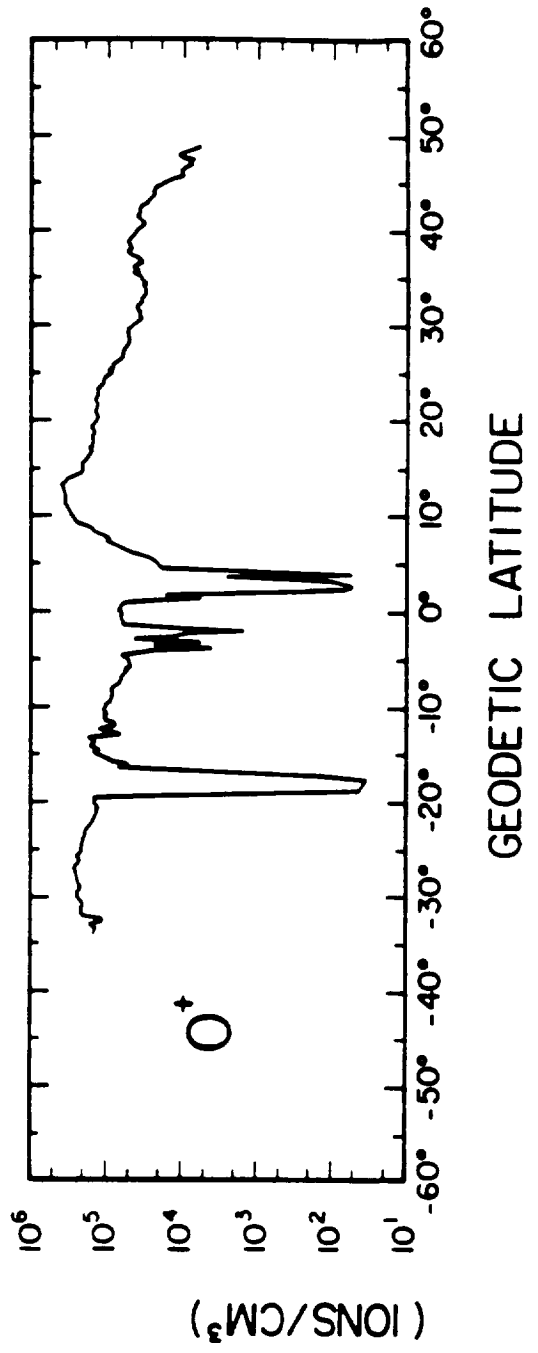
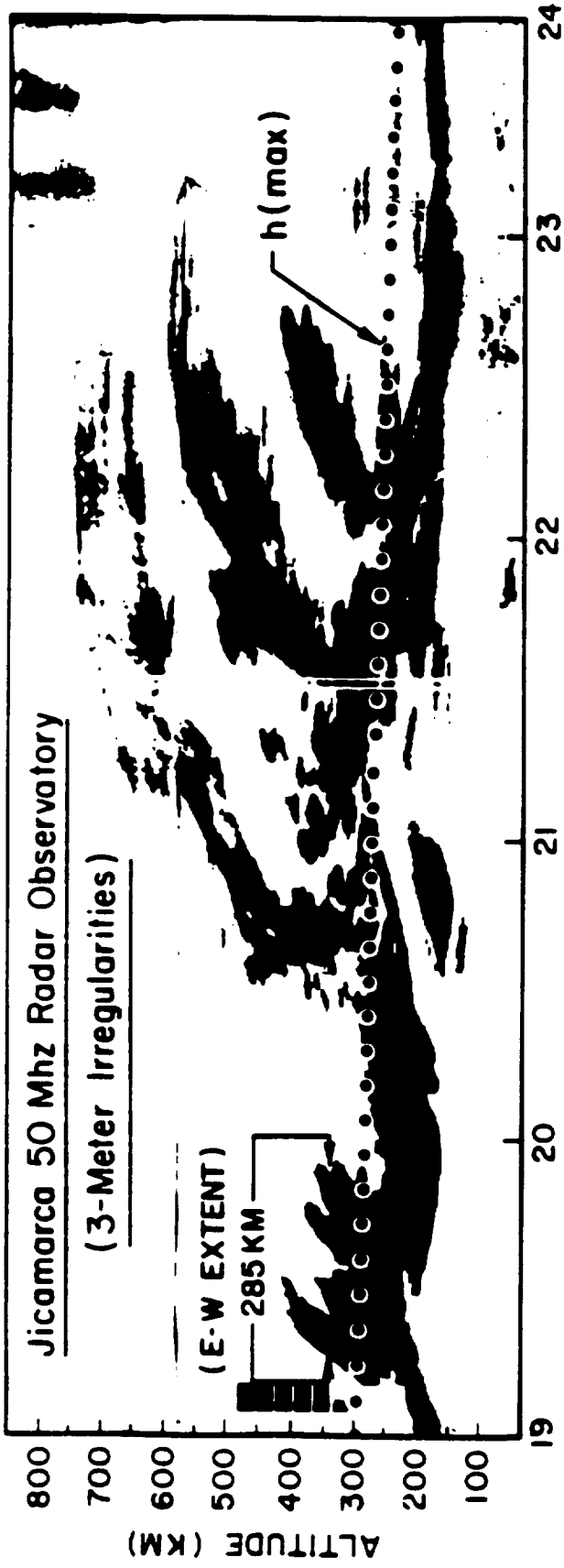


FIG. II.C-11 Jicamarca Radar Map of Intense Equatorial Plume Structure on the Second Day of the SUNDIAL Period, 6 October 1984 (from R. Woodman, in SUNDIAL Interim Report, Szuszczewicz, 1985).

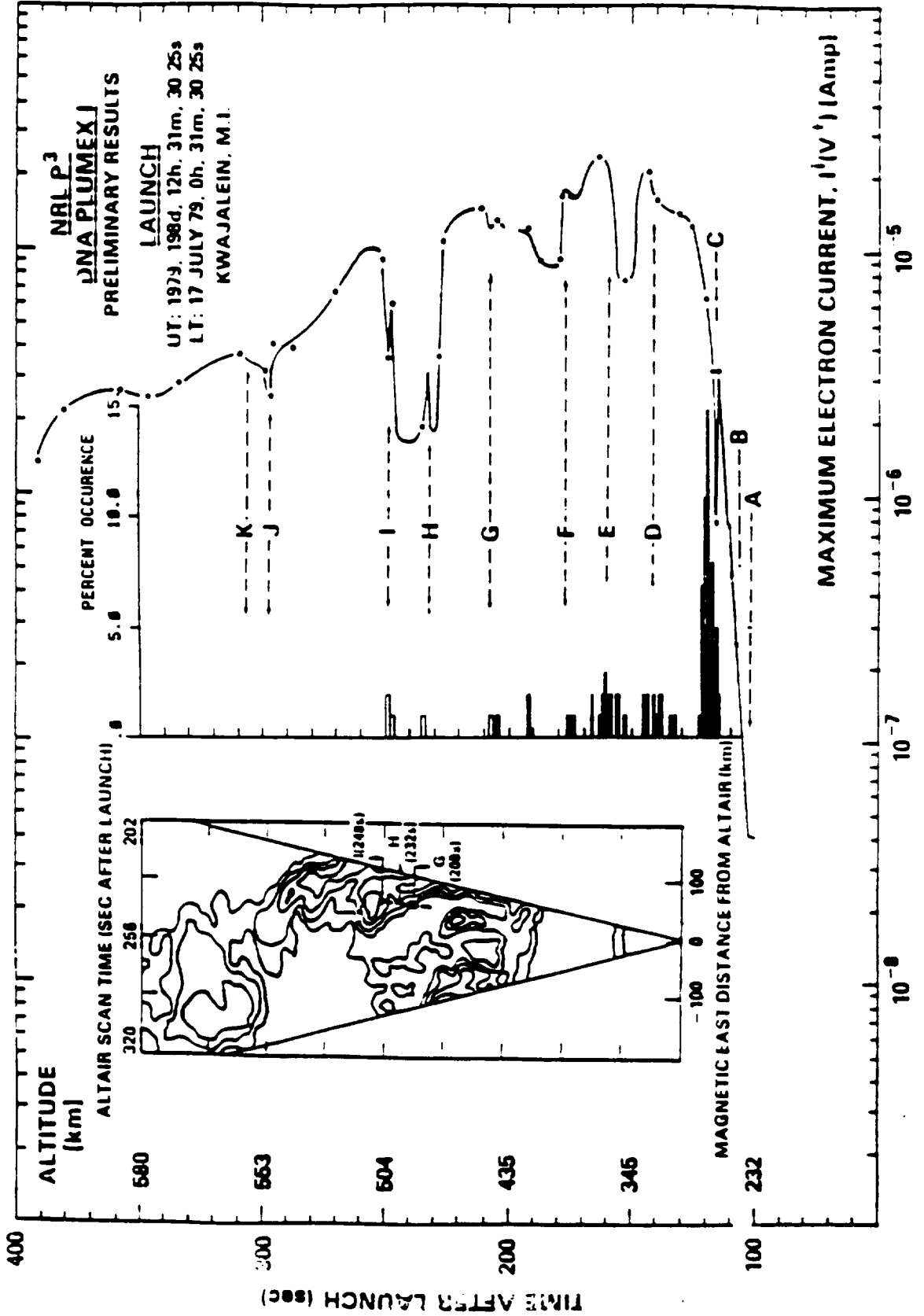


PLASMA PHYSICS DIVISION
Space and Laboratory Plasmas
McLean, Virginia

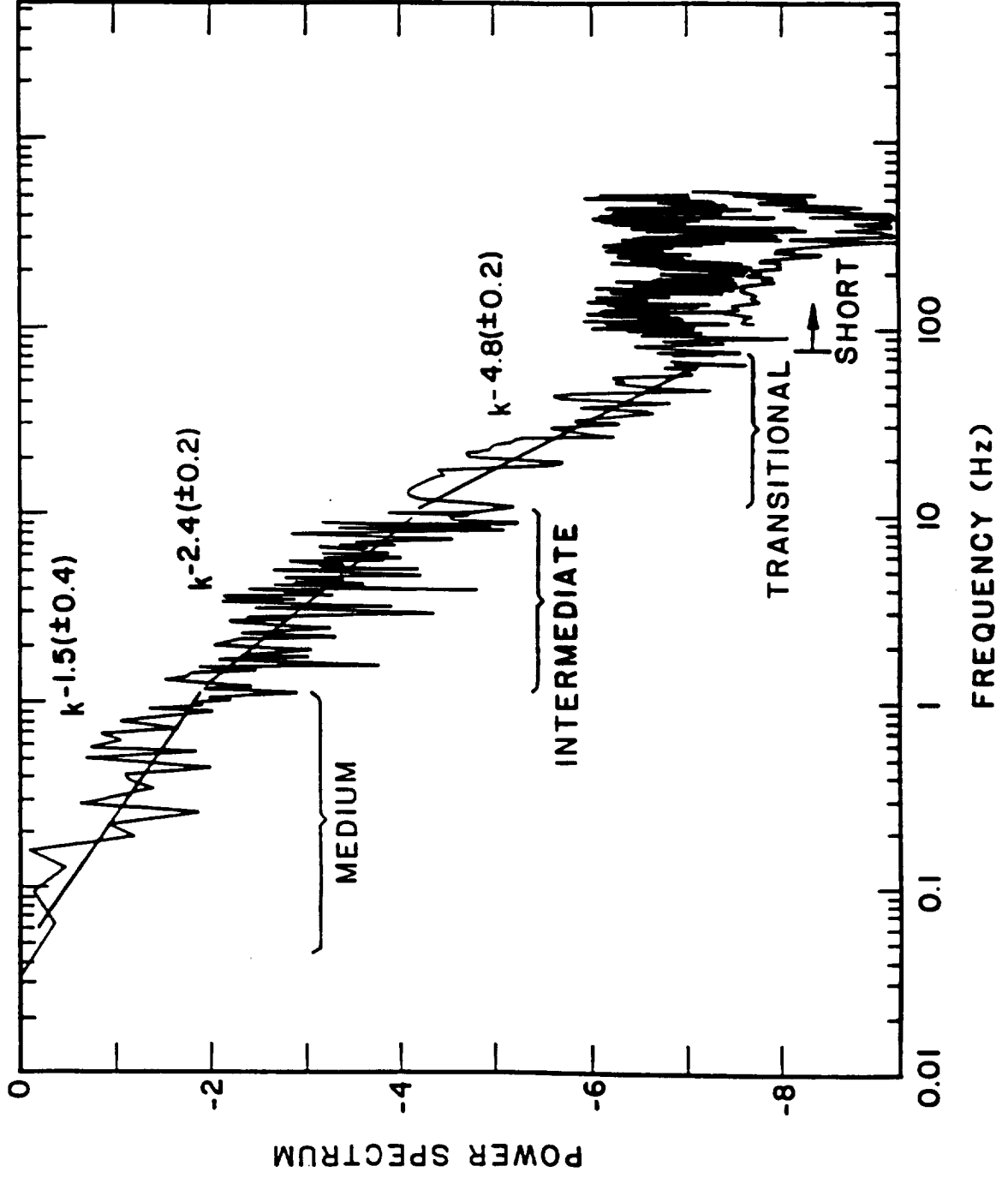
25-28



X 24-67 i

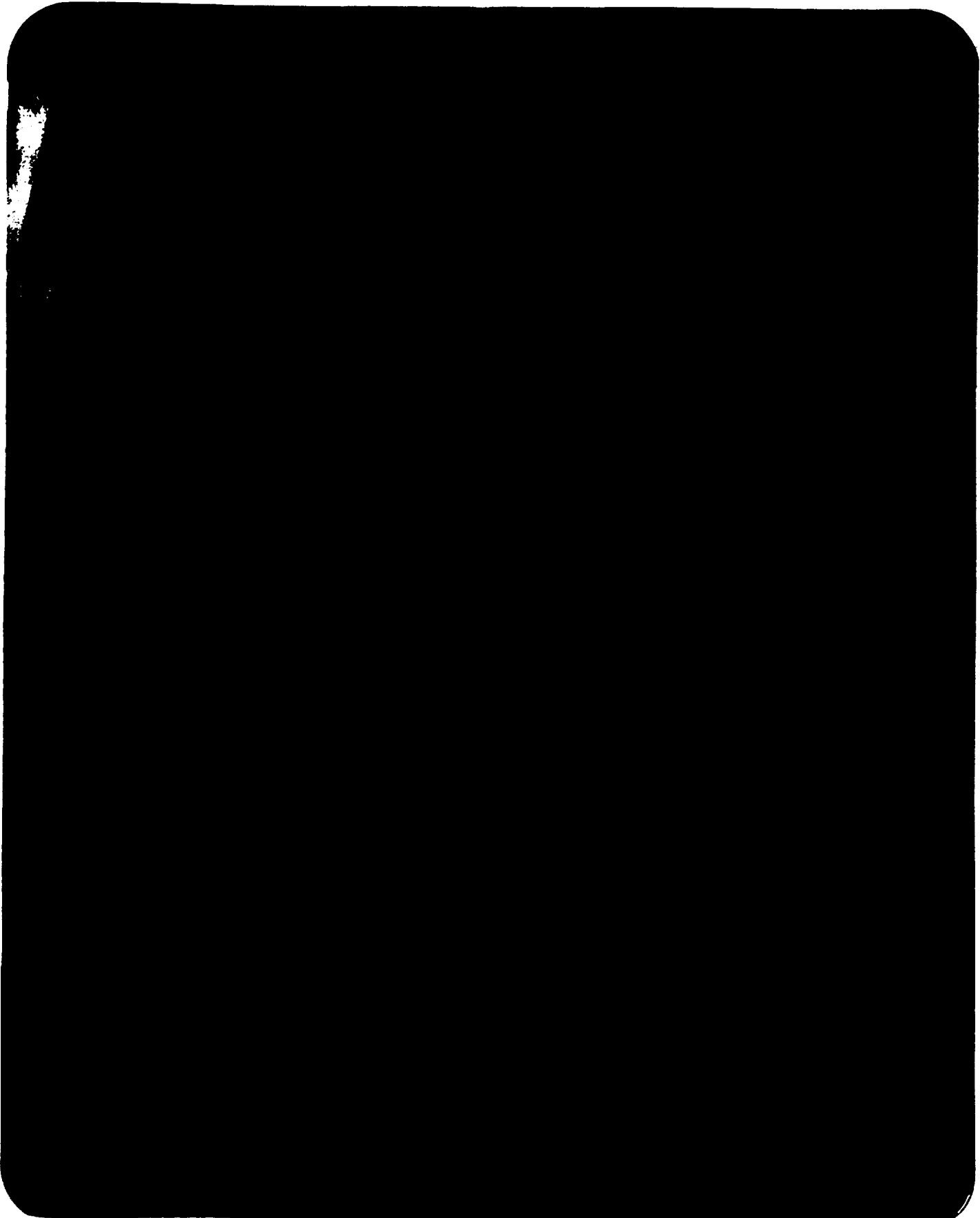


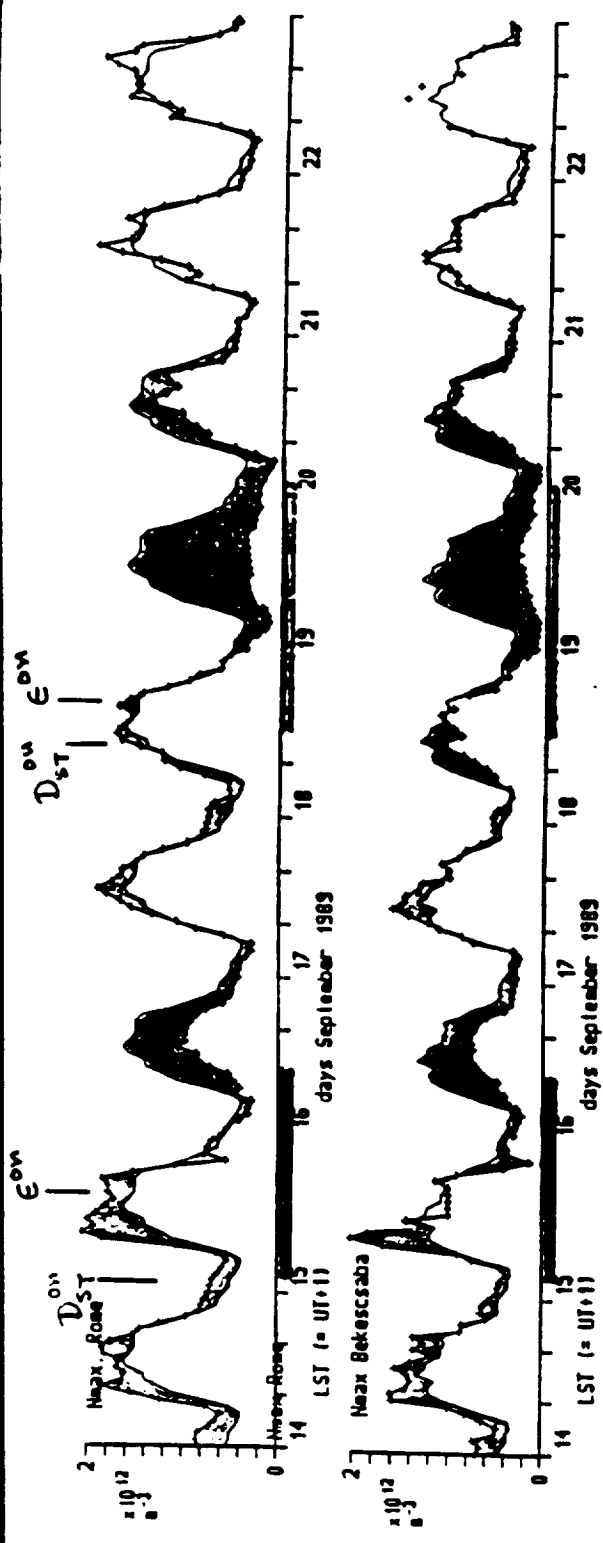
PLUMEX-1 POWER SPECTRA



24.14

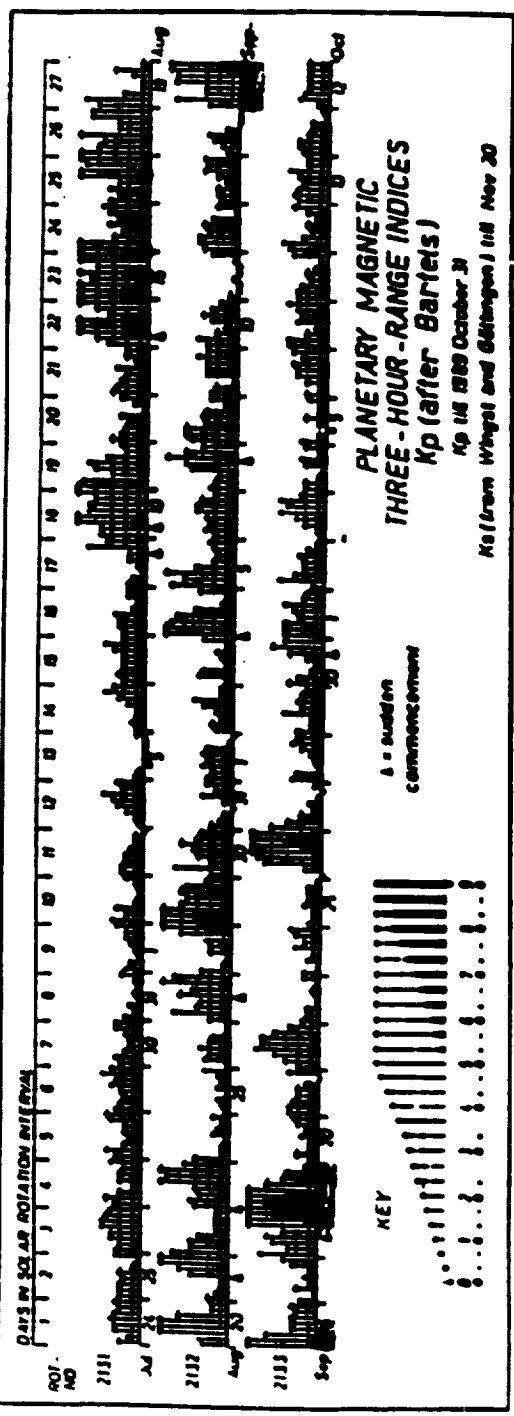
X27.149





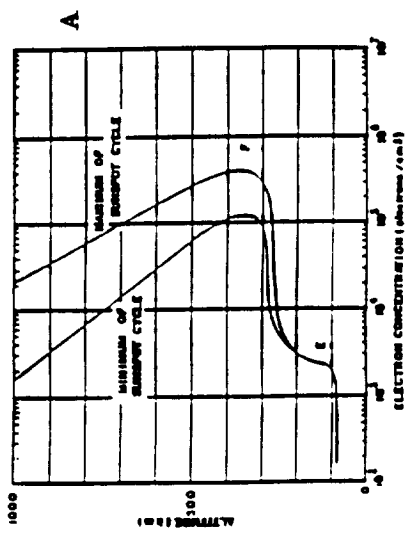
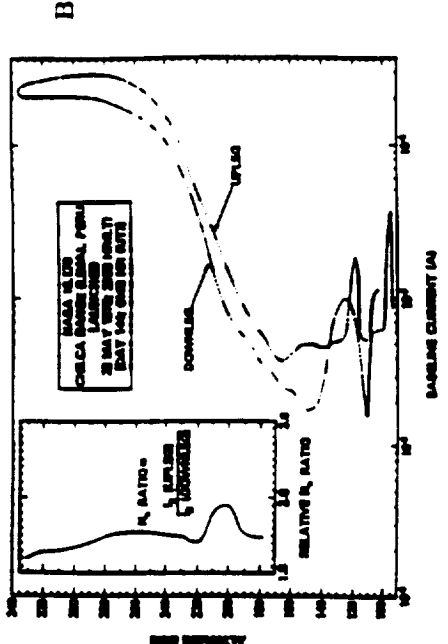
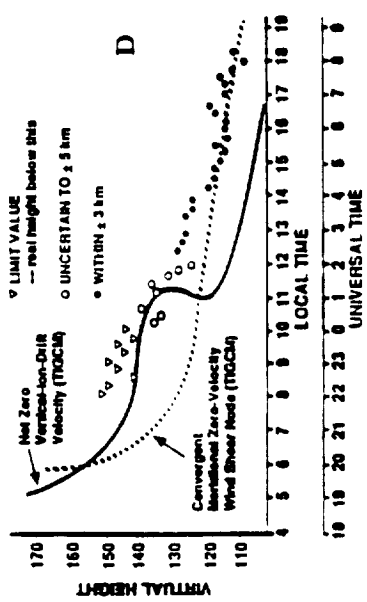
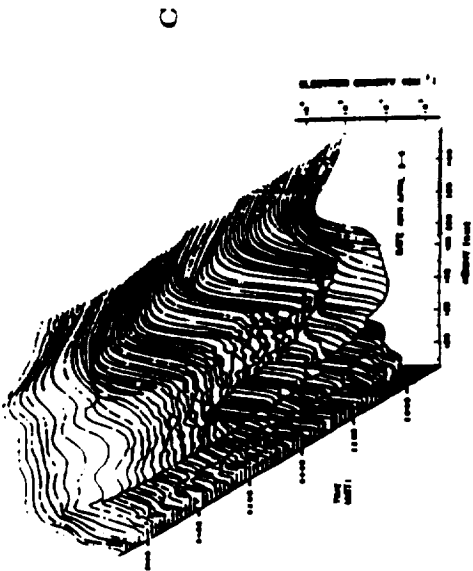
Kp through October 31, 1989

University of Göttingen



Laboratory for Atmospheric and Space Sciences
 Mountain View, Virginia 22102

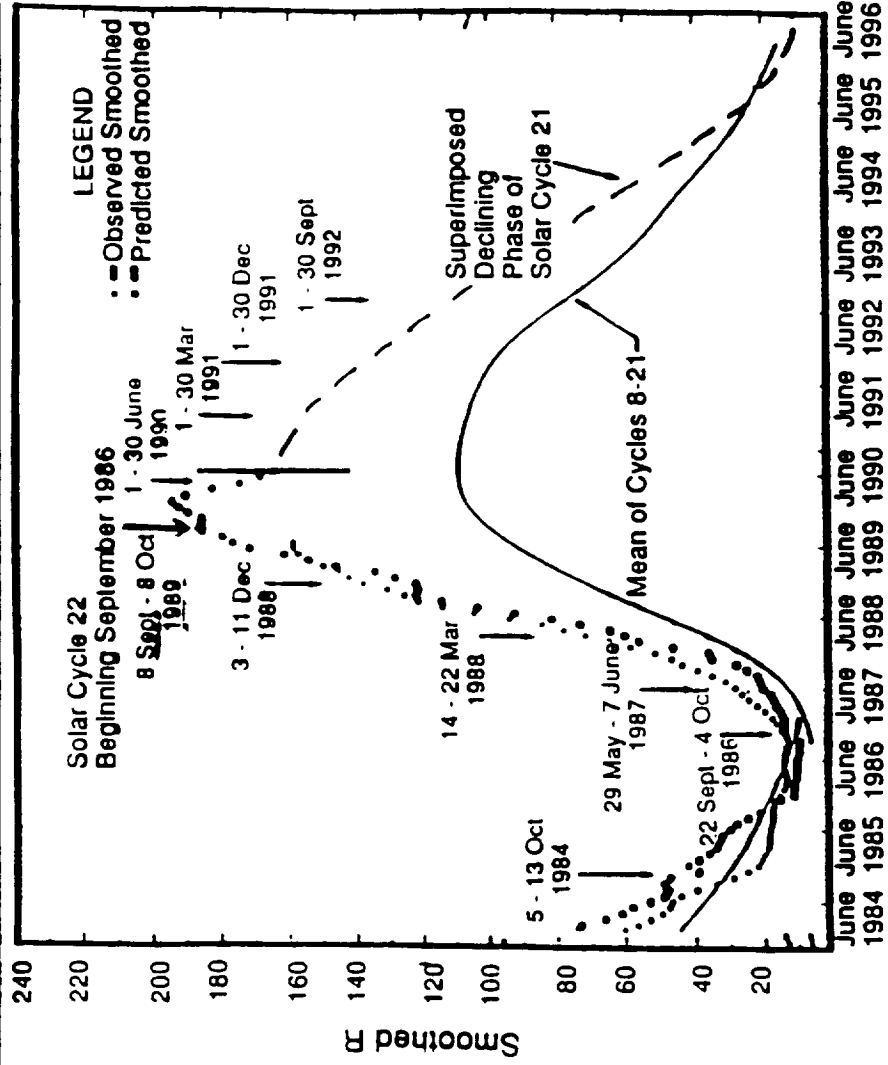
DESCENDING LAYERS IN THE LOWER IONOSPHERIC-THERMOSPHERIC DOMAIN



125.213 (40)
X 27.28 M

2:30 f

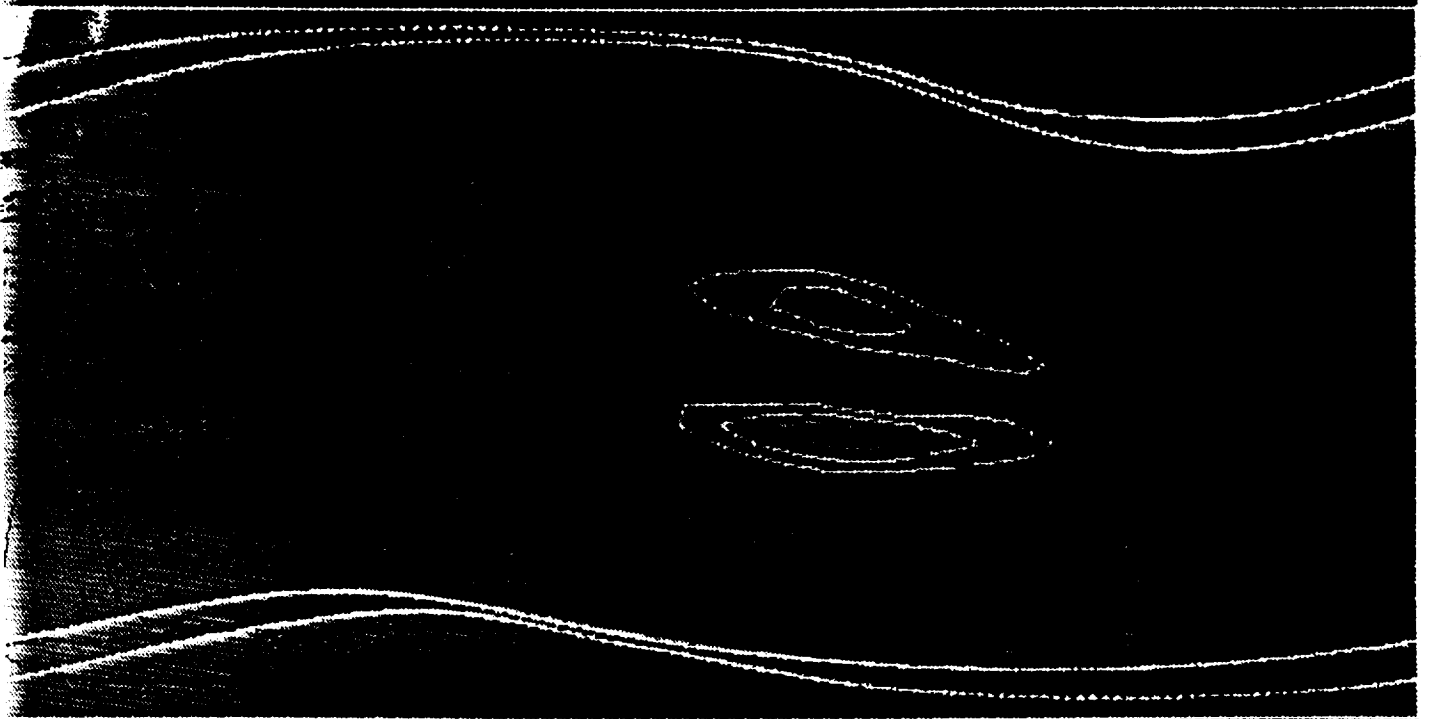
SUNDIAL CAMPAIGNS IN THE CURRENT SOLAR CYCLE



February '96 UT=0

IRI: R=10

Feldstein Oval: Q=4



foF2 (MHz)

1.7

4.4

7.1

9.6

12.5



February '96 UT=0
IRI: R=10
Feldstein Oval: Q=4



hmF2 (KM)

175.0

237.5

300.0

362.5

425.0



Difference (2/96 - 8/92) UT=0
Feldstein Oval: Q=4
(contours for 2/96)



foF2 % difference

-40.0

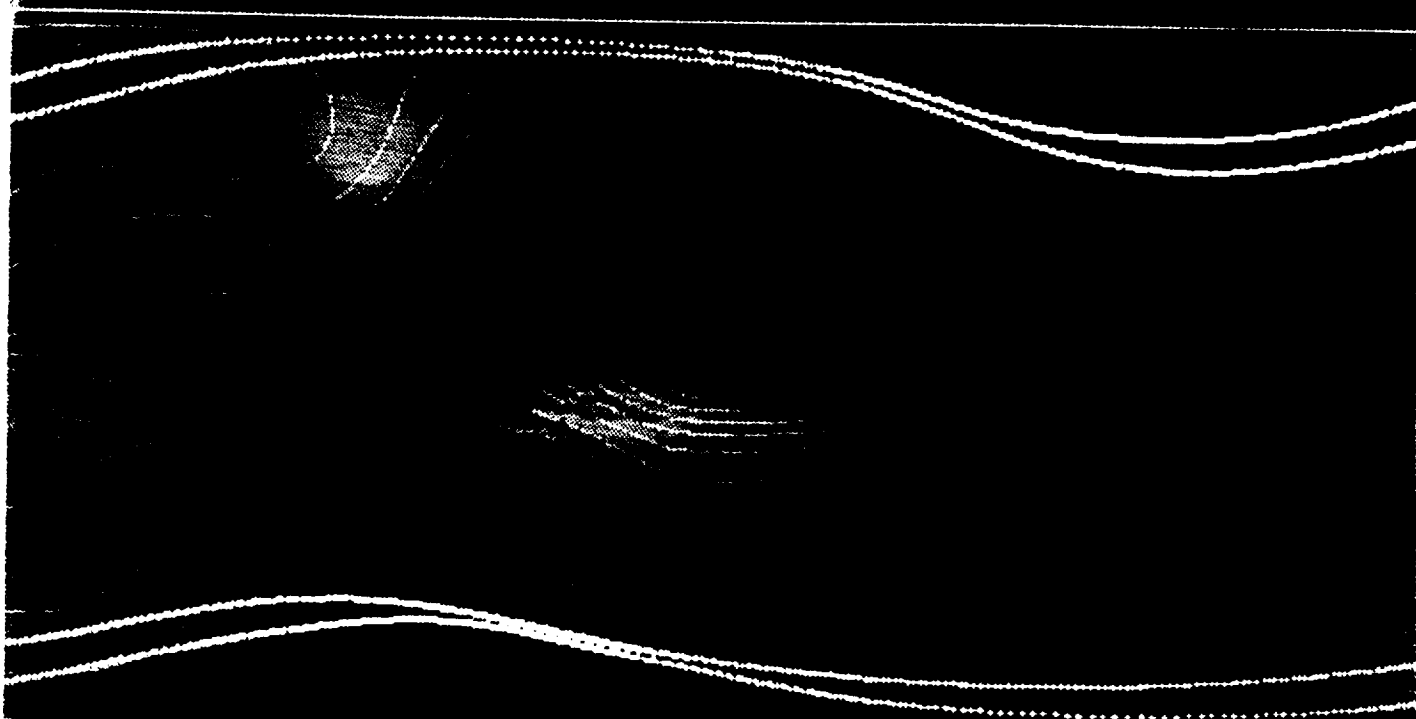
-20.0

0.0

20.0

40.0

Difference (2/96 - 8/92) UT=0
Feldstein Oval: Q=4
(contours for 2/96)



hmF2. % difference

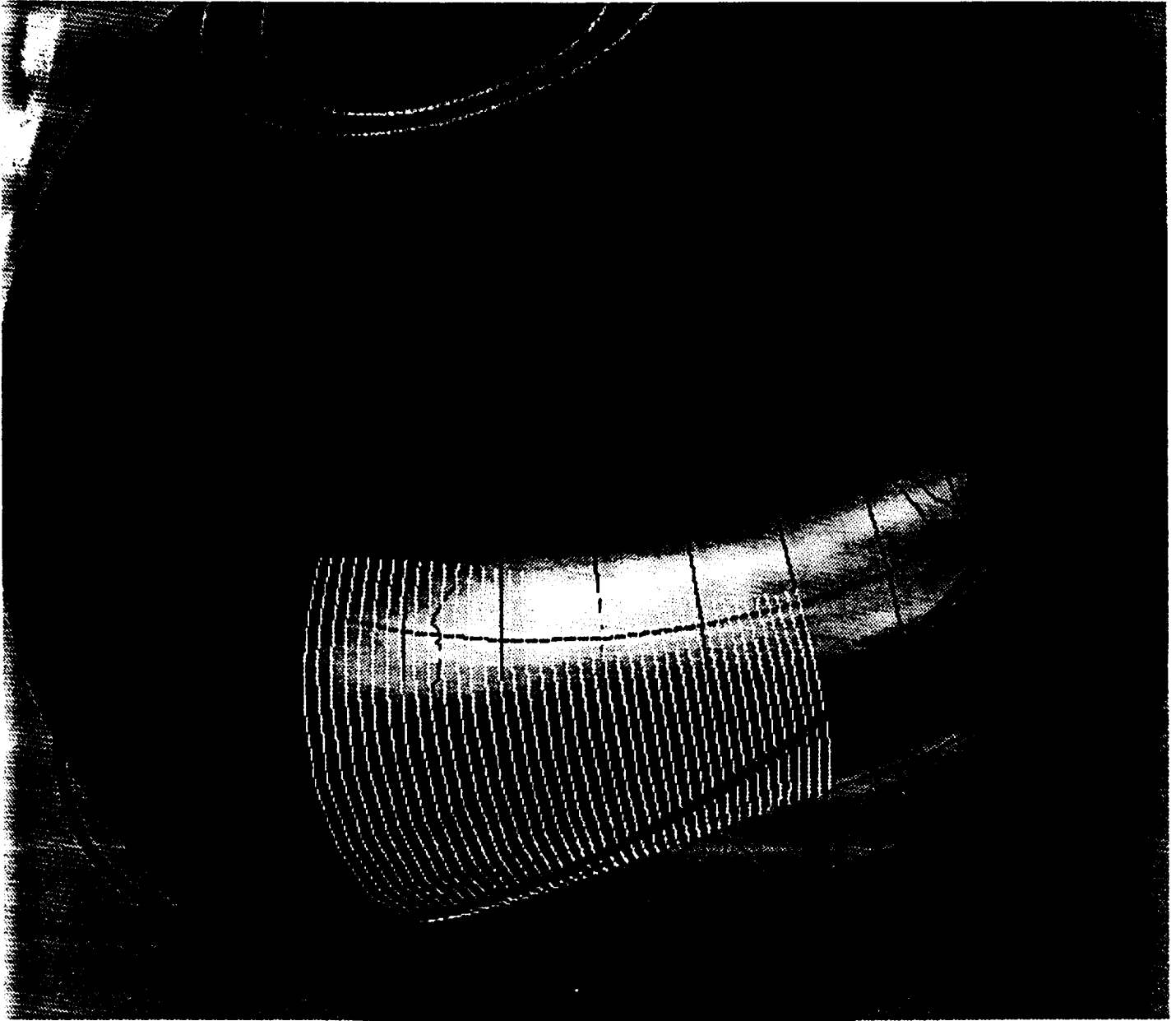
-25.0

-12.5

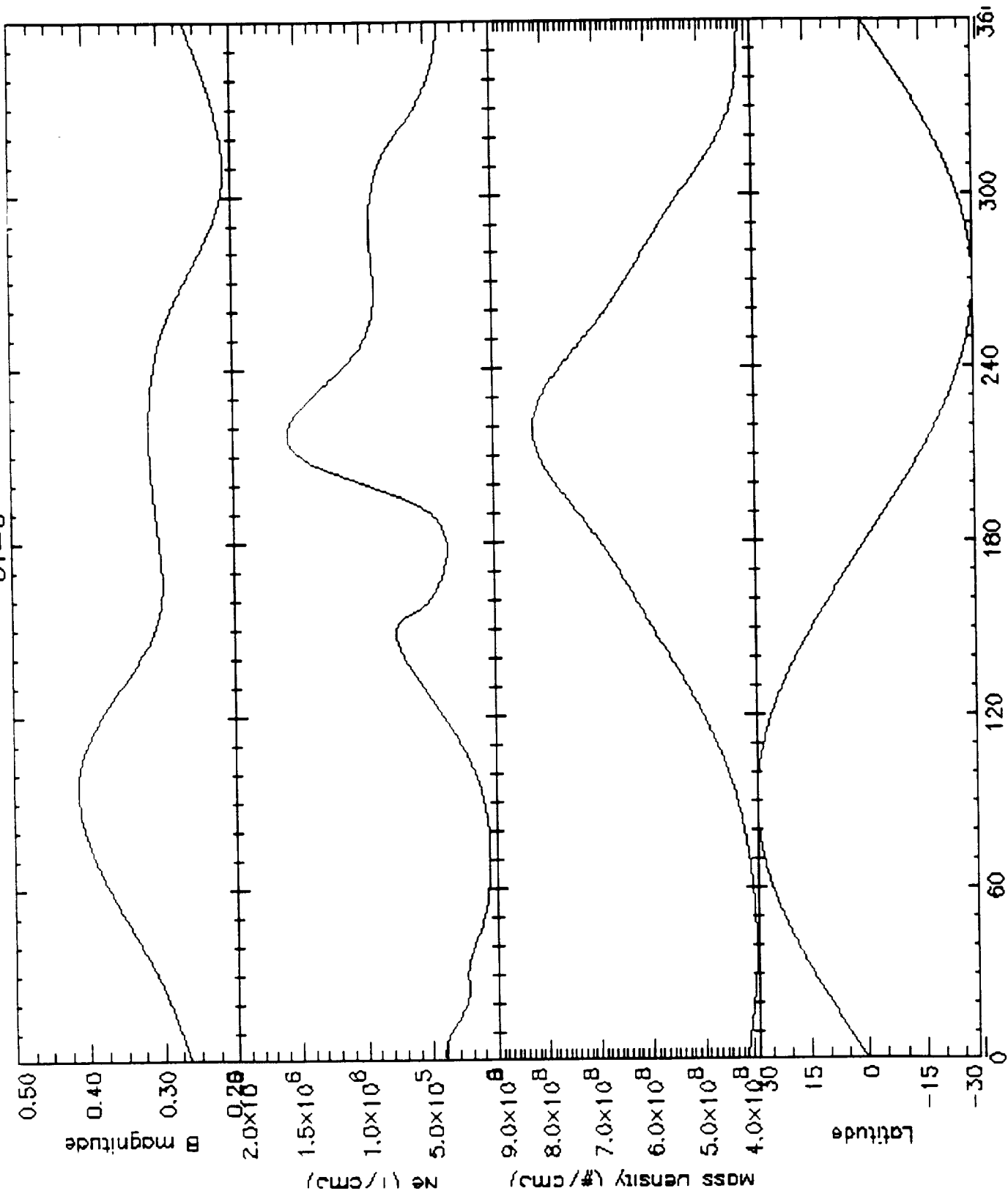
0.0

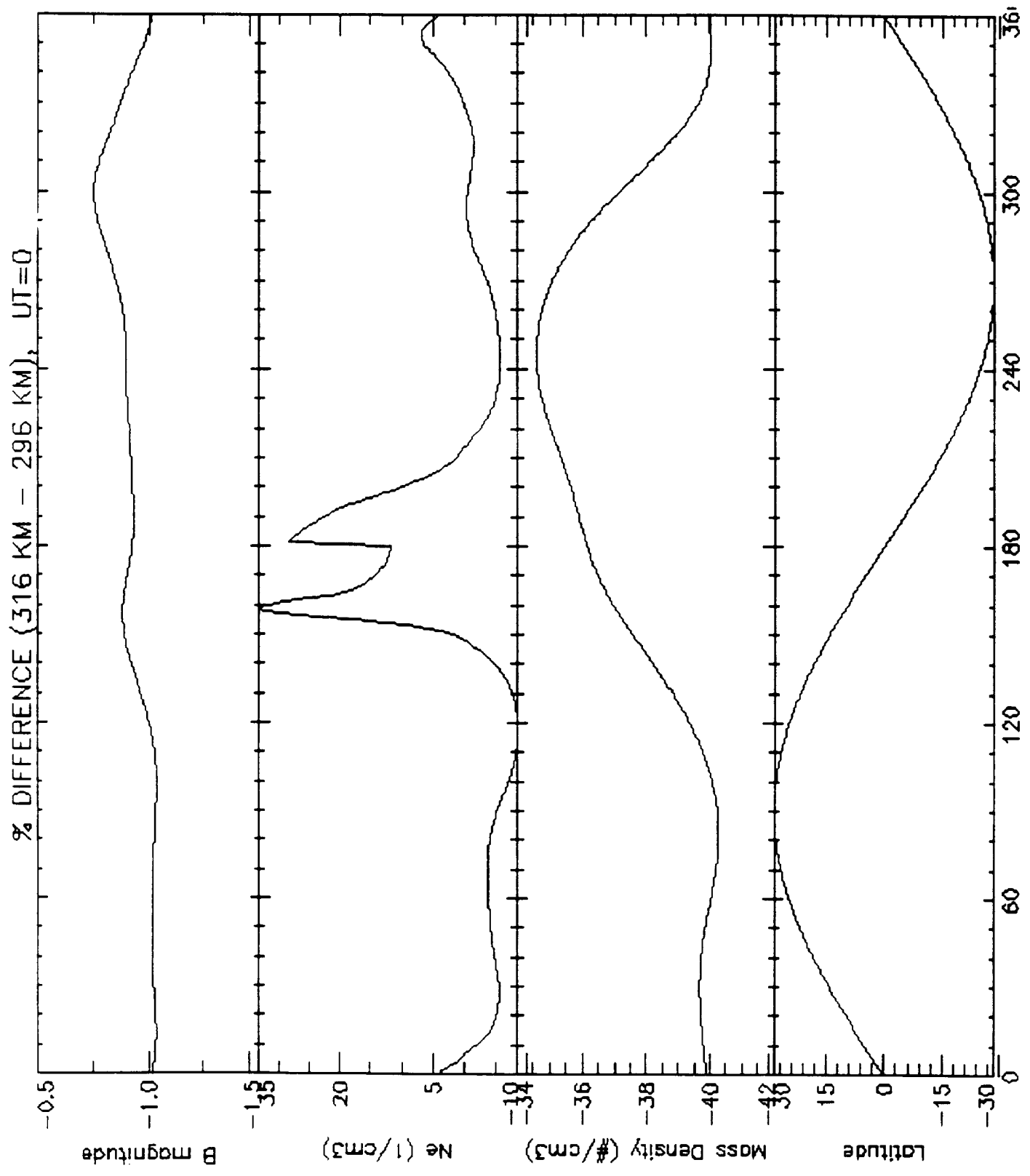
12.5

25.0



UT=0





APPENDIX 6

TSS 1R Quick-Look Science Assessment

NASA Headquarters

March 28, 1996

TSS 1R Quick-Look Science Summary

- **Overview (Nobie Stone)**
- **Dynamics of Deployment (Franklin Chang-Diaz)**
- **Electrodynamic Science (Adam Drobot)**
- **Summary (Nobie Stone)**

Scientific Rationale for TSS

- **Facility Requirements Definition Team (FRDT) ‘Blue Book’ (1980)**
 - **Electrodynamics**
 - **Electrical Currents in Space**
 - **Wave Generation and Propagation**
 - **Satellite Potential Control**
 - **Atmospheric/Geophysical**
 - **Global Mapping of Lower Thermospheric Currents**
 - **Atmospheric Composition**
 - **Crustal Induced Magnetic Field Variations**
 - **Gravity Gradient Measurements**

TSS 1R Program Goals

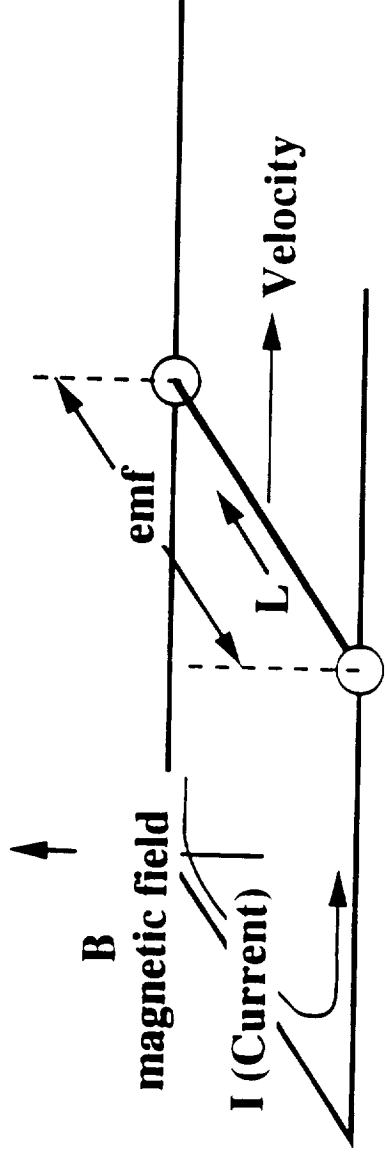
- **The primary goals of the TSS 1R mission are the characterization of:
 - the electrodynamics
 - and dynamicsof long tethered systems deployed in space.**

TSS-IR SCIENCE INVESTIGATORS

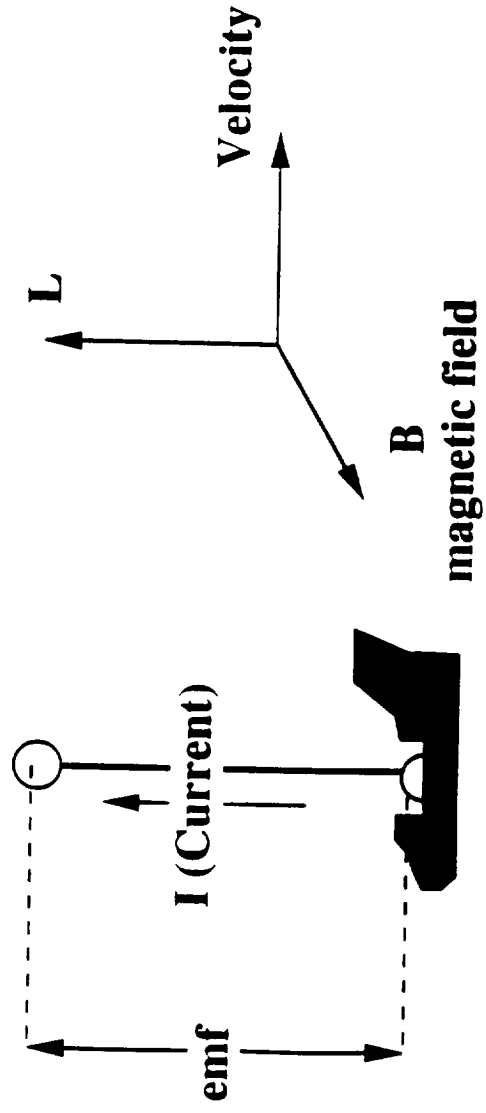
PI/INSTITUTION	INVESTIGATION	INSTRUMENTATION
GILCHRIST, U. OF MICHIGAN	SHUTTLE ELECTRODYNAMIC TETHER SYSTEM (SETS)	FPEG, SRPA, SLP, CCP, TETHER CURRENT- VOLTAGE MONITOR
BERGAMASCHI, PADOVA UNIVERSITY	A THEORETICAL & EXPERIMENTAL INVESTIGATION OF TSS DYNAMICS (TEID)	THEORETICAL (DYNAMICS)
DROBOT, SAIC	THEORY & MODELING IN SUPPORT OF TETHER (TMST)	THEORETICAL (ELECTRODYNAMICS)
DOBROWOLNY, CNR/IFIS	RESEARCH ON ELECTRODYNAMIC TETHER EFFECTS (RETE)	E-FIELD ANTENNA, SEARCH-COIL MAGNETO- METER, LANGMUIR PROBE (SAT DRB MOUNTED)
ESTES, SAO	INVESTIGATION OF EM EMISSIONS BY THE ELECTRODYNAMIC TETHER (EMET)	GROUND-BASED
GULLAHORN, SAO	INVESTIGATION OF DYNAMIC NOISE IN THE TSS (IMDN)	THEORETICAL (DYNAMICS)
MARIANI, U. OF ROME	MAGNETIC FIELD EXPERIMENT FOR TSS MISSIONS (TMAG)	3-AXIS MAGNETOMETERS (SAT. BOOM MOUNTED)
STONE, NASA/MSFC	RESEARCH ON ORBITAL PLASMA- ELECTRODYNAMICS (ROPE)	DIPP & 2 SPES's (SAT BOOM-MTD.) 3 SPES's (SAT. SURFACE-MTD.)
TACCONI, U OF GENOA	OBSERVATION AT EARTH'S SURFACE OF ELECTROMAG. EMISSIONS BY TSS (OESEE)	GROUND-BASED
BONIFAZI, ASI	DEPLOYER/SATELLITE CORE EQUIPMENT (DCORE/SCORE)	ELECTRON-GUNS, TETHER I-V MONITOR., SAT. ACCELEROMETER
HARDY, USAF PHILLIPS LAB	SHUTTLE POTENTIAL & RETURN ELECTRON EXPERIMENT (SPREE)	ELECTRON/ION ELECTROSTATIC ANALYZERS
MENDE, LOCKHEED	TETHER OPTICAL PHENOMENA (TOP)	LOW-LIGHT LEVEL TV CAMERA

TSS Electric Generator Analogy

1. The motional electro motive force (emf)



2. The Tethered Satellite System Generator



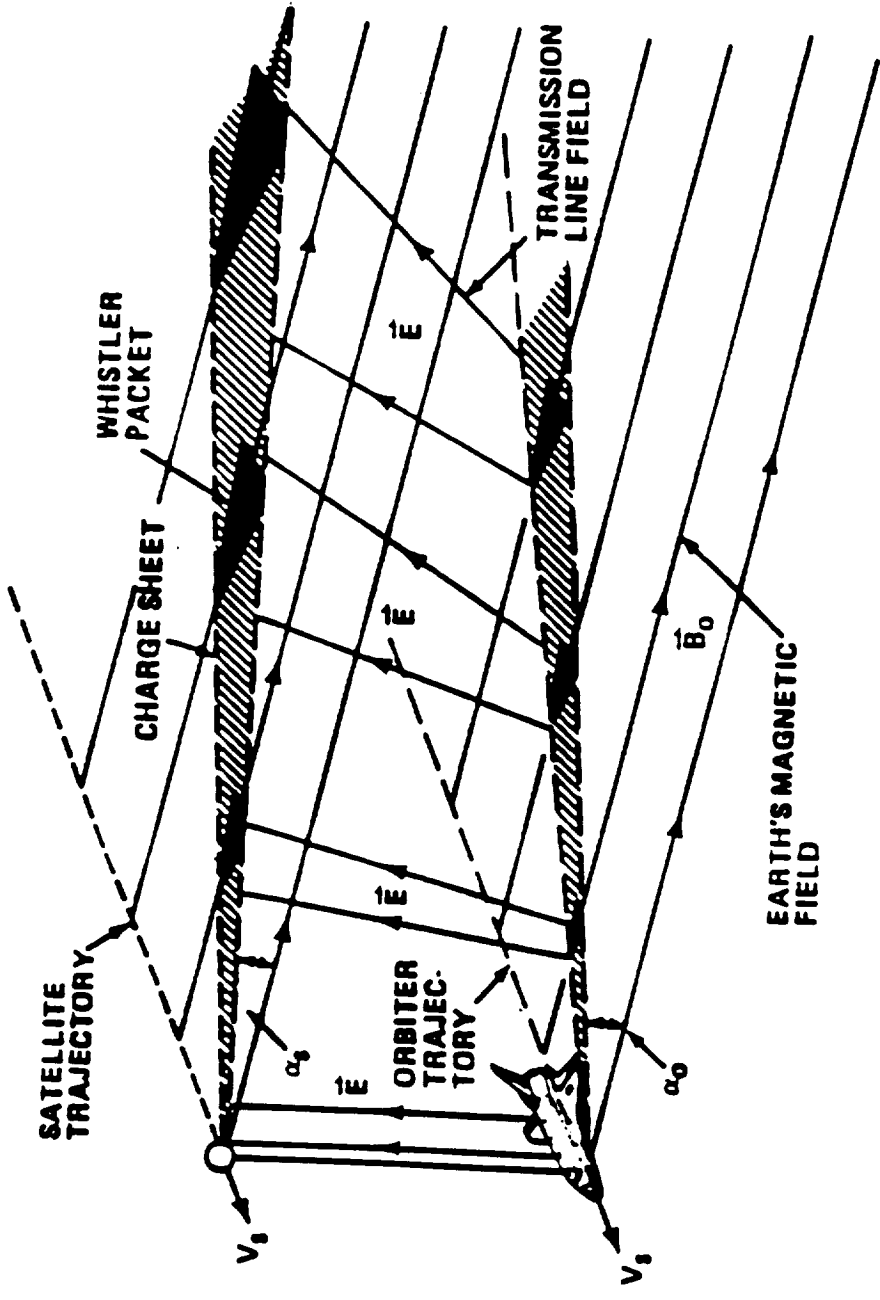
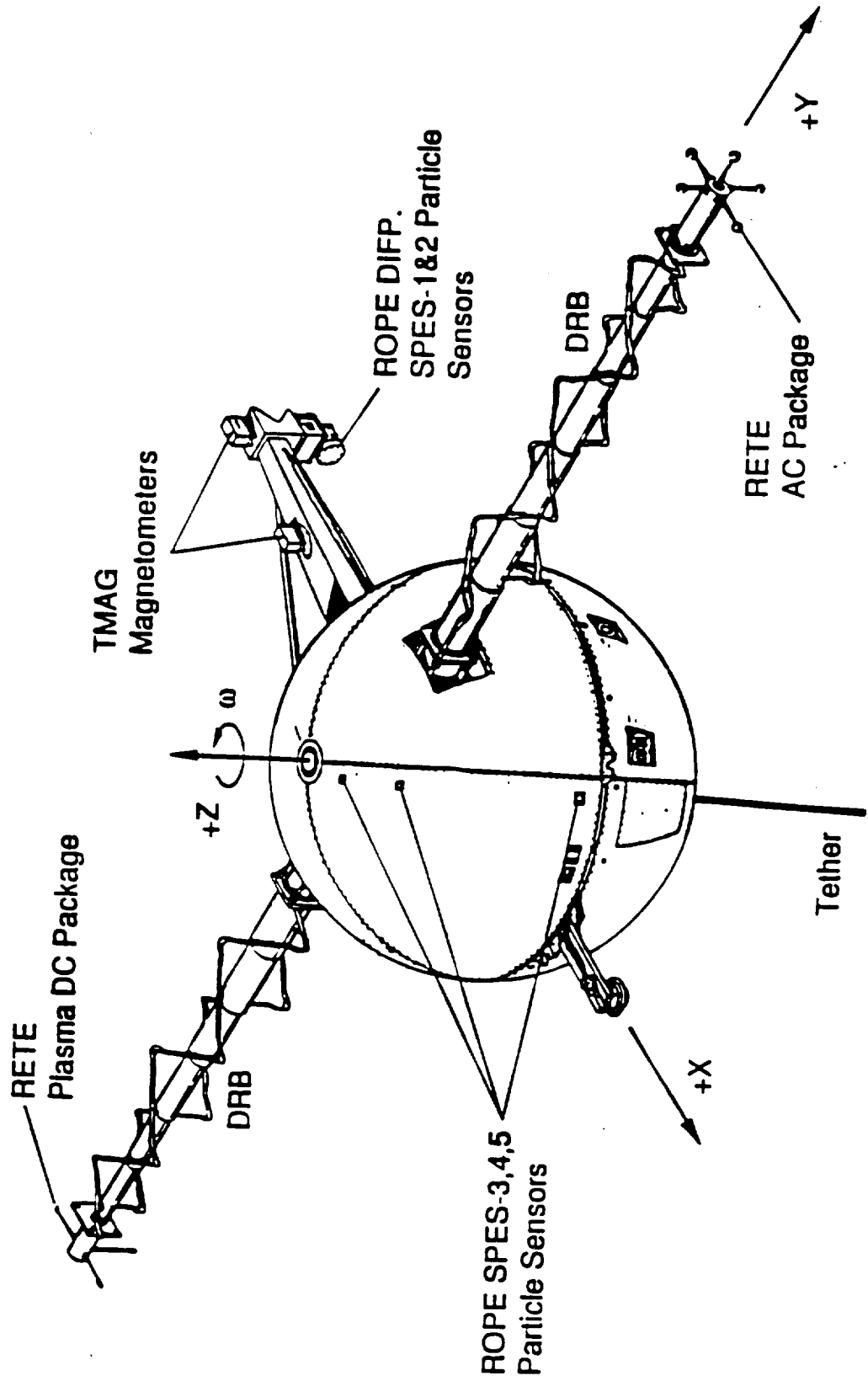
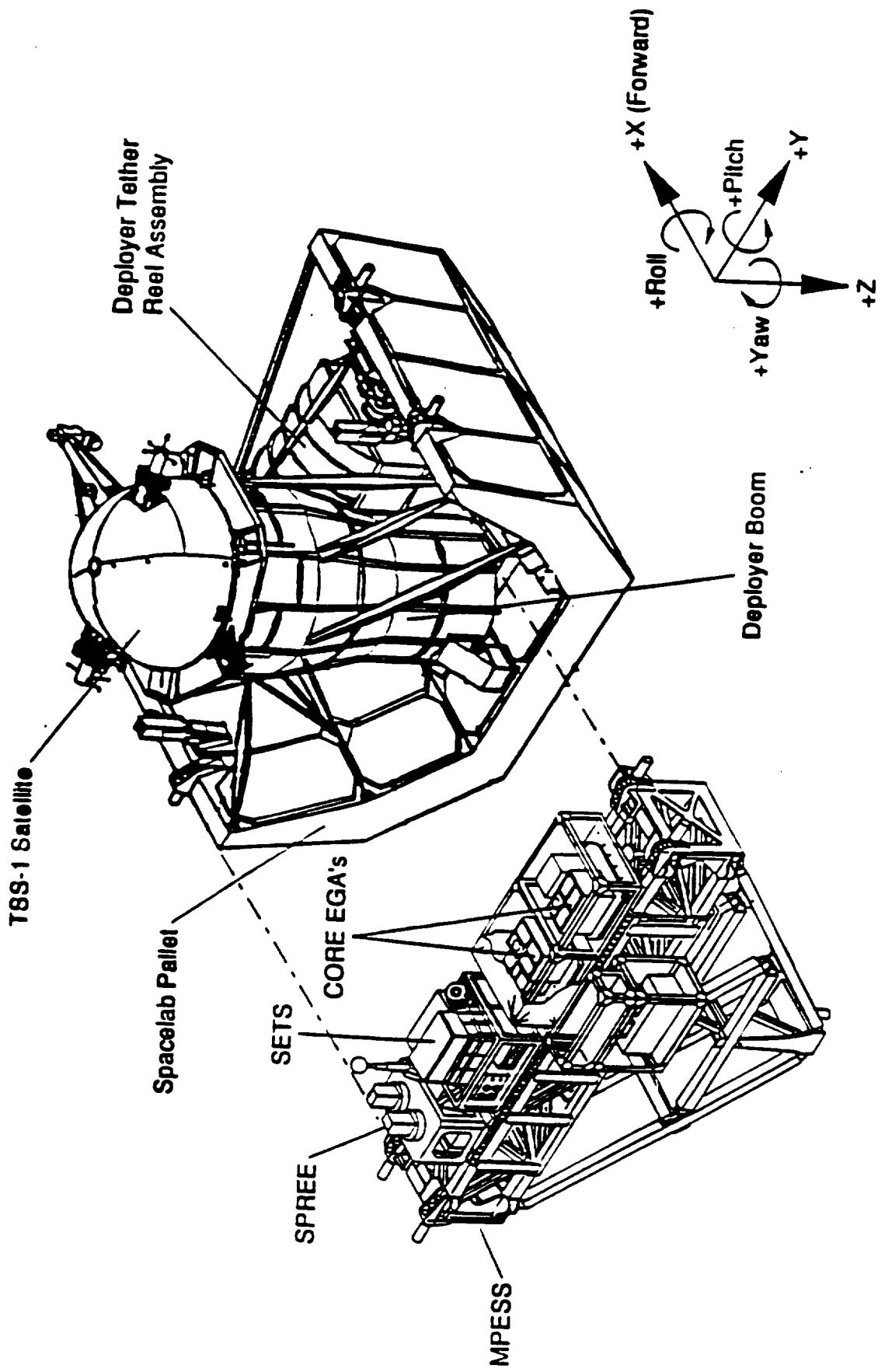
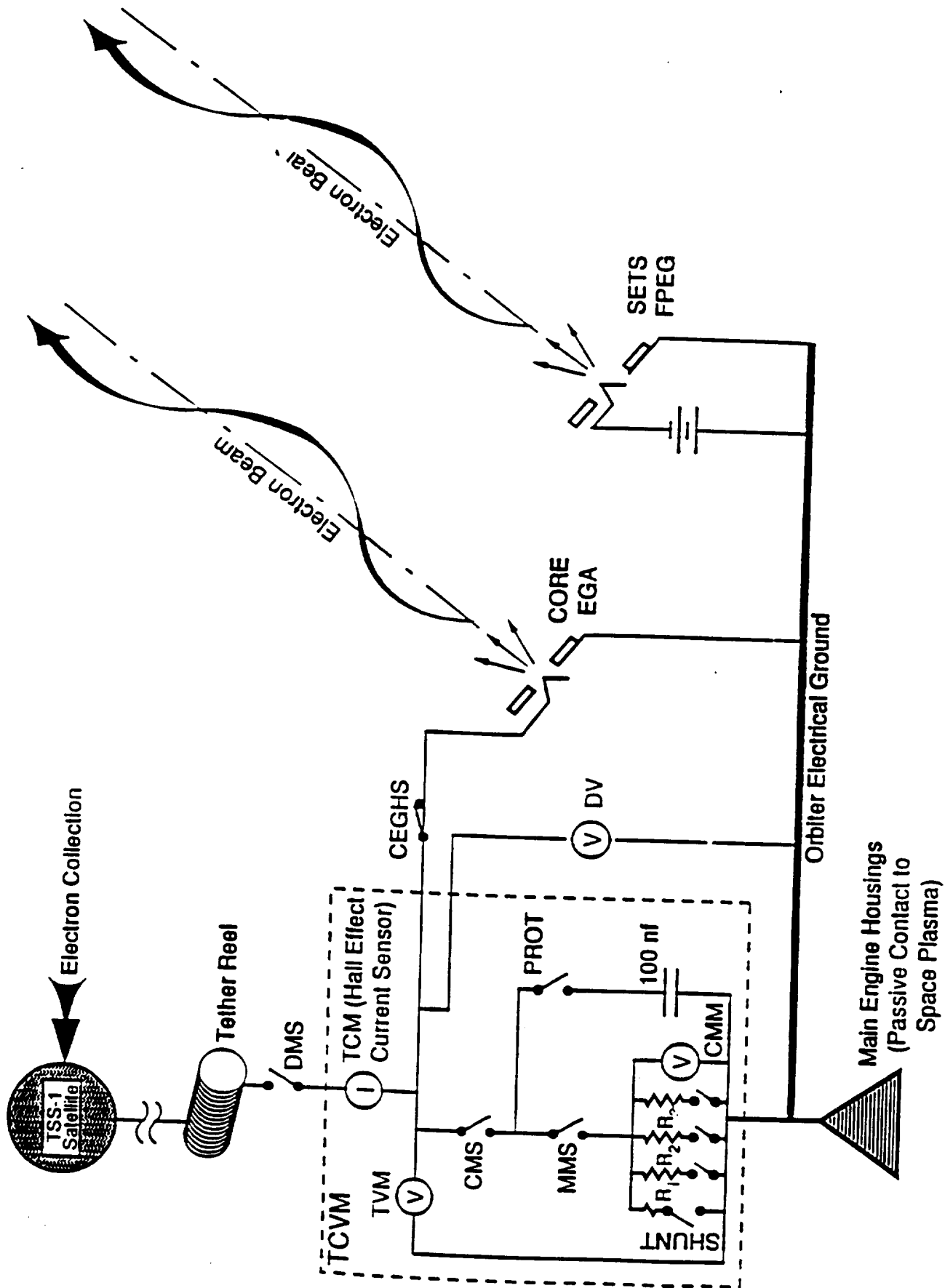
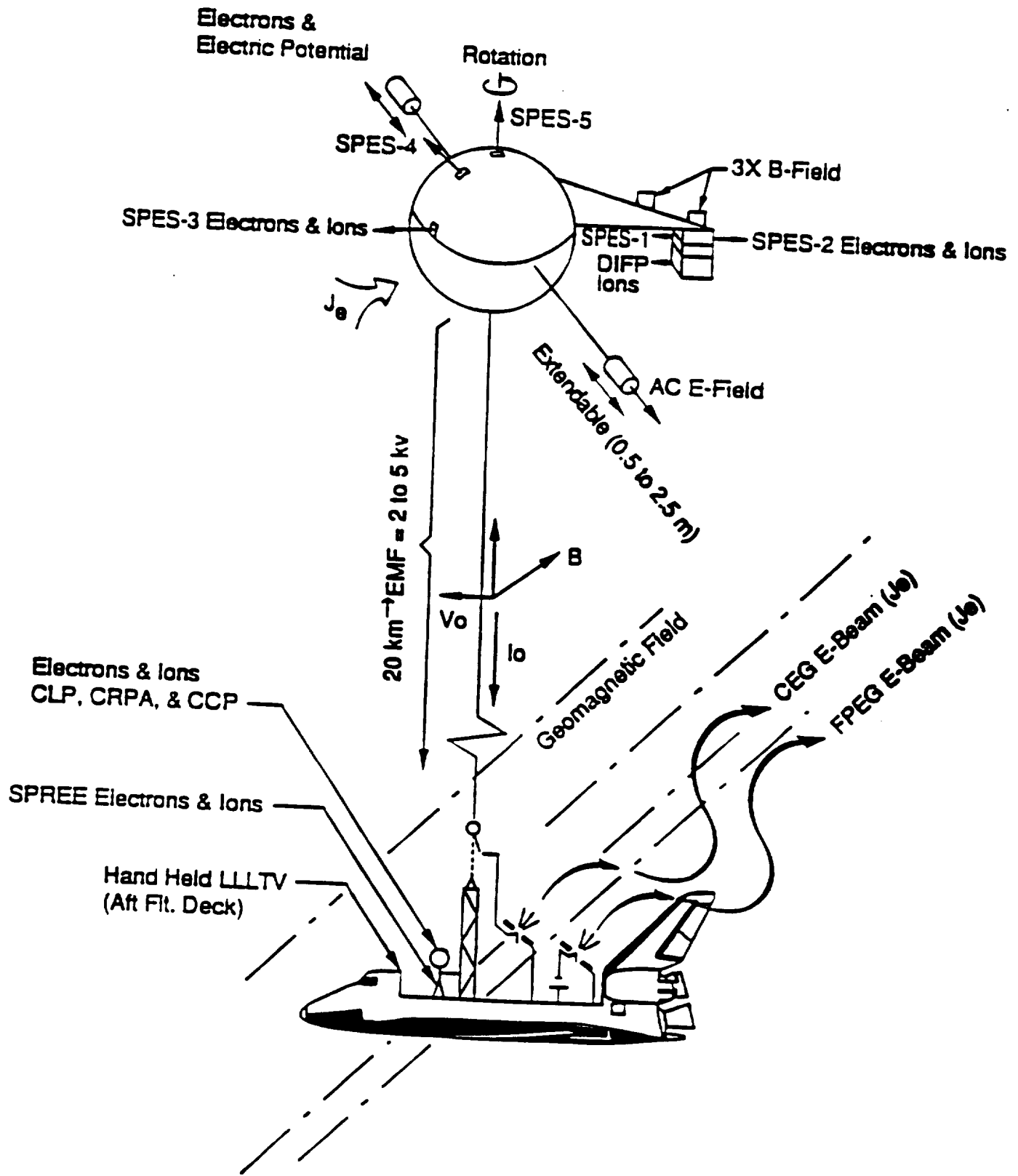


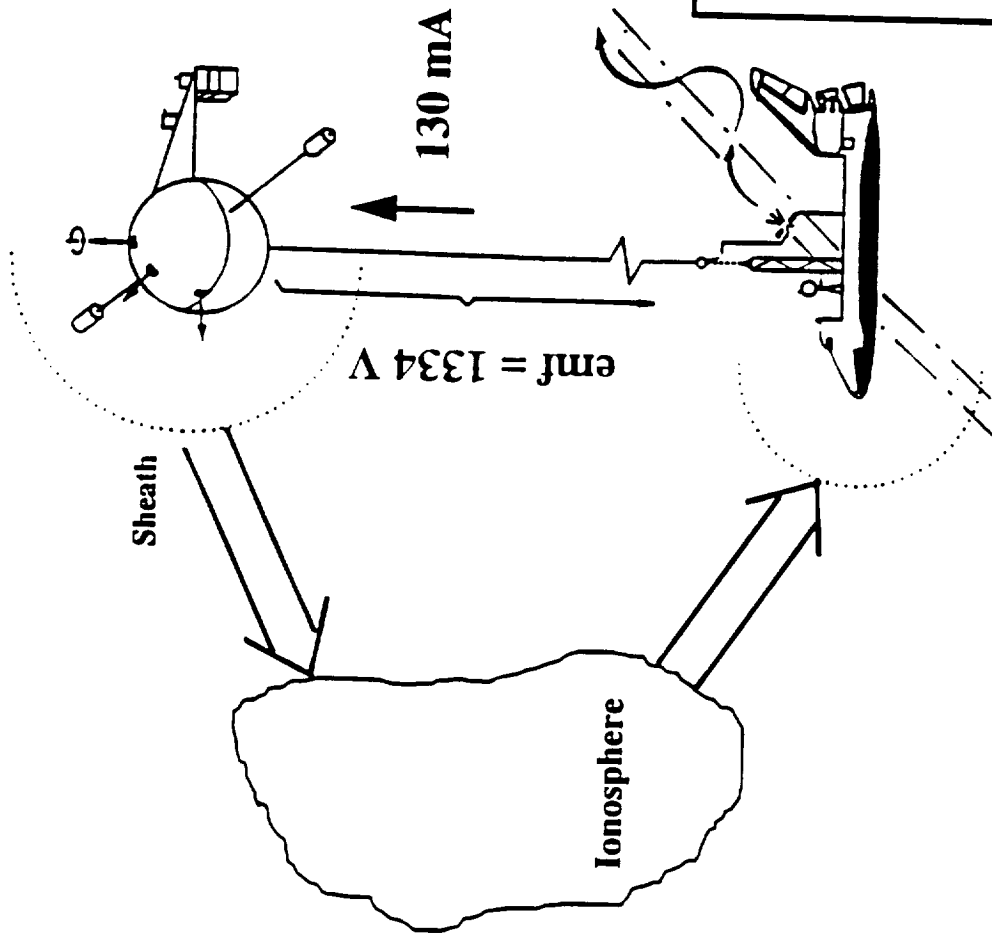
FIGURE 1.





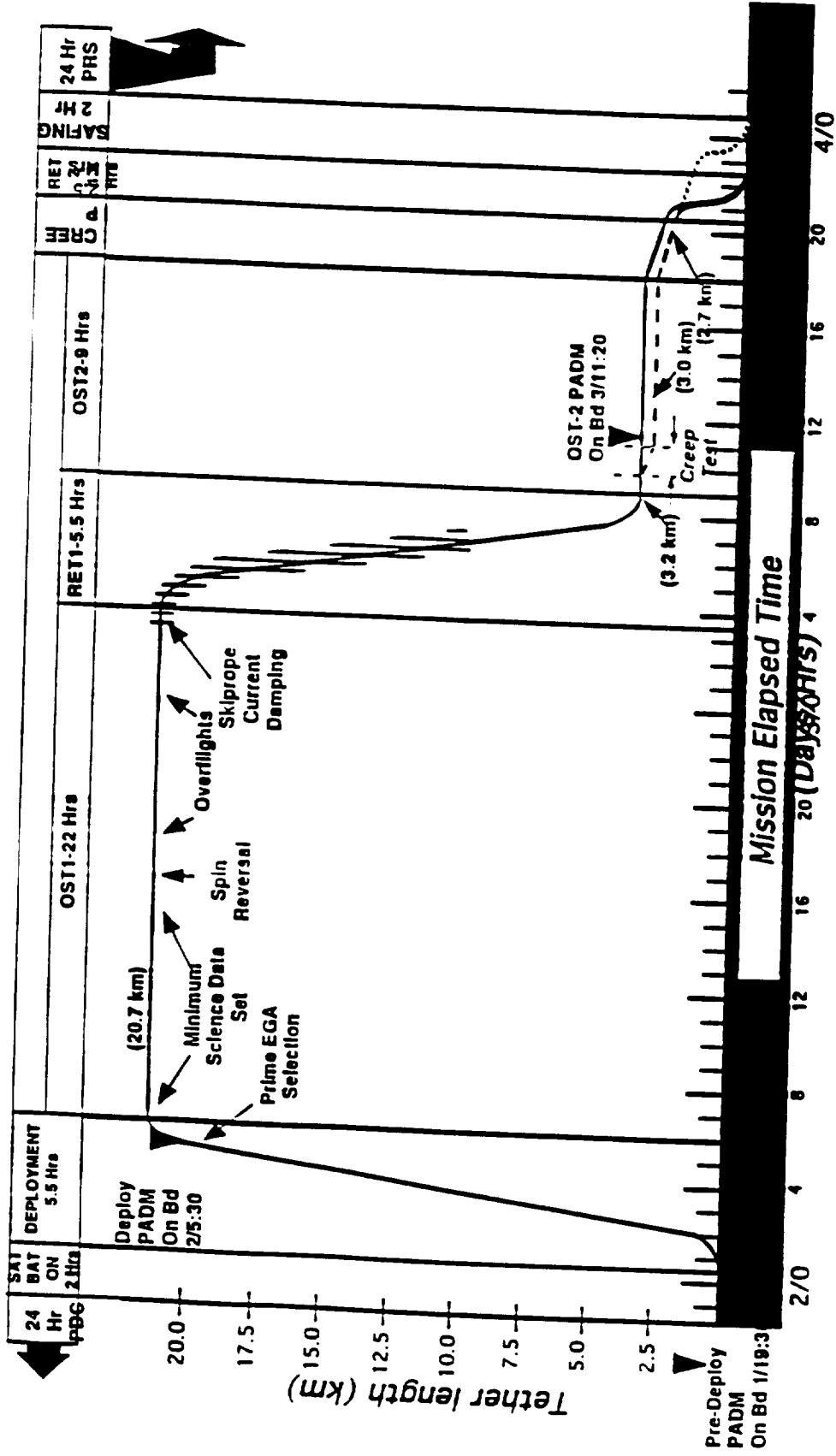






<u>Potentials</u>	
Satellite	= 200 V
Tether (IR)	= 234 V
Orbiter	= -150 V
Electron Gun	= 750 V

Tether Length \approx 6.3 km



TSS IR Dynamics

- **Demonstrated**
 - Deployment Dynamics: Benign
 - Stability: Excellent
 - Controllability: Excellent
- **Unplanned Observations**
 - Bowing: Benign for deploy (retrieval?)
 - Free Tether Dynamics: Observed for first time
 - Orbital Boost: Demonstrated
 - Tether Lifetime - 25 Days
- **Still to be Demonstrated for Long Tethers**
 - On Station Dynamics and Electrodynamics
 - Retrieval
 - Electrodynamic Coupling During Retrieval
- **Demonstrated Tether Technology has Unique Advantages for Science and Technology Applications**

TSS 1R Electrodynamics

- **I-V Characteristics**
 - Motional \leftrightarrow Electrical Power
 - Induce Geophysical Processes
- **Important Physics**
 - Ionospheric Closure (charge transport, waves)
 - Satellite Sheath (electron collection, ionization)
 - Orbiter Sheath (ion collection, electron emission, ionization)

TSS IR Electrodynamics

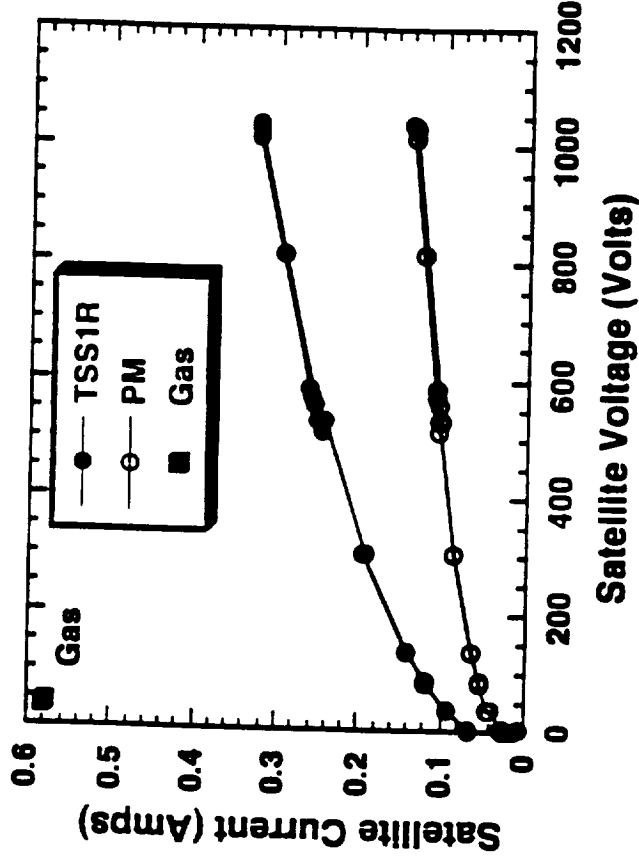
- **I-V Characteristics**
 - Sheath Dynamics Affected by:
 - Gas Injections
 - Electron/Ion Injections
 - Ambient Conditions
 - High Velocity Plasma
 - No Walls
 - Vehicle Attitudes
 - Extended Operations

TSS 1R Electrodynamic

- **I-V Characteristics**

24 Full I-V Sweeps

- TSS EMF
0 - 3700 Volts
- Satellite Potential
0 - 1200 Volts
- Satellite Current
> 580 milliamps
maximum, limited
by gun circuit.



TSS IR Electrodynamics

DATA:

CORE

RETE

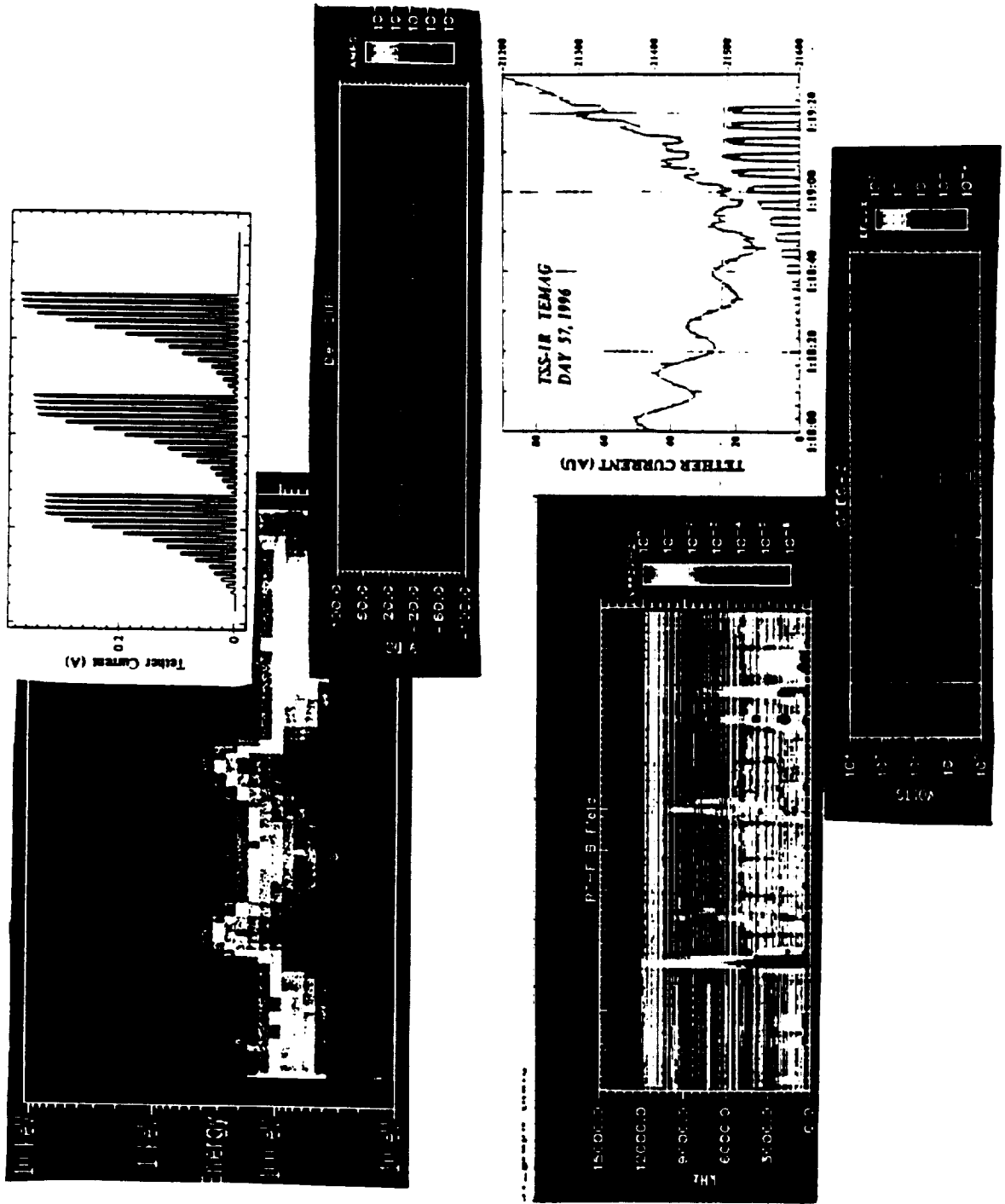
ROPE

SETS

SPREE

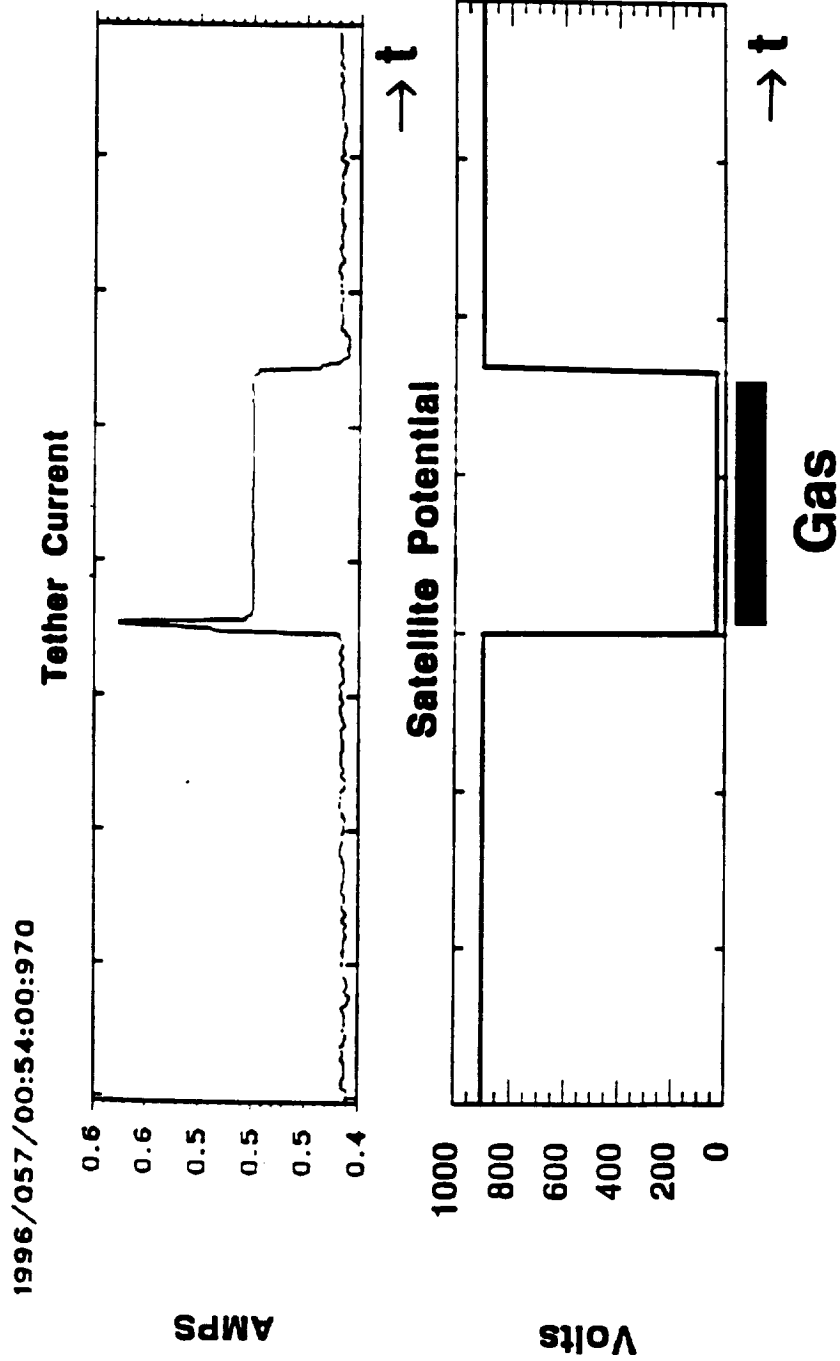
SUNDIAL

TMAG



TSS 1R Electrodynamics

- **Gas Release at Satellite**
 - Current Increases while Satellite Voltage Decreases
 - Collection Efficiency Increases by a Factor of 10



TSS IR Electrodynamics

- **I-V Characteristics**
 - High Current Collection
 - Efficiency \gg Equilibrium Models
 - Energized Sheath Electrons
 - Dynamics Dominate Current Collection
 - Ionization in Sheaths
- **No Limits Seen from Ionospheric Closure**

TSS 1R Electrodynamics

- **Post-Mission TSS 1R Science Investigations**
 - **Fundamental Current-Voltage Characteristics of the TSS**
 - **Effects of Gas Releases**
 - **Tether Current Charge Carrier Identification**
 - **Satellite High-Voltage Plasma Sheaths**
 - **Tethered Double Probe Detection of Long-Scale Ionospheric Electric Field Signatures**
 - **Simultaneous Tethered Double Point Detection of Ionospheric Equatorial Structures**
 - **Orbiter Charging Characteristics**

TSS IR Electrodynamics

- **Post-Mission TSS IR Science Investigations**
 - Tether Antenna System Characteristics
 - Satellite Position Estimation with Respect to the Orbiter
 - Electron Beam Emission Characteristics
 - Near Orbiter Environment Plasma Survey
 - Satellite Wake Studies
 - Pick-Up Ions
 - Optical Survey of Long Wavelength Gravity Waves
 - Survey of Airglow Altitude Distribution

TSS IR Electrodynamics

- **I-V Characteristics**

Future Uses of Tethers

- **Efficient Power Generation/Electrical Propulsion**
 - Demonstrated 3.5kW (> 1.5kW usable)
- **Perturb Space Plasmas for Cause/Effect Studies.**

Post Break Experiments

- **Generation and Propagation of Magnetosonic Waves**
- **Differential Spacecraft Charging**
- **Tether Lifetime ~ 25 Days**
- **Orbit Transfer**

Summary

- **Accomplishments**
 - Significant Progress in Key Mission Objectives
 - Characterization of Current-Voltage Relation
 - Demonstrated Effect of Gas Release
 - Controlled Deployment to 19.7km
 - Orbital Transfer
 - Long Tether Lifetime
- **Significance**
 - New Current Collection Processes Discovered
 - Demonstrated Electrical Power Generation
 - Ionization Processes in Space Plasmas
 - Viability of Tether Applications
 - Orbital Boost/Deboost
 - Low Gravity Experiments

Summary - continued

- **Outstanding objectives**
 - External Ionospheric Current Loop
 - Plasma Wave Response
 - Dynamic/Electrodynamic Coupling
 - Retrieval for Long Tether Systems

Conclusions and Recommendations

- **Quick-look assesment of the data set indicates the potential for profound scientific discoveries**
- **TSS 1R has already provided significant findings**
 - Collection of Current by Bodies in Space
 - Effects of Injected Neutral Gas Clouds
 - Dynamic Stability and Control
- **The tether break will be resolved shortly and is not expected to preclude future uses of tethers**
- **NASA headquarters should implement a program of tether science and technology for use on space shuttle missions and space station**

APPENDIX 7

ELECTRON COLLECTION BY THE TSS SATELLITE

by

**C.L. Chang, A.T. Drobot, P. Satya-Narayana
K. Papadopoulos (SAIC)**

D. Winningham, C. Gurgiolo (SWRI)

N. Stone (NASA/MSFC)

K. Wright (UAH)

D. Intriligator (CRC)

at

1996 Spring AGU, Baltimore, Maryland

OUTLINE

- **IV** characteristics of the TSS satellite is constructed
- **Electron current** is collected by the TSS satellite at a **higher level** than that of the Parker-Murphy model
- Enhancement of electron collection could be due to
 - dynamic collection
 - electron energization
 - ionization of neutrals
- **Hot electrons** were observed by the particle sensors (**ROPE** investigation) onboard satellite
- **3D fluid model** shows that current collection by a positively charged sphere can be enhanced in the presence of a hot electron population

IV CHARACTERISTICS OF TSS SATELLITE

- Current-Voltage sweeps cover a range of 1100 volts and 0.5 amperes parameter space
- Ambient density varies from 10^{**5} /cc up to 10^{**6} /cc based on IRI model along the shuttle orbit
- TSS IV points are plotted against the Parker-Murphy values
- Parker-Murphy model

$$\frac{I_{PM}}{I_o} = 1 + 2 \sqrt{\frac{V_{Sat}}{V_o}}$$

where

$$I_o = 2\pi a^2 J_o = \pi a^2 e N_o v_{the} / 2$$

$$V_o = m_e \Omega_e a^2 / 2e$$

- Satellite current is **consistently higher** than the Parker-Murphy current, except at very low voltage ($\ll 10$ volts)

SCENARIOS FOR HIGHER ELECTRON CURRENT

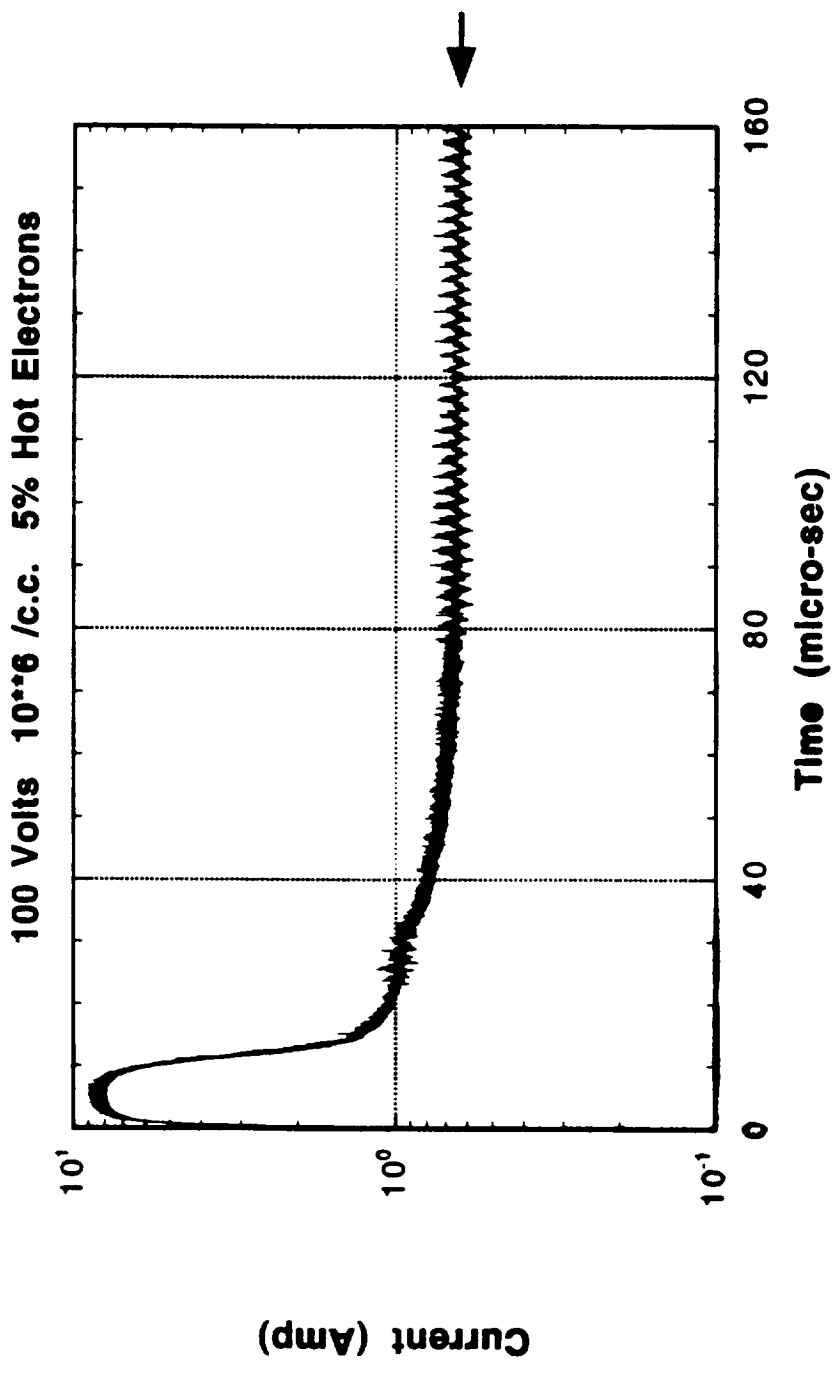
- TSS satellite moves into undisturbed ionospheric regions continuously, causing a surge of electron current attracted by the satellite in these regions
- Ambient electrons are heated to a higher temperature, presumably through some wave-particle processes, that results in a higher electron flux entering the sheath
- Ionization of neutrals (ambient & outgassed)

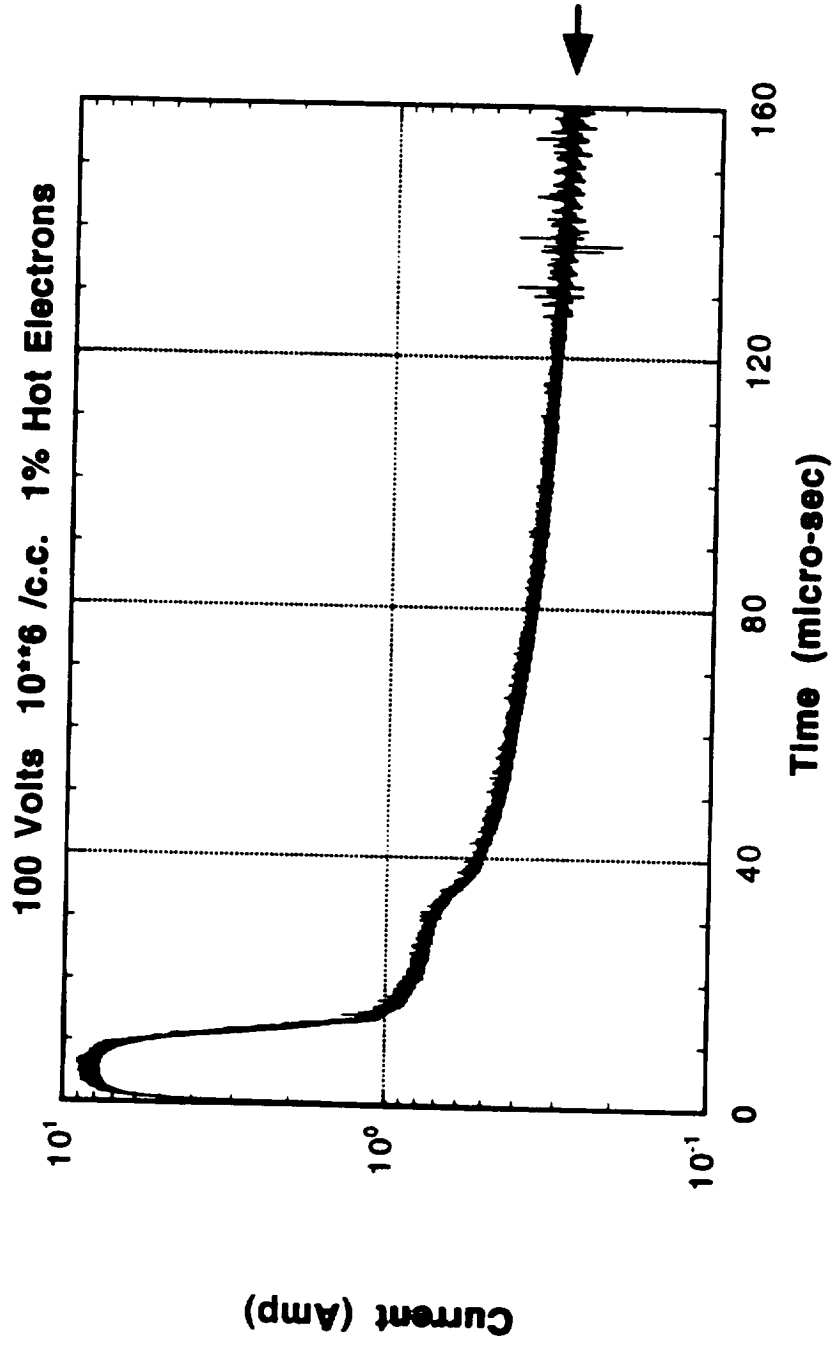
OBSERVATIONS OF HOT ELECTRONS

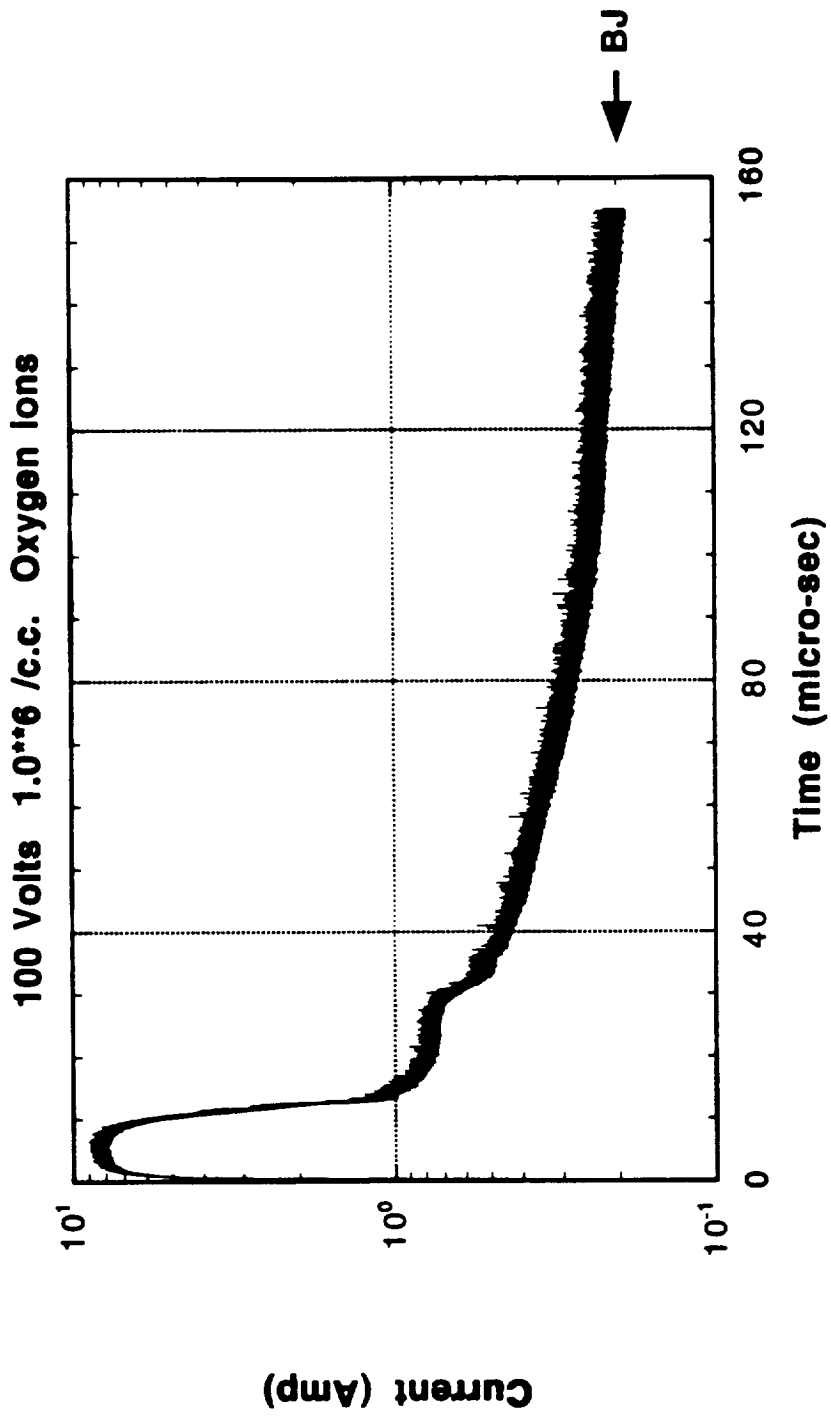
- ROPE electron measurements show that energy spectra of accelerated electrons by the satellite potential can be followed only up to 30 - 40 eV.
- A 100 - 200 eV peak in the electron energy spectra emerges and intensifies with the increasing satellite potential
- Intensity of these "hot" electrons peaks near ram and/or along the ambient B field

3D FLUID SIMULATION

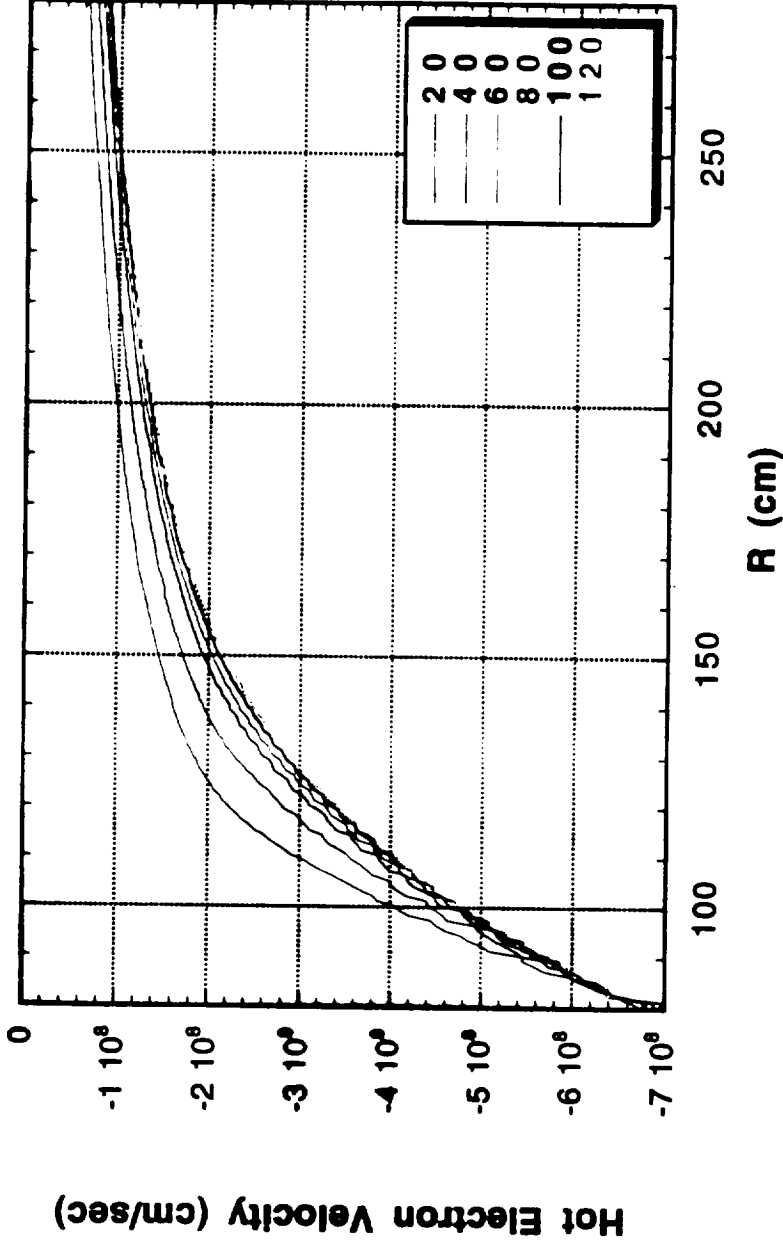
- Starting condition: sphere in uniform ambient plasma
 - plasma density: 10^{*6} /cc
 - temperature: 1000 degree K
 - stationary plasma
 - no magnetic field
- Voltage of 100 volts is applied to the sphere in 1 μ s
- Compare 3 cases of hot (100 eV) electrons
 - (1) No hot electrons
 - (2) 1% hot electron population
 - (3) 5% hot electron population
- Initial current surge after voltage is switched on
- Satellite current approaches a steady level after 150 μ s
- Higher the hot electron population, higher the current collection

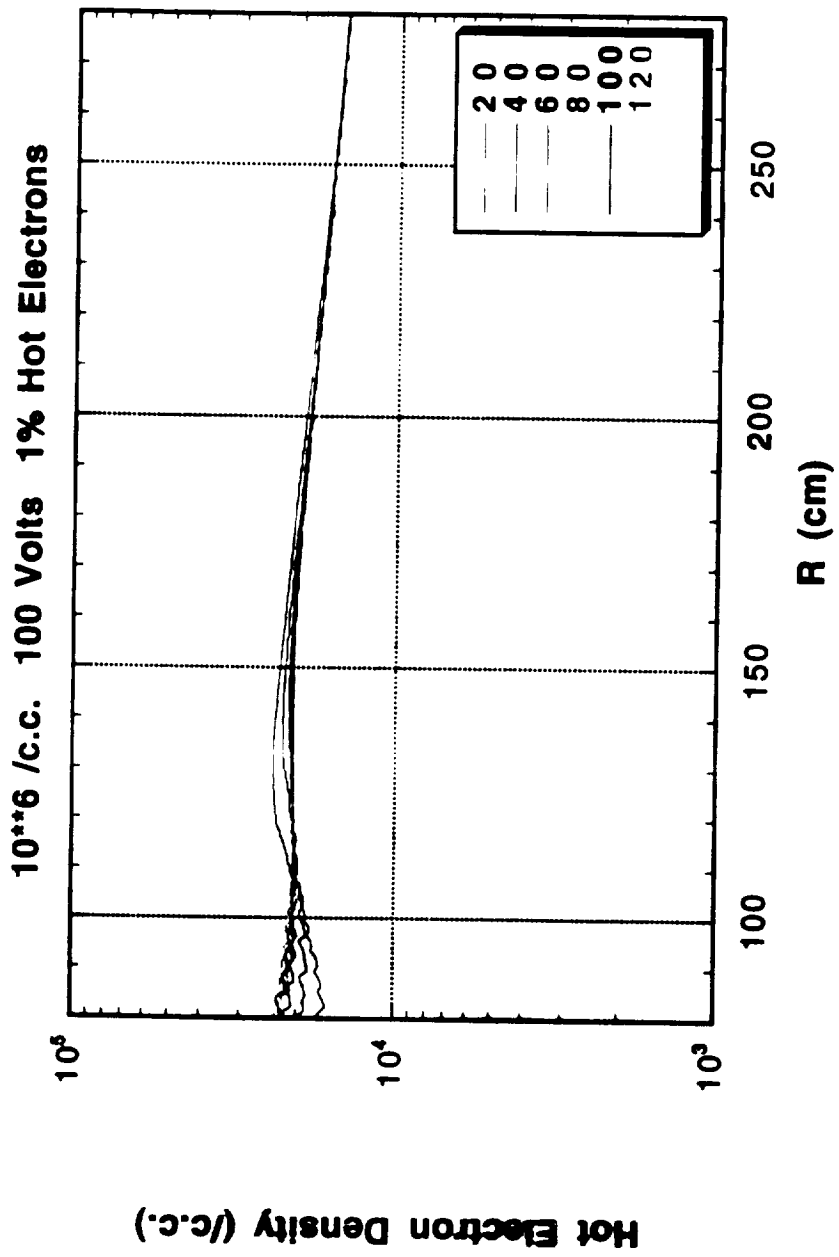


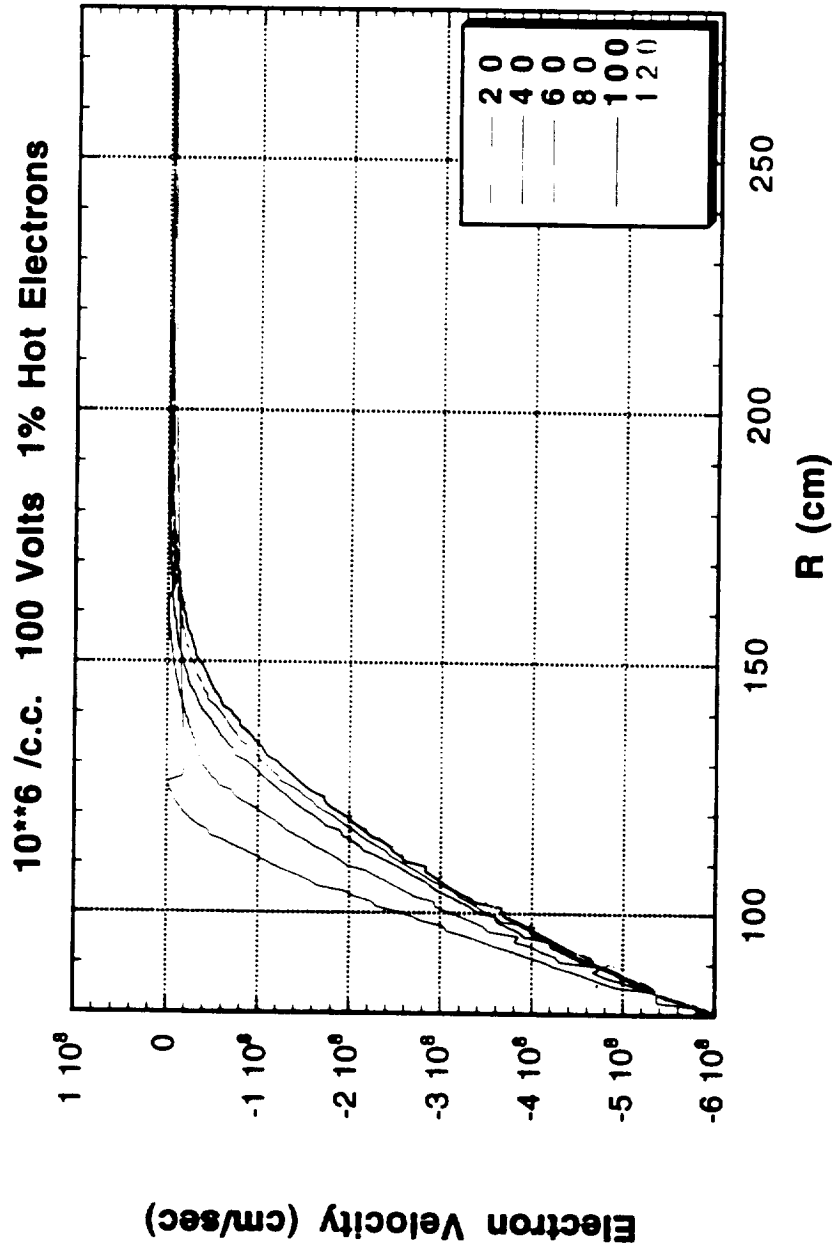




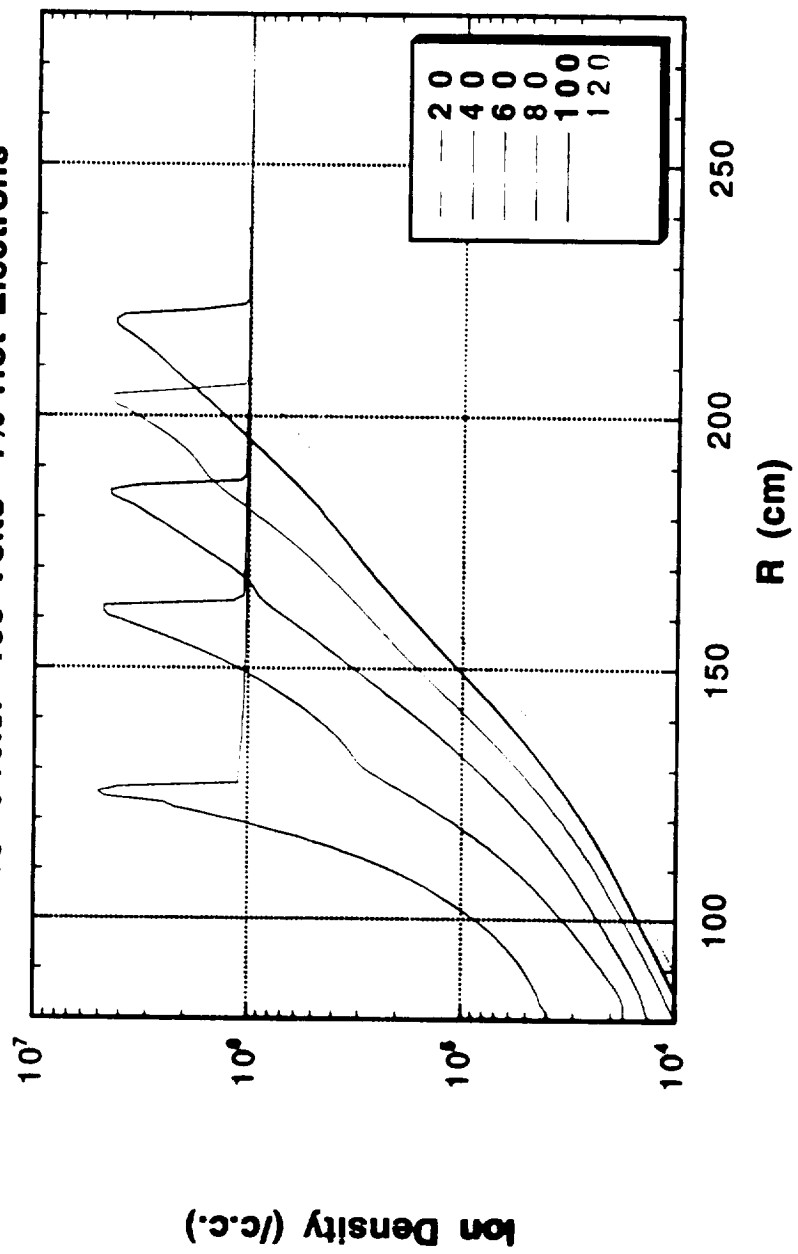
10^{16} /c.c. 100 Volts 1% Hot Electrons



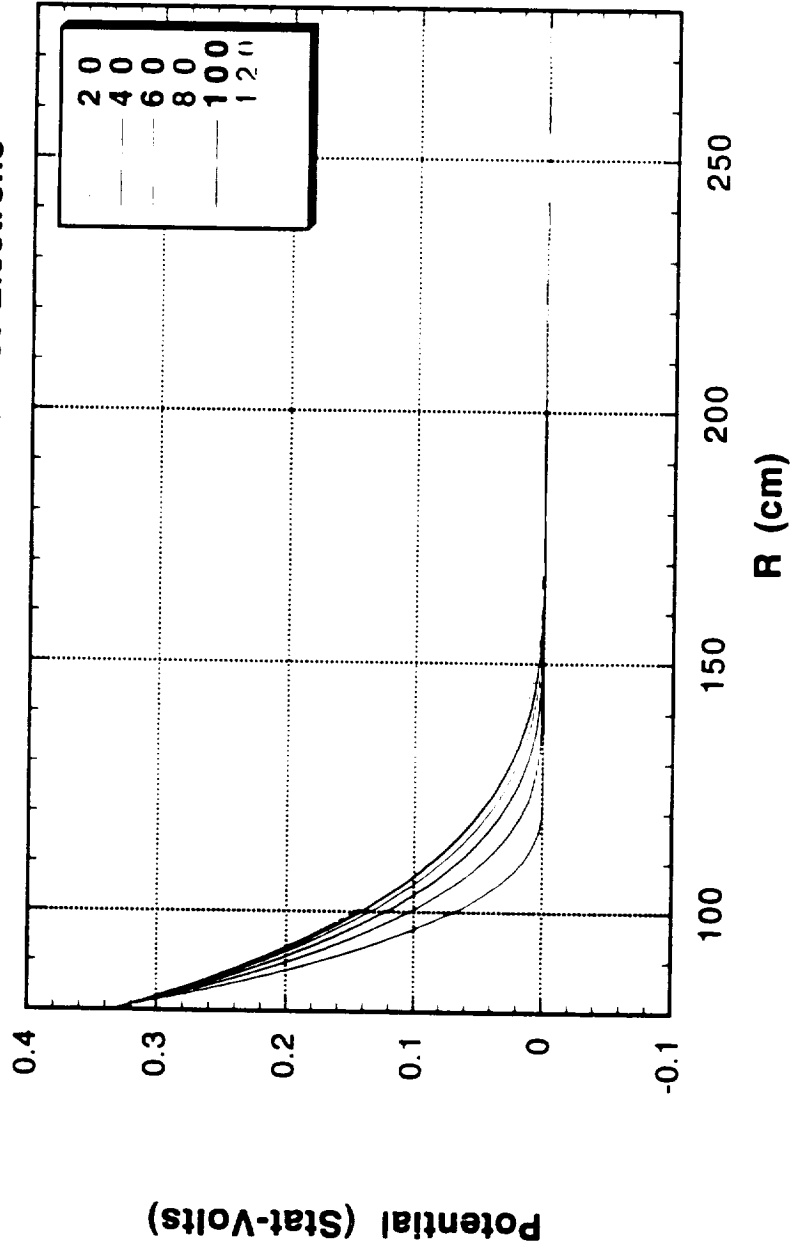




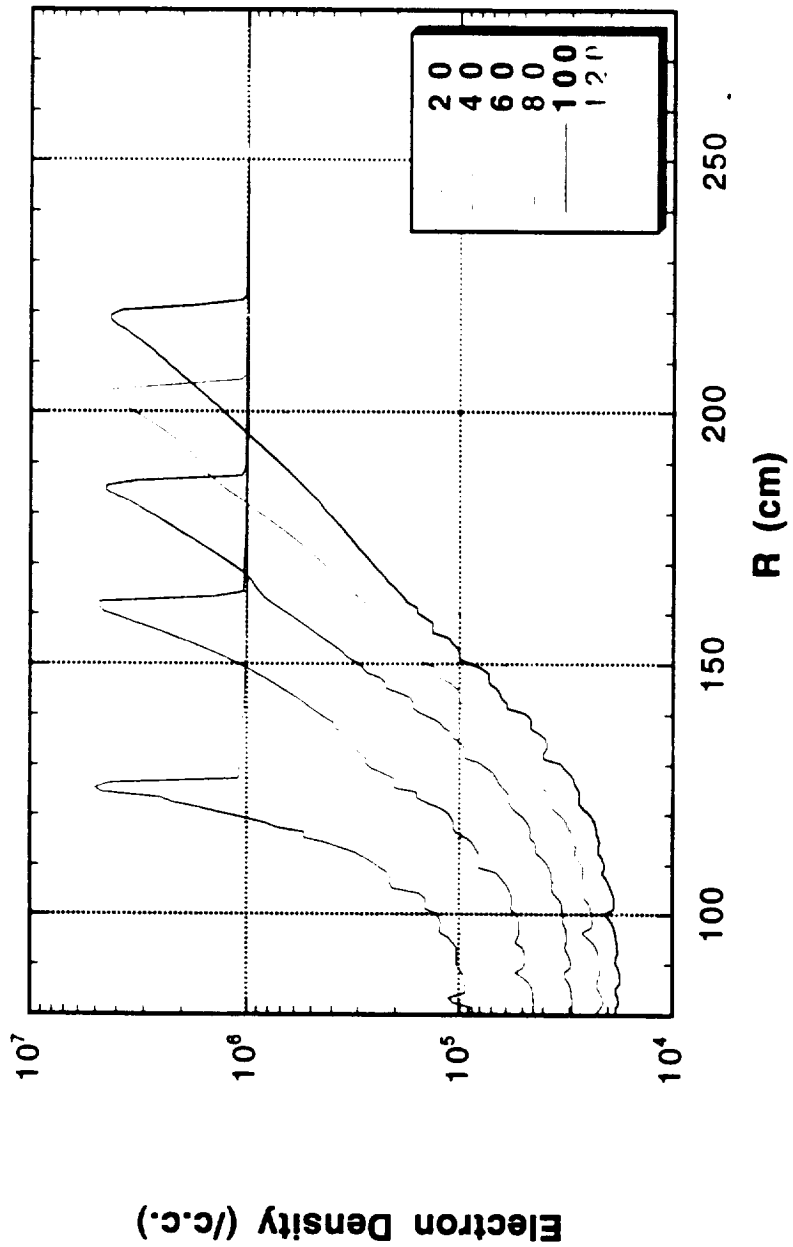
10^{16} /c.c. 100 Volts 1% Hot Electrons

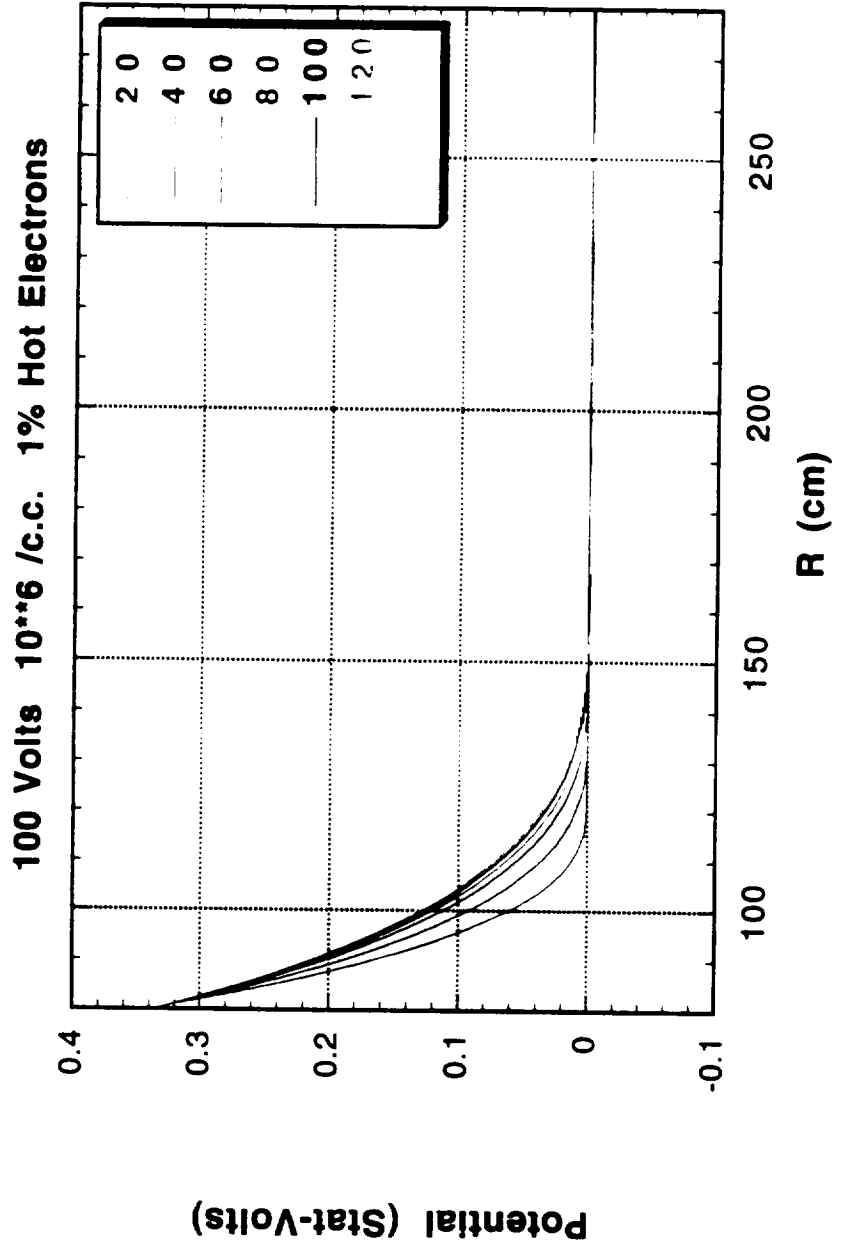


10^{16} /c.c. 100 Volts No Hot Electrons



106 /c.c. 100 Volts 1% Hot Electrons**





APPENDIX 8

Neutral Environment of the TSS Satellite and its Effects on Current Collection

D. F. Rault, NASA Langley Research Center

C.L. Chang, Science Applications International Corporation

**American Geophysical Union Fall Meeting
Dec 15 - 19, San Francisco, CA , 1996**

OUTLINE

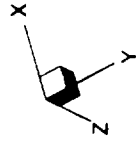
- **Purpose of study**
- **Analysis method**
- **Numerical tools**
- **Results**
- **Conclusion**

Purpose of Study

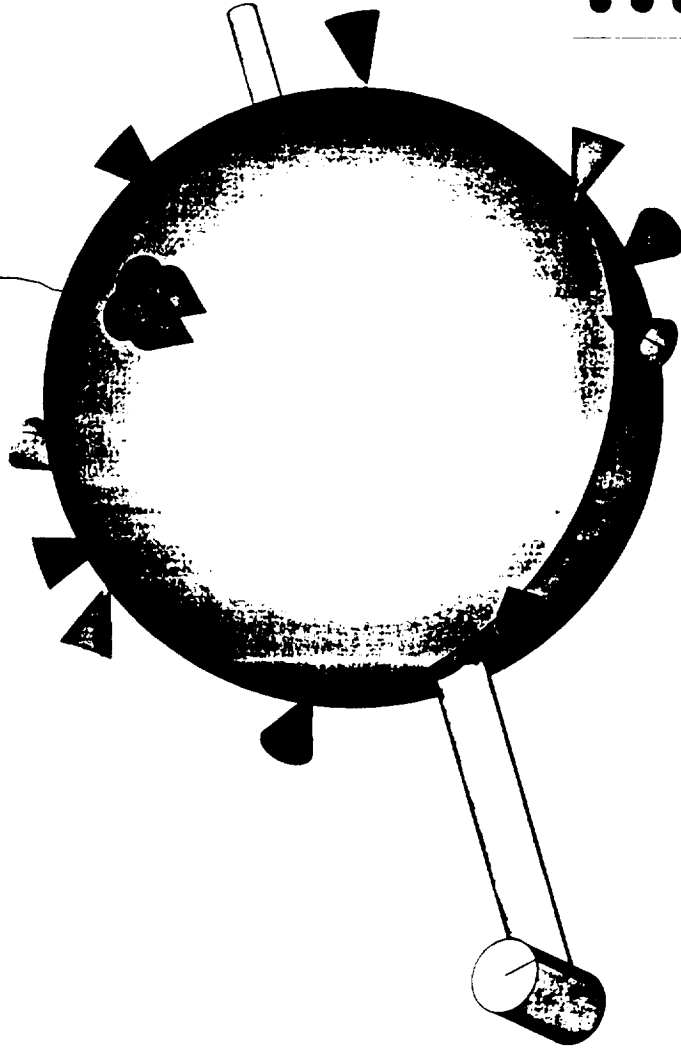
To characterize the artificial neutral atmosphere around TSS created by thruster firings (14 thrusters mounted on TSS surface)

- . To provide first order assessment of neutrals (Density, Velocity, Temperature)**
- . To investigate "secondary effects":
Plume impingement (Yaw)
Multi plume interaction (In Line)**

TSS Satellite Thrusters



Tether



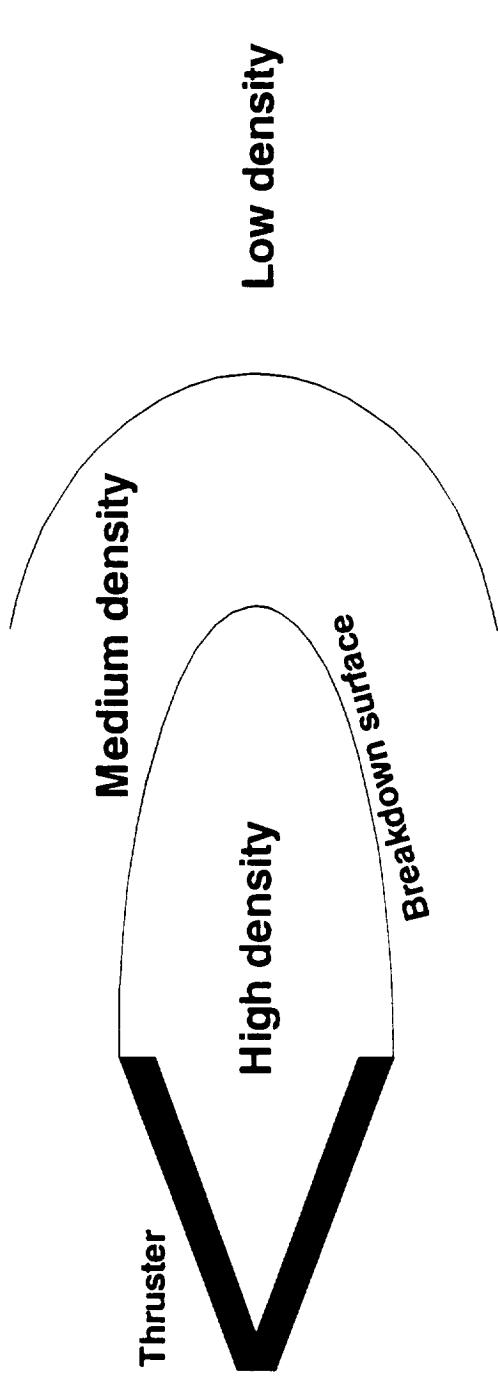
- In line thrusters
- In plane thrusters
- Out plane thrusters
- Yaw thrusters

Thruster properties

Nozzle	Mass flow rate (g / s)	Thrust (Newtons)	Exit radius (mm)	Throat radius (mm)	Prandtl-Meyer (degrees)
InLine	1.45	1.13	4.56	0.455	53.5
InPlane	2.30	6.12	4.25	1.105	76.2
OutPlane	4.60	2.39	3.10	0.685	67.7
Yaw	0.85	0.50	4.00	0.300	50.4

Stagnation pressure = 10 atmospheres, Temperature = 300 K, Gas = Nitrogen

Analysis Method (I)



Flow Regimes: Continuum Transition Free Molecule

Simulation codes: Navier Stokes DSMC Free Molecule

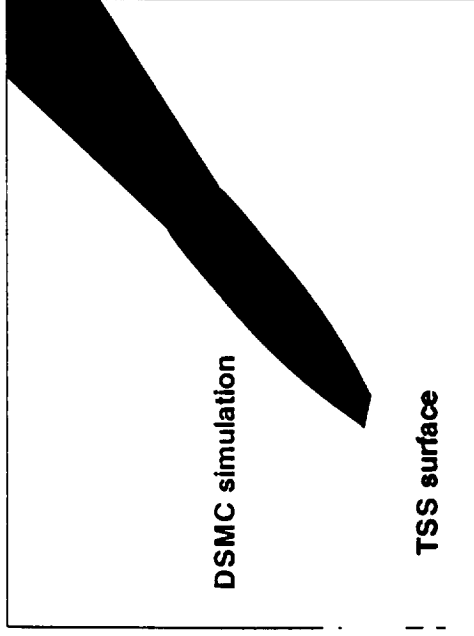
Numerical Tools

- **Continuum:** NASA JSC Navier Stokes solver, specially adapted for thruster plume simulation (Axisymmetric)
- **Transition:** NASA LaRC Direct Simulation Monte Carlo code (3D, for arbitrarily complex geometry)
Gas simulated as a large ensemble of molecules, which are tracked thru intermolecular collisions and wall collisions.
Density, velocity, temp. = Moments of velocity distribution
- **Free Molecule:** NASA LaRC Plume Free Molecule code (3D)
Breakdown surface is discretized into a series of point sources.

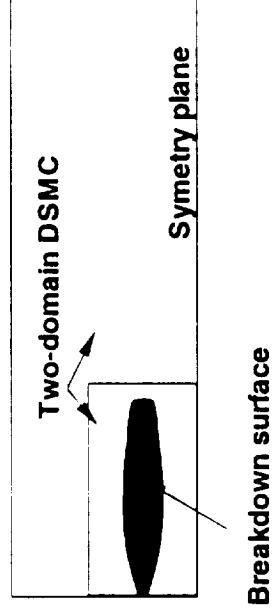
$$\text{Density, velocity, temp.} = \sum_{\text{all sources}} F(X, Y, Z), F = \text{Analytical}$$

Analysis Method (II)

Impingement



Multi plume interaction



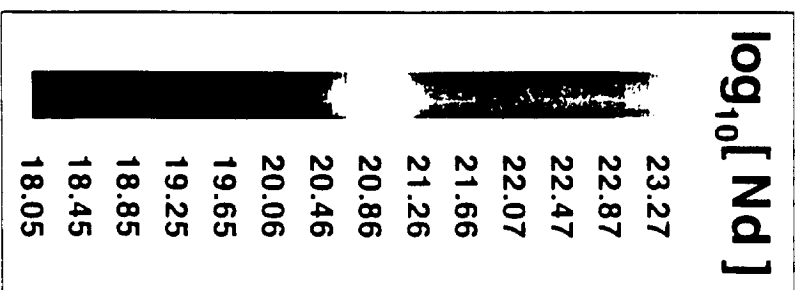
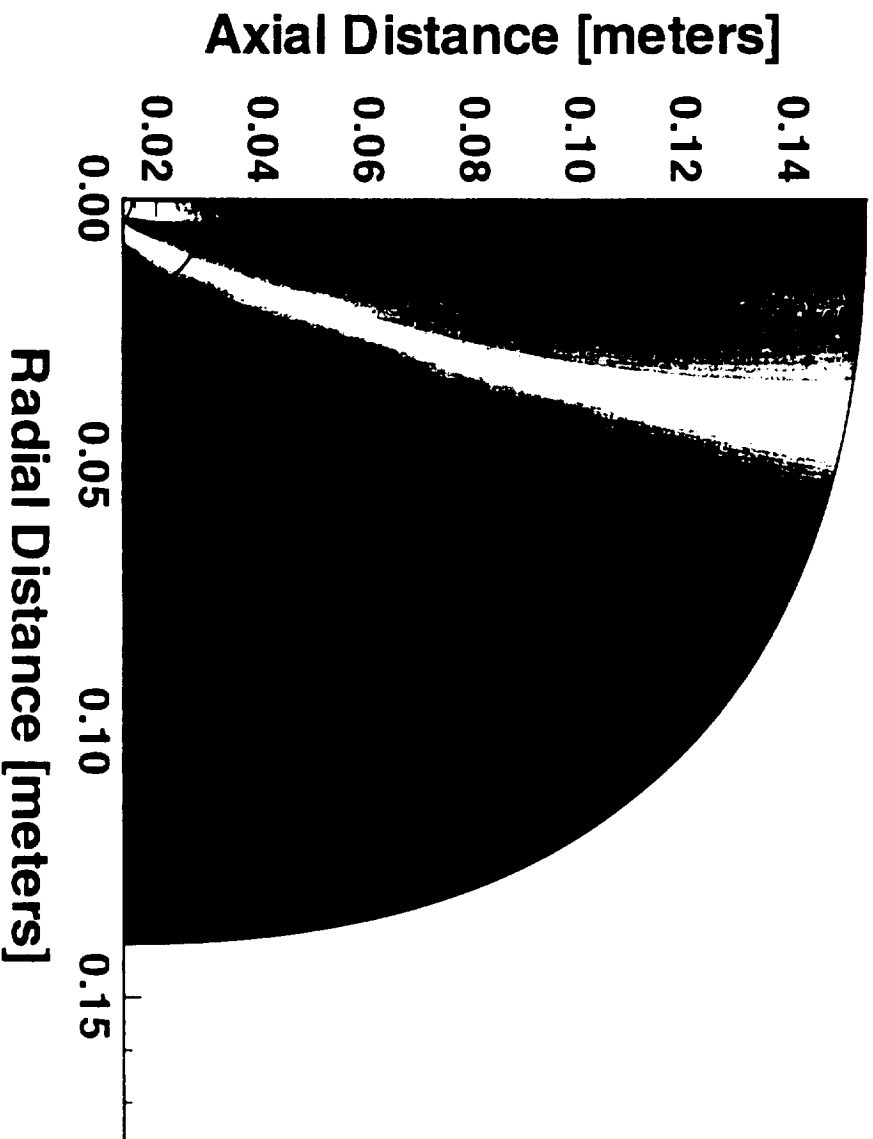
Conclusion

We have

- **developed methods to assess the characteristics of the neutrals around TSS**
- **obtained a first order estimate of the neutral densities**
- **Assessed the effects due to impingement and plume interaction**

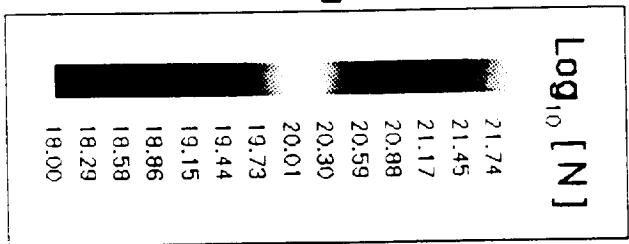
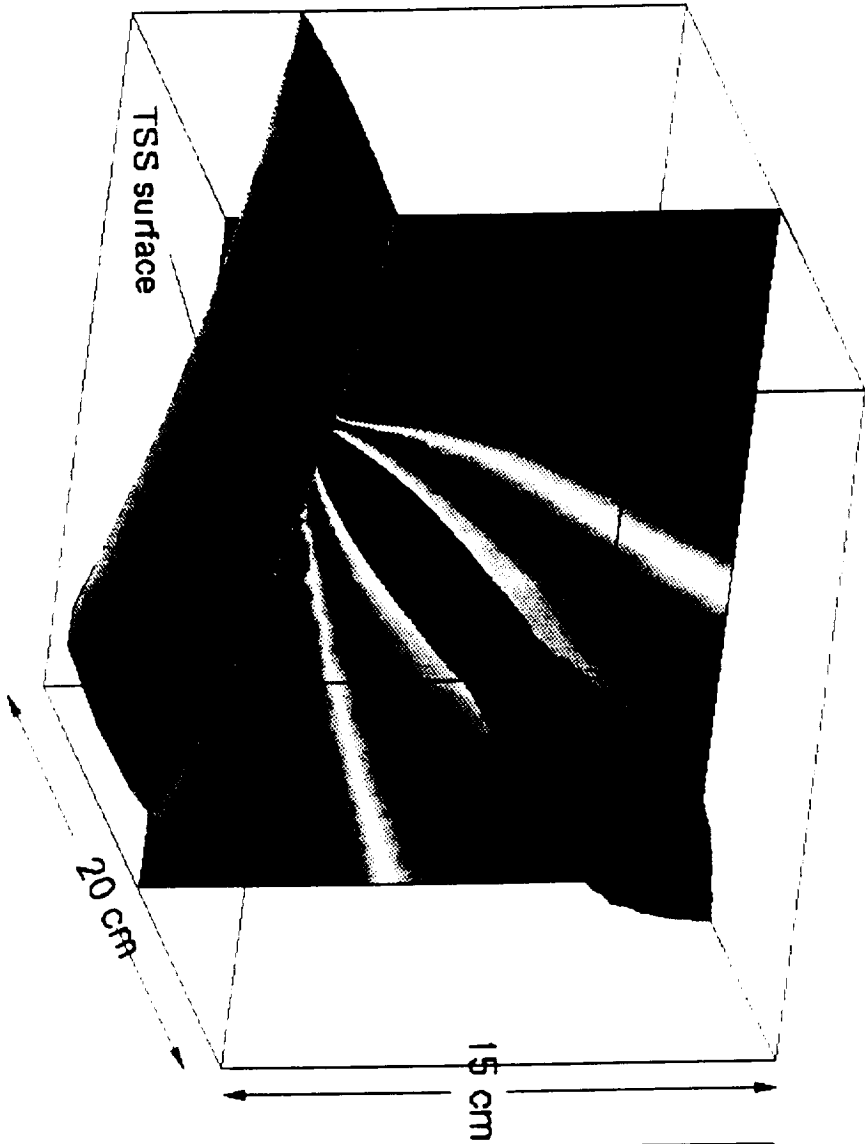
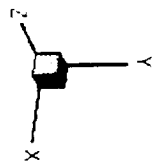
TSS Yaw Thruster Near Flowfield

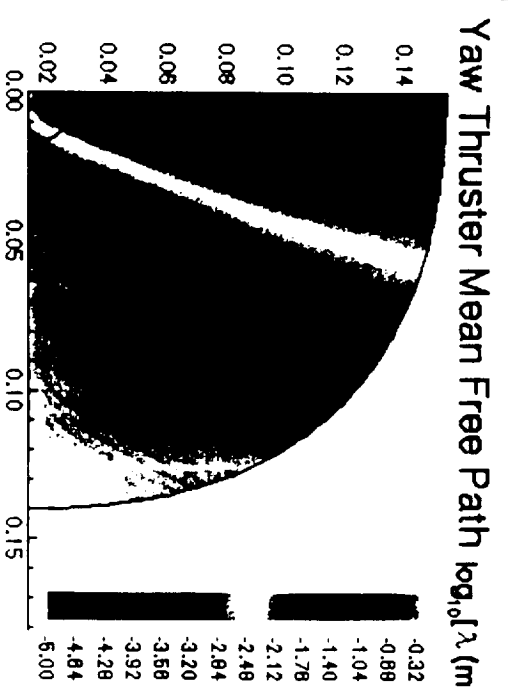
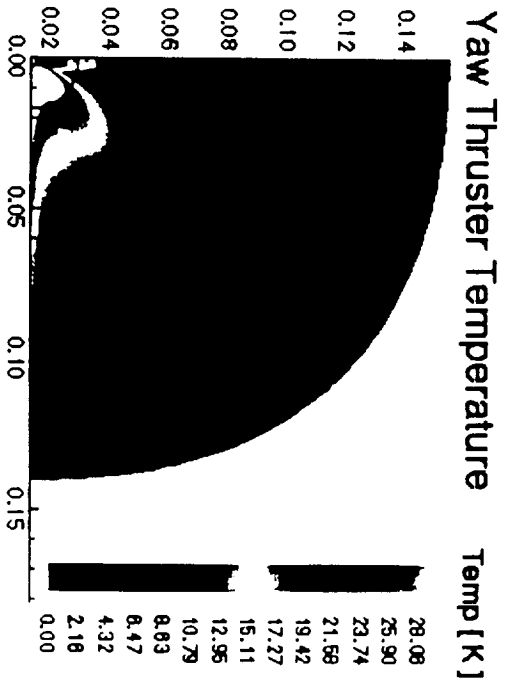
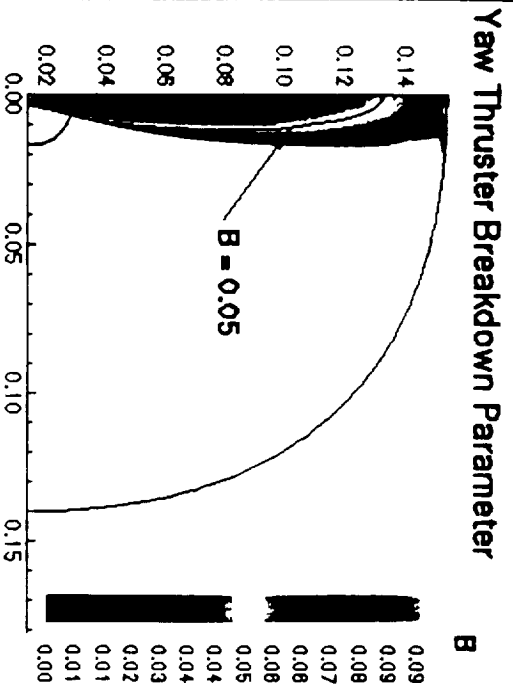
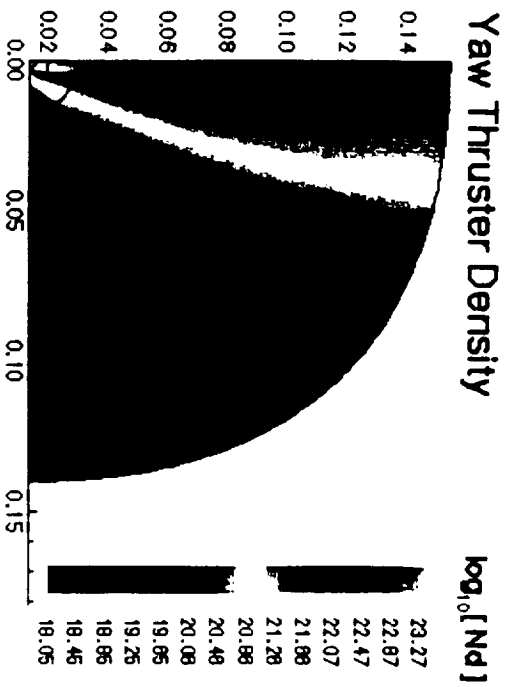
Continuum CFD simulation (P. Stuart, NASA JSC)



TSS Yaw thruster flowfield

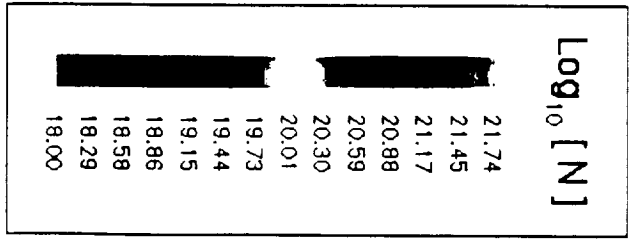
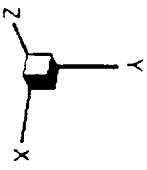
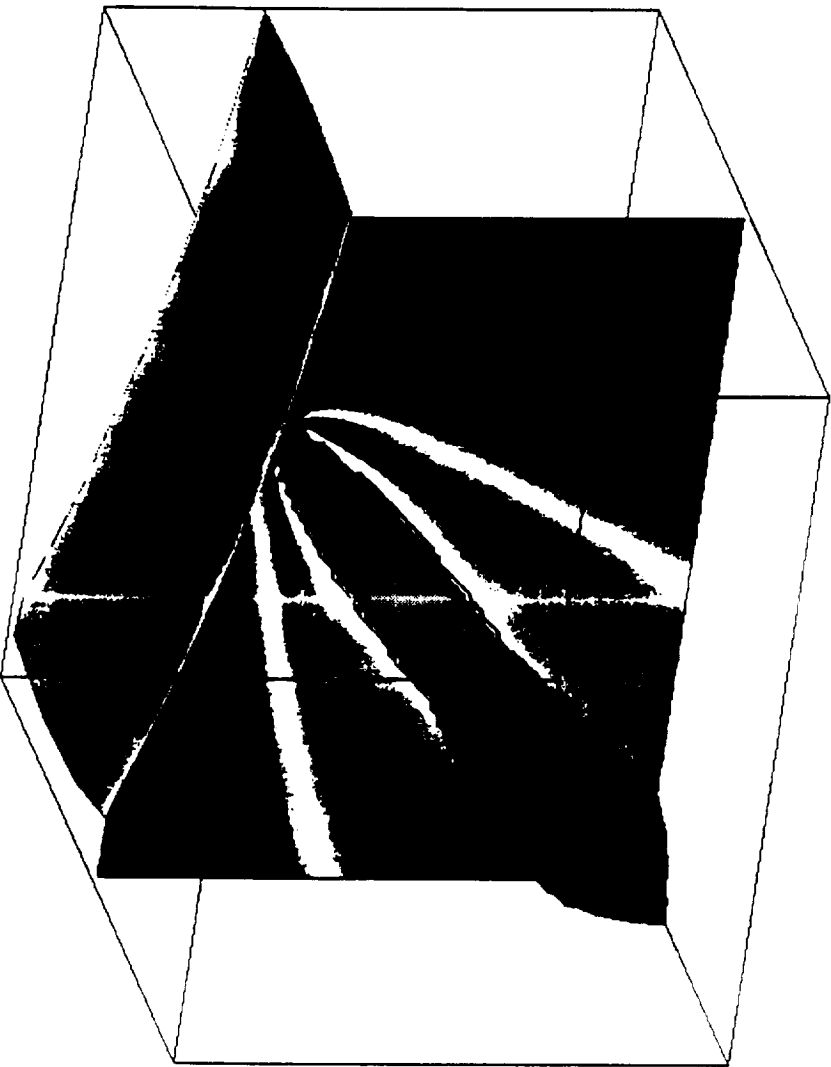
DSMC simulation (D.Rault, NASA, LaRC)





Yaw thruster vicinity

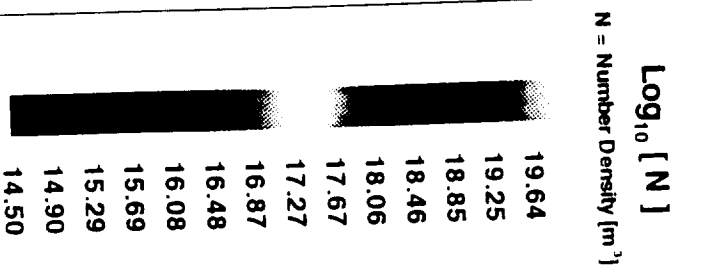
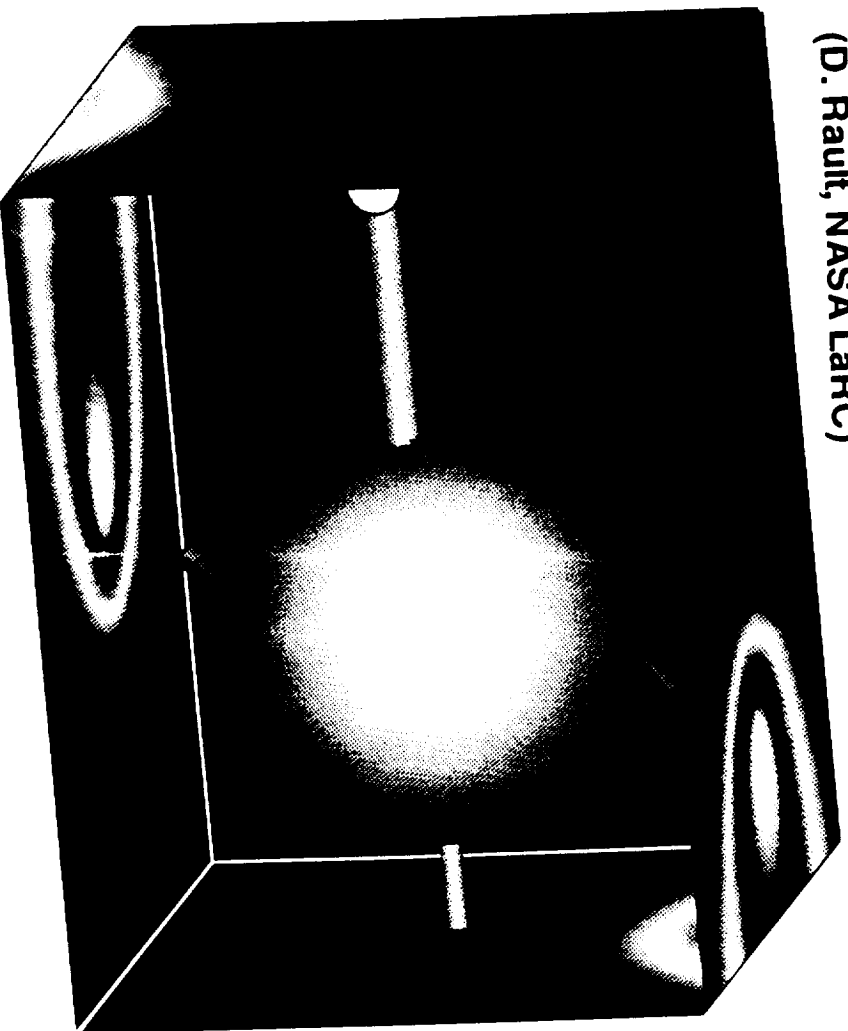
Free Molecule simulation / CFDflow 1.dat



Neutral environment of TSS-1R with 2 Yaw nozzles firing

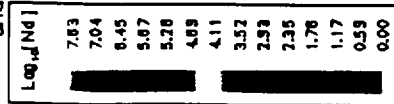
Free Molecule expansion downstream of Breakdown surface

(D. Rault, NASA LaRC)



Neutral density around TSS-1R

CFD within Breakdown surface
and Free Molecule downstream

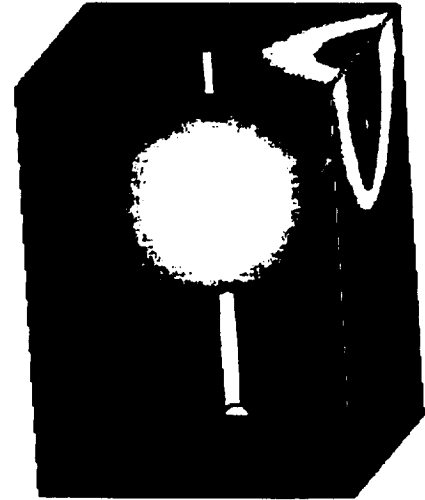


$$Nd = \frac{\text{Number density}}{10^{13} \text{ molecules / m}^3}$$

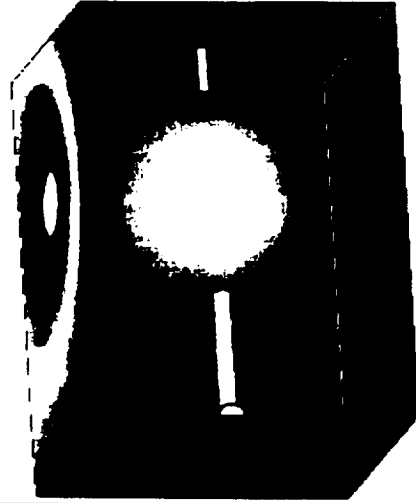
- In line thrusters
- In plane thrusters
- Out plane thrusters
- Yaw thrusters



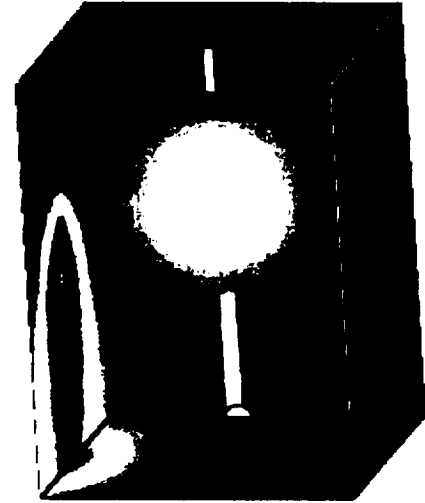
Effect of Yaw Thruster # 2



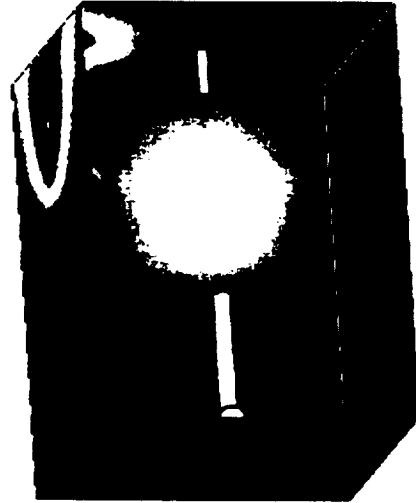
Effect of OutPlane Thruster # 1



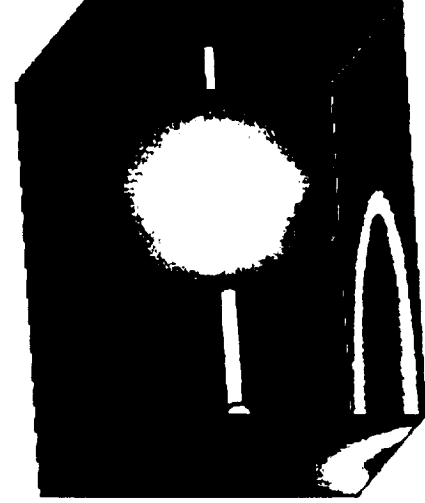
Effect of Yaw Thruster # 3



Effect of Yaw Thruster # 1



Effect of Yaw Thruster # 4



Neutral density around TSS-1R

CFD within Breakdown surface
and Free Molecule downstream

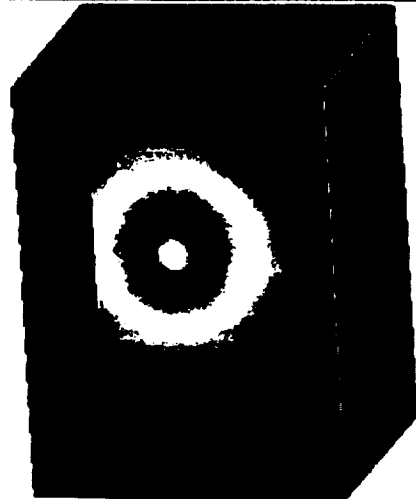
Log ₁₀ (Nd)
7.83
7.04
6.45
5.87
5.28
4.69
4.11
3.52
2.93
2.35
1.76
1.17
0.58
0.00

$$Nd = \frac{\text{Number density}}{10^{18} \text{ molecules / m}^3}$$

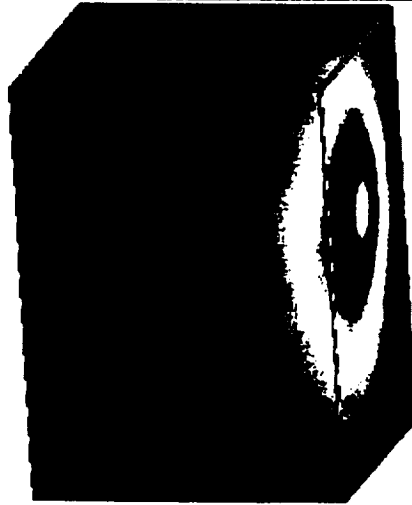
- In line thrusters
- In plane thrusters
- Out plane thrusters
- Yaw thrusters



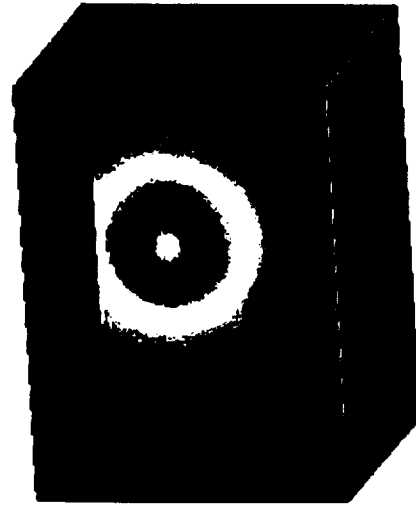
Effect of InLine Thruster # 2



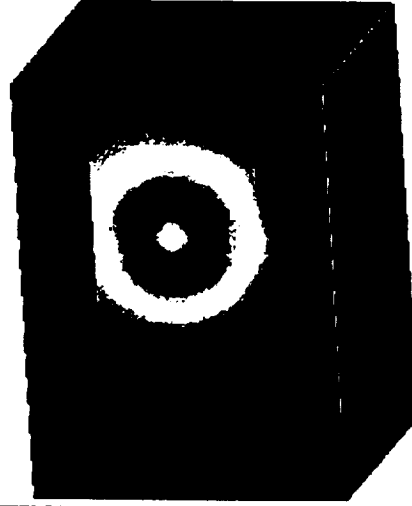
Effect of OutPlane Thruster # 2



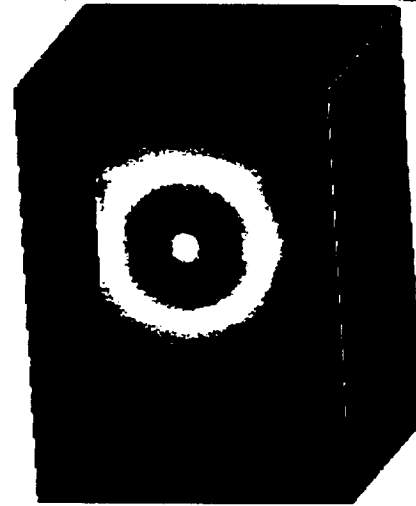
Effect of InLine Thruster # 3



Effect of InLine Thruster # 1

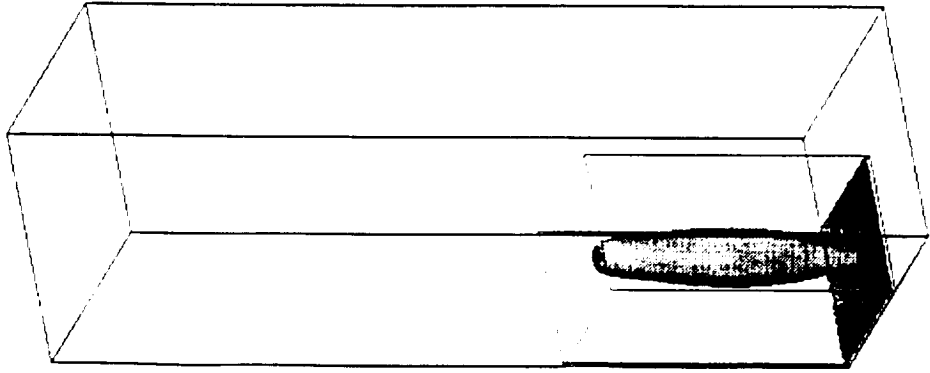
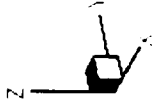


Effect of InLine Thruster # 4



TSS InLine thruster

DSMC computation domain



TSS InLine Thruster

Density map

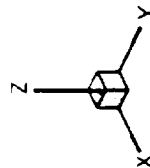
Free Molecule

With symetry planes



$\text{Log}_{10} [\text{Nd}]$

21.81
21.59
21.37
21.16
20.94
20.73
20.51
20.29
20.08
19.86
19.65
19.43
19.22
19.00

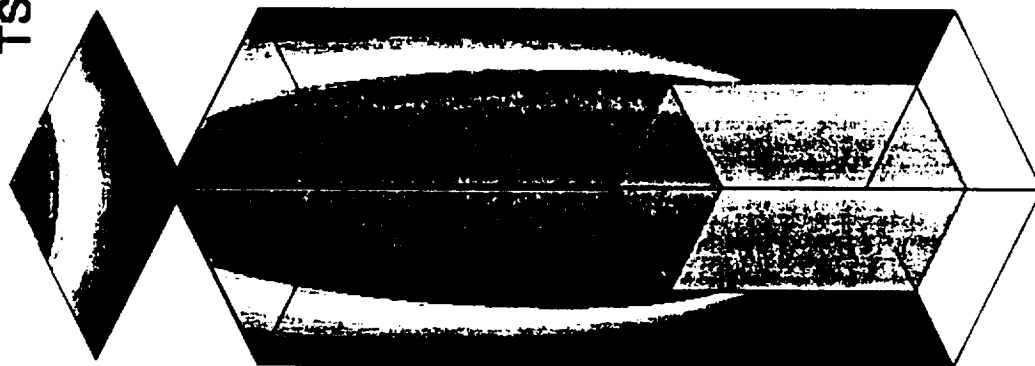


TSS InLine Thruster

Density map

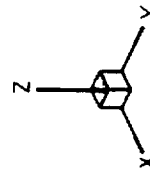
Free Molecule

With symetry planes



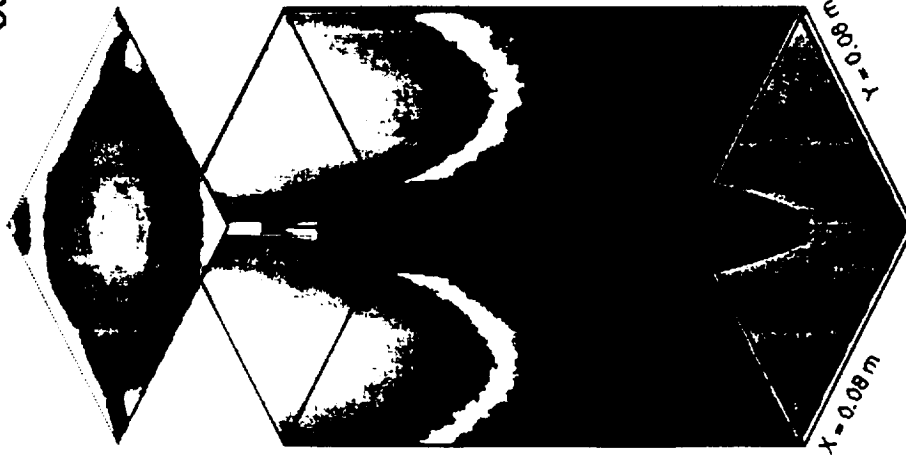
$\text{Log}_{10} [\text{Nd}]$

21.81
21.59
21.37
21.16
20.94
20.73
20.51
20.29
20.08
19.86
19.65
19.43
19.22
19.00



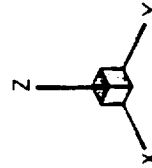
TSS InLine Thruster

Density map
Collisional DSMC



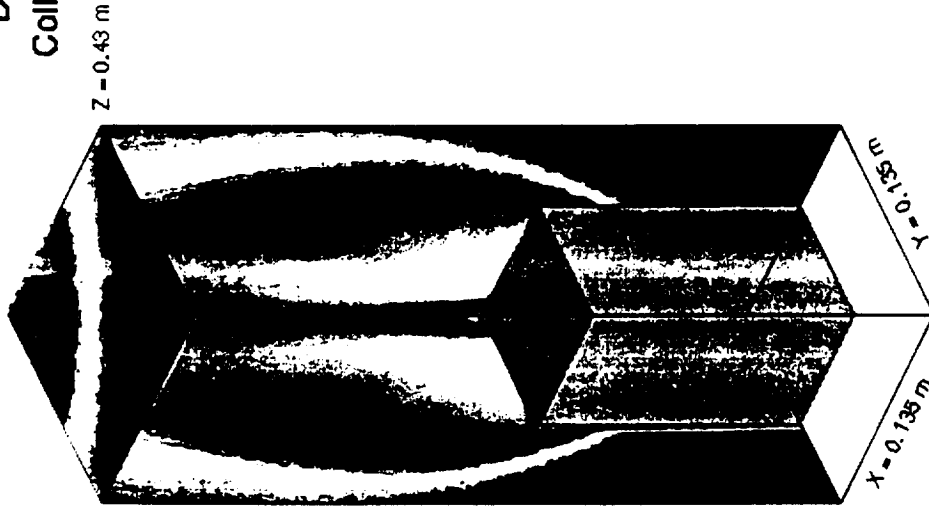
$\text{Log}_{10} [\text{Nd}]$
(Nd = molecules / m^3)

21.81
21.59
21.37
21.16
20.94
20.73
20.51
20.29
20.08
19.86
19.65
19.43
19.22
19.00



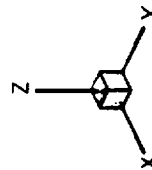
TSS InLine Thruster

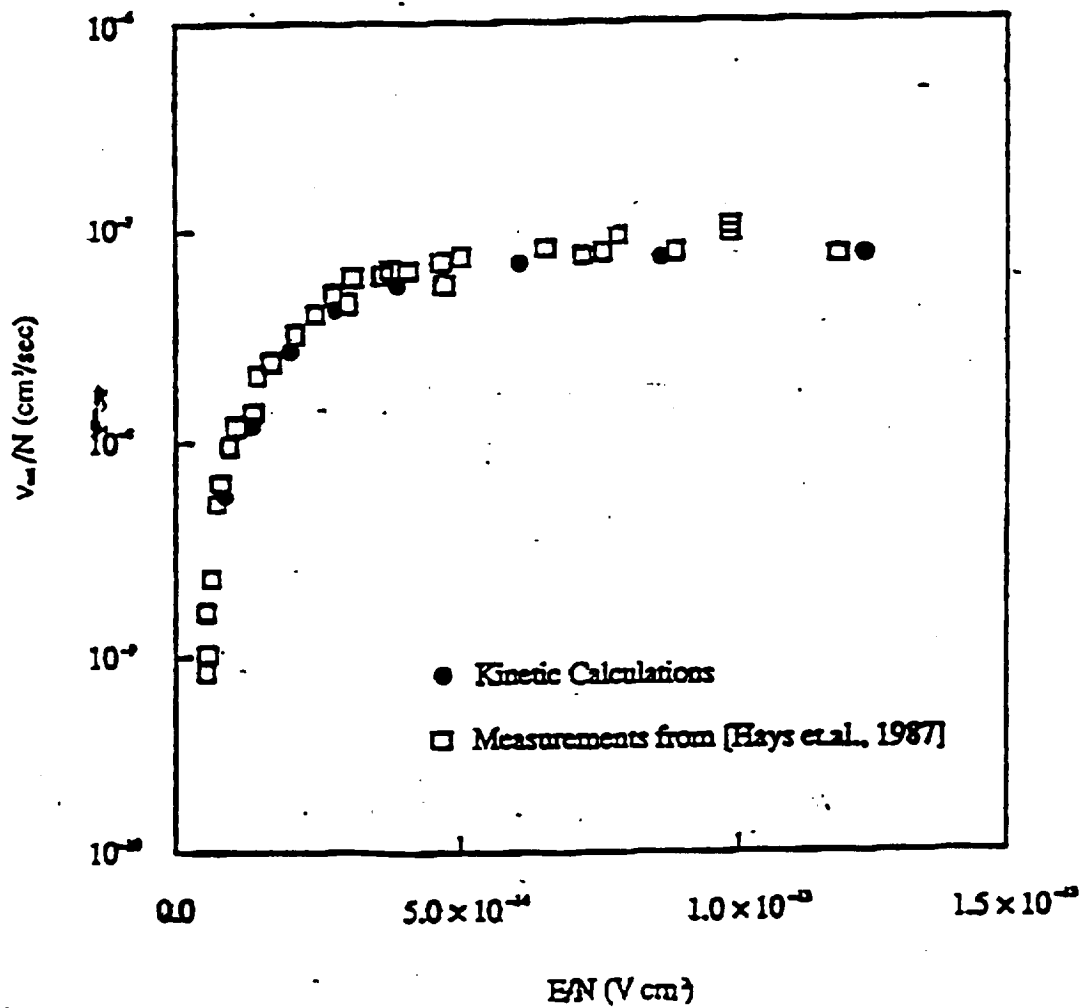
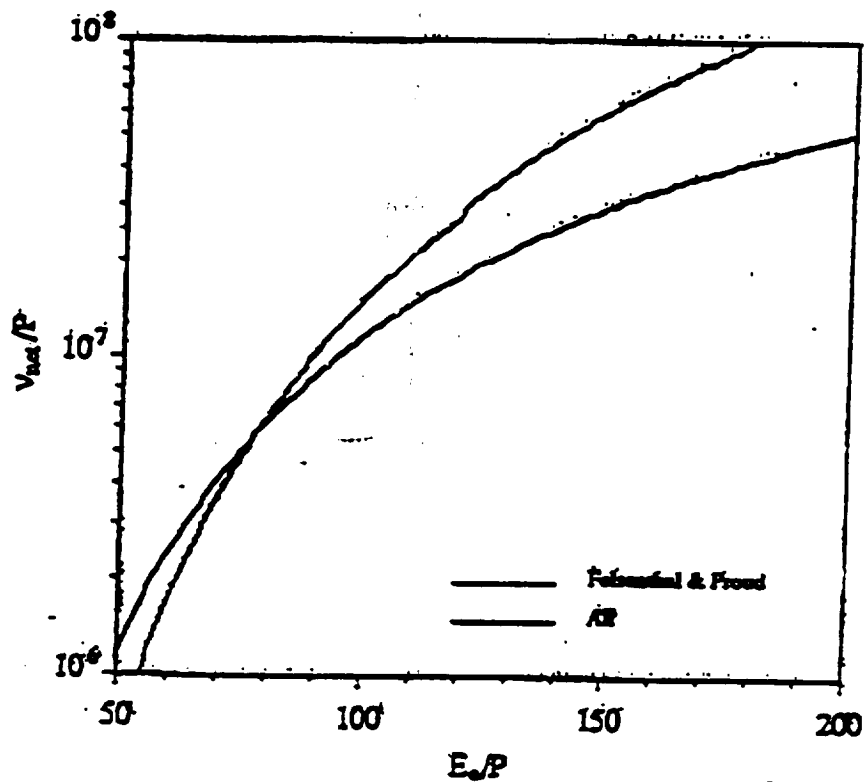
Density map
Collisional DSMC



$\text{Log}_{10} [\text{Nd}]$

21.81
21.59
21.37
21.16
20.94
20.73
20.51
20.29
20.08
19.86
19.65
19.43
19.22
19.00

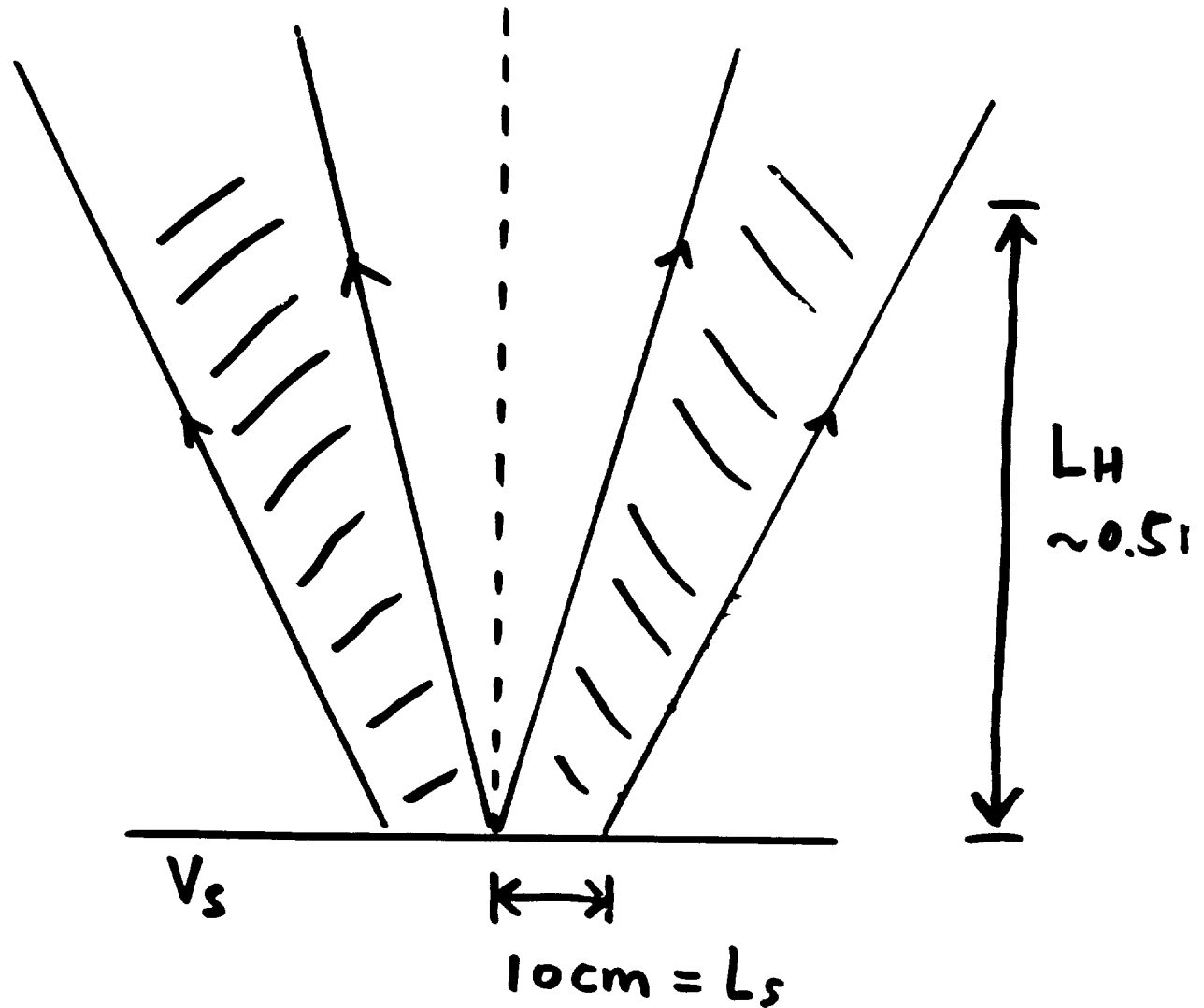




ZERO ORDER ESTIMATE

$$\frac{E}{P} > 10^2$$

FOR DISCHARGE
TO OCCUR



$$E \sim \frac{V_s}{L_s} \cdot P \sim 10 \text{ mTorr}$$
$$N \sim 3.5 \times 10^{20} / \text{m}^3$$

$$\frac{E}{P} \sim 10^3$$

ZERO ORDER ESTIMATE

$$\frac{E}{P} \sim 10^3 \rightarrow \frac{v_i}{P} \sim 2 \times 10^9 \text{ sec}^{-1} \text{ Torr}^{-1}$$

$$I = 2e n_e v_i V_{02}$$

$$n_e = 10^6 / \text{cc} = 10^{12} / \text{m}^3$$

$$v_i = 2 \times 10^7 \text{ sec}^{-1}$$

$$V_{02} = L_s \cdot L_H \cdot 2\pi (L_H \tan \theta + \frac{1}{2} L_s)$$

$$I \sim 0.2 \text{ Amp}$$

IMPLICATIONS

- (1) SHEATH COLLAPSE AROUND YAW NOZZLE IF ENOUGH e^- IS GENERATED BY GAS DISCHARGE.
- (2) POWER GENERATION
DESIGN OF GAS BLEEDER.
OPTIMAL USE OF GAS IN DISCHARGE.
TOOLS ARE AVAILABLE

Conclusion

We have

- **developed methods to assess the characteristics of the neutrals around TSS**
- **obtained a first order estimate of the neutral densities**
- **Assessed the effects due to impingement and plume interaction**

APPENDIX 9

**TEMPERATURE DEPENDENT
TETHER RESISTANCE AND ITS EFFECTS
ON THE
IV CHARACTERISTICS OF THE TSS SYSTEM**

Chia-Lie Chang	SAIC
Adam Drobot	SAIC
Dennis Papadopoulos	SAIC
Ken Wright	UAH
Nobie Stone	MSFC
Chris Gurgiolo	BBRI
David Winningham	SWRI
Carlo Bonifazi	ASI

**American Geophysical Union
Annual Meeting at San Francisco, CA
December 19, 1996**

OUTLINE

- Tether resistance R is an essential component in the TSS circuit. It was not directly measured during the mission.
- R is calculated indirectly from the IV24 cycles, using satellite potentials determined by ROPE, and measured quantities such as tether current, EMF, and EGA voltage.
- R is obtained within a range of uncertainty, and is shown to be temperature dependent.
- IV characteristics of the TSS system is presented based on the calibrated R , with error bounds due to uncertainty.
- Implications

R AND IV DETERMINATION

- Satellite potential V_{sat} is measured by the boom-mounted sensor package (BMSP) of ROPE

Upper limit BMSP measured is 500 Volts

For analysis, use $1 \text{ Volt} < V_{sat} < 100 \text{ Volts}$

- V_{sat} is substituted into the circuit equation to obtain R
- Mean-value R (R_m) and standard-deviation dR are calculated by statistics
- R_m is substituted back into the circuit equation to obtain IV relations for the entire range of V_{sat} ($> 100 \text{ Volts}$ included)
- Voltage uncertainty on the IV curves is $dV = I dR$

$$V_{EMF} = V_{SAT} + IR + V_{EGA} + V_{ORB}$$

ASSUME $R = 1.8 \text{ K}\Omega \Rightarrow V_{SAT}$

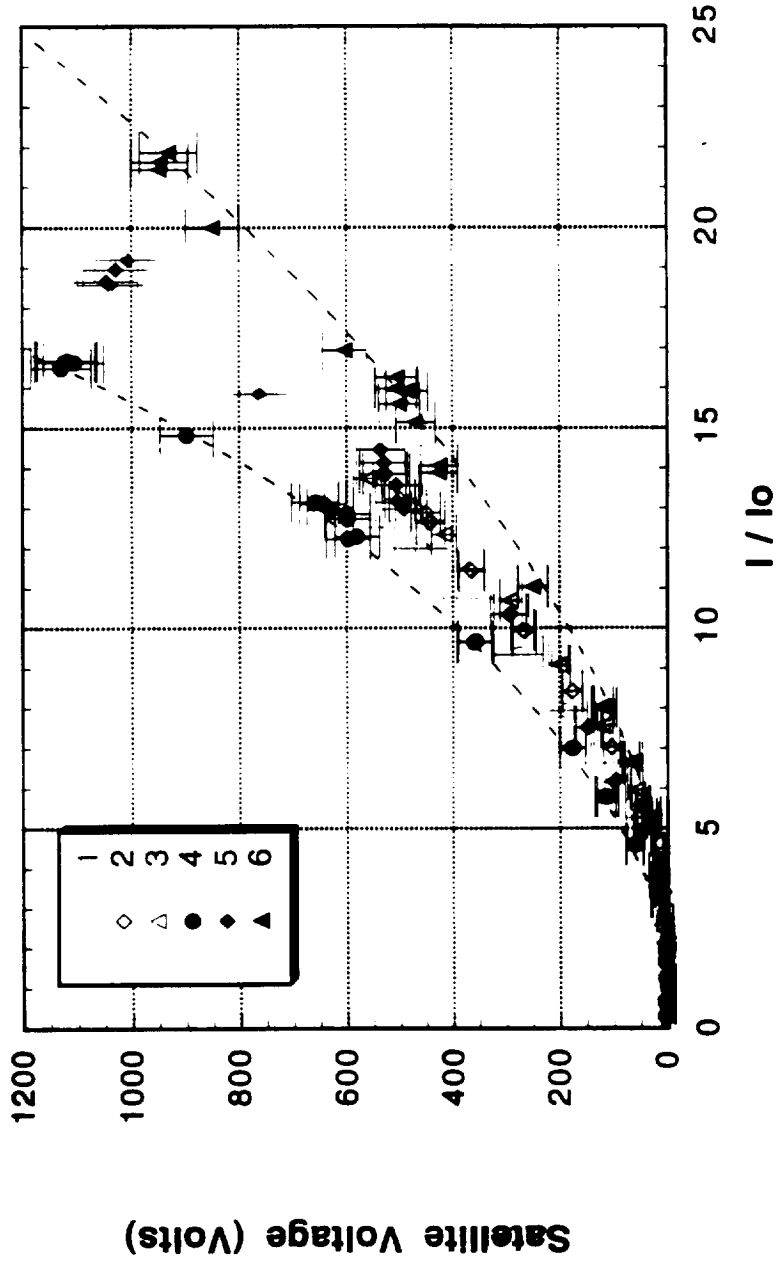
OR

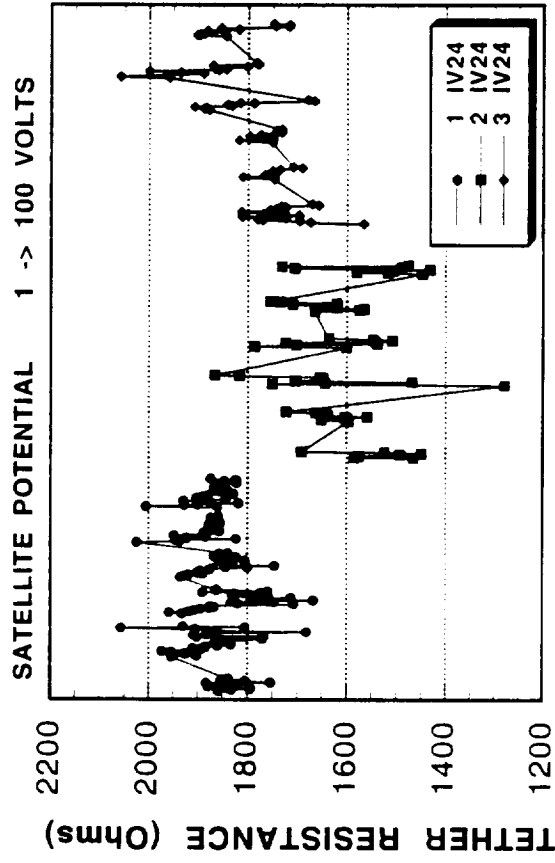
MEASURE $V_{SAT} \Rightarrow R$

RESISTANCE CALIBRATION TABLE

FO	Mean R (Ohms)	Std. Dev. (Ohms)	
1 IV24 - 1	1837.0	38.9	DAY
2	1885.5	74.2	
3	1828.0	79.3	
4	1859.6	45.3	
5	1887.3	41.8	
6	1868.6	41.1	
2 IV24 - 1	1626.8	254.6	NIGHT
2	1673.8	142.2	
3	1648.7	169.2	
4	1652.9	136.8	
5	1651.1	64.0	
6	1543.2	108.4	
3 IV24 - 1	1725.8	59.9	DAY
2	1745.4	30.3	
3	1763.1	29.1	
4	1818.2	84.7	
5	1887.2	86.7	
6	1821.4	71.2	

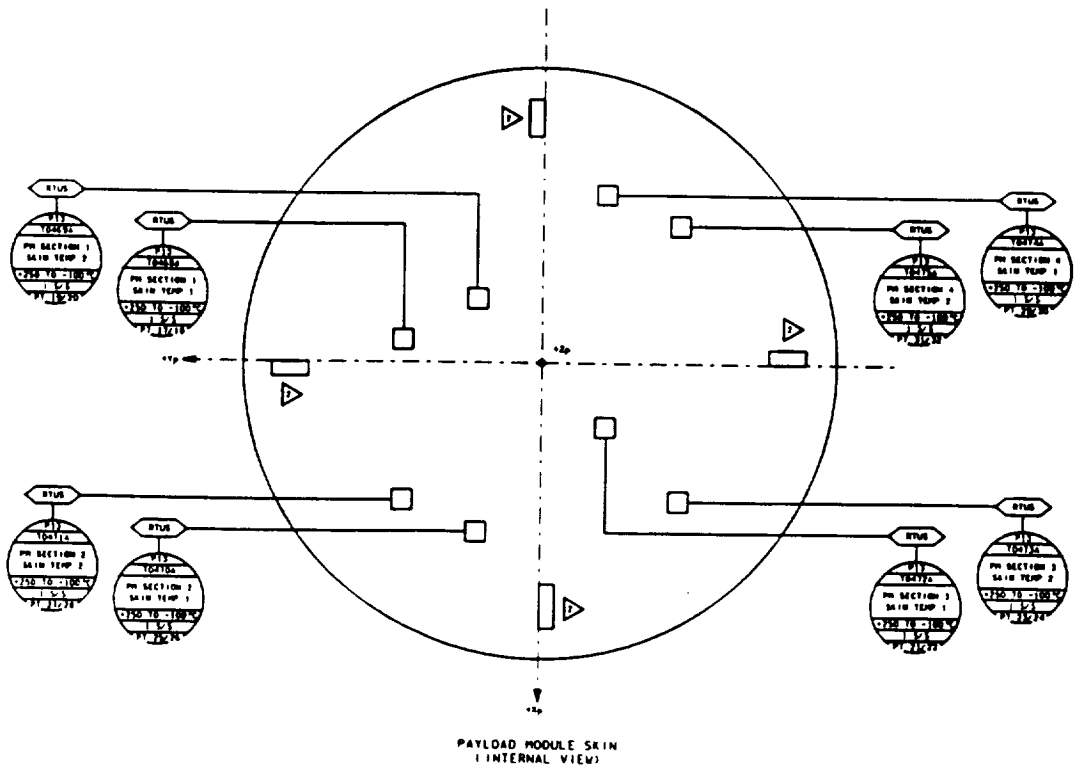
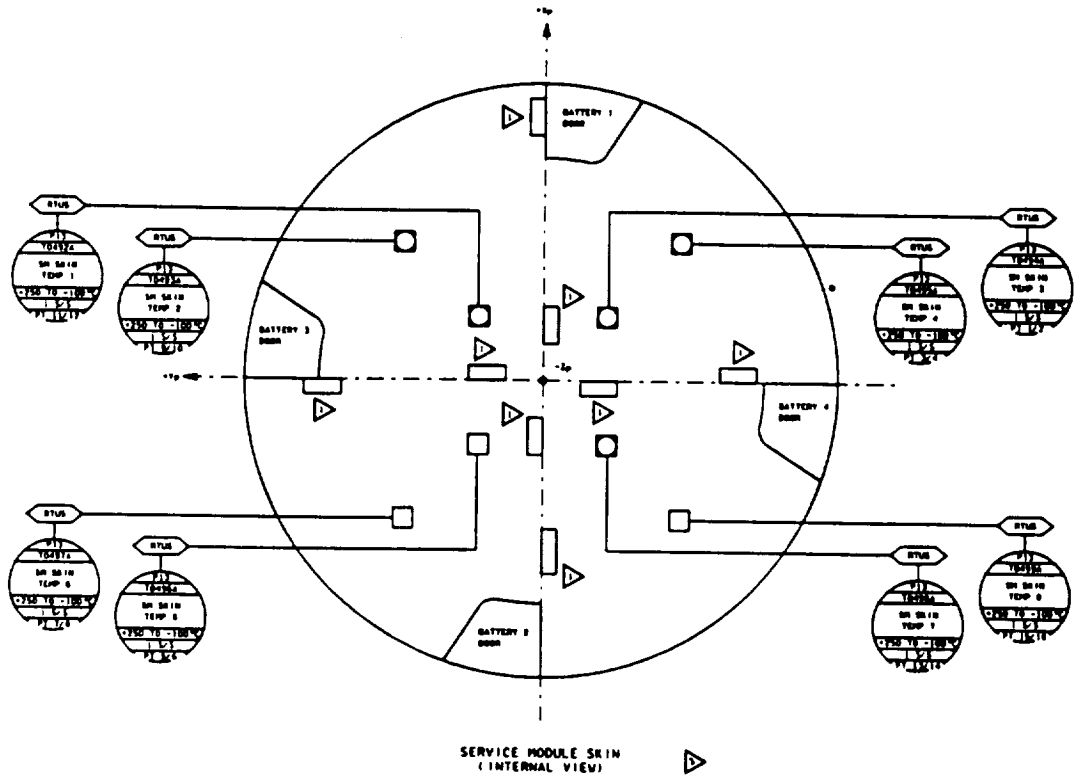
3IV24 - 1 to 6



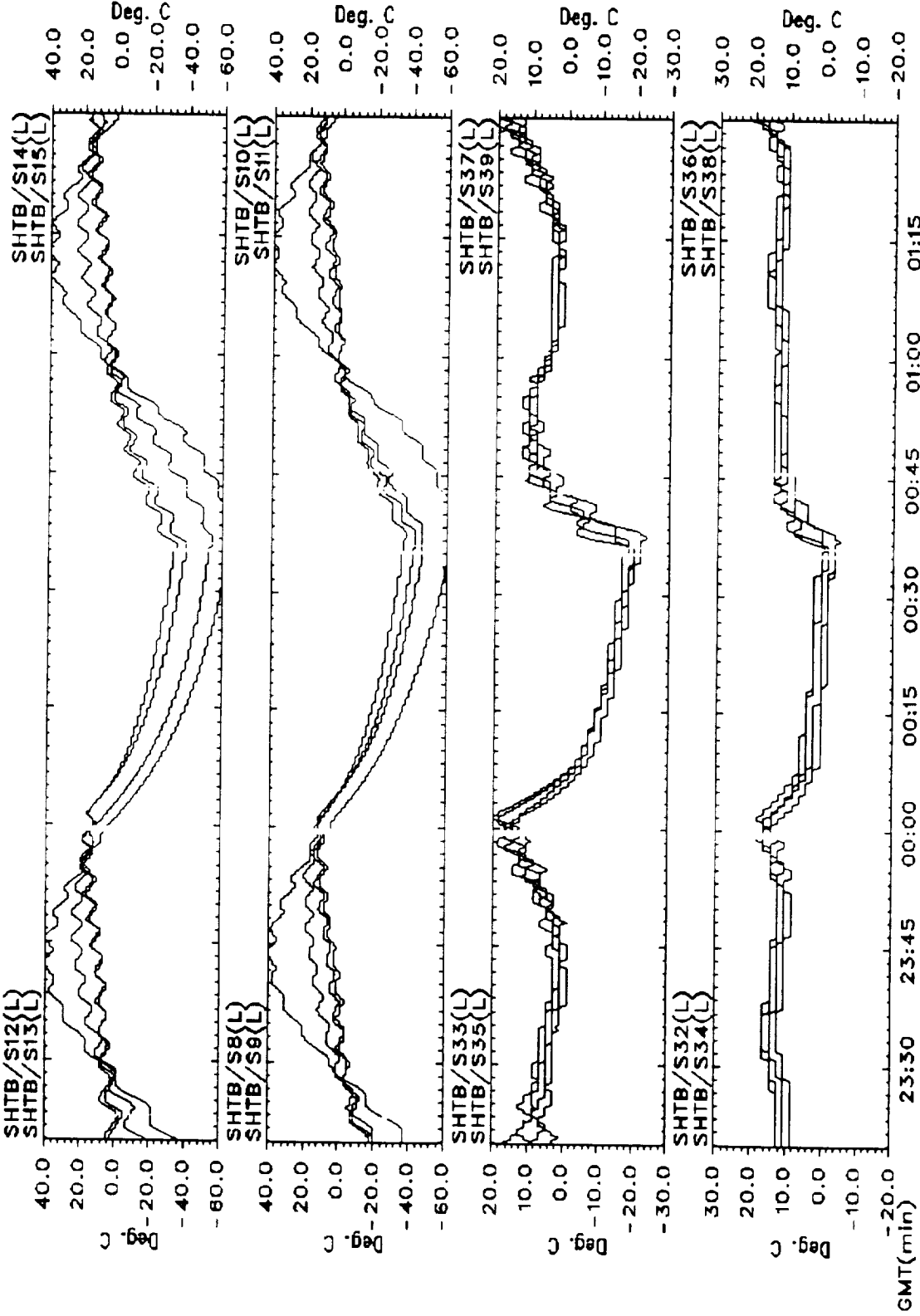


TIME →

G | F | E | D | C



1996/056/23:19:59:100



1 IV-24

2 IV-24

3 IV-24

TEMPERATURE DEPENDENCE OF R :

$$R = R_r [1 + \alpha (T - T_r)]$$

$$\alpha = 0.0068 / ^\circ\text{C}$$

(COPPER
HANDBOOK.
CHEM. PHYS.,

$$T_r = 27^\circ\text{C}$$

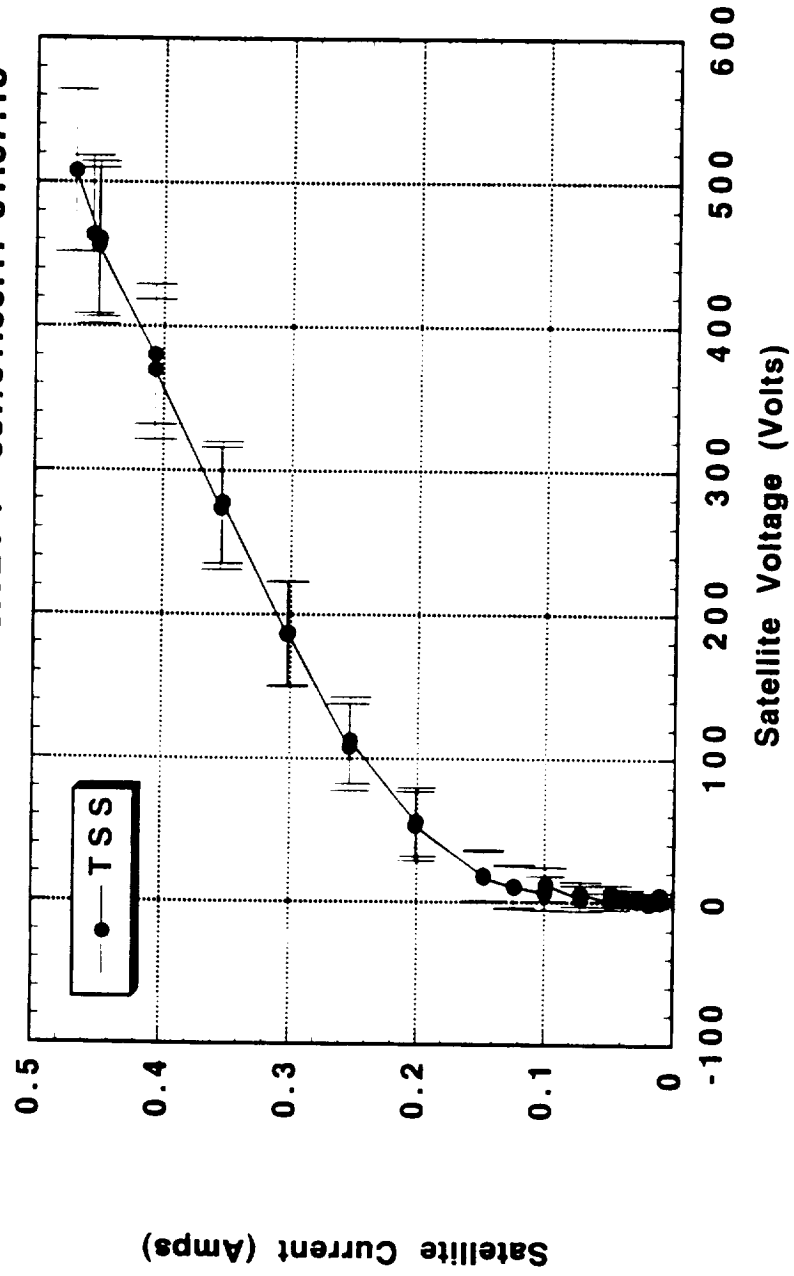
$$R_r = 2.1 \text{ K}\Omega$$

$$T = 10^\circ\text{C} \quad R_{10} = 1.86 \text{ K}\Omega$$

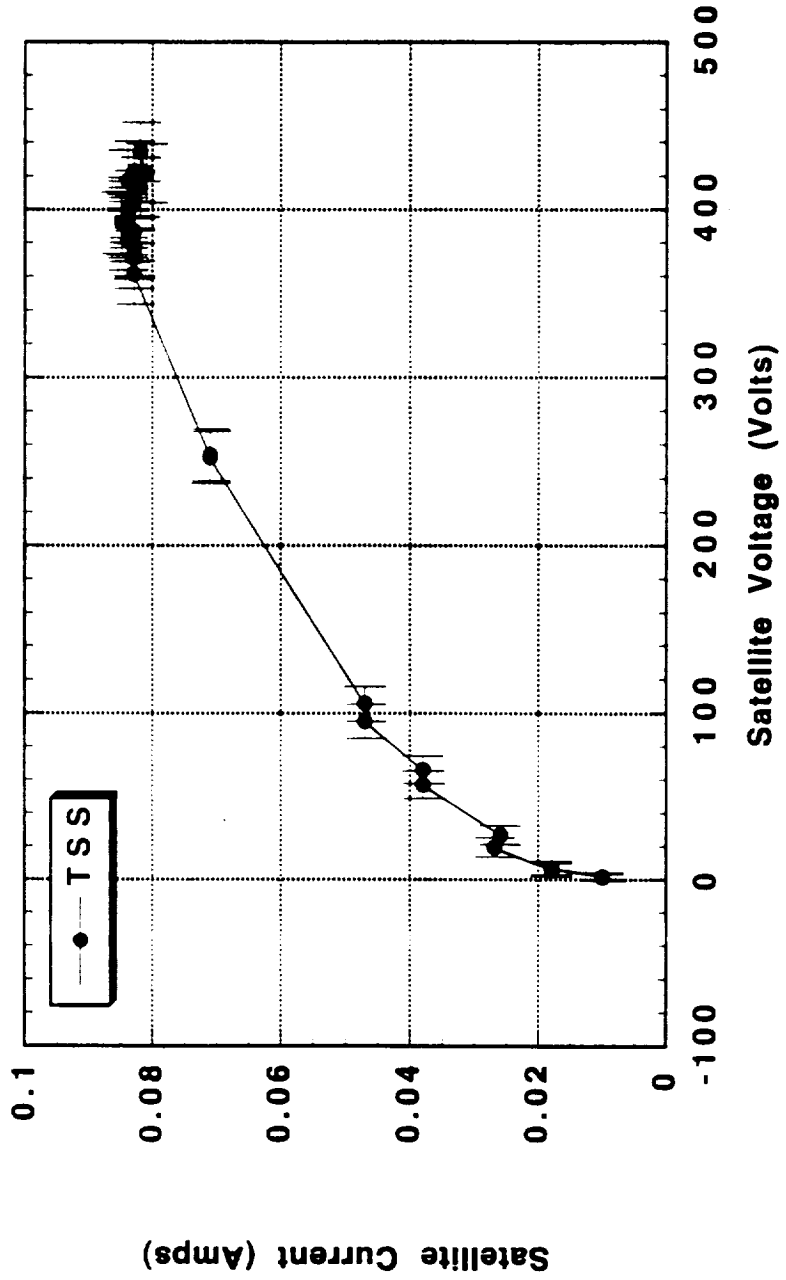
$$T = 0^\circ\text{C} \quad R_0 = 1.71 \text{ K}\Omega$$

$$T = -10^\circ\text{C} \quad R_{-10} = 1.57 \text{ K}\Omega$$

8.5e5 /cc 2030 K 3IV24-1 057/01:06:17-01:07:18



1.0e5 /cc 1100 K 2IV24-6 057/00:26:00-00:27:11

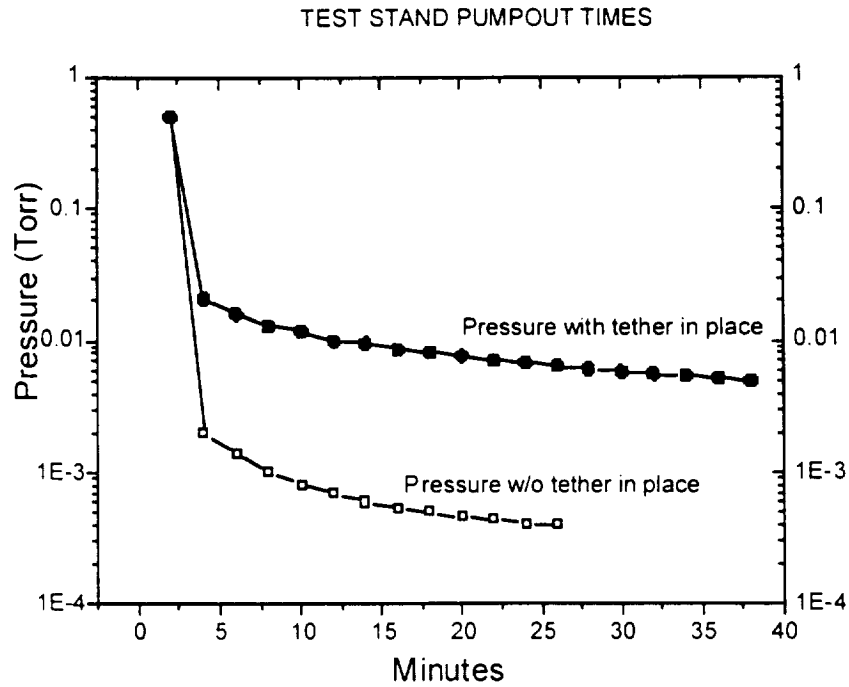


✓

SUMMARY

- Tether resistance is calculated from the satellite potential measured by ROPE.
- Tether resistance is temperature dependent, therefore, it is NOT constant throughout the TSS mission.
- Tether resistance is averaged over each IV24 cycle, a mean-value resistance is used to construct IV characteristics. Uncertainty on tether resistance is shown as error bounds on the potential V .
- At low voltage (< 50 Volts), the error bounds are comparable to the voltage value, therefore, it is not likely to derive a reliable scaling law in this regime.

APPENDIX 10



Some pump-out data:

With tether in place:

Time: Pressure:

Start 5:15pm Atmospheric

5:30 1×10^{-2}

6:37 2.4×10^{-3}

Another test:

With tether removed: (3/28/96)

Time: Pressure:

Start 6:38 pm Atmospheric

6:40 5×10^{-1}

6:42 2×10^{-3}

6:44 1.4×10^{-3}

6:46 1.0×10^{-3}

6:48 8.2×10^{-4}

6:50 7.0×10^{-4}

6:52 6.0×10^{-4}

6:54 5.3×10^{-4}

6:56 5.0×10^{-4}

6:58 4.6×10^{-4}

7:00 4.4×10^{-4}

7:02 4.1×10^{-4}

7:04 4.0×10^{-4}

Note: Here there was some "jumping around" of pressure, to mid -3 scale

7:06 3.8×10^{-4}
Left overnight
10:25 am 2.1×10^{-4}

Replaced tether in stand (slit piece toward ground)

Start 11:17am	Atmospheric
11:19	5.0×10^{-1}
11:21	2.1×10^{-2}
11:23	1.6×10^{-2}
11:25	1.3×10^{-2}
11:27	1.2×10^{-2}
11:29	1.0×10^{-2}
11:31	9.6×10^{-3}
11:33	8.6×10^{-3}
11:35	8.2×10^{-3}
11:37	7.7×10^{-3}
11:39	7.1×10^{-3}
11:41	6.8×10^{-3}
11:43	6.5×10^{-3}
11:45	6.1×10^{-3}
11:47	5.8×10^{-3}
11:49	5.6×10^{-3}
11:51	5.4×10^{-3}
11:53	5.2×10^{-3}
11:55	5.0×10^{-3}
11:57	4.8×10^{-3}

At this point system was left to pump.

3:41pm 9.7×10^{-4}

An Expedient Model of Electron Sheath Around Charged Conductor and Its Applications to the Current Collection by the TSS Satellite

A. T. Drobot and C. L. Chang

Science Applications International Corporation

1710 Goodridge Drive, McLean, Virginia 22102

Abstract

We have developed a simple steady state sheath model for current collection by a charged conductor in a plasma. Important quantities such as sheath size and particle transit time can be readily estimated from this model by an easy-to-use graphical method. We have applied this model to the TSS satellite under typical ambient and operational conditions in the mission. From the estimated sheath formation time, we conclude that the conventional steady state models are only applicable when the voltage of the satellite is low ($< 50\text{V}$). For voltages exceeding 500 V , the motional effect of the TSS system becomes an important factor in the current collection process because the motional transit time of the satellite is comparable to the sheath formation time. It remains to be seen that the motional effect can induce the observed high level of current collection by the TSS system at high voltages.

Introduction

A primary science objective of the TSS mission is to specify the current-voltage (IV) characteristics of the Tethered Satellite System (TSS) in space. From the dataset obtained by the IV survey cycles [Bonifazi et al., 1996; Gilchrist et al., 1996], it has been shown that the amount of current collected is higher than the values predicted by the known steady state models, such as the isotropic collection model by Beard and Johnson [Beard & Johnson, 1961; Alpert et al., 1965] or the magnetized model by Parker and Murphy [Parker & Murphy, 1967; Linson, 1969]. Several possible physical mechanisms have been proposed to explain the apparently more efficient collection processes by TSS. These mechanisms include (but not limited to) the potential contribution from a sub-population of energetic electrons [Chang et al., 1996; Cooke & Katz, 1996], the enlarged collection area [Laframboise, 1996], and the transient effects on current collection due to tether motion [Petillo et al., 1996; Zhang et al., 1996]. In particular, the transient collection scenario state that the electron collection may occur at a higher level because the conventional steady state can not be attained around the TSS. This is based on the

consideration that the TSS system traveled at 7.8 km/sec, therefore with respect to a fixed point in space, the satellite of size 1.6 m in diameter has a transit time of 0.2 msec. This transit time could be shorter than the time required for the sheath formation, which is dictated by the slow process of ions evacuation (O+) in the sheath. Such scenario is further supported by the time dependent particle simulation results, which shows an initial surge of electron current after the voltage of the collector is switched on in the plasma [Calder & Laframboise, 1990]. In order to validate the transient collection process, it is necessary to provide a good estimate of the sheath formation time, which can only be roughly estimated by dividing the steady state sheath size with an averaged ion speed. However, the information of sheath size around a collecting sphere is very difficult to extract from the conventional steady state models. Moreover, the average speed of the ion around a charged conductor is a vague concept. In this letter we provide an expedient steady state model which can be used self-consistently to determine the sheath size, the particle transit time across the sheath, and thus a good estimate of the sheath formation time.

In a magnetized plasma, electron collection by a positively charged spherical conductor can be described by the consideration of two limiting cases. At high voltages, the collection process is dominated by the electron dynamics along the field line. The resulting electron sheath is highly elongated in the B field direction and the formation time is determined mainly by the ions leaving that region. Therefore, the electron sheath problem is essentially unmagnetized and 1D in nature. At low voltages, the electron gyro-radius is comparable to the sheath size, therefore the collection process becomes isotropic and the problem resembles a 3D unmagnetized case. To address both situations, we have constructed a unified current collection sheath model of arbitrary spatial dimension. Major assumptions in our model are the existence of a steady state electron sheath and an unmagnetized collection process. Sheath size is readily available from a universal graph based only on the applied voltage and the ambient plasma parameters.

Analytic Model for Electron Sheath

Physically, the steady state electron sheath is similar to a diode system, with the electrons emitting from the cathode (edge of the sheath) at $r = r_c$ and collecting by the anode (the satellite surface) at $r = r_a$. The structure of the sheath can be obtained by solving a multi-dimensional Poisson's equation of the form

$$\frac{1}{r^{n-1}} \frac{\partial}{\partial r} r^{n-1} \frac{\partial}{\partial r} \phi(r) = \frac{e}{\epsilon_0} N(r) , \quad (1)$$

where e is the unit charge, ϵ_0 is the free space permittivity, $N(r)$ is the electron density profile, $\phi(r)$ is the potential function, and $n = 1,2,3$ is the spatial dimension of spherical, cylindrical, and planar geometries, respectively. The potential function ϕ approaches zero at $r = r_c$, therefore, we can relate the electron velocity $V(r)$ to the potential by

$$\frac{1}{2}mV^2 = e\phi . \quad (2)$$

Substituting (2) into (1), the Poisson's equation can be re-written in the form of V as

$$V \frac{\partial}{\partial r} r^{n-1} V \frac{\partial V}{\partial r} = \frac{e^2}{m \epsilon_0} N V r^{n-1} = K = \text{constant} . \quad (3)$$

It is interesting to note that the factor K in the equation above is constant because at steady state the integrated electron flux (total current) is a conserved quantity. Since the space and the time coordinates are interchangeable, the above equation can be simplified further by replacing

$$V = \frac{\partial r}{\partial t} ; V \frac{\partial}{\partial r} = \frac{\partial}{\partial t} , \quad (4)$$

to yield the following

$$\frac{\partial}{\partial t} r^{n-1} \frac{\partial^2 r}{\partial t^2} = - \frac{e^2}{m \epsilon_0} N |V| r^{n-1} . \quad (5)$$

To facilitate the solution process, this equation can be casted into a non-dimensionalized form by normalizing both space and time with the following choice

$$R = \frac{r}{r_c} ; T = \frac{1}{r_c} \left(\frac{K}{6} \right)^{1/3} t . \quad (6)$$

Substituting (6) into (5) we will obtain a generalized sheath equation as

$$R^{n-1} \frac{\partial^2 R}{\partial T^2} = - 6 T . \quad (7)$$

An integration constant can be added to the RHS of this equation. Applying the boundary conditions at $r = r_c$, $R = 1$, $T = 0$, and assuming that both the potential and the electric field vanishes

$$\phi(r_c) = 0 \rightarrow V(r_c) = 0 \rightarrow \left. \frac{\partial R}{\partial t} \right|_{r_c} = 0, \quad (8)$$

and

$$\left. \frac{\partial \phi}{\partial r} \right|_{r_c} = 0 \rightarrow \left. \frac{\partial V}{\partial r} \right|_{r_c} = 0 \rightarrow \left. \frac{\partial^2 R}{\partial r^2} \right|_{r_c} = 0, \quad (9)$$

we can show that the arbitrary integration constant is zero in equation (7).

In order to find the solution for the sheath size, the boundary condition at the satellite surface $r = r_a$ (the anode) is needed. A first order equation is obtained by rewriting (6) in the following form

$$\frac{\partial r}{\partial t} = V \rightarrow \frac{\partial R}{\partial t} = V \left(\frac{K}{6} \right)^{-1/3}. \quad (10)$$

At $r = r_a$, this equation is can be converted into a matching condition at the anode as

$$\left. \frac{1}{R_a^{2/3}} \frac{\partial R}{\partial t} \right|_{r_a} = - \left[12 \sqrt{2} \left(\frac{e}{m} \right)^{1/2} \epsilon_0 \right]^{1/3} \frac{\phi_a^{1/2}}{r_a^{2/3} J_c^{1/3}}. \quad (11)$$

where $R_a = r_a / r_c$, $\phi_a = \phi(r_a)$ is the satellite potential, $J_c = e N(r_c) V(r_c)$ is the (ambient) thermal current density at r_c , and flux conservation $N(r_a) V(r_a) r_a^{n-1} = N(r_c) V(r_c) r_c^{n-1}$ is used in deriving the condition above.

Size of Electron Sheath

We would like to point out that it is not necessary, as in Langmuir's formula, to specify the sheath thickness *a priori* in our approach [Langmuir, 1923]. In fact, both the spatial structure and the thickness of the electron sheath can be self-consistently determined from the sheath equation (7) and the anode boundary condition (11) (henceforth referred to as the matching term) simultaneously. Since the sheath equation (7) does not depend on the external parameters, it needs to be integrated numerically only once from $T = 0$ and onward, starting with the initial

conditions $R = 1$ and $dR/dT = 0$ (see Eq. (8)). The numerical results of (7) is presented in Figure 1 in the form of the matching term versus both R and T , in one, two, and three dimensions, separately. Under such construction, figure 1 will be most useful in providing fast graphical solution to (7) and (11) for arbitrary cases. For instance, given ambient thermal current J_c , satellite radius r_a , and potential ϕ_a , the value of the matching term can be calculated according to (11). By locating this value on the curves in figure 1, one can determine the anode location R_a and the electron transit time T_a expediently. Once R_a is found, sheath size is given by $r_a(1/R_a - 1)$.

A specific example of using this graphical method to solve the sheath problem is demonstrated in Figure 2. In particular, the current-voltage characteristics of a 3D spherical conductor in an ambient plasma of density $5(10^{25})/\text{cc}$ and electron temperature 2000 eV is constructed in this figure. Since the cathode position $r_c = r_a/R_a$, the total current collection can be calculated as $I = \pi r_c^2 J_c$. By stepping through the satellite voltage V , an I-V curve is constructed based on the graphic approach, which is shown in figure 2 with solid dots (SS). For comparison purpose, we also plot the I-V curves derived from the unmagnetized Beard-Johnson model (BJ, triangles) and from the magnetized Parker-Murphy model (PM, squares) in the same figure. We can see that the graphical solution follows closely with the Beard-Johnson results at all voltages, which indicates that it is an excellent approximation to the unmagnetized Beard-Johnson (BJ) solution. On the other hand, both the SS and the BJ currents exceed the Parker-Murphy current, which is an expected result. The graphical method can also be used to determine the sheath size. In Figure 3, we plot the sheath size versus the satellite voltage in 1D and 3D geometries. Overall, the sheath thickness in 3D shows a slower dependence on voltage than that in 1D. The size of a 3D sheath increases from one-tenth of a meter at low voltage (~ 10 Volts) to over 2 meters at high voltage (~ 2 kV), while the size of a 1D sheath can increase to more than 6 meters at high voltage. The difference is due to the fact that the sheath volume around a spherical conductor increases faster than that of the planar one as the sheath expands. Therefore, a relatively smaller increase of the sheath size around the sphere can provide same amount of space-charge shielding to the conductor.

Sheath Formation Time

A potential application of the current model is to provide a first order estimate of the formation time of electron sheath. By applying the conventional steady state current collection theories (such as BJ or PM) to the TSS, the implicit assumption is that the sheath formation time is much shorter than the motional transit time of the TSS satellite. Since the TSS satellite collected more

current than those of the steady state theories predict, it has been suggested that the opposite occurred. Namely, as the TSS moved into an undisturbed plasma region, the satellite received a transient surge of electron current prior to the formation of the sheath, thus enhancing the current collection. This interesting scenario needs further validation. From physics point of view, an electron sheath is formed when the ions are completely expelled from the sheath region. Therefore, the sheath formation time is determined by how fast the ions leave that region. The sheath model developed in this letter can provide a quick estimate of such timescale. Specifically, for every anode position R_a in Figure 1, there is also a corresponding anode time T_a . This is the electron transit time across the steady state sheath, i.e. the time it takes for electron to travel from cathode ($T=0$) to anode ($T=T_a$). Likewise, we can estimate the ion transit time by multiplying the square root of the ion-electron (O^+/e) mass ratio to the electron transit time. Since the ion transit time is the time of flight for ions from anode to cathode, i.e. from the satellite surface to the edge of the sheath, it can be deemed as a good approximation to the sheath formation time. In Figure 4, we plot both transit times versus satellite potential in 1D and 3D, based on same plasma parameters as the previous figures. The ion transit time is in solid curves and the electron transit time is in dashed curves. From this figure, we can see that the transit time is increased monotonically with the voltage. As the voltage is increased from 10 V to 2000V, the transit time is increased by a factor of 2.5 in the 3D geometry and by a factor of 4 in the 1D geometry. A longer transit time at lower spatial dimension is in correspondence with the increase of sheath size as shown in figure 3.

Summary And Discussion

We have presented here an expedient steady state model of electron sheath around a charged conductor in multi-spatial dimensions. In this model essential information about the sheath, such as its structure, size, and particle transit time are readily obtainable through an easy-to-use graphical method. We have applied this model to the plasma conditions and satellite voltage typical for the TSS mission. The analytical I-V, sheath size, and particle transit time are provided in figures 2, 3, and 4, respectively based on a demonstrative set of ambient plasma parameters.

The question of whether the enhanced current collection during the TSS mission above the level predicted by the steady state models was due to the motional effect of the TSS system shall be discussed here. The TSS satellite of diameter 1.6 meters and travelling at an orbital velocity of 7.8 km/sec will pass a fix point in space in ~ 0.2 msec (the motional transit time). If a sheath is not formed within this timeframe, the electric field from the positively charged satellite is able to

extend to large distance and pull in more electrons along the magnetic field line than the steady state picture suggests. From figure 4, we can see that at low voltages (< 50 V) the sheath formation time, which is roughly the ion transit time, is about an order of magnitude smaller than the motional transit time. Therefore, a steady state sheath is likely to develop around the satellite and the current enhancement by TSS motion is likely to be unimportant in this regime. At medium to high voltages (> 500 V), the electron collection process resembles a 1D problem along the magnetic field. From figure 4, we can see that the sheath formation time approaches 0.1 msec as the voltage exceeds 1kV. This is comparable to the motional transit time and therefore the steady state picture does not apply. Current collection is likely to be a transitory process tied to the tether motion. However, it remains to be seen, either by analytical or by numerical means, that the tether motion can indeed induce the observed enhanced level of current collection at high voltages.

Acknowledgement

This work was supported by NASA under contract NAS8-36811.

Reference

- Al'pert, Ya. L., A. V. Gurevich, and L. P. Pitaevskii, *Space Physics with Artificial Satellites*, Consultants Bureau, New York, 1965.
- Beard, D. B., F. S. Johnson, Ionospheric limitations on attainable satellite potential, *J. Geophys. Res.*, 66, 4113, 1961.
- Bonifazi, C., F. Svelto, B. Gilchrist, P. Musi, P. Franceschetti, Measurement of the TSS-1R satellite current-voltage characteristics by the CORE equipment, SA41B-03, AGU Spring Meeting, Baltimore, 1996.
- Chang, C. L., A. T. Drobot, P. Satya-Narayana, K. Papadopoulos, D. Winningham, C. Gurgiolo, N. Stone, K. Wright, D. Intriligator, Electron Collection by the TSS satellite, SA41-B13, AGU Spring Meeting, Baltimore, 1996.
- Cooke, D. L., I. Katz, TSS-1R electron currents: magnetic limited collection from heated presheath, SA32A-06, AGU Fall Meeting, San Francisco, 1996.
- Calder, A. C., J. G. Laframboise, Time-dependent sheath response to abrupt electrode voltage changes, *Phys. Fluids B*, 2, 655, 1990.
- Gilchrist, B. E., N. R. Voronka, S. G. Bilén, D. C. Thompson, W. J. Raitt, S. D. Williams, C. Bonifazi, Measurement of current and voltage in the TSS-1R system using passive current

- closure and electron beam emission from the orbiter structure, SA41B-04, AGU Spring Meeting, Baltimore, 1996.
- Laframboise, J. G., Why the TSS-1 subsatellite collected so much electron current, SA41B-11, AGU Spring Meeting, Baltimore, 1996.
- Langmuir, I., The effect of space charge and initial velocities on the potential distribution and thermionic current between parallel plane electrodes, *Phys. Rev.*, 21, 419, 1923.
- Linson, L. M., Current-voltage characteristics of an electron-emitting satellite in the ionosphere, *J. Geophys. Res.*, 74, 2368, 1969.
- Petillo, J., K. Papadopoulos, C. L. Chang, A. T. Drobot, Transient current collection by a charged satellite moving in the ionosphere, SA41B-12, AGU Spring Meeting, Baltimore, 1996.
- Parker, L. W., B. L. Murphy, Potential buildup on an electron-emitting ionospheric satellite, *J. Geophys. Res.*, 72, 1631, 1967.
- Zhang, T. X., K. S. Hwang, S. T. Wu, N. Stone, Current collection by a highly charged and moving satellite, SA32A-05, AGU Fall Meeting, San Francisco, 1996.

Figure Captions

- Figure 1: Solutions of the electron sheath equation (7) in 1D, 2D, and 3D are plotted versus the matching condition given in (11). Graphical determination of cathode position R_a and electron transit time T_a can be made at the matching point.
- Figure 2: The solution from equations (7) and (11) is compared with the results from the steady state models. Solution is found in good agreement with the Beard-Johnson model. Specific plasma parameters are given at the top of the figure.
- Figure 3: The size of electron sheath in 1D and 3D are plotted against the voltage on the conductor, using the same plasma parameters as in figure 2.
- Figure 4: Electron and ion transit time transverse the sheath are estimated based on the plasma parameters in previous figures. The ion transit time is a good approximation to the sheath formation time.

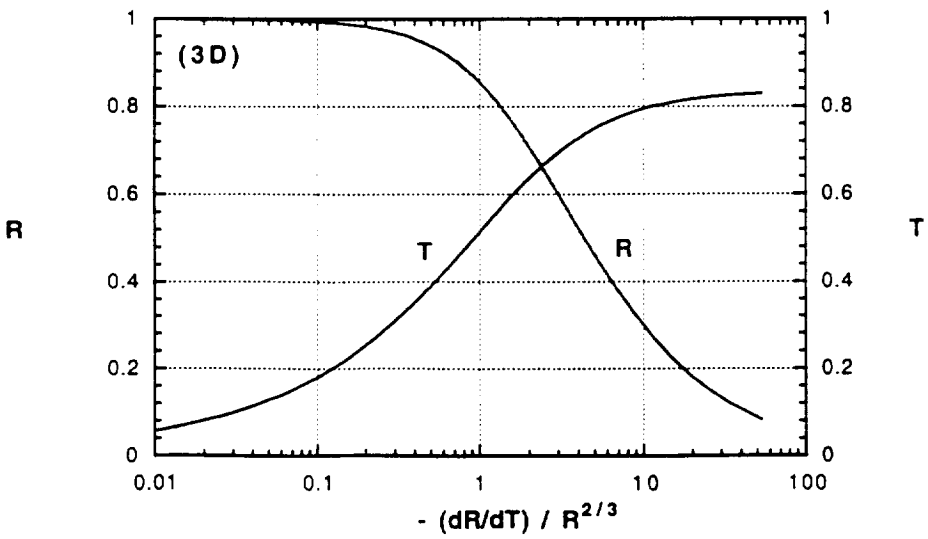
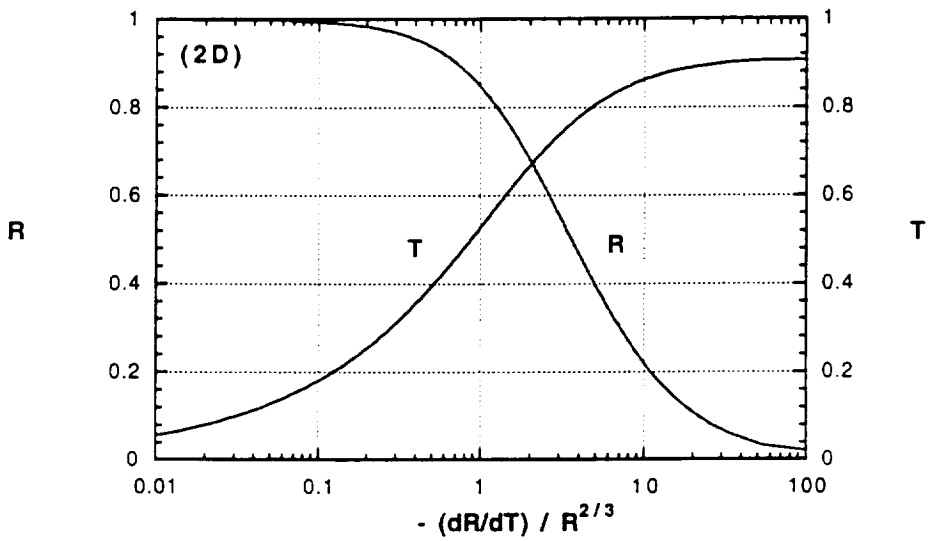
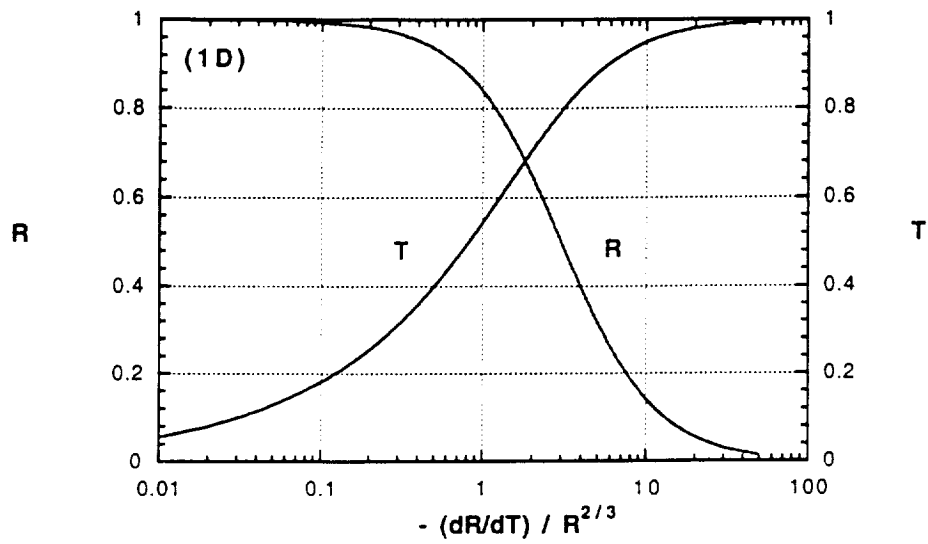


Figure 1

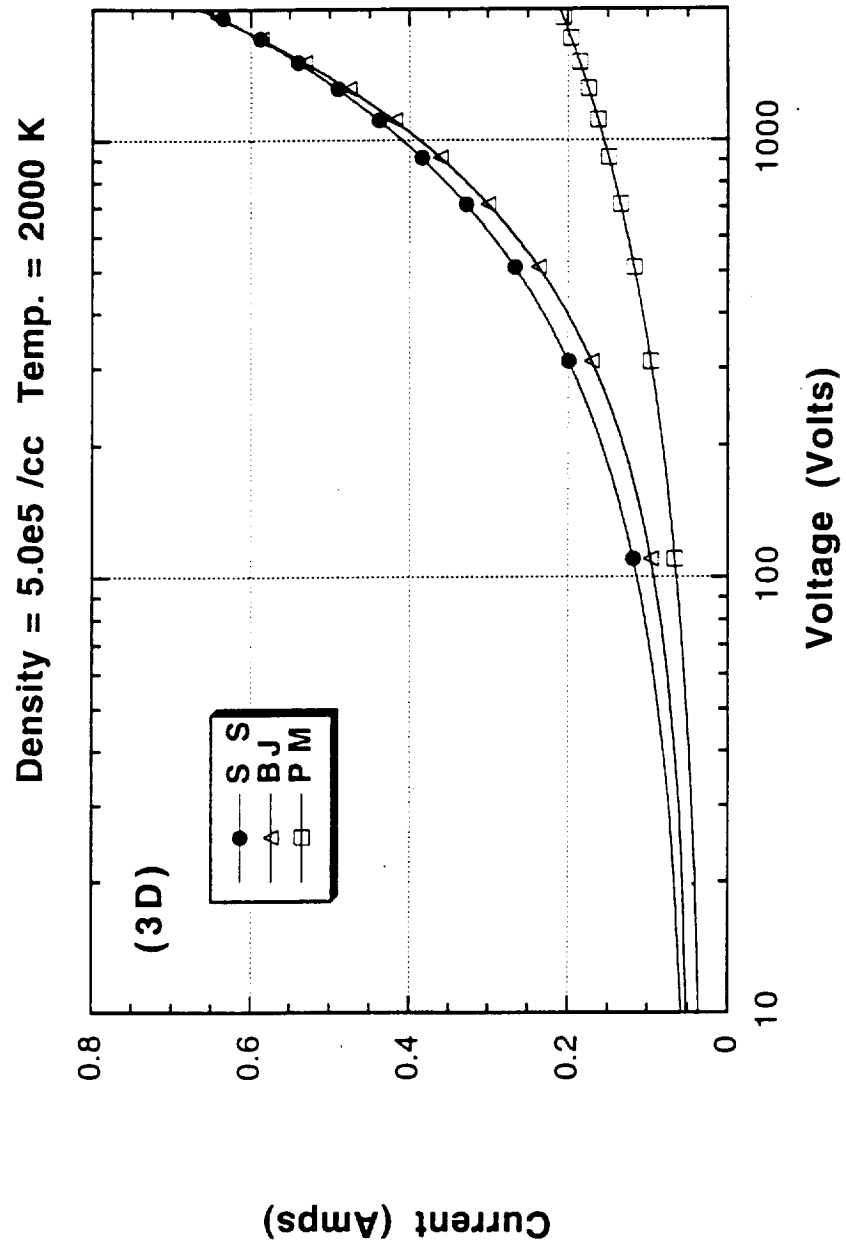


Figure 2

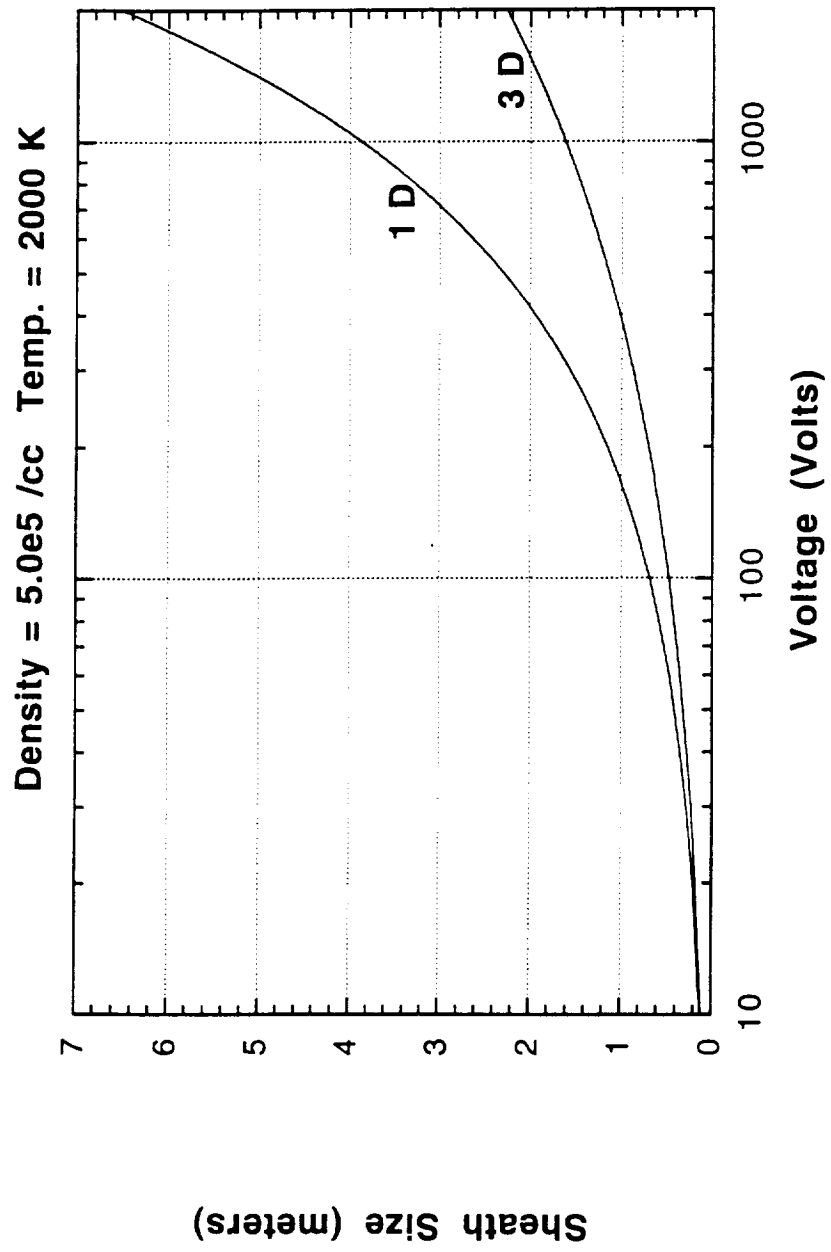


Figure 3

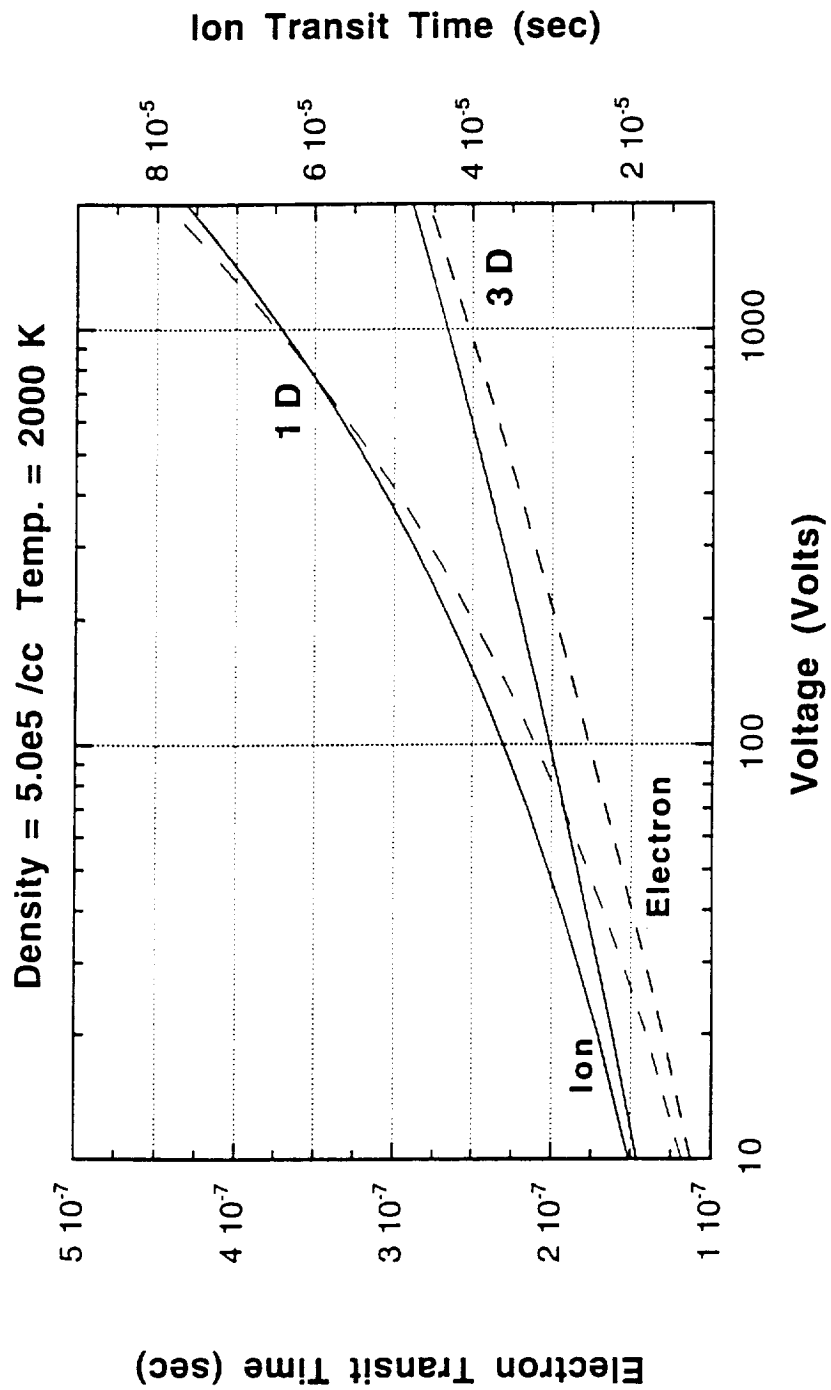


Figure 4

APPENDIX 11



AIAA 97-0584

**I-V CHARACTERISTICS OF THE TETHERED
SATELLITE SYSTEM**

C.-L. Chang, A. T. Drobot, and K. Papadopoulos
Science Applications International Corporation
McLean, VA 22102

**35th Aerospace Sciences
Meeting & Exhibit
January 6-10, 1997 / Reno, NV**

I-V CHARACTERISTICS OF THE TETHERED SATELLITE SYSTEM

C.-L. Chang, A. T. Drobot, and K. Papadopoulos
Science Applications International Corporation
1710 Goodridge Drive, MS 2-3-1
McLean, VA 22102, USA

Abstract

The TSS-1R science mission was conducted on the space shuttle STS-75 at the end of February 1996. During the flight, the Tethered Satellite was deployed to a distance of 19.7km and current was collected by the Satellite. Over the course of science operations, a rich dataset of current-voltage measurements was collected from instruments onboard both the satellite and the shuttle. We have constructed I-V curves including the uncertainties from Mission data. Comparing the TSS I-V characteristics with known theoretical models, we find that the level of electron current collected exceeds those predicted by the steady state models. At high voltages (> 300 V), the I-V characteristics scale with potential according to the Parker-Murphy model, implying a magnetically insulated collection process. The absolute value of the current collected greatly exceeds predictions of present models. The fact that TSS collected large currents at relatively low potentials bring many of the tether applications, such as power and thrust generation, closer to realization.

Introduction

The reflight mission of the Tethered Satellite System (TSS-1R) was launched on February 22, 1996 aboard shuttle Columbia (STS-75) from Kennedy Space Center into a Low Earth Orbit (LEO). On the third day of the mission (056/2045 UT), the tethered satellite was deployed from the payload bay of the Orbiter. The satellite was connected to the Orbiter through a thin conducting tether, which reached an eventual length of 19.7 km above the Orbit before it separated. As the satellite-Orbiter system moved through the Earth's magnetic field, an induced $V \times B \cdot L$ voltage was generated across the endpoints of the tether. This voltage reached a peak value of ~ 6 kV at the maximum extension of the tether. For an eastward moving TSS, the satellite was biased positive relative to the ambient plasma. Thus it was able to collect an electron current from the surrounding ionosphere. One of the primary science objectives of the TSS-1R mission was to determine the I-V characteristics of the TSS-Ionosphere

system. From a physics viewpoint, the I-V curves contain important information about the ambient space conditions, the sheath surrounding the charged satellite, and the physical processes involved in current collection. From a technological prospective, determination of the I-V has practical implications for the concepts of using TSS to generate electric power for orbiting space platforms such as space station, or to provide electric propulsion for spacecrafts designed for planetary exploration.

Generally speaking, finding the I-V characteristics addresses the fundamental question: how much voltage needs to be applied to a conductor in order to collect a prescribed amount of current. The underlying physics of current collection by a charged body in the magnetized plasma has been an interesting and challenging problem in the history of the plasma physics. In pioneering works Langmuir¹ developed models of current flow between plates or concentric spherical electrodes with biased potential in an unmagnetized plasma. The well known Child-Langmuir Law² sets the maximum amount of current, the so-called space-charge-limited current, that can be flown between electrode plates. In the 1960s, theoretical models were developed specifically for unbounded plasma, which apply directly to current collection in space. The model by Beard and Johnson³ (BJ) neglected the effects due to earth's magnetic field and solved the spherical space-charge-limited flow problem. The BJ model predicts a current-voltage relation

$$\frac{I_{BJ}}{I_0} = \left(\frac{N V_e}{2.5 \times 10^{12}} \right)^{-\frac{4}{7}} a^{-\frac{3}{7}} \left(\frac{V}{40} \right)^{\frac{6}{7}}, \quad (1)$$

where N is the plasma number density in the unit of electrons per c.c., a is the radius of the collecting sphere in meters, V is the potential of the sphere in volts, V_e is the thermal speed of the electrons defined as

$$V_e = \left(\frac{8 T_e}{\pi m_e} \right)^{\frac{1}{2}}, \quad (2)$$

and I_0 is the electron thermal current defined as

$$I_0 = e N V_e \left(\pi a^2 / 2 \right) \quad (3)$$

Since the effects of magnetic field is to reduce the amount of current flowing to the conductor, the BJ current in (1) represents an upper limit of the current collection by the conductor in space. The I-V model that includes magnetic field effects was developed by Parker and Murphy⁴ (PM). Linson⁵ summarized the results and listed an upper limit for the current reaching the conductor in a magnetic field as

$$\frac{I_{PM}}{I_0} = 1 + 2 \left(\frac{V}{V_0} \right)^{\frac{1}{2}} \quad (4)$$

where V_0 is a threshold potential defined by the strength of the magnetic field and the size of the conductor,

$$V_0 = \frac{m_e \Omega_e^2 a^2}{2 e} \quad (5)$$

As can be seen in (4), the current collection would not increase substantially above I_0 unless the voltage on the conductor is large compared to V_0 .

In the presence of the earth's magnetic field, current collection by the TSS satellite scales like PM with respect to potential at large voltages. However, factors such as satellite motion (~ 7.8 km/sec), ram and wake, and geometric shape of the collection area could also affect the current collection processes. Therefore, one would expect deviations from the PM results.

TSS I-V Measurements

The I-V characteristics of the TSS system was measured by a pre-programmed science operation called the IV-24 operating cycle. During the IV-24 cycle, a current sequence was performed by stepping the command current delivered by the Electron Generator Assemblies (EGAs) in the payload bay of the Orbiter, thus modifying the satellite potential. A complete IV-24 cycle contains six repeating current sequences with each sequence lasting four minutes. Figure 1(b) illustrates the command current pulses for each sequence as delivered by the EGAs and Figure 1(b) illustrates the layout of a complete IV-24 cycle. During the TSS-1R mission, three IV-24 cycles were completed. The first IV-24 cycle lasted from 056/23:20:30 to 056/23:44:30 UT in a day orbit. The second IV-24 cycle lasted from

057/00:12:00 to 057/00:36:00 UT in the subsequent night orbit. The last IV-24 cycle lasted from 057/01:06:00 to 057/01:30:00 UT during a day orbit.

During each of the command current pulses, the actual current I flowing through the tether is measured directly by the Tether Current and Voltage Monitor (TCVM) of the Shuttle Electrodynamic Tether System (SETS) investigation⁶ and by the Satellite Ammeter (SA) of the Satellite Core Equipment (SCORE) investigation⁷. The satellite voltage V_{sat} , defined by the potential difference between the satellite and the ionospheric plasma, is measured by the boom-mounted sensor package (BMSP) operated by the Research on Orbital Plasma Electrodynamic (ROPE) investigation⁸. We have taken a two-steps approach to construct the I-V curves for the entire range of the satellite potential. The first step is to calibrate the tether resistance R using the BMSP data of $1 \text{ volt} < V_{sat} < 100 \text{ volts}$. The second step is to compute V_{sat} based on the calibrated R value and impose error bounds according to the uncertainties associated with the statistical measurements. Both steps utilize the equivalent TSS circuit as shown in Figure 2. In this figure, V_{sat} and V_{orb} represent the potential drops across the plasma sheaths surrounding the satellite and the Orbiter. Correspondingly, V_{orb} is the potential drop between the cathodes of the electron accelerators and the Orbiter body; I is the Tether current and R is the overall dc resistance of the tether wire, which is approximately 2.1 K Ω at room temperature. Taking the motional induced EMF generated by a moving TSS-Orbiter system to be V_{emf} , the TSS circuit equation can be expressed as

$$V_{emf} = V_{sat} + IR + V_{ega} + V_{orb} \quad (6)$$

To perform calibration in the first step, the tether resistance R is determined by substituting V_{sat} and other directly measured quantities such as I , V_{emf} , V_{ega} , and V_{orb} into equation (6). In the second step, a reverse process is taken, namely, using mean values of R and standard deviation ΔR into (6) to obtain V_{sat} as a function of I .

TSS Resistance Calibration

Direct measurements of various potential terms in (6) were performed by instruments onboard the Orbiter and the satellite during the TSS-1R mission. For instance, the Vega was measured by the voltmeter of the Deployer Core Equipment (DCORE-DV)⁷ and by the Tether Current and Voltage Monitor (TCVM) of the

Shuttle Electrodynamic Tether System (SETS)⁶ as shown in Figure 2. The V_{emf} was measured by the TCVM and the DCORE-DV in between the current pulses when the EGAs were off and the current $I=0$. The Shuttle potential V_{orb} , although not directly measured, was inferred from the Electrostatic Analyzers (ESAs) of the Shuttle Potential and Return Electron Experiment (SPREE)⁹ located in the payload bay, which recorded the energy spectrum of the ions returning to the Shuttle.

Each current pulse in the IV-24 cycle provides a set of values for I , V_{ega} , V_{orb} , and V_{emf} . Using the V_{sat} obtained from the ROPE measurements, we can calculate the tether resistance R directly from (6). Figure 3 shows the R values for the first, the second, and the third IV-24 cycles as represented by the solid circle, square, and rhombic data points, correspondingly. Each data point is associated with a current pulse that gives rise to a satellite potential in the range of $1 \text{ V} < V_{sat} < 100 \text{ V}$. Adjacent data points are linked by a straight line. From this figure, we can see that for a given IV-24 cycle, the tether resistance data points form a distribution, which can be quantified statistically by a standard deviation around a mean value. Table 1 shows the mean and the standard deviation of the tether resistance (in Ω) for each IV-24 cycle:

The mean resistance in table 1 reveals an interesting fact, namely, the mean tether resistance varies from cycle to cycle. Its value reaches the highest level in the first IV-24, then drops to the lowest level in the second IV-24, finally settles at an intermediate value in the third IV-24. This variation is obviously correlated with the diurnal pattern of the three cycles. It is therefore logical to attribute the tether resistance variations to the temperature changes in the tether, which is directly influenced by exposure to sun light. Since there is no direct temperature measurement of the tether, we look for variations in the temperature data taken by sensors attached to the skin of the satellite as corroborative evidence. Figure 4 displays temperature data (in $^{\circ}\text{C}$) versus time from 16 sensors, which are part of the satellite thermal control system, located at various places on the surface of the satellite. The IV-24 periods are high-lighted with heavy lines beneath the time axis. From this figure, we can see small periodic oscillations on the temperature curves at a period of roughly 4 minutes. These oscillations correspond to satellite spin at a rate of roughly 0.25 rpm. A major temperature decline occurs at around 057/0000 UT, which is the time the TSS enters the night orbit. From the first IV-24 to the second IV-24, the temperature

decrease recorded by these sensors range from 10 to 50 $^{\circ}\text{C}$, depending on where the sensor is located. Likewise, from the second IV-24 to the third IV-24, the temperature increases by similar amounts.

We can independently verify the temperature change based on the variation of mean resistance. The analytic temperature-resistance formula for copper is given in the Handbook of Chemistry and Physics [1980]¹⁰

$$R = R_0 [1 + \Theta (T - T_0)] \quad (7)$$

where $T_0 = 20 \text{ }^{\circ}\text{C}$, $R_0 = 2.0 \text{ K}\Omega$, and $\Theta = 0.00393 \text{ }^{\circ}\text{C}^{-1}$. This formula relates the change of resistance to the change of temperature as

$$\Delta R = R_0 \Theta \Delta T \quad (8)$$

Using the changes of mean resistance ΔR_1 (from 1st to 2nd IV-24) and ΔR_2 (from 2nd to 3rd IV-24) in above equation, we can estimate the temperature change to be $\Delta T_1 = -32 \text{ }^{\circ}\text{C}$ and $\Delta T_2 = +23 \text{ }^{\circ}\text{C}$. These numbers are in line with the temperature changes shown in Figure 4. It is interesting to point out another feature that indicates temperature dependent resistance change of the TSS system. In Figure 3, data points of the last IV-24 cycle shows a slanted distribution, which implies that the tether resistance increases with time during the cycle. In Figure 4, the satellite temperature measurements made at the last IV-24 show a similar trend of increase in time. This provides added evidence that the tether resistance is indeed sensitive to the temperature change.

TSS I-V Characteristics

Using the calibrated tether resistance in Table 1, we can construct the entire I-V curves from equation (6). However, since the tether resistance varies with time during the TSS-1R mission, and can only be determined with some uncertainty, it is appropriate to impose error bounds on the I-V characteristics to indicate its limits. As an example, in Figure 5 we plot the I-V curve obtained from the first stepping sequence of the third IV-24 cycle. This IV-24 cycle was performed during daytime, at high ambient plasma density ($\sim 8.5 \times 10^{25} \text{ /c.c.}$ from the real-time SUNDIAL model)¹¹, and with the tether near its full extension. In this figure, the tether current I for the entire current pulse sequence is plotted against the satellite potential, which is calculated from (1) based on the directly measured V_{emf} and V_{ega} from DCORE.

Each current pulse contributes two data points, as shown by solid dots, and adjacent data points are connected by a straight line. The error bounds are imposed on voltage as horizontal bars because of the uncertainty on the measured tether resistance value. The actual length of the error bar is calculated by multiplying the tether current I with the standard deviation ΔR . From this figure, it is interesting to see that the I-V curve exhibits distinctly different scaling properties at low and at high voltages. At high voltage ($V_{\text{sat}} > 300$ volts), the error constitutes a small percentage of the overall voltage reading. Therefore, it is of no practical consequence. However, at low voltage ($V_{\text{sat}} < 50$ Volts), the error bars are comparable in magnitude to the potential values, i.e. $I \Delta R \sim V_{\text{sat}}$. Therefore, it is not possible to derive a reliable scaling law in this regime. The uncertainty on tether resistance presents an ambiguity in the physical interpretation of the I-V characteristics in this regime.

To compare the TSS results with the predictions from the analytic models, we plot both the Beard-Johnson (BJ) I-V values from (6) as triangle points, and the Parker-Murphy I-V values from (4) as square points, in Figure 5. It is clear that the TSS satellite collected more current than both the BJ and the PM models predict. The TSS current is higher than the PM current by more than a factor of two throughout the entire voltage range. In addition, it is also consistently higher than the BJ current except at very low voltages (< 10 volts). This result is very surprising because the BJ current represents the upper limit of current collection by a charged conductor in an unmagnetized plasma. The fact that TSS satellite collected more current indicates the need for complete revision of the current collection theories for spacecrafts traveling at orbital velocities.

I-V Scaling An important question is how do the TSS I-V characteristics scale. We plot in Figure 6 the fractional deviation of the TSS current from the PM and the BJ values. The fractional deviation is defined as $(I_{\text{TSS}} - I_{\text{mod}}) / I_{\text{TSS}}$ where I_{TSS} is the TSS current data and I_{mod} is the current predicted by the models. If the TSS I-V and the model I-V have the same scaling, the fractional deviation should be constant. This is true even if the TSS current is different from the model current in magnitude. From Figure 6, we can see that the TSS I-V scales like the PM model for $V > 50$ volts. On the other hand, there is no similarity between the TSS scaling and that of the BJ model. This indicates that at high voltages (> 100 volts) the TSS current collection is likely to be magnetically limited, which is PM like. We would like to emphasize that even though

the TSS I-V scales like PM, the TSS current exceeds the PM value by a large margin.

Gas Event Gas was released by thrusters onboard satellite during a planned science operation called the DC-24 cycle. The DC-24 cycle performed I-V operation similar to the IV-24 cycle, except in a dc mode. Two DC-24 cycles were completed during the TSS mission and the gas event occurred in the middle of the second DC-24 cycle. The event lasted 2 second, starting from 057/00:54:04. Prior to the gas release, the satellite potential was about 1050 volts and the tether current was about 0.44 amps. Immediately after the gas release, tether current surged to 0.6 amps and was subsequently capped by the electron guns at 0.5 amps. The satellite potential, however, dropped to about 100 volts. This indicates that the satellite can collect the same amount of current at a much lower voltage because the gas discharge provides a new source of electrons near the satellite surface. In Figure 7, we plot the gas I-V (large solid square), the DC-24 I-V prior to the event (large solid dot), and the entire I-V curves from the last IV-24 cycles for comparison. The gas point, as we can see, occurs way above the nominal TSS I-V performance, which is represented by the IV-24 curves within the bounded dashed lines, while the DC-24 point is nominal. Therefore, the TSS system can perform more efficiently with neutral gas present in the electron sheath around the satellite.

Power Generation It is useful to calculate the maximum amount of electrical power available from TSS. This is defined as the tether current multiplying the voltage difference between V_{emf} and V_{sat} . This quantity is plotted in Figure 8 using the I- V_{sat} obtained from the TSS dataset and from the analytic models. From this figure, it is interesting to see that the PM power saturates at a low level of 500 watts, while both the TSS and the BJ power are still increasing at the end of the TSS data range. The available power provided by the TSS system reaches 1200 volts at $I = 0.5$ amps. The reason that the PM power saturates early is because a much higher voltage is required to collect a prescribed amount of current in the PM model. Therefore, a comparatively larger amount of power ($I V_{\text{sat}}$) is wasted in the satellite sheath. In this regard, gas release from the charged satellite will provide the most cost effective mean of generating useful electrical power by the TSS. This is because the gas event showed a large amount of current collection at a very low satellite potential. Using the numbers provided in the last section, we can estimate that the maximum power available from the gas event is roughly 1700 watts. This number is substantially higher than the maximum power delivered

by the TSS system. We remark that this number could only improve if the tether current were not limited by the electron guns during the gas event.

Conclusion

It is appropriate to conclude that the I-V results obtained by the TSS-1R mission far exceeded the expectation from the existing analytic models. The fact that the TSS current exceeds even the BJ limit presents a challenge to the understanding of physics involved in the high voltage current collection in space. There is an unquestionable need to improve the theoretical understanding of the TSS results. Several possible scenarios have been proposed and are currently under investigation. For instance, the motion of the TSS at orbital velocity may enhance the electron collection by sweeping; the heating of electrons by the O^+ ions reflected from the satellite could increase the thermal flux entering the sheath; or the discharge of neutrals within the satellite sheath may provide a new source of electrons, just to name a few. Based on the encouraging results from the TSS-1R mission, it is timely to recognize the potential of using TSS technology for practical applications in space, such as generating electrical power or providing thrust to the spacecrafts.

Acknowledgments

This research was sponsored by the NASA under contract NAS8-36811. We would like to acknowledge the contributions from the entire science team in the TSS-1R mission. In particular, the data from the ROPE investigation⁸ and the DCORE investigation⁷ has been crucial in performing this analysis. Finally, we would like to thank the crew members onboard STS-75 Drs. J. A. Hoffman, F. R. Chang-Diaz, C. Nicollier, U. Guidoni, M. Cheli, Lt. Col. S. J. Horowitz, and Lt. Col. A. M. Allen for their dedication to the mission and for their encouragement of this work.

References

1. Langmuir, I., "The Effect of Space Charge and Initial Velocities on the Potential Distribution and Thermionic Current Between Parallel Plane Electrodes," *Phys. Rev.*, **21**, p. 419 (1923); Langmuir, I. and K. B. Blodgett, "Currents Limited by Space Charge Between Concentric Spheres," *Phys. Rev.*, **24**, p. 49 (1924).
2. Child, C.D., "Discharge from Hot CaO," *Phys. Rev.* **32**, p. 492 (1911); Langmuir, I., *Phys. Rev.* **3**, p. 238 (1931).
3. Beard, D.B., and F.S. Johnson, "Ionospheric Limitations on Attainable Satellite Potential", *J. Geophys. Res.*, **66**, p. 4113 (1961).
4. Parker, L.W., and B.L. Murphy, "Potential Buildup on an Electron-Emitting Ionospheric Satellite", *J. Geophys. Res.*, **72**, p. 1631 (1967).
5. Linson, L.M., "Current-Voltage Characteristics of an Electron-Emitting Satellite in the Ionosphere", *J. Geophys. Res.*, **74**, p. 2368 (1969).
6. Agüero, V., P.M. Banks, B. Gilchrist, I. Linscott, W.J. Raitt, D. Thompson, V. Tolat, A.B. White, S. Williams, and P.R. Williamson, **The Shuttle Electrodynamic Tether System (SETS) on TSS-1**, Special TSS-1 Issue, Edited by M. Dobrowolny, *IL Nuovo Cimento*, **17C**, N. 1, p. 49-65, (1994).
7. Bonifazi, C., F. Svelto, and J. Sabbagh, **TSS Core Equipment. I. - Electrodynamic Package and Rationale for System Electrodynamic Analysis**, *ibid*, p. 13-47, (1994).
8. Stone, N.H., K.H. Wright Jr., J.D. Winningham, J. Biard, and C. Gurgiolo, **A Technical Description of the TSS-1 ROPE Investigation**, *ibid*, p. 85-99, (1994).
9. Oberhardt, M.R., D.A. Hardy, W.E. Slutter, J.O. McGarity, D.J. Sperry, A.W. Everest III, A.C. Huber, J.A. Pantazis, and M.P. Gough, **The Shuttle Potential and Return Electron Experiment (SPREE)**, *ibid*, p. 67-83, (1994).
10. **Handbook of Chemistry and Physics. Properties of Metals as Conductors**, E85, 60th Ed., (1980).
11. Szuszczewicz, E. P., P. E. Blanchard, **Monitoring and real-time forecasting of global-scale ionospheric weather during the TSS-1R mission**, SA41B-10, AGU Spring Meeting, Baltimore. (1996).

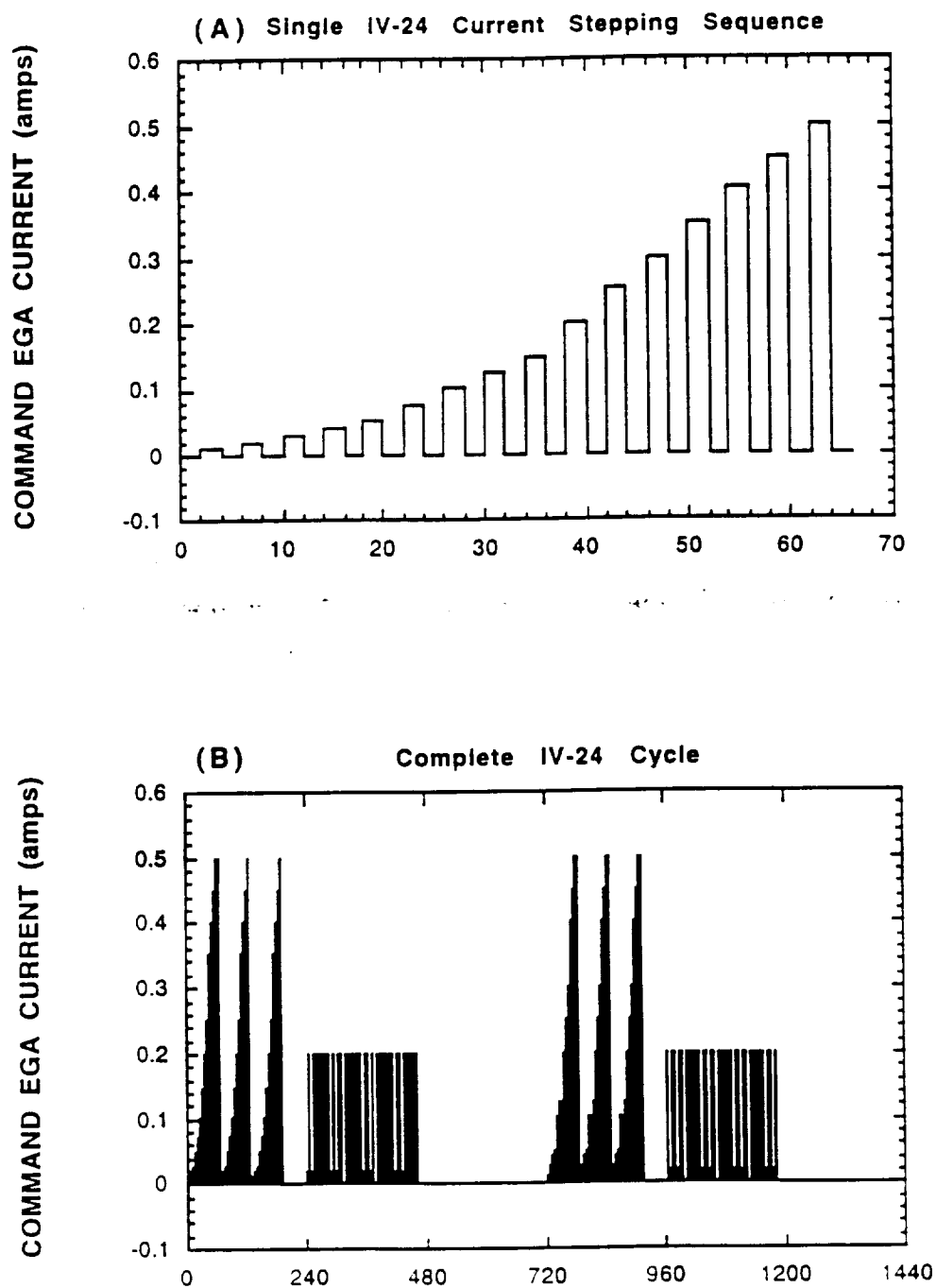
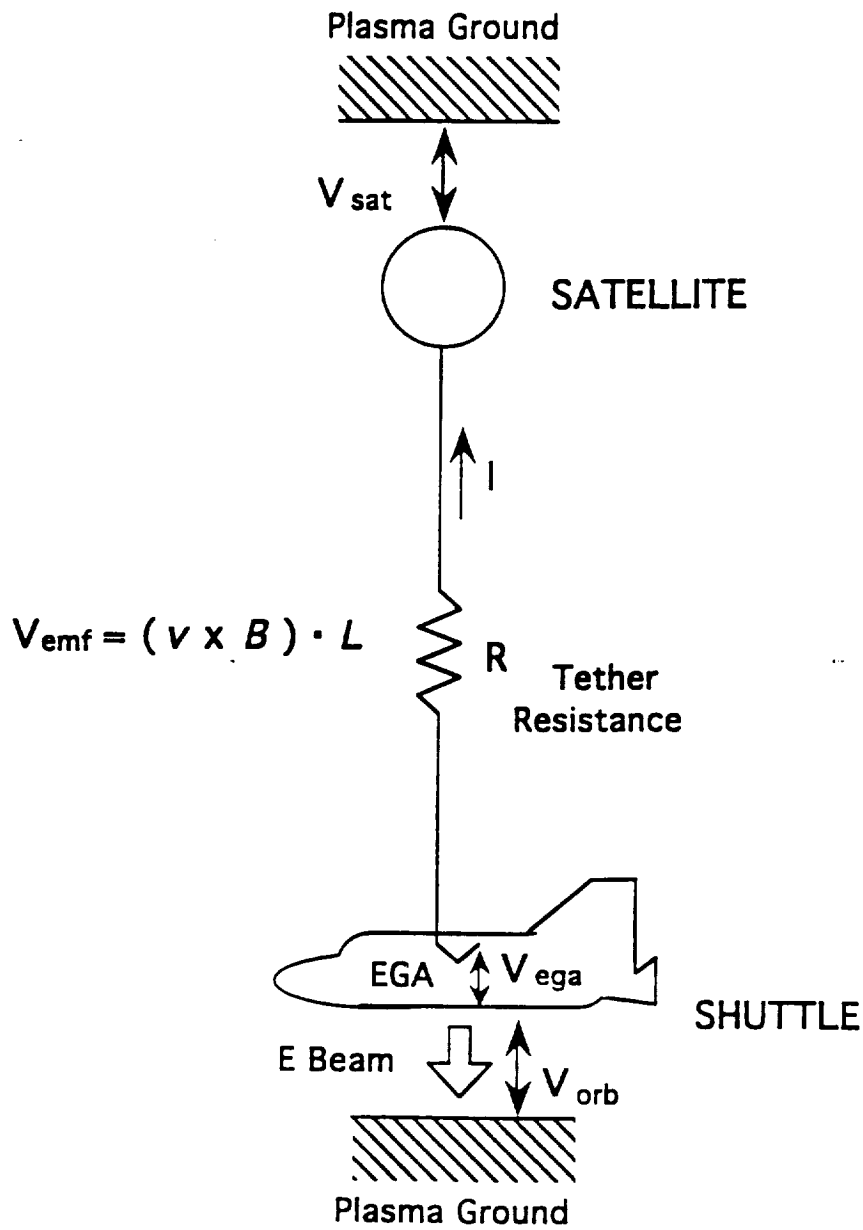


Figure 1. (a) A single current stepping sequence consists of 16 current pulses in the IV-24 operation; (b) A complete IV-24 cycle contains 6 single current stepping sequences (the dark spikes) which lasts 24 minutes.



$$V_{emf} = V_{sat} + I R + V_{ega} + V_{orb}$$

Figure 2. Schematic presentation of the TSS circuit under EGA operation

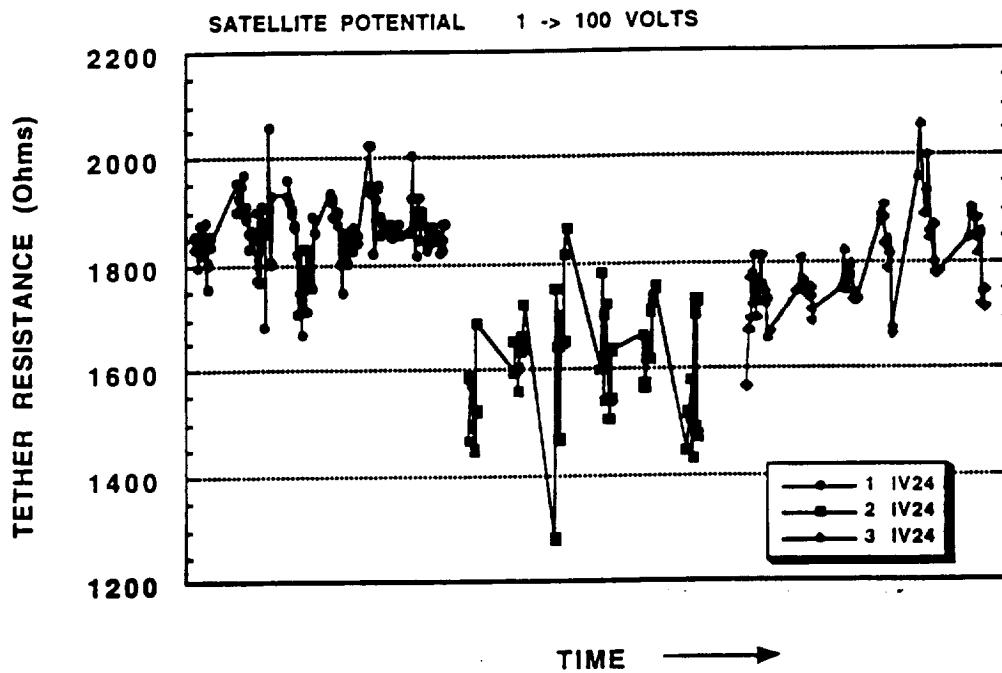


Figure 3. Tether resistance calculated from (6) using ROPE satellite potential measurements. Solid, square, and rhombus dots are data points from the first, the second, and the third IV-24 cycles, correspondingly.

IV-24 Cycle	Orbit	Time (UT)	Mean Resistance	Standard Deviation
1st	Day	056/2320:30 - /2344:30	1864.2	60.2
2nd	Night	057/0012:00 - /0036:00	1610.0	109.5
3rd	Day	057/0106:00 - /0130:00	1788.4	84.3

Table 1. Calibration of tether resistance in three IV-24 cycles.

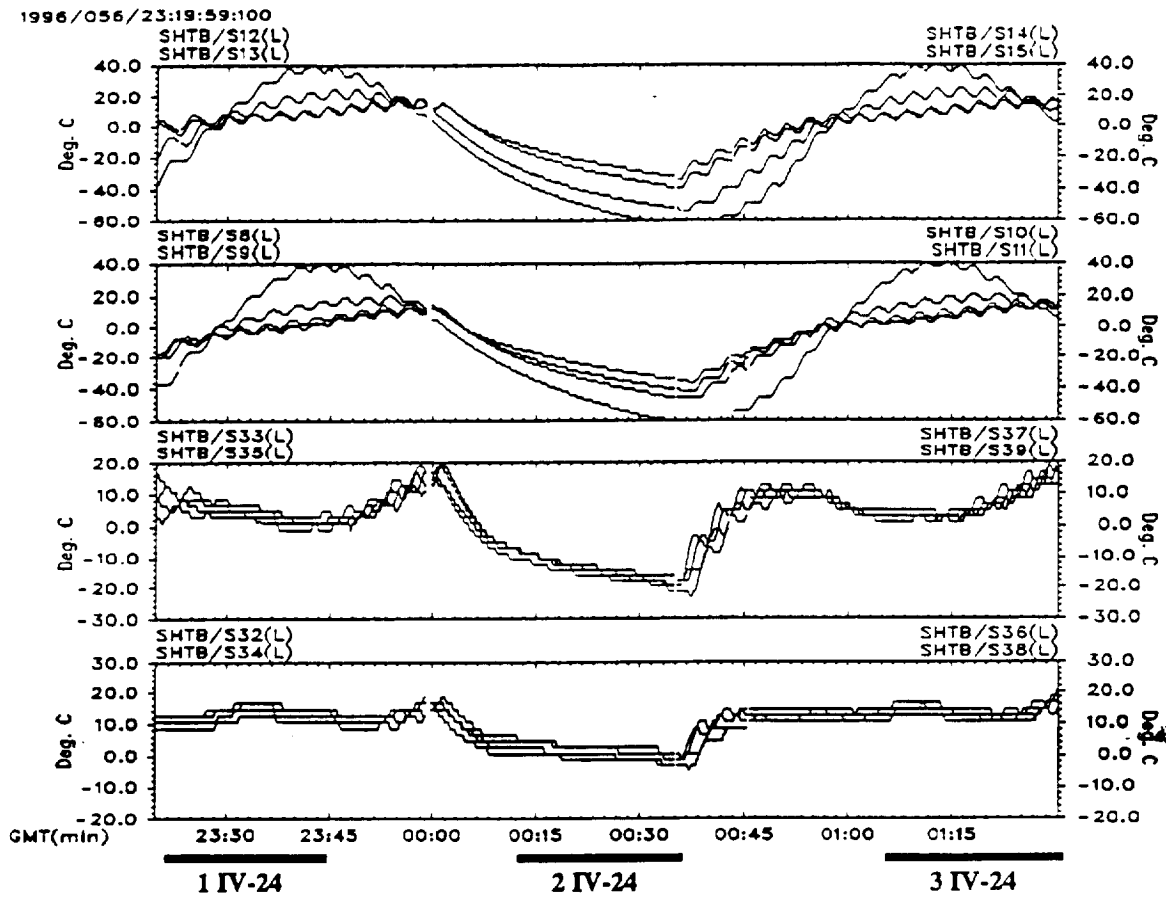


Figure 4. Temperature data from 16 sensors located on the satellite surface are plotted as function of time. Dark broad lines below the time axis indicate the periods of three IV-24 cycles.

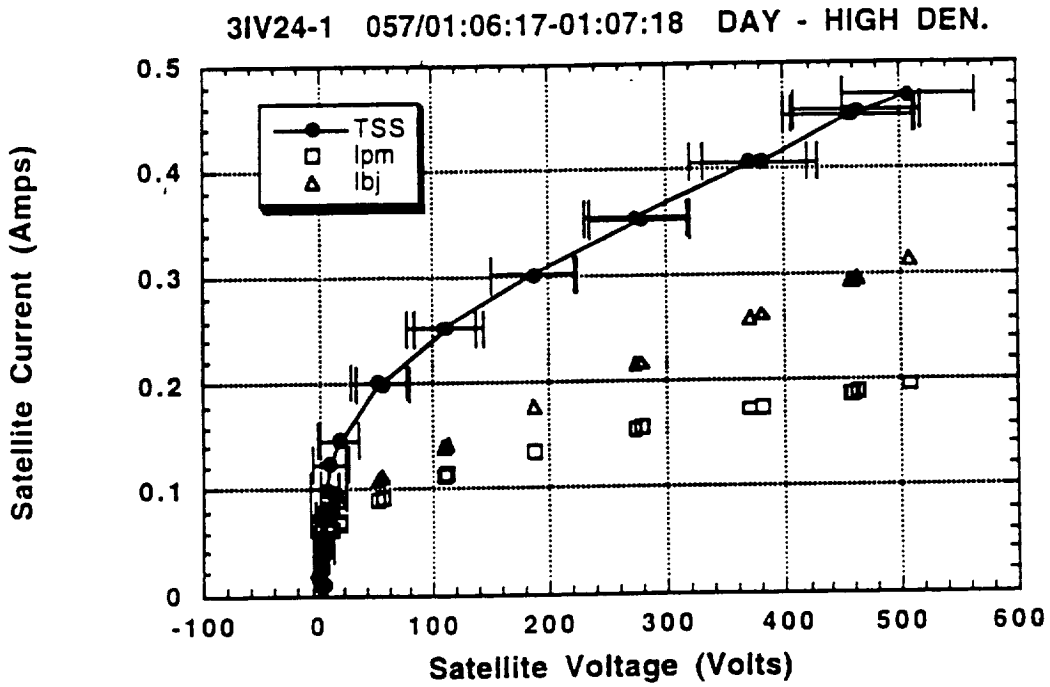


Figure 5. I-V characteristics of the TSS satellite from the third IV-24 cycle. Error bars on satellite voltage are due to the uncertainties of the tether resistance. I-V relations from the Parker-Murphy model (squares) and the Beard-Johnson model (triangles) are also shown.

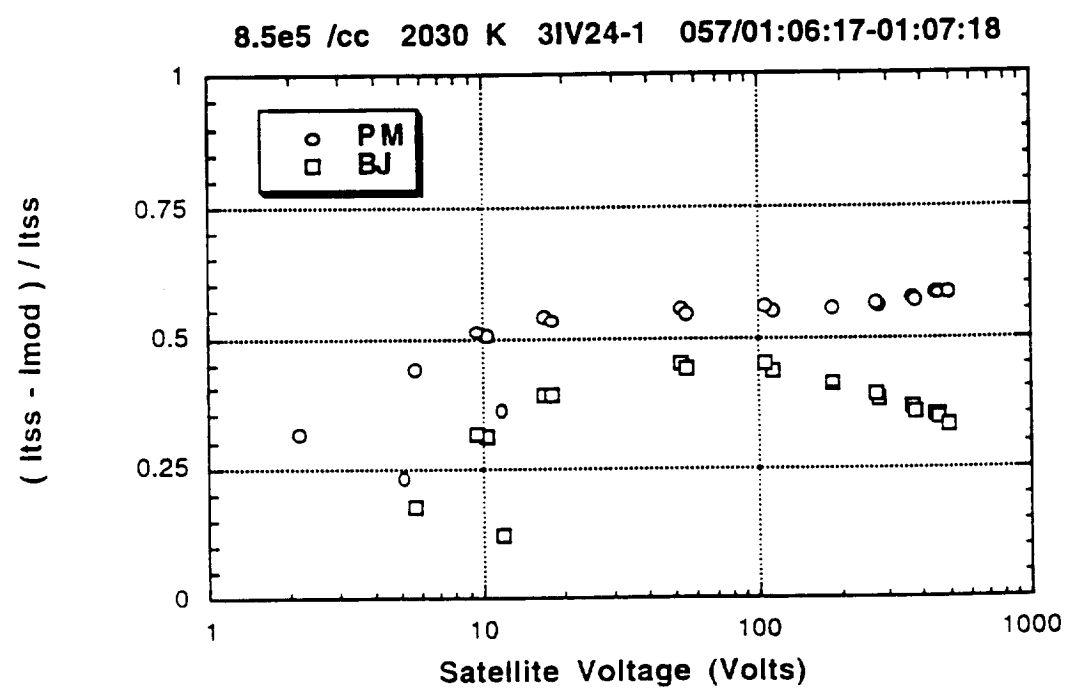


Figure 6. I-V scaling of the TSS data. Fractional deviation from the PM and the BJ models are plotted versus satellite voltage. Constant fractional deviation value implies same I-V scaling with the model.

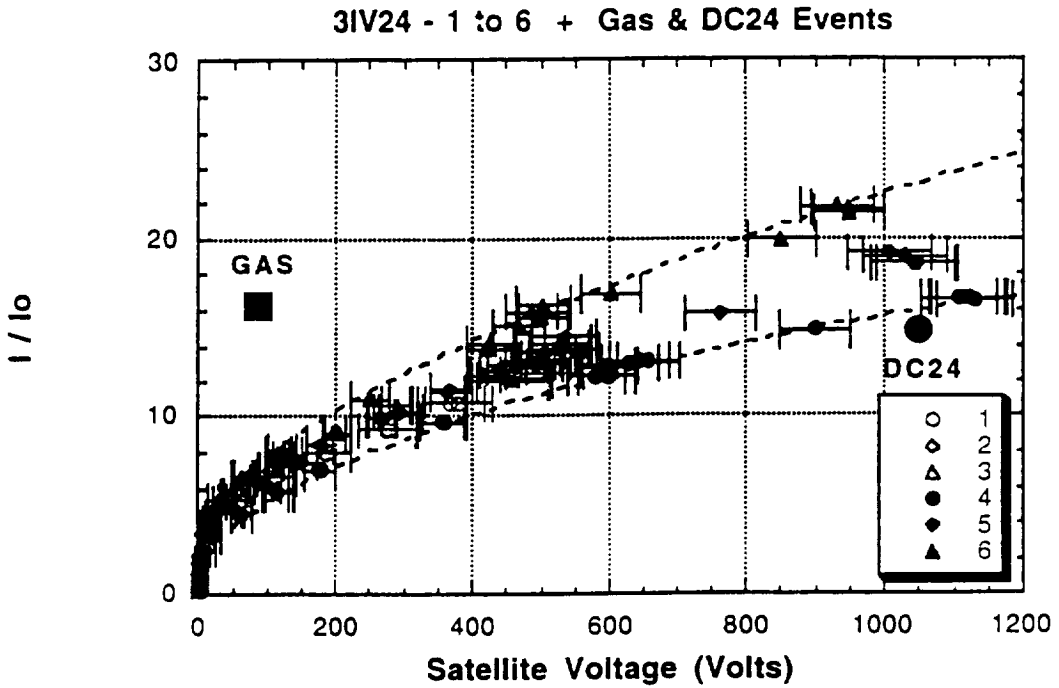


Figure 7. The complete I-V survey from the last IV-24 cycle. Gas event and DC24 cycle reference point prior to the gas event are shown as large solid square and dot, respectively.

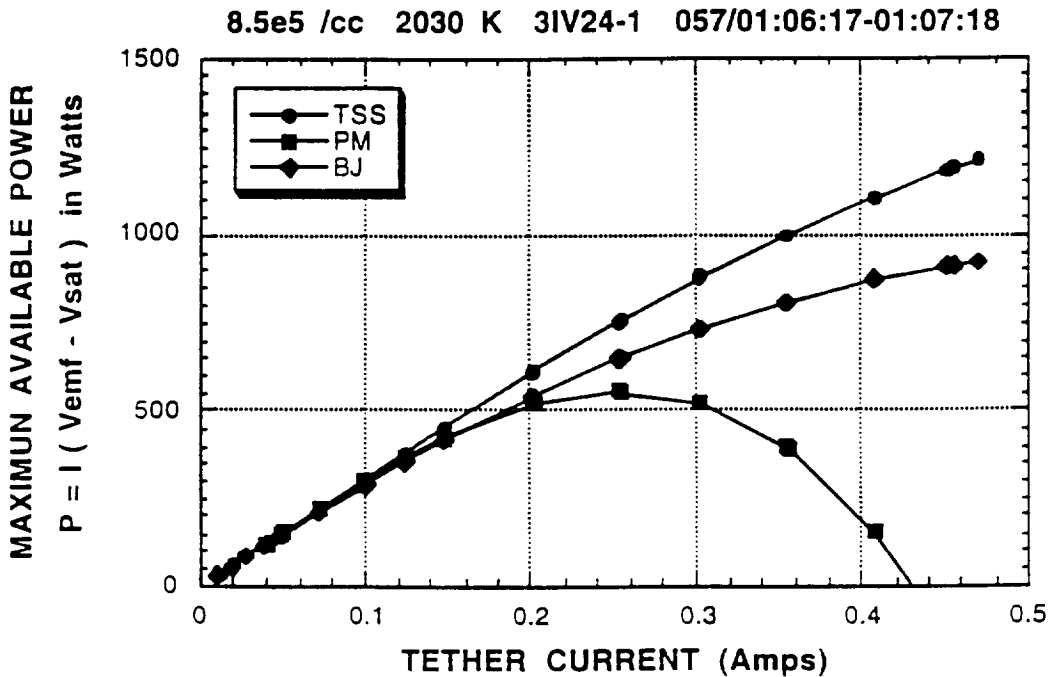


Figure 8. Maximum power available from the TSS system is plotted against the tether current. As comparison, power available from both PM and BJ models are also plotted.

APPENDIX 12



AIAA 97-0583
**Neutral Environment of the Tethered
Satellite System (TSS)**

D. F. G. Rault
NASA Langley Research Center
Hampton, VA

C. L. Chang
Science Applications International Corporation
McLean, VA

**35th Aerospace Sciences
Meeting & Exhibit**
January 6-9, 1997 / Reno, NV

NEUTRAL ENVIRONMENT OF THE TETHERED SATELLITE SYSTEM (TSS)

Didier F. G. Rault*
NASA Langley Research Center
Hampton, VA 23881

Chia Lie Chang
Science Applications International Corporation
1710 Goodridge Drive, McLean, Virginia, 22102

Abstract

The neutral gas environment of the TSS satellite is simulated using Navier Stokes, Free Molecule and DSMC methods. The simulation is performed in two steps. The first step yields first-order estimates of the gas cloud enveloping the satellite. The second step is more accurate, but computationally expensive, and is used to study secondary effects such as plume impingement and multiple plume interactions.

Nomenclature

A	Constant
B	Breakdown parameter
C	Constant
D	Distance (m)
L	Gradient length (m)
$N = 1/B$	Number of collisions per characteristic flow time τ
N	Source number flux (sec^{-1})
U	Stream velocity (m/s)
Q	Source term
T	Temperature (K)
M	Mach number
k	Boltzmann constant
v	Molecular velocity (m/s)
n	Source point normal direction cosine
$s = \beta U$	Speed ratio
r	Distance to nozzle (m)
w	Molecular mass (Kg)
$\alpha, \phi, \theta, \varepsilon$	Azimuthal and Euler angles
β	$1/\sqrt{2kT/w}$
λ	Collision mean free path (m)
ν	Intermolecular collision frequency (sec^{-1})
$\tau = L/U$	Flow characteristic time (sec)

ρ	Gas density (Kg/m^3)
δ	Dirac function

Introduction

The primary goal of the Tethered Satellite System (TSS) mission was to test and demonstrate an alternative method for generating electrical power in space, namely flying a long conductor across the Earth magnetic field and inducing a $V \times B$ electrical field along the tether. The magnitude of the current through the tether, and therefore the net power generated, depends on several factors, among which the plasma conductance in the near vicinity of the spherical satellite attached at the end of the tether. The ambient ionosphere is locally perturbed by the presence of the highly charged satellite, which results in the formation of a plasma sheath, the electrical properties of which have been simulated on computers (Ref. 1). The effect of neutral gases on the plasma sheath and return current has however not been well characterized to date. The neutral gases, which are mostly emanating from 14 attitude control thrusters distributed on the TSS surface, could dramatically alter the electrical properties of the plasma near the satellite and increase the overall conductance of the tether system and hence, the current.

To study this effect, the gas plume emitted from each of the control thrusters is being simulated in this paper and the neutral flowfield in the vicinity of the satellite is characterized. Section 1 describes the geometrical features of the TSS satellite and presents the thruster main features. The simulation of plume flowfields is notoriously complex since, during expansion, the gas traverses all three flow regimes, as shown in Section 2: Continuum inside the thruster nozzle and, possibly some distance downstream, Transition afterwards and finally, Free Molecule in the nozzle far field. An accurate simulation of plume flowfields, therefore, requires the use of a variety of fluid flow models, such as Navier Stokes solvers, Direct Simulation Monte Carlo (DSMC) and analytical Free Molecule codes, to individually deal with each region of the flowfield. The simulation methodology, which

*Aero-Space Technologist, Aerosol Research Branch, Atmospheric Science Division

Copyright © 1997 by the American Institute of Aeronautics and Astronautics, Inc. No copyright is asserted in the United States under Title 17, U. S. Code. The U. S. Government has a royalty-free license to exercise all rights under the copyright claimed herein for Governmental Purposes. All other rights are reserved by the copyright owner.

was used in the present study, is outlined in Section 3, and the numerical codes are described in Section 4. The simulation is performed in two steps. The first step yields a first-order estimate of the neutral gas cloud characteristics. It is based on the findings by Rault (Ref. 2) that, for simple plumes, the gas is essentially "frozen" downstream of the breakdown surface, i.e., downstream of the interface between the Continuum and Transition domains. In the second step, a more accurate method is used to characterize secondary effects such as plume impingement on the satellite surface and multiple plume interaction.

Results are presented in Section 5 in the form of neutral density maps around the satellite. The effect of the impingement of the Yaw thruster plumes is quantified in Section 6, and the interaction of the InLine thruster plumes is studied in the last section.

TSS Geometry and Thruster Characteristics

The Tethered Satellite System was deployed from the Space Shuttle STS-75 in February 1996 in a circular orbit at 250 km altitude. The satellite basic geometric shape is spherical with a 1.6 m diameter and a mass of 518 Kg. Figure 1 shows the TSS main features. The satellite is equipped with a series of 14 thrusters to control its attitude during deployment and in orbit. The thrusters are surface mounted and are strategically distributed over the surface as depicted in Figure 1. The thrust level, mass flow rate and geometrical dimensions of each thruster are shown in Table 1. The thruster exit nozzles are conical. The thrusters operate at a stagnation pressure of 10 atmospheres and a stagnation temperature of 300 degrees Kelvin. Their working gas is Nitrogen.

Plume Flowfield Characteristics

Figure 2 schematically shows the typical structure of a plume flowfield, from the thruster nozzle exit to the far field. In the near vicinity of the nozzle, gas densities are relatively large and local Knudsen numbers are small. The flow is in the Continuum regime, where Navier Stokes solvers can be used to characterize the flow field. Further downstream, the Knudsen numbers become too large and continuum methods are no longer applicable. In this Transition flow regime, the Chapman-Enskog transport relationships are no longer valid and the gas is typically non-isotropic and non-Maxwellian, as collisions between molecules are too infrequent to maintain the gas in equilibrium in any energy mode (Translational, Rotational, Vibrational, Chemistry). The particle tracing Direct Simulation Monte Carlo technique of Bird (Refs. 3, 4), which is

described below, must be used in this region. Finally, in the plume far field, collisions among molecules are very rare and the flow is in the Free Molecule regime, where the analytical tools presented in Section 4 can be used to characterize the flowfield properties. The boundaries between these three flow regimes depend on the number N of intermolecular collisions per characteristic time of the flow τ :

$$N = v \tau \quad (1)$$

where v is the intermolecular collision frequency and

$$\tau = L / U \quad (2)$$

The gradient length L is defined as

$$L = \rho / \nabla \rho \quad (3)$$

where ρ is the gas density and U is the flow bulk velocity.

The parameter N is related to Bird's Breakdown parameter B (Ref. 4):

$$N = 1 / B \quad (4)$$

Upon analysis of experimental data corresponding to a series of plume expansions, Bird has proposed a value of $B = 0.05$ for the boundary between the Continuum and Transition flow domains. This value corresponds to $N = 20$ collisions per characteristic time of the flow.

The boundary between the Transition and Free Molecule domains has not yet been similarly characterized, but, from a simulation viewpoint, this boundary can be set at the point where the collision mean free path approaches the size of the computational domain.

Methodology for Plume Simulation

A detailed simulation of the gas cloud around TSS would be extremely complex, requiring a CFD simulation for each thruster, feeding into a large DSMC simulation over the whole satellite. However, several simplifying assumptions can be made, based on geometrical considerations and past research work on plumes. As shown in Figure 1, the thrusters are widely separated, (with exception for the InLine thrusters) and the plumes would interact only far downstream where conditions are close to Free Molecular. Hence, for all but the InLine thrusters, each thruster can be studied independently and their effects superimposed arithmetically. Moreover, Rault (Ref. 2) has shown that the flowfield downstream of the breakdown surface is essentially free molecular. The intermolecular

collisions in the Transition domain are very weak as they occur between molecules with very small relative velocities. Hence, a very good first-order estimate of the density field around the satellite can be obtained with the following steps:

- (1) Perform a CFD simulation for the gas within the thruster nozzle and near vicinity.
- (2) Construct the Breakdown surface from the CFD solution
- (3) Perform a Free Molecule simulation downstream of the Breakdown surface.
- (4) Superimpose the effects of all the thrusters by adding the density contribution of each one.

This methodology was used to provide the neutral density maps presented in Section 5.

The Yaw nozzles are slightly inclined with respect to the satellite surface normal. To study the impingement of the Yaw nozzle gas and its effect on the plume geometry, a detailed DSMC simulation was performed. Figure 3 shows the layout of the computation domain used in the simulation. Since only the gas on the outer edge of the plume can interact with the satellite surface, the plume core gases are excluded from the simulation. Downstream of the Breakdown surface, the plume expansion flowfield is mostly radial and the streamtubes are correspondingly close to conical in shape. In the simulation, the core gas is therefore represented by a solid conical surface with zero accommodation. The gas core contains more than 95% of the total number of molecules, and excluding it from the simulation allows one to focus on the important region of the flowfield, namely the plume edge, and significantly increase the simulation molecule weight factors (Refs. 3, 4). The InLine thrusters are close to each others and a detailed DSMC-based study was performed to quantify the level of interaction between them. Figure 3 shows the computation domain used in the DSMC simulation. The two planes parallel to the plume axis are set to be planes of symmetry in order to simulate the presence of the three other InLine thrusters. As described in Ref. 2, the domain is divided into two subdomains, with the inner one containing the CFD derived Breakdown surface and the outer one representing the "far field". The DSMC simulation is performed in a parallel computing environment on two-processor workstations, each processor being assigned to a subdomain.

Numerical Tools DSMC and Free Molecule

The Direct Simulation Monte Carlo (DSMC) Method

In engineering studies, DSMC is commonly used as a flow simulation code whenever the flowfield is in the Transition regime, i.e., when the characteristic Knudsen number of the flowfield is in the range of 0.01 to 10 (Refs. 3, 4). Such conditions arise, for example, in the case of reentry vehicles at high altitudes such as the Space Shuttle in the altitude range of 170 km to 100 km (Ref. 5). To simulate flowfields in this regime, conventional Computational Fluid Dynamic (CFD) numerical tools, which are based on solving the Navier Stokes equations, cannot be used. Instead, the gas is simulated as a large ensemble of discrete molecules, and computers are used to track a representative sample of simulated molecules as they move thru a computational domain and collide with other molecules and solid surfaces (Refs. 3, 4). The computational domain is subdivided into a grid of cells, the size of which is on the order of the local collision mean free path. The molecular velocity distribution is evaluated within each cell and its moments are evaluated to obtain the species density (0th moment), flow mean velocity (first moment) and the temperature in each of the three spatial directions (second moments).

The three-dimensional DSMC code used in the present study was devised by Bird (Ref. 6) and further developed by Rault (Refs. 2, 5, 7-8). High computational and setup efficiencies are achieved thru the use of an unstructured grid overlaid on a cubic Cartesian mesh. The code has previously been used to simulate flowfields surrounding slender hypersonic vehicles (Ref. 7), blunt reentry vehicles (Ref. 5) and spacecraft (Ref. 8). Good agreement has been shown to exist between code predictions and wind tunnel/flight data, when available. The code has been complemented with a set of utilities for graphical diagnosis, preprocessing, postprocessing and grid adaption. A CAD interactive graphical preprocessor was developed to allow simulations over bodies of arbitrarily complex geometry. The algorithm has been implemented on scalar, vector and parallel processors.

Free Molecule analytical code

Free Molecular codes are based on analytical expressions derived by integrating the Boltzmann equation for a given source term (Ref. 4). Woronowicz

and Rault (Ref. 9) have described a Free Molecular model which is specially suited for plume flowfield simulations. It is using a source term Q representing a drifted Maxwellian velocity distribution of stream velocity U and temperature T :

$$Q = A \delta(x) N |v \cdot n| \exp(-\beta(v - U)^2). \quad (5)$$

where

$$\beta = w / 2 k T \quad (6)$$

v is the molecular velocity and $\delta(x)$ is the Dirac function defined at the source location x . This source term corresponds to a physical gas source, of infinitesimal geometric dimensions, emitting a gas of molecular weight w at a flux rate \dot{N} with a uniform bulk exit velocity U and a temperature T . The density, velocity, temperature and other parameters can be computed analytically at any point within the source "field-of-view". For example, the gas density

$$n(x) = \frac{\beta \dot{N} \cos \phi}{C \pi r^2} e^{-s^2 \sin^2 \theta} ((s \cos \theta) \exp(-s^2 \cos^2 \theta) + (\frac{1}{2} + s^2 \cos^2 \theta) \sqrt{\pi} (1 + \operatorname{erf}(s \cos \theta))) \quad (7)$$

These analytical expressions have been shown to exactly reproduce the results obtained with collisionless DSMC simulations of point gas sources, as will be shown below.

Overall Neutral Environment

Figure 4 shows the flowfield density near the exit plane of the Yaw nozzle as computed by Stuart (Ref. 10) using the NASA JSC continuum code which has been specially adapted to plume flowfield simulation. The CFD simulation was initialized upstream of the nozzle throat, but only the region downstream of the nozzle exit is depicted on the figure. Gas densities can be observed to decrease by two orders of magnitude along the plume axis within the first 15 cm of the expansion. In the radial direction, gas densities decrease even more rapidly. The CFD solution is valid only up to the Breakdown surface, which is constructed as explained in Section 2. Figure 5 displays the Breakdown surface for the Yaw nozzle. It can be seen that the Breakdown surface is very elongated in the direction of the plume axis. Similar analysis have been conducted for the InLine and OutPlane nozzles.

As described in Section 3, free molecule simulation is used to determine the gas densities downstream of the Breakdown surface for each nozzle. Figure 6 shows the

neutral environment created by the Yaw, InLine and OutPlane nozzles. It can be seen that the gas is mostly distributed along the thruster axes with little radial diffusion. The densities are shown in planes around the satellite. These planes are all located at 1.2 m from the satellite center, except the vertical plane perpendicular to the antenna, which is positioned at 2 m from the center. Downstream of these planes, the density decays as $1/r^2$.

Figure 7 shows the neutral environment when only two Yaw nozzles are fired. This thruster configuration did occur in the actual flight at a time when current was being measured, and is therefore important for data reduction.

Yaw Thruster Impingement Study

Figures 8-9 show the Yaw thruster flowfield as computed with collisionless and collisional DSMC. Collisionless and collisional DSMC refer to DSMC computations performed with and without intermolecular collisions. Only very small differences can be observed between these two simulations, which attests to the negligible role of intermolecular collisions in plume flowfield downstream of the Breakdown surface. Impingement is visible in Figure 8, with the plume appearing to be slightly "pinched" due to the presence of the satellite surface. This asymmetry of the plume geometry, however, occurs only near the outer edge of the plume. This impingement imparts only negligible forces and moments on the satellite. The DSMC code setup parameters and performance are summarized in the Appendix.

Thruster Interaction Flowfield

Figures 10-13 show the InLine thruster flowfield as computed with Free Molecule, collisionless and collisional DSMC. The excellent agreement between Free Molecule and collisionless DSMC attests to the accuracy of both of our analytical Free Molecule model and particle tracing DSMC code. The difference between the collisionless and collisional DSMC results is a measure of the plume interaction. Without interaction, i.e. for single plume, inter-molecular collisions would have little effects on the plume structure, as shown in Ref. 2. As can be seen in Figure 13, the interaction is evident in the satellite near field, with weak shock formation near the planes of symmetry. In the far field, however, the effect of the interaction is weakening and the plume structure is close to the one obtained with Free Molecule and collisionless DSMC simulations. Finally, it can be observed that, even in the near field where the interaction is the strongest, no secondary jet is formed.

Conclusion

This paper summarizes the main results of computer simulations performed to characterize the Tethered Satellite System neutral gas environment. A first-order estimate of the neutral gas density is given for several thruster firing scenarios. These results were obtained using CFD flow simulations coupled with Free Molecule analysis. The coupling interface is the CFD-derived Breakdown surface. Results from accurate DSMC simulations are also presented to quantify the effects of plume impingement (Yaw thrusters) and multiple plume interaction (InLine thrusters).

References

1. Chang, C. L., Drobot, A., Current-Voltage Characteristics of the Tethered Satellite System, AIAA Paper 97-0583, Jan. 1997.
2. Rault D. F. G., Methodology for Thruster Plume Simulation and Impingement Effects Characterized using DSMC, AIAA Paper 95-2032, June 1995.
3. Bird, G. A., Molecular Gas Dynamics, Clarendon Press, Oxford, 1976.
4. Bird, G. A., Molecular Gas Dynamics and the Direct Simulation of Gas Flows, Clarendon Press Oxford, 1994.
5. Rault, D. F. G., Aerodynamics of Shuttle Orbiter at High Altitudes, AIAA Paper 93-2815, July 1993.
6. Bird, G. A., Application of the Direct Simulation Monte Carlo Method to the Full Shuttle Geometry, AIAA Paper 90-1962, June 1990.
7. Rault, D. F. G., Aerodynamic Characteristics of a Hypersonic Viscous Optimized Waverider at High Altitudes, AIAA Paper 92-0306, Jan. 1992.
8. Rault, D. F. G., Spacecraft Aerodynamics During Aerobraking Maneuver in Planetary Atmospheres, AIAA Paper 96-1890, June 1996.
9. Woronowicz, M. S., Rault, D. F. G., On Plume Flowfield Analysis and Simulation Techniques, AIAA Paper 94-2048, June 1994.
10. Stuart, P. Private communication.

Appendix

DSMC simulation setup and performance. The DSMC simulations were performed on two-processor SUN SPARC 10 workstations with 256 MBytes of RAM. For the InLine thruster computation, the simulation was run in a parallel environment using the Parallel Virtual Machine (PVM. See Ref. 2) software. Details of the simulation setup and performance for both the InLine thruster plume interaction analysis and Yaw impingement study are summarized in Table A1.

Table 1. Thruster Properties

Nozzle	Mass flow rate (g/s)	Thrust (Newtons)	Exit radius (mm)	Throat radius (mm)	Prandtl Meyer angle (Degrees)
InLine	1.45	1.13	4.56	0.455	53.5
InPLane	2.30	6.12	4.25	1.105	76.2
OutPLane	4.60	2.39	3.10	0.685	67.7
Yaw	0.85	0.50	4.00	0.300	50.4

Table A1. DSMC Code Setup and Performance

Test case	Yaw thruster	Inline thruster Inner domain	Inline thruster Outer domain
Grid resolution (Ref.2)			
CCG	87 × 65 × 87	64 × 64 × 124	54 × 54 × 173
FCG	5 × 5 × 5	5 × 5 × 5	5 × 5 × 5
Number of molecules	750,000	825,000	860,000
Number of cells	75,000	60,000	65,000
Time step (sec)	7.0E-7	2.5E-7	8.2E-7
RAM memory (MBytes)	50	50	50
CPU time (Hours)	50	50	40

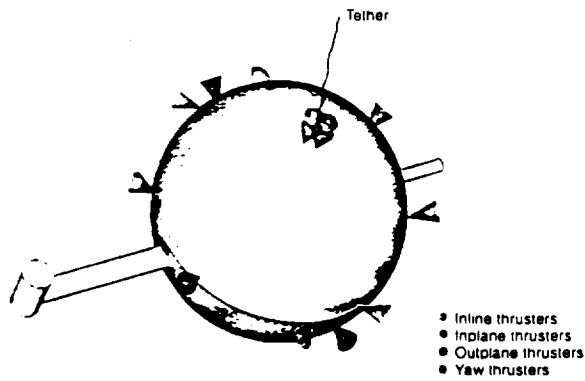


Figure 1. TSS satellite geometry and thrusters position.

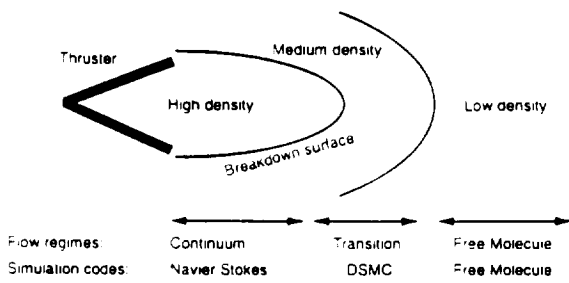


Figure 2. Flow regimes in expansion plumes.

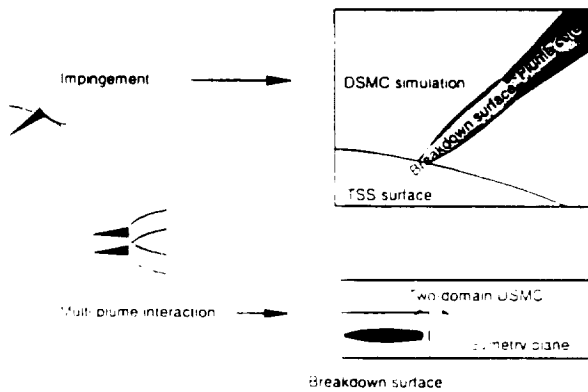


Figure 3. DSMC simulation setup for impingement and multiple interaction studies

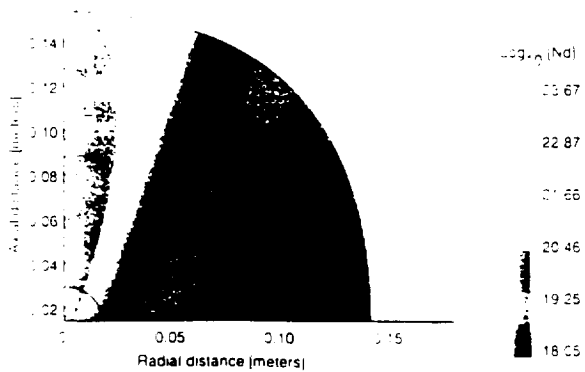


Figure 4. Continuum CFD simulation in Yaw nozzle near vicinity.

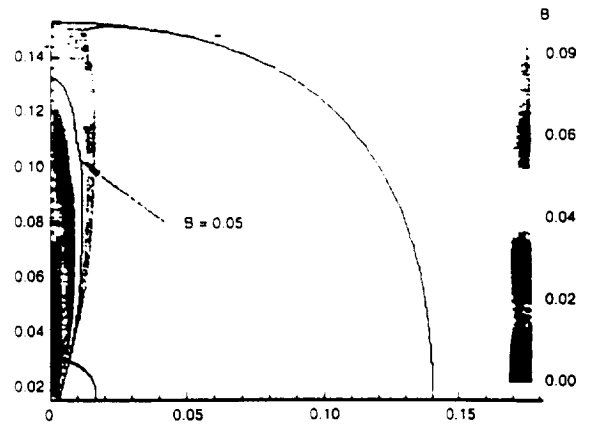


Figure 5. Breakdown parameter and breakdown surface for Yaw thruster.

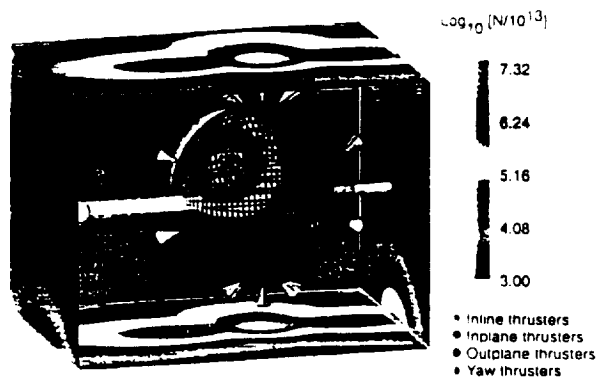


Figure 6. Neutral environment of TSS satellite with Yaw, inline and outplane thrusters.

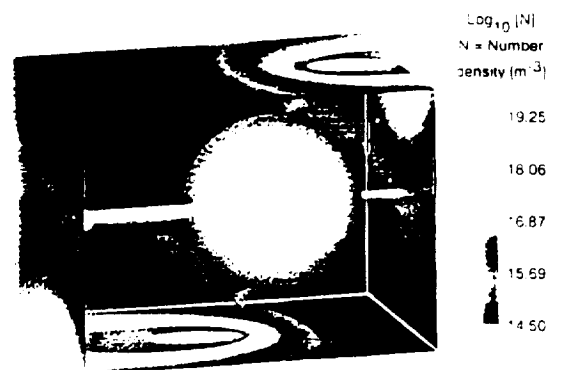


Figure 7. Neutral environment of TSS satellite with 2 Yaw thrusters.

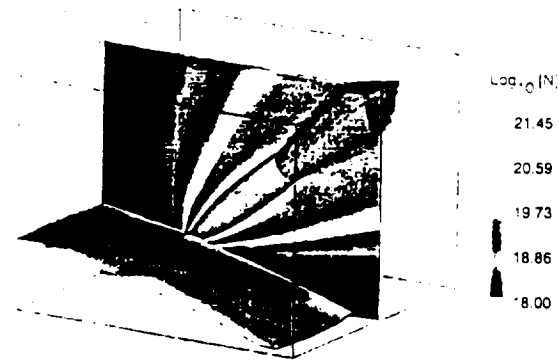


Figure 8. Yaw thruster flowfield. Collisionless DSMC simulation.

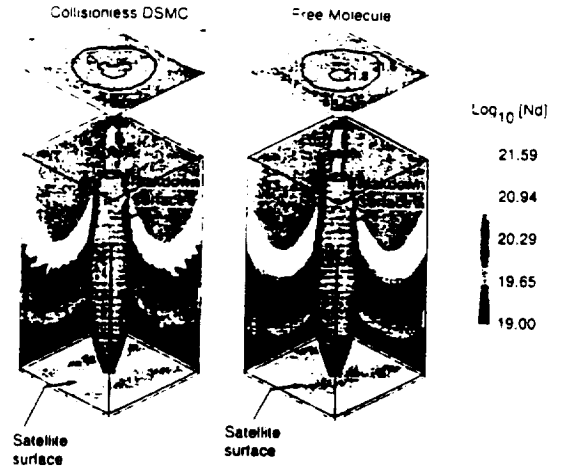


Figure 11. Inline thruster flowfield. Free Molecule and collisionless DSMC (inner domain).

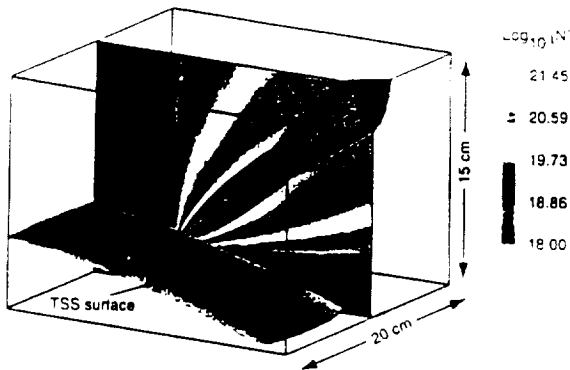


Figure 9. Yaw thruster flowfield. Collisional DSMC simulation.

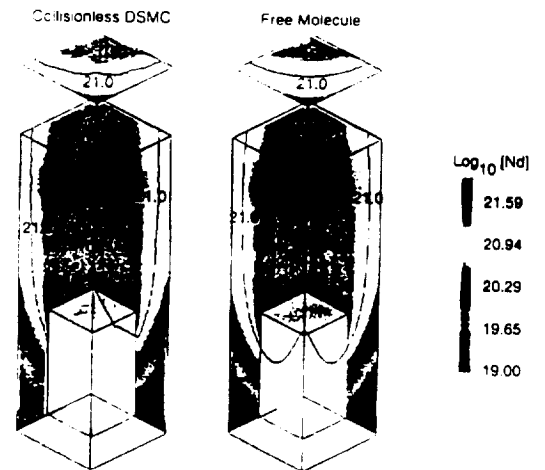


Figure 12. Inline thruster flowfield. Free Molecule and collisionless DSMC (outer domain).

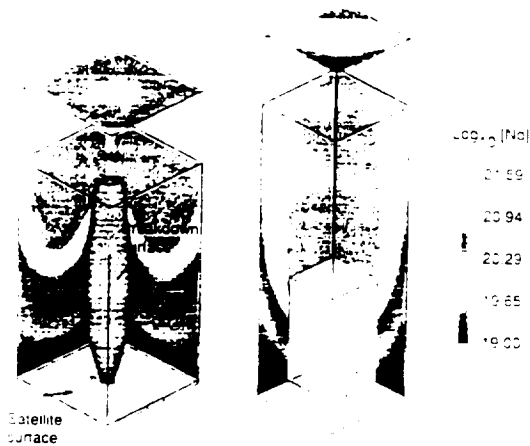


Figure 10. Inline thruster flowfield. Free Molecule simulation.

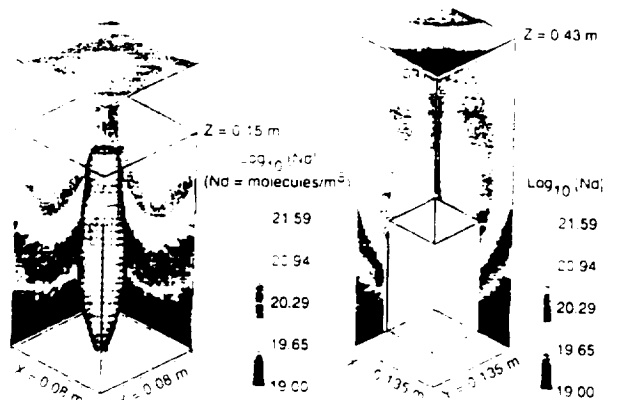


Figure 13. Inline thruster flowfield. Collisional DSMC simulation.

THE TETHERED SATELLITE MISSION SURPRISES AND PUZZLES

K. Papadopoulos*, C.L. Chang*, A.T. Drobot*,

N. Stone[†], C. Bonifazi[‡], B.E. Gilchrist[‡],

D.A. Hardy, and W.J. Burke****

*Science Applications International Corporation, 1710 Goodridge Drive,
McLean, VA 22102

[†]Space Science Laboratory, NASA/George C. Marshall SFC, Huntsville, AL
35812

[‡]ASI, viale Regina Margherita 202, 00198 Roma, Italia

[‡]The University of Michigan, 2455 Hayward Street, Ann Arbor, MI 48109-
2143

**Geophysics Directorate, Phillips Laboratory, Hanscom AFB, MA

The key objective of the Tethered Satellite System (TSS) Reflight (TSS-1R) mission was the exploration of the physical processes controlling current collected by an object charged to large positive potentials and moving at orbital speed in the dilute space magnetoplasma. The TSS was deployed upwards from the Shuttle Columbia to a distance 19.7 km and operated nominally over a period of 5.5 hours. At that point, the tether was accidentally broken. During the mission, unexpectedly large currents of up to 1.1 A, were observed. The collecting potentials measured on the satellite during the current collection were by an order of magnitude or more lower than required by the space charge limited, magnetically insulated, pre-mission models. A surprisingly large power generation efficiency was measured. Over a large current range, the observed current/voltage scaling was significantly different from the theoretical models, laboratory experiments, and space experiments at suborbital speeds. It is clear that orbital speed radically alters the physics of current collection in space plasmas. The facility used to collect large currents favors the use of tethers in space applications.

The collection of current by a charged object at high potentials in a magnetoplasma is a fundamental physics problem first addressed by Langmuir¹ in pioneering work that established plasma physics as a discipline. Laboratory experiments by Langmuir and Blodgett² established that the steady state current I flowing between two concentric spheres at a relative voltage Φ obeys the scaling law

$$I \sim \Phi^{3/2}. \quad (1)$$

This is known as the current/voltage (I/V) characteristic for space charge limited flow. In the intervening years, the physics of the current collection was studied theoretically and experimentally for unbounded plasmas of interest to space science. It was found that a spherical sheath that excludes the positive charge develops around a positively charged collecting sphere. The size of the outside surface of the sheath depends on voltage and plasma density; this surface plays a role equivalent to the emitter in Langmuir's experiments. A collection law was found, known as Beard and Johnson³(BJ) or Alpert⁴ scaling. It is given by

$$I_{BJ}/I_0 = A \Phi^{6/7} \quad (2a)$$

where A is a function of plasma density n and electron thermal speed V_e only. I_0 is the cold ionospheric current defined as

$$I_0 \equiv \pi a^2 e n V_e$$

(2b) where a is the radius of the collecting object. The BJ law given by Eqs. (2a-b) represents a theoretical upper limit of the current collection efficiency. The modification of the collection law by an ambient magnetic field B was first addressed by Parker and Murphy⁵. Parker and Murphy (PM) used conservation of angular momentum and energy, along with adiabatic invariance, to find that the upper limit of the current collection for $B > 0$ is given by

$$I_{PM}/I_0 = (1/2) [1 + (4\Phi/\Phi_0)^{1/2}] \quad (3a)$$

where Φ_0 depends only on a , and B and is given by

$$\Phi_0 = (e/2m_e) B^2 a^2. \quad (3b)$$

The PM law, represented by Eqs. (3a-b), represents space charge limited, magnetically insulated flow and is characterized by the $\Phi^{1/2}$ dependence. Over the last 30 years, laboratory experiments and rocket based space experiments have verified the laws represented by Eqs. (2) and (3) in their validity regime.

The TSS-1R mission was the first experiment to explore the physics and scaling of current collection at orbital speeds. Orbital speed is a key consideration in space applications of tethers. Pre-mission expectations were based on the steady state upper limit BJ or PM models, with minor variations due to transient effects induced by the satellite motion. As a result, the measurements of the TSS-1R mission are totally puzzling and indicate that the physics of the current collection changes radically for objects moving at orbital speeds. The purpose of this letter is to present for the first time some of the more puzzling measurements from the TSS-1R mission and briefly discuss their implications for future current collection physics and models.

The TSS mission was unique in two respects⁶. It marked the first time that the shuttle, in addition to its customary role as a launch and observation platform, was an intrinsic part of the experimental circuit (i.e., the negative pole of a "battery"). The mission was conducted as a "single experiment" with the instruments and operational procedures designed to characterize the circuit's properties. The TSS⁷ was composed of a spherical conducting satellite of radius $a=0.8$ m, connected to the shuttle by a tether with a diameter of 2.54 mm (Fig. 1). The tether consisted of a Nomex core containing 10 strands of wrapped copper wire to provide electrical contact between the shuttle and the satellite. The tether was insulated by impermeable Teflon lines, a Kevlar braid, and an outer layer of Nomex. Its total length was 22 km and its resistance at room temperature ~ 2.1 k Ω . The TSS was carried aboard the shuttle Columbia and deployed upwards to a distance of 19.7 km over a period of 5.5 hours, after which a fault in the insulation caused the tether to melt and break, separating the TSS system from the shuttle.

The orbital motion of the TSS system across the earth's geomagnetic field \mathbf{B} induced an electromotive force (emf) E across the system

$$E = (\mathbf{u} \times \mathbf{B}) \cdot \mathbf{L} \quad (4)$$

where \mathbf{u} is the orbital velocity and \mathbf{L} the length of the tether. During the 5.5 hours of operation, the emf varied from a few volts to 3.7 kV. For the upward tether configuration and the west to east orbital motion, the satellite is charged positive with respect to the plasma and the shuttle is charged negative. The collected electrons flow through the tether to the shuttle. The end of the tether at the shuttle is connected to an onboard network through a master switch. The circuit allows the tether to be isolated or connected to orbiter ground or shunted through resistors. In the results presented here, the current from the tether flows through and powers two electron guns (EGA's) with a perveance 7.2 μ pervs. The guns discharge the electrons collected at the satellite and accumulated on the shuttle, to the surrounding ionosphere⁷.

The data were collected by a larger number of sensors located on the shuttle and the satellite. Space limitations do not allow a detailed description of the comprehensive diagnostic instrumentation. We refer the reader to Ref. 7.

From the numerous scientific accomplishments of the TSS-1R mission, we have chosen to focus on the most spectacular results: those concerning current collection at orbital speeds. With the tether electrons discharged through the EGA guns, the tether circuit response is given by

$$E = \Phi_s + IR + \Phi_g + \Phi_{or} . \quad (5)$$

In Eq. (5), R is the tether resistance and Φ_s , Φ_g and Φ_{or} are the potentials between the satellite and the plasma, across the EGAs, and between the orbiter and the plasma. In our experiments, the control variable was the current I commanded by the EGA's. A pre-programmed current sequence, named IV-24, was used to study the electrical response of the circuit. The IV-24 cycle was composed of six repeating four minute current sweeps. In each sweep, the EGA's were directed to emit current pulses with an on-off duration of 2 secs. The amplitude of the commanded current pulse increased in 16 steps from zero to 500 mA. During the off periods, the appropriate instruments monitored ambient conditions. The emf was measured by the deployer voltmeter. The results shown correspond to a particular IV-24 cycle under daytime conditions. The ambient density was $8.5 \times 10^5 \text{ \#/cm}^3$ and the temperature was 1800 K. Similar features were apparent in all of the IV-24 cycles and were reproduced with high reliability.

Figure 2 shows the value of the maximum available power, defined as $P = I \times (E - \Phi_s - \Phi_{or})$, as a function of the current I . P is the difference between the maximum power $I E$ minus the power $I \times (\Phi_s + \Phi_{or})$ required to collect the current. This is an essential figure of merit for the motor and generator utility of tethers. The results are totally puzzling. The applicable PM relationship would have limited power to less than 600 W. Moreover, the power would have saturated at currents of about 260 mA. The results indicate efficiencies well above even the energetic upper limit given by BJ. Furthermore, no saturation was observed even at the maximum current of 1.1 A when P was approximately 2 KW. At this point, we should mention that while the data below 0.5 A were acquired during an IV-24 cycle, the last point, at 1.1 A, occurred immediately following the tether break. During this time, the lower terminal of the tether was not connected to the shuttle, but was directly shunted to the ionosphere. The large current drawn under this shunted configuration was totally unexpected; the underlying physics of this result is currently under study.

Figure 3 shows the Φ_s/I plot and compares it with PM and BJ. The 1.1 A current event is not included here since we could only determine the value

of $(\Phi_s + \Phi_{or})$ but not the individual potential. The results indicate that currents between 300-500 mA are collected with potentials an order of magnitude lower than predicted by PM, and by factors of two to three lower than BJ.

The final set of graphs (Fig. 4) compares the observed Φ_s/I scaling to PM and BJ. It shows the percentage deviations $(\Phi_{PM} - \Phi_s)/\Phi_s$ and $(\Phi_{BJ} - \Phi_s)/\Phi_s$ as a function of I . It is clear that within the 0.5 A range of measurements, the scaling is inconsistent with the isotropic collection expected from BJ, even as modified by Linson⁸. On the other hand, the observed scaling seems to converge towards PM for $I > 300$ mA. However, a different coefficient of proportionality is required because collection at orbital speeds caused a large deviation from the PM law.

In summary, we have presented the first experimental results on current collection in space plasmas at orbital speeds. The results indicate that a new physics regime with beneficial properties for tether applications in space emerges at orbital speeds. The effect of the orbital speed on the physics can be best seen from a reference frame moving with the satellite. In this frame, the ambient O^+ ions appear as an energetic 5 eV beam that exerts a ram pressure on the sheath. At low potentials, the ram pressure does not permit the formation of a stable sheath. Thus current collection becomes essentially orbit limited. At higher potentials, when the sheath pressure exceeds the ram pressure exerted by the ions, ion reflection ahead of the satellite provides a significant free energy source to modify the plasma conditions and allow for collection of larger current. These are some of the theoretical undertakings currently being pursued by the TSS-1R team.

- [1] Langmuir, I., Phys. Rev. **21**, p. 419 (1923).
- [2] Langmuir, I. and K.B. Blodgett, Phys. Rev. **24**, p. 49 (1924).
- [3] Beard, D.B. and F.S. Johnson, J. Geophys. Res. **66**, p. 4113 (1961).
- [4] Alpert, Y.L., A.V. Girevoch, L.P. Pitaevskii, in "Space Physics with Artificial Satellites," p. 186, Consult. Bur., New York, (1965).
- [5] Parker, L.W. and B.L. Murphy, J. Geophys. Res. **72**, p. 2368 (1969).
- [6] Papadopoulos, K., A.T. Drobot, and N. Stone, EOS, **73**, No. 30, p. 321, July 28 (1992).
- [7] Special TSS-1 issue edited by M. Dobrowolny, IL Nuovo Cimento, **17c**, N1, P. 13-47 (1994).
- [8] Linson, L.M., J. Geophys. Res., **74**, p. 2368 (1969).



Figure 1. Left panel: The artist drawing of the Tethered Satellite System (TSS) in space.
Right panel: The different layers of tether are shown in this photograph.

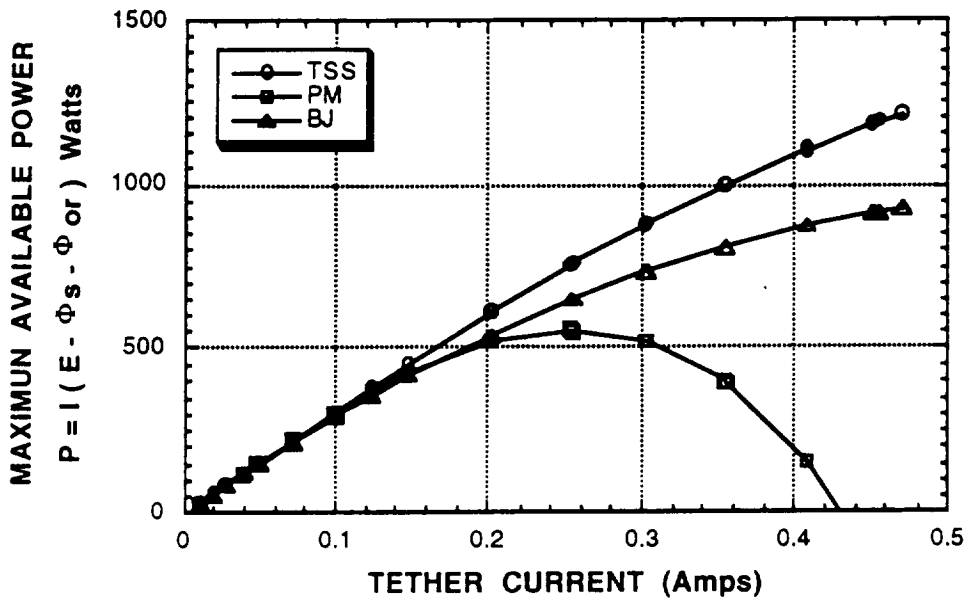


Figure 2. Maximum available power from the TSS mission in contrast to the results from the PM and BJ models.

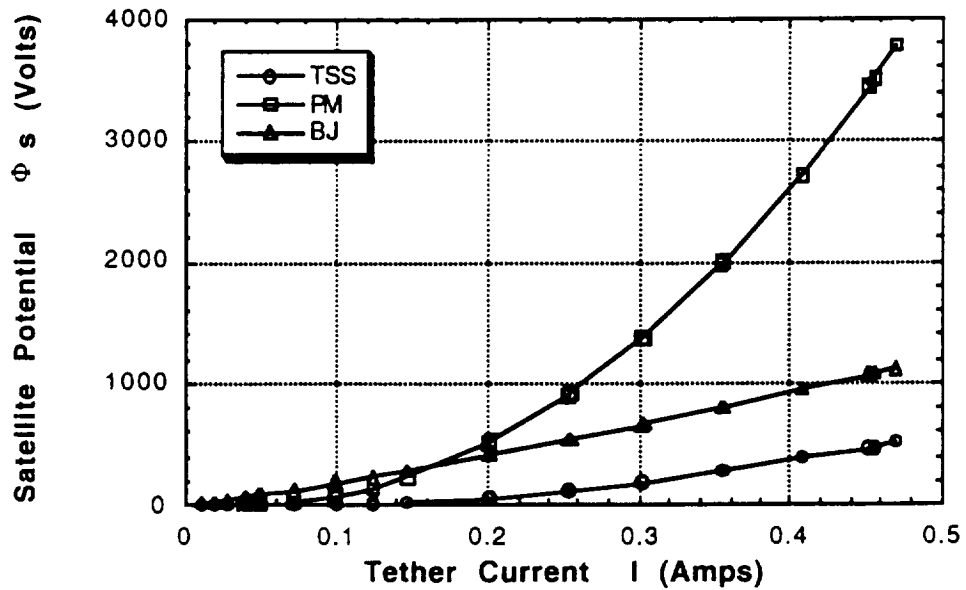


Figure 3. Potential versus current curves from TSS mission, PM and BJ models.

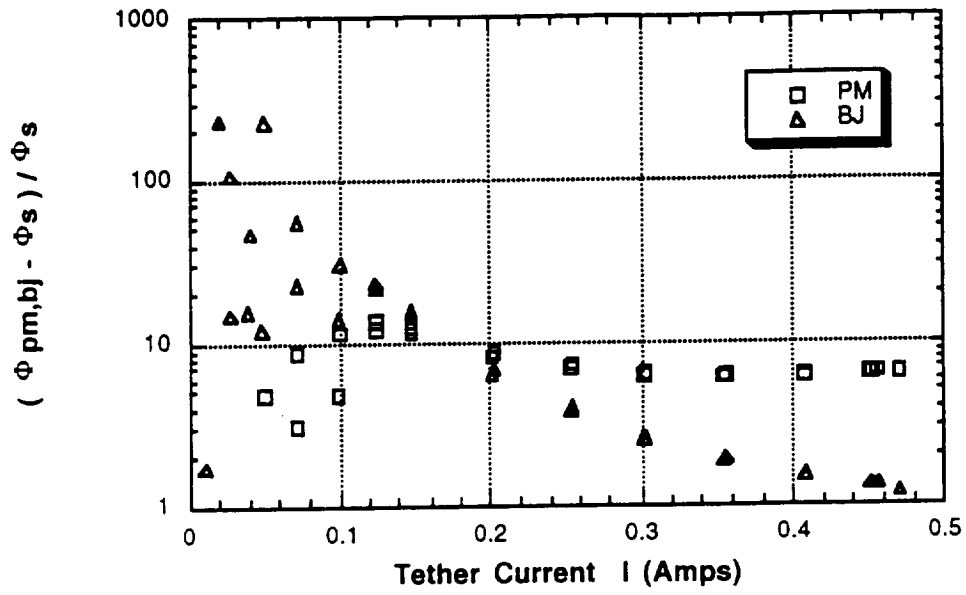


Figure 4. Comparison between the TSS Φ/I scaling and those of the PM and the BJ models.

APPENDIX 14

Current-Voltage characteristics of the tethered satellite system: Measurements and uncertainties due to temperature variations

C.L. Chang,¹ A.T. Drobot,¹ K. Papadopoulos,¹ K.H. Wright,² N.H. Stone,³
C. Gurgiolo,⁴ J.D. Winningham,⁵ and C. Bonifazi⁶

Abstract. One of the primary goals of the Tethered Satellite System reflight mission (TSS-1R) is to determine the current-voltage characteristics of the TSS satellite orbiting in the ionosphere. While the collected current was measured directly with high reliability, the satellite potential could only be deduced from a circuit model or from interpretation of measurement data below satellite potentials of 500 Volts. The greatest uncertainty in the circuit model is the value of tether resistance R . We have provided quantitative calibration of the resistance based on instrument data for $V_s < 100$ Volts. We have reached the important conclusion that the R value in the TSS circuit model is correlated to temperature changes associated with the diurnal cycles along the TSS flight path. We have also applied the calibrated R value in the TSS circuit equation to construct the I-V curves that extend to high voltages. The resulting I-V characteristics are presented with error bounds on satellite potential to indicate the uncertainty associated with the tether resistance determination. The I-V relation exhibits different scalings in the high (> 100 Volts) and low (< 10 Volts) voltage regimes, which indicates a fundamental transition for the current collection physics in the ionospheric plasma surrounding the satellite.

I-V Measurement of the TSS Satellite

A major objective of the TSS-1R mission was to determine the current-voltage (I-V) characteristics of the tethered satellite moving at the orbital velocity of the Low Earth Orbit (LEO) [Stone and Bonifazi, 1997]. The I-V characteristic was determined by a pre-programmed TSS science operation called the IV-24 operating cycle. During the IV-24 cycle, a current sequence was performed by stepping the command current delivered by the Electron Generator Assemblies (EGAs) in the payload bay of the Orbiter, thus modifying the satellite potential. A complete IV-24 cycle contains six repeating current sequences with each sequence lasting four minutes [Dobrowolny and Stone, 1994]. During the TSS-1R mission, three IV-24 cycles were completed. The first IV-24 cycle lasted from 056/23:20:30 to 056/23:44:30 UT in a day orbit. The second IV-24 cycle lasted from 057/00:12:00 to 057/00:36:00 UT in the subsequent night orbit. The last IV-24 cycle lasted from 057/01:06:00 to 057/01:30:00 UT in a day orbit.

During each of the command current pulses, the actual current flowing through the tether is measured directly by the Tether Current and Voltage Monitor (TCVM) of the Shuttle Electrodynamic Tether System (SETS) investigation [Aenero *et al.*, 1994] and by the Satellite Ammeter (SA) of the Satellite Core Equipment (SCORE) investigation [Bonifazi *et al.*, 1994]. The satellite voltage V_s , defined by the potential difference between the satellite and the ionospheric plasma, can be deduced from the boom-mounted sensor package (BMSP) operated by the Research

on Orbital Plasma Electrodynamics (ROPE) investigation [Stone *et al.*, 1994]. The BMSP records the current collected by the instruments located on the fixed boom (1 m in length) of the satellite. It is electrically isolated from the satellite and its potential is powered by the Floating Supply (FS), which links the BMSP to the satellite through a 700 K Ω resistance. The FS can bias the BMSP in the range of 0 to -500 Volts relative to the satellite in incremental voltage steps of 0.122 Volts. For satellite potentials up to 500 Volts, the FS is automatically adjusted to minimize the current collected by the BMSP, thus maintaining its potential near the local plasma potential. The potential adjustment made by FS to keep the BMSP at floating potential can be interpreted as the satellite potential, V_s , subject to a number of caveats regarding the electron distribution function. Operationally, the determination of satellite potential V_s is accomplished by a seek and track routine. In the seek mode, the FS bias voltage is adjusted in steps until the current collected by the BMSP approaches zero. Following the seek mode, the track routine is activated. Under this condition the FS bias voltage is fine-tuned continuously to keep the BMSP current around zero. The satellite potential relative to the ionospheric plasma is determined when the FS bias potential reaches a plateau. To ensure accurate readings of V_s , we took into account two practical considerations. First, the FS potential correction corresponds to the actual satellite potential provided that the BMSP is situated outside the sheath surrounding the satellite. Second, for large potentials the FS cannot step the bias potential fast enough to reach a plateau within the two seconds time period of the current pulse. Both of these considerations can be satisfied at low satellite potential. Therefore, we restrict ourselves to the V_s measurements in the range of 1 Volt $< V_s < 100$ Volts. The lower bound of V_s is set to be 1 Volt to ensure sufficient instrument sensitivity.

We took a two-step approach to construct the I-V curves for the entire range of the satellite potential. The first step is to calibrate the tether resistance R using the BMSP data of 1 Volt $< V_s < 100$ Volts. The second step is to compute V_s based on the calibrated R value and to impose error bounds based on the uncertainties associated with the statistical measurements. Both steps use the equivalent TSS circuit as shown in Figure 1. In this figure, V_s and V_0 represent the potential drops across the plasma sheaths surrounding the satellite and the Orbiter. Correspondingly, V_g is the potential drop between the cathodes of the electron accelerators and the Orbiter body; I is the tether current and R is the overall dc resistance of the tether wire, which is approximately 2.1 K Ω at room temperature. Taking the motional induced EMF generated by a moving TSS-Orbiter system to be V_e , the TSS circuit equation can be expressed as

$$V_e = V_s + IR + V_g + V_0 \quad (1)$$

To perform calibration in the first step, the tether resistance R is determined by substituting V_s and other directly measured quantities such as I , V_e , V_g , and V_0 into Eq. (1). In the second step, a reverse process is taken, namely, using mean values of R and standard deviation ΔR in (1) to obtain V_s as a function of I .

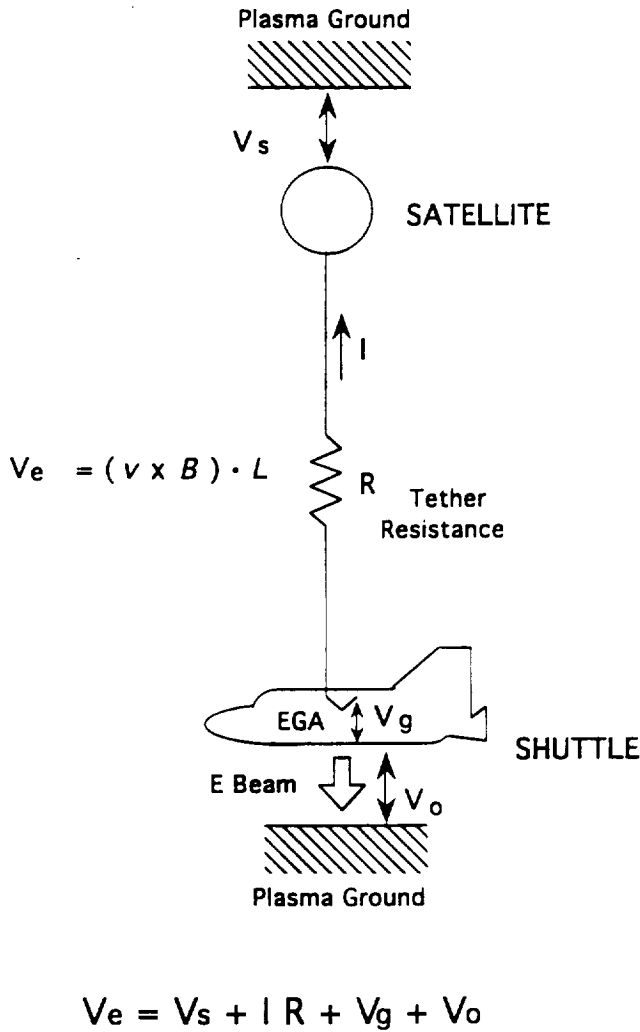


Figure 1. Schematic layout of the equivalent TSS circuit that corresponds to equation (1).

Temperature Dependent Tether Resistance

Direct measurements of various potential terms in (1) were performed by instruments onboard the Orbiter and the satellite during the TSS-1R mission. For instance, the V_g was measured by the voltmeter of the Deployer Core Equipment (DCORE-DV) [Bonifazi et al., 1994] and by the Tether Current and Voltage Monitor (TCVM) of the Shuttle Electrodynamic Tether System (SETS) [Aguero et al., 1994, Thompson et al., 1997]. The V_e was measured by the TCVM and the DCORE-DV in between the current pulses when the EGAs were off and the current $I=0$. The Shuttle potential V_o , although not directly measured, was inferred from the Electrostatic Analyzers (ESAs) of the Shuttle Potential and Return Electron Experiment (SPREE) [Oberhardt et al., 1994; Burke et al., 1997] located in the payload bay, which recorded the energy spectrum of the ions returning to the Shuttle. With the TSS satellite deployed vertically upward, the EMF induced by eastward motion of the Orbiter in a southward Earth's magnetic field $(\mathbf{v} \times \mathbf{B}) \cdot \mathbf{L}$ as shown in Fig. 1) results in a positively charged satellite, thus enabling it to collect electrons from ambient plasma. Take the last data point in the last stepping sequence of the third IV-24 cycle as an example (see Fig. 4). With Orbiter traveling at ~ 7.8 km/s, tether length of ~ 19.5 km, and the magnetic strength of ~ 0.4 gauss, the measured potentials distributed in the TSS circuit are: $V_e = 3479.7$ Volts,

$V_g = 1866.3$ Volts, and $V_o < 10$ Volts. The measured tether current is $I = 0.375$ Amperes. Using a mean tether resistance of 1821.4Ω calculated specifically for this IV sequence, the satellite potential would be $V_s = 930.4$ Volts.

Each current pulse in the IV-24 cycle provides a set of values for I , V_g , V_o , and V_e . Using the V_s dataset obtained from the ROPE measurements, we can calculate the tether resistance R directly from (1). Figure 2 shows the R values for the first, second, and third IV-24 cycles as represented by the solid circle, square, and rhombic data points, correspondingly. Each data point is associated with a current pulse that gives rise to a satellite potential in the range of $1 \text{ Volt} < V_s < 100 \text{ Volts}$. Adjacent data points are linked by a straight line. From this figure, we can see that for a given IV-24 cycle, the tether resistance data points form a distribution, which can be quantified statistically by a standard deviation around a mean value. Table 1 shows the mean and the standard deviation of the tether resistance (in Ω) averaged over each IV-24 cycle:

This table reveals an interesting fact: the mean tether resistance varies from cycle to cycle. Its value reaches the highest level in the first IV-24, then drops to the lowest level in the second IV-24 and, and finally settles at an intermediate value in the third IV-24. This variation is obviously correlated with the diurnal pattern of the three cycles. It is therefore logical to attribute the tether resistance variations to the temperature changes in the tether, which are directly influenced by exposure to sunlight. Since there is no direct temperature measurement of the tether, we look for variations in the temperature data taken by sensors attached to the skin of the satellite as corroborative evidence. Figure 3 displays temperature data (in $^{\circ}\text{C}$) versus time from 16 sensors, which are part of the satellite thermal control system, located at various places on the surface of the satellite. The IV-24 periods are highlighted with heavy lines beneath the time axis. From this figure, we can see small periodic oscillations on the temperature curves at a period of roughly 4 minutes. These oscillations correspond to satellite spin at a rate of 0.25 rpm [Stone and Bonifazi, 1997]. A major temperature decline occurs at around 057:00:00 UT, which is the time the TSS enters the night orbit. From the first IV-24 to the second IV-24, the temperature decrease recorded by these sensors ranges from 10°C to 50°C , depending on where the sensor is located. Likewise, from the second IV-24 to the third IV-24, the temperature increases by similar amounts.

We can independently verify the temperature change based on the variation of mean resistance. The analytic temperature-

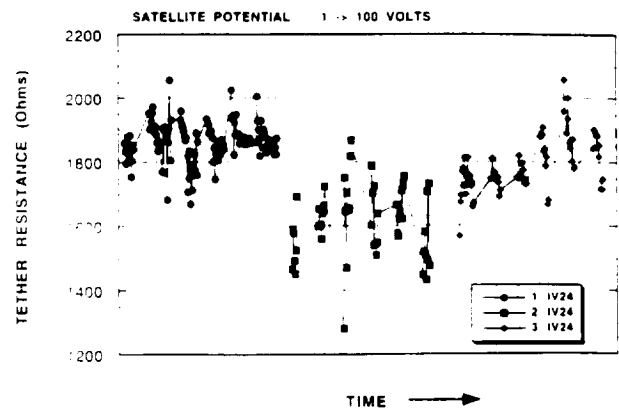


Figure 2. Tether resistance values derived from equation (1) based on ROPE measured $V_s (< 100 \text{ Volts})$. Solid dots, squares, and rhombus are data points from the first, the second, and the third IV-24 cycle, respectively.

Table 1. Tether resistance calibration for the three IV-24 cycles

IV-24 Cycle	Orbit	Time (UT)	Mean Resistance	Standard Deviation
1st	Day	056/23:20:30 - /23:44:30	1864.2 Ω	60.2 Ω
2nd	Night	057/00:12:00 - /00:36:00	1610.0 Ω	109.5 Ω
3rd	Day	057/01:06:00 - /01:30:00	1788.4 Ω	84.3 Ω

resistance formula for copper is given in the Handbook of Chemistry and Physics [1980]

$$R = R_0 [1 + \Theta (T - T_0)] \quad (2)$$

where $T_0 = 20^\circ\text{C}$, $R_0 = 2.0 \text{ K}\Omega$, and $\Theta = 0.00393 / ^\circ\text{C}$. This formula relates the change of resistance to the change of temperature as

$$\Delta R = R_0 \Theta \Delta T \quad (3)$$

Using the changes of mean resistance ΔR_1 (from 1st to 2nd IV-24) and ΔR_2 (from 2nd to 3rd IV-24) in Eq. (3), we can estimate the temperature change to be $\Delta T_1 = - 32^\circ\text{C}$ and $\Delta T_2 = + 23^\circ\text{C}$. These numbers are in line with the temperature changes shown in Fig. 3. It is interesting to point out another feature that indicates temperature dependent resistance change of the TSS system. In Fig. 2, data points of the last IV-24 cycle show a slanted distribution in contrast to the first two cycles. This implies that the tether resistance increases with time during the last cycle. In Fig. 3, the satellite temperature measurements made at the last IV-24 show a similar trend of increase in time. This provides added evidence that the tether resistance is indeed sensitive to the temperature change.

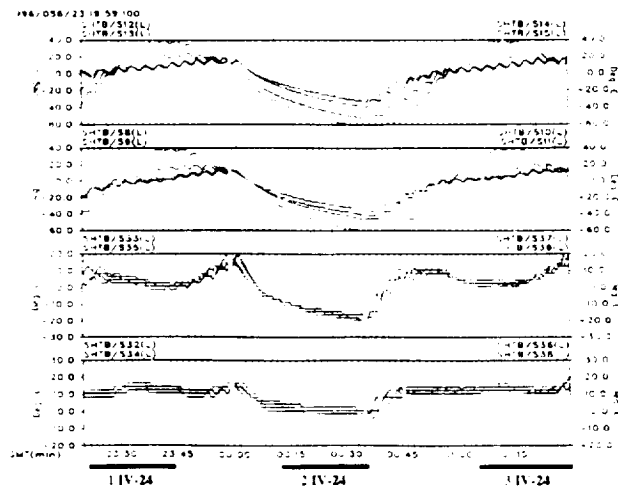


Figure 3. Temperature data from 16 sensors located on the satellite surface are plotted as functions of time. Dark broad lines below the time axis indicate the periods of three IV-24 cycles.

I-V Characteristics of the TSS Satellite

Using the calibrated tether resistance in Table 1, we can construct the entire I-V curve from Eq. (1). However, since the tether resistance varies with time during the TSS-1R mission, and can only be determined with some uncertainty, it is appropriate to impose error bounds on the I-V characteristics to indicate its limits. As an example, in Fig. 4 we plot the I-V curve obtained from the last stepping sequence of the third IV-24 cycle. This IV-24 cycle was performed during daytime, at high ambient plasma density ($\sim 8.2 \times 10^{25} / \text{c.c.}$ from real-time SUNDIAL model) [Szuszczewicz et al., 1996], and with the tether near its full extension. In this figure, the tether current I for the entire current pulse sequence is plotted against the satellite potential, which is calculated from (1) based on the directly measured V_e and V_g from DCORE. Each current pulse contributes two data points, as shown by solid dots, and adjacent data points are connected by a straight line. The error bounds are imposed on voltage as horizontal bars because of the uncertainty on the measured tether resistance value. The actual length of the error bar is calculated by multiplying the tether current I with the standard deviation ΔR . As comparison, the Parker-Murphy I-V points obtained from the formula [Parker and Murphy, 1967]

$$(I / I^*) = 1 + 2 (V_s / V^*)^{1/2} \quad (4)$$

are also plotted in this figure (represented by squares), where $V^* = 114 \text{ Volts}$ for TSS and I^* is the ambient thermal current collected by the resting satellite with no potential ($I = I^* \text{ as } V_s = 0$). In calculating I^* , the along-track TSS-1R electron density and temperature obtained by Szuszczewicz et al. [1997] are used. It is interesting to see that the TSS I-V curve exhibits distinctly different scaling properties at low and high voltages. At high voltage ($V_s > 50 \text{ Volts}$), the TSS I-V scaling seems to follow that of the Parker-Murphy model (i.e. $I \sim V^{1/2}$) as pointed out in a companion paper by Thompson et al. [1997]. At low voltage ($V_s < 10 \text{ Volts}$), the TSS I-V curve deviates from the $V^{1/2}$ scaling, implying a shift in the physical processes involved in the current collection. Such distinct transition is typical in all of the third IV-24 sequences that involve high satellite potentials. It is also consistent with the observations that the ram ions are reflected when the satellite potential exceeds 5 Volts, which may cause significant modification on the plasma conditions surrounding the satellite at the transition [Wright et al., 1997; Winningham et al., 1997]. The possibility of a foreshock region upstream of the satellite created by the reflected ram ions which causes intense electron heating are currently being studied by the TSS-1R team [Papadopoulos et al., 1997].

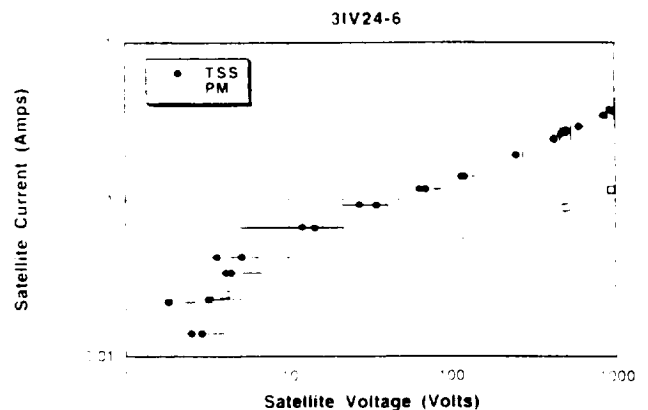


Figure 4. Typical I-V characteristics at high plasma density at the last stepping sequence of the 3rd IV-24 cycle. Error bars on satellite potential are due to the uncertainties of the resistance measurement.

Summary

We conducted a detailed calibration of the tether resistance by using the satellite potential measurements performed by the ROPE investigation in the TSS-1R mission. An important finding is that the tether resistance varies along the TSS orbit, as shown by Table 1. This variation correlates closely with the temperature changes of the TSS system. In addition, the tether resistance can only be determined with uncertainty. The uncertainty on tether resistance is reflected in the I-V characteristics of the TSS satellite because the resistance is an integrated part of the tether circuit. We constructed the I-V characteristics and imposed error bounds on the voltage value. The I-V curve exhibits distinctly different scalings at low (< 10 Volts) and high voltage regimes, which suggests fundamental changes in the physics and/or plasma conditions directly contributing to the current collection by the TSS satellite in the F region of the ionosphere.

Acknowledgment. This work was supported by NASA under contract NAS8-36811 and by ESA. We would like to acknowledge the contributions from the entire science team in the TSS-1R mission. We would also like to thank the crew members onboard STS-75 Drs. J. A. Hoffman, F. R. Chang-Diaz, C. Nicollier, U. Guidoni, M. Cheli, Lt. Col. S. J. Horowitz, and Lt. Col. A. M. Allen for their dedication to the mission and for their participation in performing the science investigations.

References

- Aguero, V., P.M. Banks, B. Gilchrist, I. Linscott, W.J. Raitt, D. Thompson, V. Tolat, A.B. White, S. Williams, and P.R. Williamson, The Shuttle Electrodynamic Tether System (SETS) on TSS-1, *IL Nuovo Cimento*, 17, 49, 1994.
- Bonifazi, C., F. Svelto, and J. Sabbagh, TSS Core Equipment. I - Electrodynamic Package and Rationale for System Electrodynamic Analysis, *IL Nuovo Cimento*, 17, 13, 1994.
- Burke, W.J., C. Bonifazi, D.A. Hardy, J.S. Machuzak, L.C. Gentile, D.G. Olson, C.Y. Huang, B.E. Gilchrist, J.-P. Lebreton, and C.A. Gurgiolo, Shuttle Charging during EGA Beam Emissions of TSS-1R, *Geophys. Rev. Lett.*, this issue, 1997.
- Dobrowolny, M., and N.H. Stone, A Technical Overview of the TSS-1 - the First Tethered-Satellite System Mission, *IL Nuovo Cimento*, 17, 1, 1994.
- Handbook of Chemistry and Physics, Properties of Metals as Conductors, ERS, 60th Ed., (1980).
- Oberhardt, M.R., D.A. Hardy, W.E. Slutter, J.O. McGarity, D.J. Sperry, A.W. Everest III, A.C. Huber, J.A. Pantazis, and M.P. Gough, The Shuttle Potential and Return Electron Experiment (SPREE), *IL Nuovo Cimento*, 17, 67, 1994.
- Papadopoulos, K., C.L. Chang, and A.T. Drobot, Ion Reflection by the TSS-1R Satellite, *Geophys. Res. Lett.*, this issue, 1997.
- Parker, L.W., and B.L. Murphy, Potential Buildup on an Electron-Emitting Ionospheric Satellite, *J. Geophys. Res.*, 72, 1631, 1967.
- Stone, N.H., K.H. Wright Jr., J.D. Winningham, J. Biard, and C. Gurgiolo, A Technical Description of the TSS-1 ROPE Investigation, *IL Nuovo Cimento*, 17, 85, 1994.
- Stone, N.H., and C. Bonifazi, The TSS-1R Mission: Overview and Scientific Context, *Geophys. Res. Lett.*, this issue, 1997.
- Szuszczewicz, E. P., P. E. Blanchard, P. Wilkinson, G. Crowley, T. Fuller-Rowell, P. Richards, M. Abdu, T. Bullett, R. Hanbaba, J.P. Lebreton, M. Lester, M. Lockwood, G. Millward, M. Wild, S. Pulinetz, B.M. Reddy, I. Stanislawski, G. Vannaroni, and B. Zolesi, The First Real-Time Worldwide Ionospheric Predictions Network: TSS-1R Support Operations, *Geophys. Res. Lett.*, this issue, 1997.
- Thompson, D.C., C. Bonifazi, B.E. Gilchrist, S.D. Williams, W.J. Raitt, J.-P. Lebreton, and W.J. Burke, The Current-Voltage Characteristics of a Large Probe in Low Earth Orbit: TSS-1R Results, *Geophys. Res. Lett.*, this issue, 1997.
- Wright, K.H. Jr., N.H. Stone, J. Sorensen, J.D. Winningham, and C. Gurgiolo, Observations of Reflected Ions and Plasma Turbulence for Satellite Potentials Greater than the Ion Ram Energy, *Geophys. Res. Lett.*, this issue, 1997.
- Winningham, J.D., N.H. Stone, C.A. Gurgiolo, K.H. Wright, R.A. Frahm, and C.A. Bonifazi, Suprathermal Electrons Observed on the TSS-1R Satellite, *Geophys. Res. Lett.*, this issue, 1997.
- C.L. Chang, A.T. Drobot, and K. Papadopoulos, Applied Physics Operation, Science Applications International Corporation, McLean, Virginia, 22102.
- K.H. Wright, CSPAR, University of Alabama in Huntsville, Huntsville, Alabama 35899.
- N.H. Stone, Space Science Laboratory, NASA/Marshall Space Flight Center, Huntsville, Alabama, 35812.
- C. Gurgiolo, Bitterroot Basic Research Inc., Hamilton, Montana, 59840.
- J.D. Winningham, Space Instrument Division, Southwest Research Institute, San Antonio, Texas 78228.
- C. Bonifazi, Agenzia Spaziale Italiana, Rome, Italy.

Received: January 14, 1997; Revised: September 26, 1997; Accepted: October 15, 1997.

APPENDIX 15

The First Realtime Worldwide Ionospheric Predictions Network: An Advance in Support of Spaceborne Experimentation, On-Line Model Validation, and Space Weather

E.P. Szuszczewicz¹, P. Blanchard¹, P. Wilkinson², G. Crowley³, T. Fuller-Rowell⁴,
P. Richards⁵, M. Abdu⁶, T. Bullett⁷, R. Hanbaba⁸, J. P. Lebreton⁹, M. Lester¹⁰,
M. Lockwood¹¹, G. Millward⁴, M. Wild¹⁰, S. Pulinets¹², B.M. Reddy¹³, I.
Stanislawska¹⁴, G. Vannaroni¹⁵, and B. Zolesi¹⁶

Abstract. We report on the first realtime ionospheric predictions network and its capabilities to ingest a global database and forecast F-layer characteristics and "in situ" electron densities along the track of an orbiting spacecraft. A global network of ionosonde stations reported around-the-clock observations of F-region heights and densities, and an on-line library of models provided forecasting capabilities. Each model was tested against the incoming data: relative accuracies were intercompared to determine the best overall fit to the prevailing conditions; and the best-fit model was used to predict ionospheric conditions on an orbit-to-orbit basis for the 12-hour period following a twice-daily model test and validation procedure. It was found that the best-fit model often provided averaged (i.e., climatologically-based) accuracies better than 5% in predicting the heights and critical frequencies of the F-region peaks in the latitudinal domain of the TSS-1R flight path. There was a sharp contrast, however, in model-measurement comparisons involving predictions of actual, unaveraged, along-track densities at the 295 km orbital altitude of TSS-1R. In this case, extrema in the first-principle models varied by as much as an order of magnitude in density predictions, and the best-fit models were found to disagree with the "in situ" observations of N_e by as much as 140%. The discrepancies are interpreted as a manifestation of difficulties in accurately and self-consistently modeling the external controls of solar and magnetospheric inputs and the spatial and temporal variabilities in electric fields, thermospheric winds, plasmaspheric fluxes, and chemistry.

¹Science Applications International Corporation, McLean, Virginia

²IPS Radio & Space Services, West Chatswood, Australia

³Southwest Research Institute, San Antonio, Texas

⁴National Oceanic and Atmospheric Administration, Boulder, Colorado

⁵University of Alabama, Huntsville, Alabama

⁶Instituto Nacional de Pesquisas Espaciais, Sao Paulo, Brazil

⁷Phillips Lab, Hanscom AFB, Massachusetts

⁸France Telecom/CNET, Lannion, France

⁹Space Science Department, ESA/ESTEC, Noordwijk, The Netherlands

¹⁰University of Leicester, Leicester, United Kingdom

¹¹Rutherford Appleton Lab, Oxon, United Kingdom

¹²IZMIRAN, Moscow Region, Russia

¹³National Geophysical Research Institute, Hyderabad, India

¹⁴Space Research Center, Warsaw, Poland

¹⁵Instituto di Fisica Dello Spazio Interplanetario, Frascati, Italy

¹⁶Instituto Nazionale di Geofisica, Italy

1. Introduction

Intelligent operations of many of today's near-Earth space experiments and the effective utilization of space-based technology assets are looking more and more to accurate and timely forecasting of the Earth's space environment. Such a capability is seen to be critical to enhancing scientific productivity during interactive on-orbit experimentation as well as to the mitigation of, or protection from, space environmental effects on man-made systems.

Realtime monitoring and prediction are also becoming increasingly important for effective and efficient execution of large system science programs like those in NASA's International Solar-Terrestrial Physics program (e.g. Berchem et al., 1995) and the National Space Weather Initiative (e.g., Szuszczewicz, 1995). These programs involve large databases with inputs from an array of ground-based and spaceborne sensors, and more often than not, employ a suite of large computational codes used in the planning, execution, and analysis of campaign investigations.

The SUNDIAL/TSS-1R activity reported here (see, e.g., Szuszczewicz et al., 1996, Dobrowolny and Stone, 1994; and Stone and Bonifazi, 1997 (this issue)) was the first demonstrated worldwide effort to meet this need. The effort focused on supporting TSS-1R objectives which dealt with the conduct and analysis of experiments exploring plasma processes and related technologies that control current generation and current closure in space, on-orbit power generation techniques, and associated manifestations in current-voltage characteristics and spacecraft charging. In meeting these objectives the primary geophysical parameter was the ionospheric electron density acting through its first-order control of conductivities and plasma sheaths.

While functional objectives and an on-orbit time-line are established well in advance of any mission, an optimized experiment scenario dictates realtime or near-realtime access and analysis of on-board data (e.g., spacecraft potentials, current-voltage characteristics, etc.), with subsequent interpretations possibly leading to the need for a repeat of certain functional objectives under identical, different, or more ideal conditions. This generated the need for a realtime worldwide ionospheric monitoring network and a capability to predict along-track plasma densities on time scales ranging from orbit-to-orbit to a full 24 hr period. We describe the network, the data ingestion procedures, prediction methodologies, and initial results on prediction accuracies.

2. Orbit Logistics, the Worldwide Monitoring Network, and the Prediction Methodology

TSS-1R was launched on February 22, 1996 (UT day/hr:min = 53/20:18) into a 28.5° inclination orbit at an altitude of 295 km. With the height of the F₂-region peak-density generally varying between 200 and 600 km, TSS-1R experiments were expected to operate in plasma density environments generally less than $4(10)^6$ cm⁻³ but greater than $(10)^4$ cm⁻³, with the orbiter and the tethered subsatellite operating variously at, above, or below the F₂-region peak.

Since the worldwide monitoring of plasma densities at 295 km is technically not feasible (this statement is true for any fixed altitude), the monitoring and predictions approach employed in this application was built upon a combination of internationally-recognized models and a globally-distributed network of ionosondes for around-the-clock measurements of F-region characteristics. The ionosonde database provided a nowcasting capability and the framework for benchmarking model accuracies, establishing optimal fits to prevailing conditions, and subsequent forecasting by the model run best matching the realtime data. The accuracy of the optimized model fit to the global ionosonde measurements of N_mF₂ and h_mF₂ was assumed to provide a measure of confidence that

model values of electron densities at the TSS-1R altitude were of comparable accuracy.

There were 33 ionosonde stations employed in support of TSS-1R, a subset of the 50-70 stations typically engaged in worldwide SUNDIAL campaigns (e.g., Szuszczewicz et al., 1996; and references therein). The reduced number reflected a conservative approach to the operation of a first realtime data ingestion procedure and an on-the-fly requirement for model optimization. The procedure was as follows:

1) Every 12 hours each of the 33 stations transmitted an up-to-the-hour set of data via Internet to the SUNDIAL Ionospheric Weather Station in the TSS-1R Science Operations Center. The data provided hourly values of f_oF_2 and $M(3000)F_2$ for that 12-hour period. $M(3000)F_2$ yielded values of h_mF_2 in accordance with the procedures of Dudeney [1983] and the critical frequency of the F_2 -peak, f_oF_2 , provided a measurement of N_mF_2 through the relationship f_oF_2 (Hz) = $8.9(10^3) \sqrt{N_mF_2}$ (cm^{-3}). (Most of the 33 stations could transmit data on a more frequent basis, e.g. hourly (or fractions thereof) if dictated by future mission requirements.)

2) The database was then compared with an on-line library of model runs that included: a) the International Reference Ionosphere, IRI (Schunk and Szuszczewicz, 1988, and references therein), b) the Field-Line Interhemispheric Plasma model, FLIP (Richards et al., 1994; and references therein), c) the Coupled Thermospheric Ionospheric Plasmasphere model, CTIP (Fuller-Rowell et al. 1996; and references therein), and d) the Thermosphere Ionosphere Electrodynamics General Circulation Model, TIEGCM (Richmond et al., 1992; and references therein). Multiple on-line runs of FLIP and TIEGCM, expected to bracket ranges of solar fluxes and geomagnetic conditions predicted by the NOAA Space Environment Center ($70 \leq 10.7 \text{ cm flux} \leq 76$, $5 \leq A_p \leq 10$, and $kp \leq 3$), were compared against the data. A single "best-guess" run of the CTIP model and several cases of the IRI (with varying values for the sunspot number and several sliding 30 day averages bracketed by 1 February and 31 March) were also compared against the data. (The first-principle model runs were completed several weeks before the mission and installed in the on-line library for on-the-fly comparisons with the data. We note that no model is rigorously "first-principle", since all rely, to varying degrees, on empirically-based boundary conditions or force descriptions. This is true of all models in the specification of solar and magnetospheric inputs; and as an example of empirically-based inputs for internal driving forces, the FLIP model uses IRI specifications of h_mF_2 to effectively allow for influences of thermospheric winds at mid-latitudes and electric fields at low-to-equatorial latitudes.)

3) The runs of each model which best fit the data were then intercompared, and the "best-of-the-best" was selected to predict the orbit-to-orbit along-track densities for the next 12 hours.

4) New data were ingested every 12 hours and the procedure repeated, with the orbit-to-orbit predictions posted on an "Ionospheric Weather Board" in the Science Operations Center.

In varying degrees the models represented the coupled ionospheric-thermospheric system - each with different approaches to the prevailing physics and different levels of computational complexity. The IRI is a PC-based empirical model. FLIP, CTIP, and TIEGCM are first-principle models. FLIP, CTIP and TIEGCM are VAX-, workstation, and Cray-based, respectively.

3. Results

We concentrate on the segment of the TSS-1R mission from the initial subsatellite deployment (UT = 56/20:45, defined as the "fly-away") to the tether break (UT = 57/01:29). This involved the four orbits shown in Plate 1, defined here as orbits 1 through 4, color-coded by the thin green, blue, red, and black lines, respectively. The black dots identify the ionosonde stations, while the two red

dots identify the locations of the initial fly-away (on green orbit #1) and the location of the orbiter at the time of the tether break (on black orbit #4). The bold red and blue overlays on the orbit tracks identify functional objective periods IV and DC (Stone and Bonifazi, 1997 (this issue)), respectively, in which tether current-voltage characteristics were studied. While there were orbit-to-orbit differences, the general diurnal characteristics of the ionospheric conditions encountered by the orbiter during orbits 1-4 were such that sunrise and sunset were approximately at 90° E and 270° E longitudes, respectively. The descending node in the late afternoon and early evening period (i.e., $210^\circ \leq \text{long} \leq 270^\circ$) therefore crossed the region of the Appleton Anomaly (see e.g., Klobuchar et al., 1991 and references therein. This was the ionospheric domain encountered just after fly-away and just after the tether break.

The SUNDIAL ionospheric weather activities supporting the four-orbits involved data ingestion, model fit, and prediction updates at UT = 56/16:00, 57/04:00, and 57/16:00. We summarize the accuracies of each best-fit-model-run in Table 1 (% accuracy = $100 \times (\text{model-data})/\text{data}$). The results show accuracies of the best-fits to f_oF_2 and h_mF_2 cataloged according to day/night (D/N) time frames. The largest-font numerical entry represents the accuracy of the model fit averaged over the full daytime (or nighttime) period, while the smaller-font numerical entries (super- and subscripted) represent the extrema of the hourly accuracies during that same period. (We note that the same best-fit run of each model prevailed from data-report-period to data-report-period. As a consequence, the 2nd and 3rd reporting periods tested the accuracy of the model predictions developed during the previous 12-hr data-ingest and model-fit period.)

Table 1 shows that during daytime periods the IRI consistently provided the best accuracies in both f_oF_2 and h_mF_2 ; while at night, best-fit honors in f_oF_2 were generally shared by the IRI and the TIEGCM, with differences generally not in excess of 2 percent. In terms of nighttime values for h_mF_2 , all model accuracies tended to be comparable, with the IRI and FLIP models the leaders. (We note that slight differences in their respective h_mF_2 accuracies [remembering that FLIP uses IRI specifications for h_mF_2] are a result of differences in selecting the sunspot numbers that initiated the IRI.) In the realtime operations, the IRI was the model selected as "best-of-the-best" as a result of its overall day/night and f_oF_2/h_mF_2 accuracies.

Discussed thus far have only been the accuracies relative to N_mF_2 and h_mF_2 as measured by the ionosondes. The ultimate TSS-1R test involved the along-track N_e accuracy at the orbiter and/or the tethered subsatellite. Plate 2 provides a measure of this accuracy for the subsatellite during orbit 4 (which involved the tether break), with each of the best-fit along-track model predictions compared against an "in situ" density measurement by a Langmuir probe that was part of the RETE (Research on Electrodynamic Tether Effects) instrument complement (Dobrowolny et al., 1994). (The discontinuities in the RETE results stem from attempts to correct for known periods involving sheath-effect perturbations and/or to delete data collected during periods of perturbed satellite potentials [G. Vannaroni and J.-P. Lebreton, private communication]).

With reference to Plate 2 we offer the following observations: 1) all models show the qualitative feature of the Appleton Anomaly (i.e., the double peaks in the time frame between 30 and 65 minutes after 57/00:48) but all differ in the intensity and location of the peaks; and 2) qualitatively and quantitatively the along-track RETE data agree best with the IRI and FLIP results between 10 and 25 minutes (after 57/00:48) and again between 33 and 40 minutes (after 57/00:48), while there is better agreement between RETE data and the TIEGCM results in the period between 25 and 32 minutes (after 57/00:48). This latter period encompasses the late afternoon

← Plate 1

← Table 1

← Plate 2

ionospheric domain with cooling temperatures and descending values for $h_m F_2$.

Plate 2 also reveals a broad range of model predictions, (with, for example, CTIP and TIEGCM differing by nearly an order of magnitude) a result that might be considered unexpected given the prevailing low-solar and low-to-moderate geomagnetic activities. However, at low latitudes ionospheric densities are particularly sensitive to electric fields (yet to be accurately modeled) with variability driven by the E and F region dynamo winds. (There may also be magnetospheric-imposed fields during storms, but such was not the case in this period.) Other issues involve the controls of the topside and bottomside gradients, which tend to dominate the domain of N_e sampling in Plate 2, a topic discussed in the following section. (In the version of CTIP used here, an equatorial zonal electric field for moderately-high solar activity was employed. This turned out to be unrealistically high for the prevailing conditions, and accounts for some of the large differences in the models. We also note that recent work on TIEGCM by Crowley and Fesen (pvt. comm., 1997) appears to provide significant improvements in low-latitude dynamo effects.)

4. Comments and Conclusions

Based on daytime and nighttime averages (Table 1), the optimized model fits to the database and subsequent predictions of F₂-region heights and densities were very good, with the "best-of-the-best" yielding averaged $f_o F_2$ and $h_m F_2$ accuracies generally better than 5%. (We note, however, that typical non-averaged hourly extrema of the "best-of-the-best" model extended to values near 15%.) Much of this goodness-of-fit is due to the fact that overall conditions were predominantly quiet-to-moderately disturbed (i.e., $0 \leq kp \leq 3$ for the majority of the reporting periods) - conditions under which models are expected to perform optimally. Other factors contributing to the overall goodness-of-fit deal with the averaging process itself, which provided more of a climatological perspective (again, a framework in which models are expected to perform optimally). The combination of these circumstances provided an environment in which the IRI would be expected to perform especially well. It is an empirically-based model which represents the sum total of all cause-effect relationships as manifested by nature itself. In the case of the first-principle models, the cause-effect terms are at the root of the individual approaches and a number of controlling forces upon which the models are based are still under investigation (see e.g., Szuszczewicz, 1995; and Szuszczewicz et al., 1996).

In comparing the along-track N_e measurements with model predictions (Plate 2), we find the results in sharp contrast with the Table 1 comparisons discussed in the previous paragraph. The difference is traceable to several issues, including relative abilities to model climatologies (i.e., averaged behaviors) versus abilities to model weather (i.e., day-to-day and hour-to-hour variability). Other issues involve, on the one hand, the comparison of densities at the F-peak (i.e., Table 1), where a great deal of data have been available for model development studies. On the other hand, there is the comparison with densities at a fixed altitude (i.e., Plate 2) which cuts across the F-peak and involves bottomside and topside gradients where little data have been available and few model development studies have been carried out. The results are rather sobering, when one notes almost an order of magnitude difference between CTIP and TIEGCM predictions, and differences as large as 140 % between the IRI and RETE values for N_e (see, e.g., Fig. 2 near 28 minutes after 48:00). This reflects the difficulty of properly and self-consistently modeling the controlling forces, with those on the topside being primarily electric fields, diffusion, and plasmaspheric fluxes, while those on the bottomside are electric fields, winds, and chemistry. These forces are fundamental to all

ionospheric-physics, but electric fields are especially critical at low-to-equatorial latitudes. It is the electric fields that are the primary agent for the development of the Appleton Anomaly, with winds playing a secondary role. Within this context we note that overall agreement is best among the data and the FLIP and IRI predictions, because those models effectively include the prevailing electric fields through their empirical specification of $h_m F_2$. (We note that the fine structure and occasional discontinuities in the FLIP results in Plate 2 are related to the fact that the model solution is carried out along separate flux tubes, each with its own unique set of conditions, and the fact that the plot requires interpolation onto the continuous orbital track between locations of flux tube solutions.)

In general, it is understood that day-to-day and hour-to-hour variability is traceable to variations in atmospheric gravity waves, tidal controls, high latitude inputs, and solar EUV fluxes. These drive the winds, thermospheric densities, temperatures, and electric fields - all of which control chemistry, diffusion, and transport - and ultimately the electron density. A recent study [Szuszczewicz et al. 1996] has shown that the modeling of these forces is not well in hand, with specific issues addressing the accuracy in climatological perspectives of thermospheric winds, plasmaspheric fluxes and electric fields. Clearly, more work is necessary on the fundamental controls of the ionosphere and on data-model comparisons in order to better understand the physics and develop a more accurate space weather predictive capability.

Plans for follow-up activities include detailed views on regional and local station results, with emphasis on model accuracies within large-scale phenomenological domains (e.g., the Appleton Anomaly, the sunrise/sunset terminator, etc.). Attention will also be directed at model-specific assumptions and the density gradients above and below the F_2 peak, since these greatly influence the degree to which models and data agree.

Acknowledgment. The SAIC activity was supported by NASA under contract NAS8-36811. Thanks are extended to the institutions throughout the world which support ionosonde operations. Thanks are also extended to NSF for supporting the modeling efforts of G. Crowley under grant ATM-9696234.

References

- Berchem, J., J. Raeder, R.J. Walker, and M. Asbour-Abdalla, Interactive visualization of numerical simulation results: A tool for mission planning and data analysis in *Visualization Techniques in Space and Atmospheric Sciences*, E.P. Szuszczewicz and J. Bredekamp, Eds., NASA SP-519, National Aeronautics and Space Administration, Washington, D.C. (1995)
- Dobrowolny, M., E. Melchioni, U. Guidoni, L. Iess, M. Maggi, R. Orfei, Y. de Conchy, C.C. Harvey, R.M. Manning, F. Wouters, J.-P. Lebreton, S. Ekholm, and A. Butler, The RETE experiment for the TSS-1 mission, *Nuovo Cimento*, 17, 101-121, 1994.
- Dobrowolny, M. and N.H. Stone, A technical overview of TSS-1: the first tethered-satellite system mission, *Nuovo Cimento*, 17, 1-12, 1994.
- Dudney, J.R., The accuracy of simple methods for determining the height of the maximum electron concentration of the F2-layer from scaled ionospheric characteristics, *J. Atmos. Terr. Phys.*, 45, 629, 1983.
- Fuller-Rowell, T.J., M.V. Codrescu, R.J. Moffett, and S. Quegan, Response of the thermosphere and ionosphere to geomagnetic storms, *J. Geophys. Res.*, 99, 3893-3914, 1994.
- Kamide, Y., R.L. McPherron, W.D. Gonzalez, D.C. Hamilton, H.S. Hudson, J.A. Joselyn, S.W. Kohler, L.K. Lyons, H. Lundstedt, and E. Szuszczewicz, Magnetic Storms, in *Proceedings of the Chapman Conference on Magnetic Storms*, B.T. Tsurutani, W.D. Gonzalez, Y. Kamide and J.K. Arballo, eds., JPL Pasadena, CA, AGU Monograph (1997, in press).
- Klobuchar, J.A., D.N. Anderson, and P.H. Doherty, Model studies of the latitudinal extent of the equatorial anomaly during equinoctial conditions, *Rad. Science*, 26, 1025-1047, 1991.
- Richards, P.G., D.G. Torr, M.J. Buonsanto, and D.P. Sipler, Ionospheric effects of the March 1990 magnetic storm: comparison of theory and measurement, *J. Geophys. Res.*, 99, 23,359-23,365, 1994.
- Richmond, A.D., Ridley, E.C., and Roble, R.G., A thermosphere/ionosphere general circulation model with coupled electrodynamics, *Geophys. Res. Lett.*, 19, 601-604, 1992.

- Schunk, R.W., and E.P. Szuszczewicz. First principle and empirical modeling of the global-scale ionosphere, *Ann. Geophys.*, 6, 19, 1988.
- Stone, N., and C. Bonifazi. The TSS-IR mission: Overview and scientific context, *Geophys. Res. Lett.*, (1997, this issue).
- Szczuszczewicz, E.P., Advances in ionospheric physics: roles, relevance and predictions in the system of solar-terrestrial plasmas, *U.S. Nat'l Rpt. to IUGG 1991-1994, Reviews of Geophys. Supplement*, 721-728, 1995.
- Szczuszczewicz, E.P., D. Torr, P. Wilkinson, P. Richards, R. Roble, B. Emery, G. Lu, M. Abdu, D. Evans, R. Hanbaba, K. Igarashi, P. Jiao, M. Lester, S. Pulinetz, B.M. Reddy, P. Blanchard, K. Miller, J. Joselyn, F region climatology during the SUNDIAL/ATLAS 1 campaign of March 1992: Model-measurement comparisons and cause-effect relationships, *J. Geophys. Res.*, 101, 26,741-26,758, 1996.

M. Abdu, Instituto Nacional de Pesquisas Espaciais, Sao Paulo, Brazil.
 P. Blanchard and E.P. Szuszczewicz, Science Applications International Corporation, 1710 Goodridge Drive, P.O. Box 1303, McLean, VA 22102.
 T. Bullett, Phillips Lab, Hanscom AFB, Massachusetts.
 G. Crowley, Southwest Research Institute, San Antonio, Texas.
 T. Fuller-Rowell, National Oceanic and Atmospheric Administration, Boulder, Colorado.
 R. Hanbaba, France Telecom/CNET, Lannion, France
 J.P. Lebreton, Space Science Department, ESA/ESTEC, Noordwijk, The Netherlands.
 M. Lester and M. Wild, University of Leicester, Leicester, United Kingdom.
 M. Lockwood, Rutherford Appleton Lab, Oxon, United Kingdom.
 G. Millward, National Oceanic and Atmospheric Administration, Boulder, Colorado.
 S. Pulinetz, IZMIRAN, Moscow Region, Russia.
 B.M. Reddy, National Geophysical Research Institute, Hyderabad, India.
 P. Richards, University of Alabama, Huntsville, Alabama.
 I. Stanislawski, Space Research Center, Warsaw, Poland.
 G. Vannaroni, Istituto di Fisica Dello Spazio Interplanetario, Frascati, Italy.
 P. Wilkinson, IPS Radio & Space Services, West Chatswood, Australia.
 B. Zolesi, Instituto Nazionale di Geofisica, Italy.

(Received January 15, 1997; revised October 27, 1997; accepted October 30, 1997)

Plate 1. Ground tracks for four TSS-IR orbits covering the period from the initial fly-away (red dot, orbit #1) through the tether break (red dot, orbit #4). Black dots identify ionosonde stations.

Plate 1. Ground tracks for four TSS-IR orbits covering the period from the initial fly-away (red dot, orbit #1) through the tether break (red dot, orbit #4). Black dots identify ionosonde stations.

Plate 2. Along-track density predictions compared with "in situ" data from the RETE Langmuir probe.

Plate 2. Along-track density predictions compared with "in situ" data from the RETE Langmuir probe.

SZUSZCZEWICZ ET AL.: REALTIME WORLDWIDE IONOSPHERIC PREDICTIONS
 SZUSZCZEWICZ ET AL.: REALTIME WORLDWIDE IONOSPHERIC PREDICTIONS
 SZUSZCZEWICZ ET AL.: REALTIME WORLDWIDE IONOSPHERIC PREDICTIONS

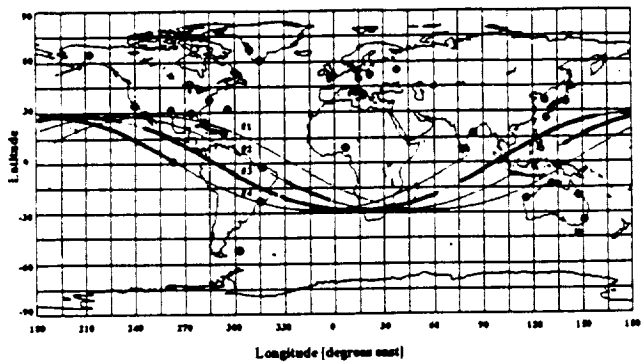


Figure 1
Plate 1

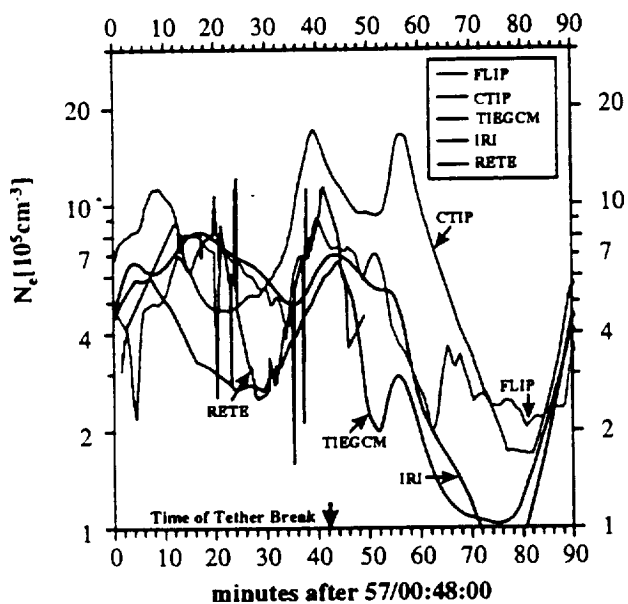


Plate 2

Table 1. Model Accuracies (%) at Low Latitudes ($\leq 30^\circ$)

Observable \rightarrow		L ₂ F ₂			h _m F ₂		
Time of Data Ingest \rightarrow		56/16:00	57/04:00	57/16:00	56/16:00	57/04:00	57/16:00
IRI	D	0.4 ^{8.3} _{-4.6}	1.3 ^{5.5} _{-4.6}	-0.7 ^{3.4} _{-6.7}	5.0 ^{12.5} _{-2.3}	5.2 ^{14.0} _{-6.3}	5.3 ^{12.1} _{-10.4}
	N	5.6 ^{14.6} _{-4.5}	3.6 ^{15.9} _{-8.9}	-3.6 ^{5.7} _{-11.1}	-0.9 ^{7.3} _{-4.9}	-3.6 ^{6.8} _{-10.8}	-5.4 ^{5.1} _{-13.2}
TIEGCM	D	-5.3 ^{21.0} _{-12.1}	-4.6 ^{7.0} _{-12.8}	-7.1 ^{7.0} _{-15.0}	6.3 ^{14.5} _{0.1}	6.6 ^{15.2} _{-1.2}	7.0 ^{14.3} _{-5.9}
	N	3.4 ^{21.6} _{-10.9}	1.1 ^{14.1} _{-8.2}	-5.2 ^{6.1} _{-10.4}	5.3 ^{11.0} _{2.3}	2.3 ^{11.4} _{-1.3}	0.5 ^{9.4} _{-5.9}
FLIP	D	3.7 ^{15.7} _{-0.8}	5.1 ^{11.6} _{0.0}	1.9 ^{6.5} _{-2.5}	5.0 ^{11.5} _{-2.3}	5.3 ^{12.9} _{-5.5}	5.7 ^{11.7} _{-10.0}
	N	18.4 ^{27.6} _{4.8}	14.6 ^{23.4} _{4.6}	5.5 ^{14.8} _{-0.9}	0.3 ^{8.2} _{-4.3}	-1.5 ^{8.7} _{-10.4}	-3.4 ^{6.9} _{-12.7}
CTIP	D	25.6 ^{43.5} _{17.1}	26.7 ^{35.7} _{16.4}	22.4 ^{28.7} _{13.9}	6.0 ^{11.9} _{1.0}	6.5 ^{13.3} _{1.1}	6.3 ^{11.8} _{-3.3}
	N	53.5 ^{-73.0} _{26.9}	49.4 ^{76.5} _{25.4}	36.7 ^{66.4} _{8.5}	-0.6 ^{7.1} _{-6.4}	-2.5 ^{7.9} _{-9.2}	-4.6 ^{5.4} _{-8.5}

APPENDIX 16

Ion Reflection by the TSS-1R Satellite

K. Papadopoulos*, C.-L. Chang and A. Drobot

Science Application International Corporation, 1710 Goodridge Drive, McLean, VA 22102 and
*University of Maryland, College Park, MD 20742

Abstract. The results of the TSS-1R mission generated several scientific puzzles. First the current collection was much more efficient than predicted on the basis of theoretical models, and previous laboratory and rocket experiments. Second, a sharp transition in the interaction physics occurred at threshold potentials between 5–10 V. Third, a significant population of suprathermal electrons, heated ionospheric ions, and enhanced plasma waves were observed in the ram direction, following the transition. The letter contains a preliminary examination of the extent to which these phenomena are related to the interaction of the impinging ambient ram O^+ ions with the sheath surrounding the TSS satellite.

1. Introduction/Theoretical Surprises

The TSS-1R measurements generated many surprising results [Stone and Bonifazi, 1998]. First, for the currents commanded by the TSS circuit, the measured satellite potential was an order of magnitude lower than predicted by space charge limited, magnetically insulated flow. Furthermore, over a large current range, the observed current/voltage scaling was significantly different from theoretical models, laboratory experiments and space experiments at suborbital speeds. Figure 1 illustrates the surprising current collection efficiency of the system. It shows the value of the maximum available power, defined as $P = I(\mathcal{E} - \phi_s - \phi_{or})$ as a function of the collected current I . Here \mathcal{E} is the system emf, ϕ_s the satellite potential and ϕ_{or} the orbital potential, measured during the mission. For the details of these mission measurements we refer the reader to the companion papers [Stone and Bonifazi, 1998; Thomson et al., 1998]. The experimental results presented correspond to a day-time IV-24 cycle, with density $8.5 \times 10^5 \text{ #/cm}^3$ and electron temperature 1800 K. Similar features are apparent in all of the IV-cycles and were reproduced with high reliability. The value of P is the difference between the maximum power $I \cdot \mathcal{E}$ generated and the power $I(\phi_s + \phi_{or})$ required to collect the current. It is an essential figure of merit. The experimental results are compared with the theoretical expectations based on the Parker-Murphy [PM] [1967] model, and the theoretical upper limit manifested by the Beard-Johnson [BJ] [1960] model. The results are puzzling. The applicable PM relationship would have limited the power to less than 600 W. Moreover the power would have saturated at currents of about 260 mA. The results indicate efficiencies even above the energetic upper limit given by BJ. Furthermore, no saturation was observed at the maximum current of 1.1 A which occurred during the tether break. At this point P was approximately 2 KW. The observed high efficiency is related to the

low potentials that were required at the satellite to collect significant currents. Figure 2 shows the ϕ_s vs I characteristics for the above event and compares it with the expected on the basis of the PM and BJ models. The results indicate that currents between 300–500 mA were collected with potentials an order of magnitude lower than PM and factors of two or three lower than BJ.

The second surprise was related to the ϕ_s/I scaling. This is explored in Fig. 3. It shows the percentage deviations $(\phi_{PM} - \phi_s)/\phi_s$ and $(\phi_{BJ} - \phi_s)/\phi_s$ as a function of I . It is clear that within the 0.5 A range, there is no scaling consistent with the isotropic collection expected from BJ, even as modified by *Linson* [1969]. On the other hand, while large deviations are evident from the PM law, the observed scaling seems to converge towards PM for $I > 300$ mA but with a different coefficient of proportionality.

The third surprise was the presence of athreshold satellite voltage in the vicinity of 5–6 V. It marks a significant change in the character of the interaction physics. Related to this transition the following are observed:

- (i) Ambient O^+ flowing from the forward direction of the satellite, with effective temperature larger than that of the ambient ionosphere [*Wright et al.*, 1998].
- (ii) Suprathermal electrons centered around 200 eV, whose number density exhibits a four-orders of magnitude jump in population [*Winningham et al.*, 1998; *Gurgiolo et al.*, 1998].
- (iii) Enhancement in wave activity in the lower hybrid (LH) range [*Jess et al.*, 1998] and evidence of turbulence in the currents measured by the BSMP in the ROPE investigation [*Wright et al.*, 1998].

These results provide conclusive evidence that physical processes different than those considered previously become important and possibly dominate the interaction physics at orbital speeds. They present a challenging theoretical problem. Here we set forth some preliminary ideas for the causes of the discrepancies and define future theoretical directions.

2. Interaction Physics at Orbital Speeds – Ion Reflection

The differences between current collection in the laboratory, collection at suborbital speeds, and the TSS-1R becomes apparent by examining the interaction from a reference frame moving with the satellite. In this reference frame the O^+ ions can be viewed as a cold ion beam with energy approximately 5 eV and temperature 0.1 eV impinging on the satellite. Since the ion cyclotron frequency Ω_i is of the order of 200–300 sec^{-1} , the O^+ beam ion beam can be considered as unmagnetized. The 5 eV O^+ beam impinging on the sheath introduces two effects that were, justifiably, neglected in the PM and BJ analysis. The first one relates to the pressure balance in the sheath and pre-sheath. In the absence of the O^+ pressure equilibrium between the expelled ions and the sheath electric field is automatically satisfied. This is not the case for large values of velocity u . Instead, the impinging ions exert on the sheath a dynamic pressure p given by $p = 1/2 n_0 M u^2$. For $n_0 \approx 10^6 \text{ #/cm}^3$ this corresponds to

$8 \times 10^{-7} \text{ J/m}^3$, and scales linearly with the ambient density. If we introduce an electric field pressure p_E in the sheath as approximately $p_E = 1/2 \epsilon_0 E^2$ we see that in order to balance $8 \times 10^{-7} \text{ J/m}^3$ sheath electric fields of the order $E \approx 450 \text{ V/m}$ are needed. Furthermore, the ram ions are not normal to the potential surfaces, which are determined by the projection of the collector on the magnetic field. As a result the effective ram pressure varies as $\cos^2\theta$ with maximum in the center of the tethered satellite and approaching zero at the ends of the sheath. It is unclear as to whether such an inhomogeneous equilibrium can exist in a laminar state or a dynamic or turbulent equilibrium will occur.

The second effect relates to O^+ reflection from the sheath. For potentials lower than 5 V the O^+ ions cannot be reflected in the ram direction. Such a low potential can only deflect them setting up a quasineutral, possibly orbit limited current collection, [Laframboise and Sonmor, 1993]. For potentials larger than 5 V ion reflection sets in. Simulations indicate total reflection at 8–10 eV potential. In the ionospheric reference frame the reflected ions form a beam moving with speed $2u$ and kinetic energy of 20 eV. Ram ion reflection has two consequences. It violates charge neutrality in the ram direction. The situation resembles charge neutralization of an ion beam injected into a plasma across a magnetic field [Chrien, 1987]. In this case large surface polarization electric fields are driven at the interface of the beam with the plasma leading to plasma ringing and electron acceleration. It is expected that this will lead to enhanced electron collection and neutralization of the reflected ions, on a few meter length scale. Accompanying this process, is the possibility of a lower hybrid (LH) instability driven by the beam which extends over an ion gyroradius ($\approx 100 \text{ m}$). The reflected ion beam constitutes a major free energy source upstream of the interaction. For an ambient density of $n_0 \approx 10^6 \text{ \#/cm}^3$, the available free energy per unit volume is $2 \times 10^{13} \text{ eV/m}^3$ and the available power $3 \times 10^{17} \text{ eV/m}^2\text{sec}$.

Understanding of the physics controlling current collection at orbital speeds requires solving the above issues, each one separately as well as their interplay. This is major research endeavor, beyond the scope of this letter. In the remaining of this paper we will address in a more detailed fashion one of the above issues. The possibility that instabilities driven by ion reflection account for the ram phenomena reported by Wright *et al.* [1998], Winningham *et al.* [1998], Gurgiolo *et al.* [1998], and Less *et al.* [1998].

3. Instabilities Driven by Reflected O^+ Ions

We examine here the observables expected by instabilities driven by the reflected ions and compare with observations. We emphasize bulk plasma waves, rather than surface waves due to the charge neutralization process. The situation is shown schematically in Fig. 4. Below 5 eV there is no ion reflection, and no free energy. For larger potential ions are reflected forming an ion beam. The free energy per unit volume available is the same independently of the sheath potential and structure. Larger potential will probably produce larger sheaths, resulting in larger total available free energy and stronger reflected O^+ – plasma interactions.

The situation resembles the physics of the electron foreshock in the earth's quasi-perpendicular bow shock at supercritical Mach numbers [Papadopoulos, 1982]. In this case ion reflection from the magnetic overshoot results in the formation of an ion beam upstream. The subsequent interaction of the beam with the plasma generates large amplitude waves in the lower hybrid range and creates suprathermal electron tails with energy exceeding 1–2 keV.

The dispersion relation for a system such as shown in Fig. 4b has been examined by many authors [Papadopoulos, 1982, 1984; Mobius *et al.*, 1987]. It incorporates two types of instabilities that have the characteristic frequency

$$\omega_k^2 = \omega_{LH}^2 [1 + (M/m \cdot k_z^2/k^2)] \quad (1)$$

where M is the O^+ mass and $B = \hat{e}_z B$. For a monoenergetic beam, there is a coherent hydrodynamic instability which turns quickly into the beam kinetic instability.

Papadopoulos [1992a] extended the infinite homogeneous analysis to systems where the beam is spatially limited, such as the case of critical velocity ionization experiments and the tether reflection case. His analysis included the three-dimensional electron nonlinearity [Shapiro and Sevchenko, 1984] which can lead to collapse and creation of localized soliton like structures. The latter effect occurs when the electron drift velocity \bar{E}/B in the presence of a low frequency fluctuating field \bar{E} exceeds the speed of sound. For values of c , ≈ 5 km/sec, the threshold field is about 10–20 mV/m. We refer the interested reader to Papadopoulos [1992a], and simply summarize the results and apply them to the tether reflection.

For a system spatially limited in the magnetic field direction (z -direction) with a length L_0 such that $L_0 < \bar{u}/\omega_{LH} \sqrt{M/m}$ where \bar{u} is the transverse velocity of the reflected ions, the maximum growth occurs at the first confined mode, i.e. $\pi/k_{z0} = L_0$. When the threshold of 10–20 mV/m is exceeded self-similar solutions indicate that in the collapsing state the wave energy W scales as [Sotnikov *et al.*, 1978]

$$\begin{aligned} k_z(t) &\sim \frac{W}{n_0 T}, & k_{\perp}(t) &\sim \sqrt{\frac{W}{n_0 T}}, \\ \frac{k_{\parallel}(t)}{k_{\perp}^2(t)} &\approx \text{const.}, & \text{and } k_z^{-1}(t) &\sim \frac{1}{t-t_0}. \end{aligned} \quad (2)$$

Equations (2) indicate that although the initial instability creates waves with strongly anisotropic polarization, the collapse tries to isotropize them.

Another profound consequence of the collapse is the suprathermal tails generated by the interaction of the electrons with collapsing wavepackets. The tail formation is described by a non-resonant Fokker-Planck equation similar to the one derived by Morales and Lee [1974] for Langmuir turbulence. The evolution of the distribution function of the suprathermal electron tails $f(\epsilon)$ is given by [Papadopoulos, 1992a,b]

$$\frac{\partial f(\epsilon)}{\partial t} = \frac{\partial}{\partial \epsilon} \epsilon D(\epsilon) \frac{\partial f(\epsilon)}{\partial \epsilon} \quad (3)$$

$$D \equiv \frac{1}{2} m \frac{\langle \Delta v \Delta v \rangle}{\tau} \approx 2\pi^2 \bar{\epsilon} \omega_{LH} \left(\frac{\epsilon_0}{\epsilon} \right)^{1/2} \times \operatorname{sech}^2 \left[0.12 \left(\frac{\epsilon_0}{\epsilon} \right)^{1/2} \right] \quad (4)$$

$$\epsilon_0 = \frac{1}{2} M \bar{u}^2, \quad \bar{\epsilon} = \frac{1}{2} \frac{e^2 E^2}{m \Omega_e^2} \quad (5)$$

The particular sech dependence is simply due to the selected form of solitons. Equation (3) describes a particular form of second order Fermi acceleration, in which the electrons E/B quiver according to eq. (5) and lose their energy adiabatically if their field aligned velocity is fast enough to transit the soliton faster than $1/\omega_k$ [Morales and Lee, 1974; Manheimer and Papadopoulos, 1975; Bingham et al., 1993].

4. Comparison with Experimental Data

We compare next the TSS-1R measurements with the above theoretical estimates. The wave measurements [Jess et al., 1998] indicate wave amplitudes of up to 12 V/m for satellite potentials of the order of 10 V/m, when ion reflection is expected. The waves have broadband frequency with maximum spectral density between 2–3 kHz, below the LH frequency which is 6.4 kHz. This exceeds by far the collapse threshold. For $E \sim 12$ V/m, $n_0 \approx 8 \times 10^5$ #/cm³ and .1 eV temperature, $W/n_0 T \approx 6 \times 10^{-2}$. On the basis of eqs. (2), we expect that the LH cavities will have dimensions of the order of 20 cm in the transverse direction and 4–6 m in the parallel direction. From Papadopoulos [1992; eq. (17)] the observed frequency ω_0 will be given by $\omega_0 \approx 2\omega_{LH} \sqrt{\frac{W}{n_0 T}}$ which for $W/n_0 T \approx 6 \times 10^{-2}$ corresponds to 2–3 kHz, consistent with the observations by Jess et al. [1998].

Consider next the transit time acceleration of electrons. Since the parallel scalelength of the wavepackets is of the order of $\ell \approx 6$ m, only electrons with parallel velocity $v \gg \ell \omega_{LH} \approx 3 \times 10^7$ cm/sec can be accelerated. From eqs. (3–5) [see also Papadopoulos, 1992b], the time required for acceleration to energy ϵ is given by

$$\tau_0(\epsilon) = \frac{\epsilon}{D} = 5 \times 10^{-2} \left(\frac{\epsilon}{\bar{\epsilon}} \right) \left(\frac{\bar{\epsilon}}{\epsilon_0} \right)^{1/2} \omega_{LH}^{-1} \quad (6)$$

For $\epsilon \approx 200$ eV, the time required for acceleration to 200 eV is 8×10^{-3} sec. For the TSS case it requires that the turbulence extends to 60 m ahead of the probe.

The expected distribution function can be found by considering a stationary process so that, eq. (3) gives

$$\epsilon D(\epsilon) \frac{\partial f}{\partial \epsilon} = \text{const} \quad (7)$$

and using eq. (4) for $D(\epsilon)$, we find $\partial f / \partial \epsilon \sim 1/\epsilon^{3/2}$ which is also consistent with the dependence reported by Winningham et al. (1998).

We finally examine heating of the reflected ions. In the presence of $E \approx 12$ V/m at the LH range the sloshing of the beam ions is $\Delta v = eE/M\omega_{LH} \approx 2 \times 10^3$ m/sec which corresponds to an effective reflected ion temperature

$\frac{1}{2}M(\Delta v)^2 \simeq .3 - .4 \text{ eV}$ consistent with the one reported by Wright *et al.* [1998].

5. Concluding Remarks

This letter is an attempt to explore and list the factors responsible for the theoretical puzzles observed in TSS-1R. The preliminary analysis indicates that the main reason for the discrepancies is associated with ion reflection from the sheath and the required dynamic pressure balance between the impinging ions and the electric fields in the sheath. From the three factors associated with reflection – pressure equilibrium, violation of charge neutrality, and ion reflection driven instabilities – we concentrated on the last. The observed 5 V threshold behavior, the enhanced wave activity and frequency, the presence of suprathermal electron tails, and the observed heating of the reflected ions are, at least to zero order, consistent with theoretical expectations instability. How and to what extent reflection, coupled with sheath equilibrium and non-neutrality produces the high current collection efficiency is a major theoretical challenge not yet resolved.

Acknowledgements: The work was supported by NASA NAG5-1101. The authors gratefully acknowledge the contributions of the astronaut crew (A. M. Allen, S. J. Horowitz, F. R. Chang-Diaz, M. Cheli, U. Guidoni, J. A. Hoffman, and C. Nicollier) and of the entire TSS team that made the experiment possible.

References

- Beard, D. B. and F. S. Johnson, Charge and magnetic field interaction with satellites, *J. Geophys. Res.*, 65, 1960.
- Bingham, R., J. J. Su, J. M. Dawson, V. Shapiro and V. Shevchenko, Acceleration of electrons and ions by nonlinear lower hybrid waves, in *Nonlinear Space Plasma Physics*, edited by R. Sagdeev, p. 347, AIP, 1993.
- Chrien, E. F., E. J. Valeo, R. M. Kulsrud, and C. R. Oberman, Propagation of ion beams through a tenuous magnetized plasma, *Phys. Fl.*, 29, 1675, 1986.
- Gurgiolo, C., J. D. Winningham, K. Wright, and N. H. Stone, TSS-1R: Superthermal electron distributions observed in low voltage satellite configurations, *Geophys. Res. Lett.*, this issue, 1998.
- Iess, L., C. Harvey, G. Vannaroni, J. P. Lebreton, M. Dobrowolny, R. Manning, Onelli, and F. De Venuto, Plasma waves in the sheath of the TSS-1R satellite, *Geophys. Res. Lett.*, this issue, 1998.
- Laframboise, J. G., and L. T. Sonmor, Current collection by probes and electrodes in space magnetoplasmas: a review, *J. Geophys. Res.*, 98, 337, 1993.
- Linson, L. M., Current voltage characteristics of an electron-emitting satellite in the ionosphere, *J. Geophys. Res.*, 74, 2368, 1969.
- Mobius, K. Papadopoulos, and A. Piel, On the Turbulent Heating and the Threshold Condition in the Critical Ionization Velocity Interaction, *Planet Space Sci.*, 35, 345, 1987.

- Morales, G., and Y. C. Lee, Effect of the localized electric field on the evolution of the velocity distribution function, *Phys. Rev. Lett.*, 33, 1534, 1974.
- Papadopoulos, K., Proceedings of 1st International school of Plasma Astrophysics, Varenna, p. 1, ESASP-161, 1982.
- Papadopoulos, K., On the Shuttle Glow (The Plasma Alternative), *Radio Science*, 19, 571, 1984.
- Papadopoulos, K., The CIV Process in the CRIT Experiments, *Geophys. Res. Lett.*, 19, 605, 1992a.
- Papadopoulos, K., Critical Ionization Velocity in Space, AIAA-92-0788, 1992b.
- Parker, L. W., and B. L. Murphy, Potential buildup on an electron-emitting ionospheric satellite, *J. Geophys. Res.*, 72, 1631, 1967.
- Shapiro, V. and V. Svechenko, Handbook of Plasma Physics, Vol. 2, p. 81, M. Rosenbluth and R. Sagdeev, Eds., North Holland, Amsterdam, 1984.
- Sotnikov, V. I., V. D. Shapiro, and V. I. Shevchenko, Macroscopic consequences of collapse at the lower hybrid resonance, *Sov. J. Plasma Phys.*, 4, 252, 1978.
- Stone, N. H., and C. Bonifazi, The TSS-IR mission: overview and scientific context, *Geophys. Res. Lett.*, this issue, 1998.
- Wright, K. H. Jr., N. H. Stone, J. Sorensen, J. D. Winningham and C. Gurgiolo, Observations of reflected ions and plasma turbulence for satellite potentials greater than the ion ram energy, *Geophys. Res. Lett.*, this issue, 1998.
- Winningham, J. D., N. H. Stone, C. A. Gurgiolo, K. H. Wright, and R. A. Frahm, Superthermal electrons observed on the TSS-IR satellite, *Geophys. Res. Lett.*, this issue, 1998.

K. Papadopoulos, C.-L. Chang and A. Drobot, Science Application International Corporation, 1710 Goodridge Drive, McLean, VA 22101. (e-mail: kp@astro.umd.edu)

(Received September 15, 1997; accepted December 17, 1997.)

Copyright 1997 by the American Geophysical Union

Paper number

PAPADOPOULOS: ION REFLECTION BY THE TSS-1R SATELLITE

PAPADOPOULOS: ION REFLECTION BY THE TSS-1R SATELLITE

PAPADOPOULOS: ION REFLECTION BY THE TSS-1R SATELLITE

Figure 1. Maximum available power in the TSS-1R mission compared to the power expected from the PM and BJ models.

Figure 2. Voltage versus current characteristics from the TSS-1R mission, and on the basis of the PM and BJ models.

Figure 3. Comparison between the TSS-1R Φ/I scaling and those of the PM and the BJ models.

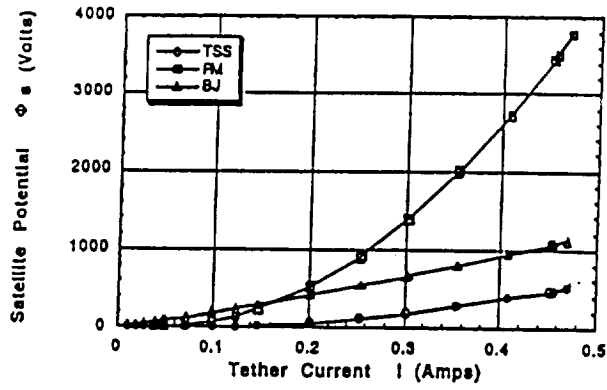
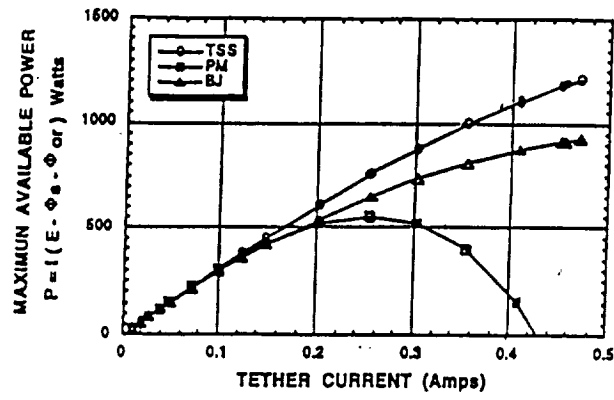
Figure 4. (a) Schematic of the reflection geometry. (b) Schematic representation of the distributions in velocity space of the background and reflected ions and the electrons.

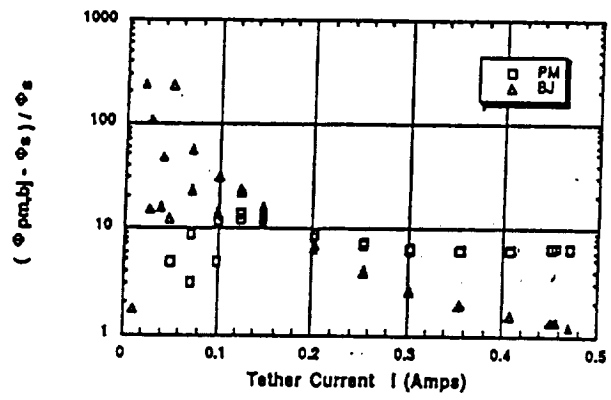
Figure 1. Maximum available power in the TSS-1R mission compared to the power expected from the PM and BJ models.

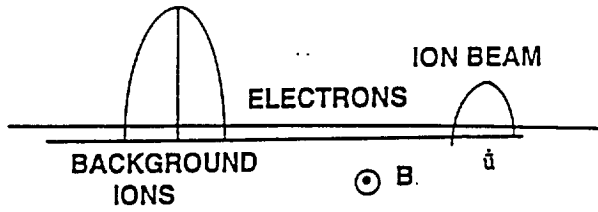
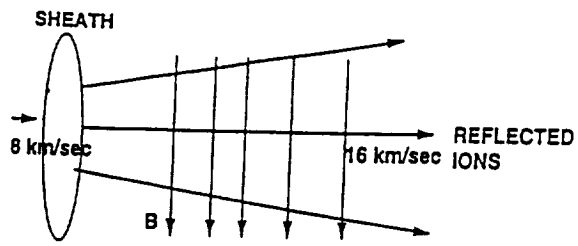
Figure 2. Voltage versus current characteristics from the TSS-1R mission, and on the basis of the PM and BJ models.

Figure 3. Comparison between the TSS-1R Φ/I scaling and those of the PM and the BJ models.

Figure 4. (a) Schematic of the reflection geometry. (b) Schematic representation of the distributions in velocity space of the background and reflected ions and the electrons.







APPENDIX 17

Satellite Motion Effects on Current Collection in LEO Space

T. X. Zhang⁽¹⁾, K. S. Hwang⁽²⁾, S. T. Wu⁽¹⁾, N. H. Stone⁽³⁾,

C. L. Chang⁽⁴⁾, A. Drobot⁽⁴⁾, and K. H. Wright Jr.⁽¹⁾

⁽¹⁾ Center for Space Plasma and Aeronomic Research, The University of Alabama in Huntsville,

AL 35899

⁽²⁾ Computer Sciences Corporation/MSFC, Marshall Space Flight Center, AL 35812

⁽³⁾ Space Science Laboratory, NASA, Marshall Space Flight Center, AL 35812

⁽⁴⁾ Science Applications International Corporation, McLean, Virginia 22102

Abstract. Recent TSS-1 and TSS-1R measurements showed that the satellite motion has important effect on the magnitude of current collection in space. The classical Parker-Murphy (PM) model [Parker & Murphy 1967] under-estimates the satellite current collection in comparison with the recent TSS-1R result [Thompson et al, 1997]. Thompson [1985] and Dobrowolny et al. [1995] considered the satellite motion but did not solve the equation of motion self-consistently to determine the sheath. In this study, the Thompson and Dobrowolny sheath models were modified by solving the equation of motion and the particle trajectory dynamics, which leads to an expression for the magnetic field aligned sheath with velocity dependence. This sheath expression shows explicitly the current collection dependence on satellite velocity and gives a realistic prediction of current being collected as observed. A general current collection expression with the satellite motion and the oblique magnetic field is derived.

1. Introduction

Current collection in space has been continuously investigated since the probe theory was developed (Langmuir and Blodgett) in 1924. With the induced electric field and the magnetic field effects, Parker & Murphy (PM) [1967] developed a current collection model for a spherically motionless probe with radius greater than the plasma Debye length. In this model, currents are collected from both direction along the magnetic field lines. ~~This result is~~ qualitatively ~~in agreement~~ with the data obtained from both laboratory experiments and computer simulations. ~~which~~ indicate that an electron torus-like distribution develops across the magnetic field near a positively biased spherical probe [Quinn & Chang 1966; Antoniadis et al., 1990; Ma and Schunk, 1989; and Shiah et al., 1997]. Furthermore, the recent chamber experiments on current collection by a sphere with radius greater than the Debye length have quantitatively confirmed the PM model prediction with the magnetic field effect [Sorensen, Stone, and Wright, 1996]. In some cases, when the external magnetic field is small, the current collection is less than the PM model prediction because the radius of the cylindrical chamber is smaller than the PM sheath radius.

The Tethered-Satellite System (TSS) was designed to investigate the electrodynamics of conducting tether systems in space [Gross, 1973; Colombo et al., 1974; Dobrowolny and Stone, 1994; Stone and Bonifazi, 1997]. The measured currents from both TSS-1 and TSS-1R revealed considerable current increases (by a factor of 4-5 for TSS-1 and 2-3 for TSS-1R) in comparison with the PM current prediction [Dobrowolny et al., 1995; Thompson et al., 1997].

~~Currently, many studies are going on to research for the physical processes of these~~ ^{hypothetical} current increases. One of the hypothesis is that the current increase is due to the satellite motion. Thompson [1985] was the first to consider such motion effect and proposed a magnetic field aligned sheath to predict the current collection, which was later modified to include the probe potential by Dobrowolny et al. [1995]. The modified model includes two contributions: (1) the

static PM current and (2) the current due to the satellite motion. However, their prediction didn't explicitly show the magnitude of the probe velocity (or plasma flow) dependence, but merely exhibits current collection being a factor of 5 as large as the PM current prediction when the satellite is moving. This result does not physically explain the motion effect. On the other hand, the numerical simulations [Singh and Chaganti 1994] showed that the plasma flow does play a role in the determination of the current being collected by the probe.

In this study, a current collection model in space is developed by including the satellite motion effect. In Section 2, the PM current collection model was reviewed and the Thompson/Dobrowolny assumptions on the field aligned sheath were discussed. In Section 3, the modified model on current collection was described. A current collection formula with the motion effect was derived with the consideration of both the PM sheath radius and the field aligned sheath length. With the potential distribution along the magnetic field line, the magnetic field aligned sheath was obtained by solving the equation of motion. This field aligned sheath is dependent on the satellite velocity. The result shows that the current collection increases with increasing the satellite velocity. When the velocity approaches to zero, the present model reduces to the PM model. The parametric study to include the orientation effect of the satellite motion with respect to the magnetic field were studied. It is shown that magnitude of the current collection is dependent on the orientation. The current collection is more efficient when the magnetic field orientation is perpendicular to the satellite motion direction. When the satellite moves parallel to the magnetic field line, the satellite collects the least which is equal to the PM current prediction. In Section 4 the numerical results were illustrated and compared with the TSS-1R measured data.

2. Brief descriptions of Parker-Murphy model and sheath assumptions

Parker and Murphy (PM) [1967] developed a space charge limited current collection model for a spherically motionless probe in a uniform magnetized plasma. In this model, current collection is carried out in the PM sheath tube along the magnetic field lines (Figure 1). The PM current is given by

$$I_{\text{PM}} = 2\pi r_0^2 j_0, \quad (1)$$

where j_0 is the thermal current density, $j_0 = n_{e0} e v_{Te} / 4$; v_{Te} is the mean electron velocity, $v_{Te} = \sqrt{8kT_e / (\pi m_e)}$; and r_0 is the PM sheath radius for current collection.

$$r_0 = a \sqrt{1 + \sqrt{\frac{8e\phi_s}{m_e a^2 \Omega_e^2}}}, \quad (2)$$

where a is the satellite radius; ϕ_s is the satellite potential; and Ω_e is the electron cyclotron frequency defined by $\Omega_e = eB / m_e$ with B the magnetic field.

For a satellite moving perpendicular to the geomagnetic field, electrons far from the satellite in the PM sheath tube cannot be collected by the satellite. This means there exists a marginal length along the magnetic field line. Only those electrons within the marginal length can be collected by the satellite. This marginal length is called the field aligned sheath which generally depends on the velocity and potential of satellite and the characteristics of ambient plasma. The electrons in the up-stream of plasma continuously enter the PM sheath tube during the motion of satellite. Therefore, current collection by a moving satellite is limited along the magnetic field line and is extended in the direction of the satellite motion.

Thompson [1985] considered the limitation and proposed a formula for the field aligned sheath with the effect of satellite motion as

$$Z_{\text{TH}} = \frac{2av_e}{V_0} \quad (3)$$

where v_e is the electron thermal velocity defined by, $v_e = \sqrt{kT_e / (2\pi m_e)}$. However, this field aligned sheath (or Thompson sheath) did not consider the effect of the satellite potential. To include the satellite potential effect on the field aligned sheath and thus on current collection, Dobrowolny et al. [1995] modified the Thompson sheath formula as

$$Z_{\text{DOB}} = \frac{2r_0 v_{Te}}{V_0} \quad (4)$$

To account for the satellite potential effect, the satellite radius a in equation (3) was replaced with the PM sheath radius r_0 . Also, the electron thermal velocity (v_e) was replaced by the mean electron velocity (v_{Te}) without indicating any reason. Therefore, the ratio of the two field aligned sheaths is $Z_{\text{DOB}} / Z_{\text{TH}} = 4r_0/a$.

To include the satellite motion effect on current collection, Dobrowolny et al. [1995] further assumed that current collection is,

$$I_{\text{DOB}} = I_{\text{PM}} + \delta I \quad (5)$$

where the first term (I_{PM}) represents the static current given by PM model and the second term (δI) is the current due to the satellite motion, which is given by

$$\delta I = n_e e V_0 A \quad (6)$$

where A is chosen to be the half of the surface area of the PM sheath tube with length Z_{DOB} and equal to ,

$$A = \pi r_0 Z_{\text{DOB}} \quad (7)$$

Substituting the sheath given by Eq. (4) into equations (5), (6), and (7), we can easily prove that the additional current δI is 4 times greater than the PM current. Hence the total current collection predicted by Dobrowolny model [Dobrowolny et al., 1995] (I_{DOB}) is 5 times greater than the PM

current. However, this current prediction model has not shown explicitly the satellite velocity dependence because Drobrowolny et al [1995] did not obtain the sheath by solving the equation of motion.

3. Analyses

In this section a current collection including the effect of motion with an arbitrary orientation is derived. For a satellite moving with an arbitrary angle (θ) with respect to the magnetic field, the current collection region is drawn in Figure 2. This configuration is obtained through shifting the PM current collection tube along the direction of the motion of the satellite. In an arbitrary time of current collection, δt , the number of electrons collected by the satellite is determined by

$$\delta N_e = 2\pi r_0^2 n_{e0} v_e \delta t + (a + r_0) V_0 \delta t Z_{sh} n_{e0} \sin \theta. \quad (9)$$

Here a is the satellite radius; r_0 is the PM sheath radius; δt is the time of current collection; V_0 is the satellite velocity; and Z_{sh} is the length of the field aligned sheath in which electrons can be collected by the moving satellite. Obviously, there are two contributions of electrons being collected by the moving satellite. One is the electrons entering the Parker-Murphy tube through both the beginning and the end of the collection tube along the magnetic field; and the second one is the electrons entering from side surface of the tube due to the motion effect. The collection area will be affected by the orientation of satellite motion and the magnetic field. In general, the derivation assumes that the satellite velocity is much less than the electron thermal velocity. In addition, we have replaced the concave configuration of the PM sheath tube with linear approximation.

With the current proportional to the rate of electron density, the total current collection is derived through

$$I_c \equiv e \frac{\delta N_e}{\delta t} = I_{PM} + (a + r_0) n_{e0} e V_0 Z_{sh} \sin \theta . \quad (10)$$

This equation shows that the current collection is which dependent on both the PM sheath (r_0) and the field aligned sheath (Z_{sh}). Substituting the PM sheath radius (Eq. 2) and the Thompson/Dobrowolny field aligned sheath formula (Eq. 4) into this current collection formula (Eq. 10), the current collection is found to be about $2.5I_{PM}$ for a satellite potential $\phi_s = 300$ Volts and at the angle of $\theta = 90^\circ$. Although this result is in good agreement with the TSS-1R measurement [Thompson et al., 1997], but, it still did not exhibit the precise dependence of the satellite velocity. This is because the assumption of the field aligned sheath inversely proportional to the satellite velocity as used by Thompson (1985) and Dobrowolny et al. (1995).

the distance a we note
~~It is clear from above discussion~~ *the extension is strongly influence* that current collection for a moving satellite essentially depends on the field aligned sheath (Z_{sh}). ~~Using different field aligned sheaths, it obviously gives~~ *will* different current predictions. ~~For example, the Thompson field aligned sheath (Eq. 3) leads to a~~ *as an example.* current about $(1 + (a + r_0) / (\pi r_0)) I_{PM}$, which is ~ 1.3 times greater than the PM current when the potential is high, namely $r_0 \gg a$, the second term toward to $1/\pi$, and ~ 1.6 times greater than the PM current for a non-biased satellite, in which $r_0 \rightarrow a$, the second term becomes $2/\pi$. the Thompson/Dobrowolny field aligned sheath (Eq. 4) leads to a current $\sim 2 - 4$ times greater than the PM current. Dobrowolny et al [1995] obtained a current ~ 5 times greater than the PM current because they thought the plasma flow is perpendicular to the side surface of the PM current collection tube everywhere. Therefore, to study the motion effect on current collection, the most important issue is how to precisely determine the field aligned sheath. Therefore, it is

important to obtain a self-consistent sheath which includes the satellite velocity explicitly in the sheath expression.

To derive a field aligned sheath during the satellite motion, the equation of motion is used to trace each single particle's trajectory,

$$m_e \frac{d\vec{v}}{dt} = -e\nabla\phi + e \frac{\vec{v} \times \vec{B}}{c}. \quad (11)$$

Here, \vec{v} is the velocity vector of electron; ϕ is the electric potential in space; \vec{B} is the external magnetic field vector; m_e is the electron mass; and c is the speed of light. In the cylindrical coordinate system Z -axis is parallel to the magnetic field lines. The origin of the coordinate system is fixed at the center of the satellite. For an electron moving along the guiding center line of the magnetic field, the equation (11) reduces to

$$\frac{dZ}{dt} = v_z = -\sqrt{\frac{2e\phi(Z)}{m_e}}. \quad (12)$$

where Z is the coordinate along the magnetic field lines. Certainly, an electron biased from the guiding center is interacted by an electric field in the direction perpendicular to the B-field. However, this interaction does not significantly affect the motion parallel to the B-field.

When a high positively charged satellite is moving with an arbitrary angle with respect to the magnetic field, there exists a limited height for the PM current collection tube. The electrons within the shaded region can be collected by the satellite as shown in Figure 2; the electrons outside the region can not be collected because, when they come down to the satellite, the satellite has shifted away. Thus, we have the following conditions to determine the arbitrary constant in the integration of equation (12),

$$Z = \frac{Z_{ch}}{2}, \quad \text{when } t = 0, \quad (13)$$

$$Z = 0, \quad \text{when } r = \frac{a}{V_0^+}. \quad (14)$$

Here $V_0^+ = V_0 \sin\theta$ is the projection of the satellite velocity vector in the direction perpendicular to the magnetic field. Therefore, giving a potential distribution along the magnetic field line, we can obtain an analytical expression for the field aligned sheath (Z_{sh}) by solving equation (12).

In general, the time-dependent potential distribution can be self-consistently obtained by solving the Poisson equation. But, the time-dependent particle density distributions are unknown in the surrounding plasmas which are perturbed by the highly biased and moving satellite. Fortunately, the transient results from simulations have indicated that the space potential decreases are quite slow along the magnetic field line relative to the variations in the direction perpendicular to the magnetic field [Singh et al, 1994; Ma & Schunk, 1989]. Thus, the space plasma may have an inverse power law potential along the magnetic field line. Hence, the space potential along the guiding center line of the magnetic field can be expressed as

$$\phi(Z) = \phi_s \left(\frac{a}{Z} \right)^\gamma, \quad (15)$$

where γ is the power index, which is equal to unity for the free space. This type of potential was also used in the PM model. In addition, the power index is shown to be equal to 2 in the distant unmagnetized plasma far from the probe [Whipple 1990].

Substituting equation (15) into equation (12), we obtain the magnetic field aligned sheath Z_{sh} as

$$Z_{sh} = 2 \left(\frac{(\gamma + 2)a}{2V_0 \sin\theta} \sqrt{\frac{2ea^\gamma \phi_s}{m_e}} \right)^{2/(\gamma+2)}. \quad (16)$$

This sheath expression is quite different from the sheaths given by both Thompson [1985] and Dobrowolny et al., [1995]. In their studies, they have assumed the sheath is linearly inverse

proportion to the satellite velocity. This self-consistent derived sheath, however, is non-linearly inverse proportion to the satellite velocity with an index equal to $2/(\gamma + 2)$ which are related to the behavior of the potential distribution. This formula only make sense when the power index γ is non-zero. When γ is zero, the parallel potential equals the satellite potential at all Z . Therefore, there is no parallel electric field and thus no electron collection, which is not physical case.

Substituting this new field aligned sheath (Eq. 16) into the current collection formula (Eq. 10), we obtain current collection with the motion effect as

$$I_c = I_{PM} + 2(a + r_0)(V_0 \sin \theta)^{\gamma/(\gamma+2)} n_{e0} e \left(\frac{3a}{2} \sqrt{\frac{2ea^\gamma \phi_0}{m_e}} \right)^{2/(\gamma+2)} \quad (17)$$

Therefore, the motion effect on current collection increases with increasing both the velocity V_0 and the angle θ only when the potential has a non-zero gradient along the magnetic field (or $\gamma \neq 0$).

When the satellite moves along the magnetic field line (*i.e.*, $\theta = 0$), the field aligned sheath (Z_{sh}) approaches to infinite long. In this case current collection is carried out exactly within the PM sheath tube and thus current collection reduces to the PM current, $I_c \rightarrow I_{PM}$. On the other hand, when the satellite moves in the direction perpendicular to the magnetic field (*i.e.*, $\theta = 90^\circ$), the field aligned sheath and current collection are given respectively by

$$Z_{sh} = 2 \left(\frac{(\gamma + 2)a}{2V_0} \sqrt{\frac{2ea^\gamma \phi_0}{m_e}} \right)^{2/(\gamma+2)} \quad (18)$$

$$I_c \equiv e \frac{dN_{e,c}}{dt_c} = I_{PM} + 2(a + r_0)(V_0)^{\gamma/(\gamma+2)} n_{e0} e \left(\frac{3a}{2} \sqrt{\frac{2ea^\gamma \phi_0}{m_e}} \right)^{2/(\gamma+2)} \quad (19)$$

Both the field aligned sheath (Z_{sh}) and the current collection (I_c) depend on the satellite velocity.

When the velocity tends to zero (or the satellite de-accelerates to the stationary state), the current

being collected by the satellite smoothly goes to the PM current. In the case of TSS-1R measured parameters, our prediction on current collection is ~ 0.5 Amp, which is about 3 times greater than the PM current, and hence in good agreement with the measured data during TSS-1R [Thompson et al., 1997]. Here we have chosen the parameters as: $B = 0.32$ Gausses, $T_e = 0.13$ eV, $n_e = 7 \times 10^{11} \text{ m}^{-3}$, $a = 0.8$ meters, $\phi_s = 300$ Volts, $V_0 = 7.6$ km/s, and $\gamma = 1.6$.

4. Numerical Results and Comparison with TSS-1R Data

To show how current collection is affected by the satellite motion, the numerical studies are performed by using Eq. (17).

Figure 3 shows the currents predicted by both the static PM model and the present model with the motion effect. The horizontal axis is the satellite velocity in meters per second; the vertical axis is the current normalized by the thermal current I_0 which is defined by $I_0 = 2\pi a^2 j_0$. The dotted-dashed line is the PM current and the solid line shows the prediction with the motion effect. To obtain these results, the TSS-1R measured parameters are used. The satellite velocity in this Figure is varied from 1 to 10^4 m/s. Other parameters are fixed as: the satellite potential $\phi_0 = 300$ Volts; the satellite radius $a = 0.8$ meters; the electron density in space $n_e = 7 \times 10^{11} \text{ m}^{-3}$; the plasma temperature $T_e = 0.13$ eV (or ~ 1500 K); the magnetic field $B = 0.32$ Gausses; the orientation angle of motion $\theta = 90^\circ$; and the power index of the potential distribution along the magnetic field line is chosen to be ~ 1.6 in this calculation. It is shown that the motion effect on current collection is dependent of the velocity. When the velocity approaches to zero, current collection smoothly returns to the PM current. However, when the velocity is the typical satellite orbit speed, current collection is approximately 2.7 times greater than the PM current, which is in

good agreement with the data obtained from TSS-1R [Wright Jr. et al., 1996; Thompson et al., 1997].

Figure 4 shows the current collection predicted the present model as a function of the orientation of the satellite movement with respect to the magnetic field (the solid line). The PM current is also plotted for comparison (the dotted-dashed line). The orientation angle is varied from 0 to 90°. The satellite velocity is fixed as 7.6 km/s and other parameters are chosen to be the same as those in Figure 3. It is shown that current collection with the motion effect depends on the orientation of the motion relative to the magnetic field. When the satellite moves perpendicular to the magnetic field, the motion effect on current collection reaches the maximum and could be several times greater than the PM current. However, when the satellite moves parallel to the magnetic field, the motion effect is negligible in which in which the current collection is equal to the value predicted by PM model.

In order to compare the present current collection model with the TSS-1R data in more detail, we plot the third set of current-voltage (IV) survey (3IV24), which yielded highest current and satellite voltage of the mission, against the current collection predicted by the present model (see Figure 5). The third set of IV survey consists 6 IV scans and hence 6 plots. Each plot has 4 curves. The red solid circles are the TSS-1R data points. The green triangles are the Parker-Murphy currents. The blue hollow circles and squares are the predictions by the present model at $\gamma = 1.6$ and at $\gamma = 2.0$ respectively. These data are deduced from Italian Langmuir probe dataset. Table 1 gives the plasma parameters for the 6 IV plots. It is found, from the 6 IV plots, that the present model predictions on current collection are very good in agreement with the TSS-1R data (the third IV survey) if the power index γ is chosen in the range of $\sim 1.6 - 2$. The present model at $\gamma = 2.0$ fits the data shown in the first two IV scans (3IV24-1 and 3IV24-2) very well and at $\gamma = 1.6$ fits the data of the 4th and 5th IV scans (i.e., 3IV24-4 and 3IV24-5). The data points shown

in the third and 6th IV scans (i.e., 3IV24-3 and 3IV24-6), however, fall between $\gamma = 1.6$ and $\gamma = 2.0$ curves

The TSS-1R data shown in different IV scans are bound to be different because they were measured in different time periods and under different plasma conditions. Even in one IV scan, the plasma parameters could also be varied since the tethered satellite system traveled at 7.732 km/s and each scan lasted 64 seconds. In the 6 IV scans, typical (averaged) plasma parameters are (deduced from Italian Langmuir probe dataset) used (Table 1). As we can see from Table 1, the first 3 IV scans have lower temperatures and higher densities in comparison with the last 3 IV scans. Therefore, in the low temperature and high density cases, the measurements are in agreement with the prediction by the present model at $\gamma = 2.0$; while, in the high temperature and low density cases, the measurements are in agreement with the prediction by the present model at $\gamma = 1.6$. We could not use a unique constant value of γ to fit all the data shown in the 6 plots. One possible reason may be due to the measurements. It is known that the both temperatures and densities of electron are indirectly measured during TSS-1R. Also the magnetic fields might not take the same angles with respect to the motion for cases corresponding to the 6 IV scans.

Another reason may be due to the plasma (or Debye) sheath effects which are not included in both the present and the PM models. From the Table 1 we see that the Debye sheath length corresponding to the first 3 IV scans is ~ 2 times smaller than that corresponding to the last 3 IV scans. That is, the Debye sheath effects are stronger in the first 3 IV scans than those in the last 3 IV scans. On the other hand, if we maintain the γ as a unique constant value, the present model only includes a constant plasma effect which are independent of the characteristics of the ambient plasma. Thus, it is understandable why less currents (relative to the currents predicted by the present model at a definite γ) were collected in the first 3 IV scans by the satellite than in the last 3 IV scans (Figure 6). The Debye sheath affects current collection probably through affecting the

PM sheath radius and the sheath size along the magnetic field lines, since the Debye sheath affects the potential distribution in ambient plasmas.

In the present model, we emphasize our study on the satellite motion effect on current collection. The power law potentials are assumed in the present model (also in the PM model). Thus, to compare the present model with the data shown in different IV scans, the power index γ is estimated as in a range (e.g. 1.6 to 2) instead of a unique value. To consider the variations of the Debye sheath effect, a better and hence more complicated potential formula than Eq. (15) is required. It must be dependent on the plasma characteristics such as the density, temperature, and the magnetic field, in which an analytical solution of the field aligned sheath may not be obtained. That is what we will study in the future.

5. Summary and Conclusions

We have studied current collection by a moving and highly biased satellite in LEO space. We first derived a current collection formula through modifying the static PM model with the motion effect which depends on how to determine the field aligned sheath. In order to obtain a realistic expression for the field aligned sheath, we then solved the equation of motion of electron. This new sheath expression leads to current collection explicitly dependence of the satellite velocity. When the satellite velocity approaches to zero, the current predicted by the present model returns to the PM current. However, for a satellite with a typical satellite velocity such as the TSS-1R mission, the predicted current is $\sim 2-4$ times greater than the PM current, which is in good agreement with the data measured during TSS-1R. We have also considered the orientation effect on current collection. To obtain the present sheath and current expressions, we have assumed that the satellite moves along a direction with an arbitrary angle relative to the magnetic field. It shows the current collection with the motion effect being orientation dependence. For a

satellite moving perpendicular to the magnetic field line, it collects a current 2-4 times greater than the PM current in agreement with the TSS-1R measurements. The motion effect, however, is negligible when the satellite moves along the magnetic field line. Finally we have numerically shown the relations in more detail between the satellite motion effect on current collection in space and various variables such as the satellite velocity and the orientation angle. We have also plotted the IV predictions in association with the third set IV survey of the TSS-1R data. It is shown that the data measured at low temperature and high density cases fit well the present $\gamma = 2.0$; while the data measured at high temperature and low density cases fit well the present model at $\gamma = 1.6$.

Acknowledgments. This work was supported by NASA under contract NAS8-37107.

References

- Antoniades, J. A., R. G. Greeves, D. A. Boyd, and R. F. Ellis, Current collection by high voltage anodes in near ionospheric conditions, NASA CP-3089, 202, 1990.
- Colombo, G., E. M. Gaposchkin, M. D. Grossi and G. L. Weiffenbach: Smithsonian Astrophys. Observatory, Rep. Geoastron., 1, Sept. issue, 1974.
- Dobrowolny, M., U. Guidoni, E. Melchioni, G. Vannaroni, and J. P. Lebreton, Current-voltage characteristics of the TSS 1 satellite, JGR, 100, 23,953, 1995.
- Dobrowolny, M., U. and Stone N. H., A technical overview of TSS-1: the first tethered-satellite system mission. IL Nuovo Cimento, 17, 1, 1994.
- Grossi M. D., NASA contractor report NAS 8-28203, May 11, 1973.

- Hwang K. S., S. T. Wu, N. H. Stone, and K. H. Jr. Wright, Current collection model on tether satellite system, AIAA-90-0723, 28th AIAA Aerospace Sciences Meeting, Reno, Nevada, Jan., 1990.
- Ma, T. Z. and R. W. Schunk, 3-D time-dependent simulations of the tethered satellite-ionosphere interaction, , 1989.
- Myers, N. B., W. J. Raitt, B. E. Gilchrist, P. M. Banks, T. Neubert, and P. R. Williams, A comparison of current voltage relationships of collectors in the Earth's ionosphere with and without electron beam emission. *GRL*, 16, 365, 1989.
- Parker, L. W., and B. L. Murphy, Potential buildup on an electron-emitting ionospheric satellite, *JGR*, 72, 1631, 1967.
- Quinn, R. G., and C. C. Chang, Laboratory observations of a stable plasma trapped in a permanent dipolar magnetic field, *JGR*, 71, 253, 1966.
- Sanmartin, J. R., Theory of a probe in a strong magnetic field, *Phys. Fluids*, 13, 103, 1970.
- Shiah, A., K. S. Hwang, S. T. Wu, and N. H. Stone, Three-dimensional simulation of current collection in space. *Planet. Space Sci.*, July, 1997 (in press).
- Singh, N., and V. S. Chaganti, Electron collection by a highly positive satellite in the ionosphere: Test particle simulation. *JGR*, 99, 469, 1994.
- Sorensen, J., N. H. Stone, and K. H. Wright (private communication), 1996.
- Stone, N. H., and C. Bonifazi, The TSS-1R mission: overview and scientific context, *GRL*, 1997.
- Thompson, D. C., C. Bonifazi, B. E. Gilchrist, S. D. Williams, W. J. Raitt, J.-P. Lebreton, W. J. Burke, The current-voltage characteristics of a large probe in low earth orbit: TSS-1R results, *GRL*, 1997.

Thompson, W. B., Preliminary investigation of the electrodynamic of a conducting tether, in
Spacecraft Environmental Technology 1983, edited by C . K. Purvis and C. P. Pike, NASA
Conf. Publ., 2359, 649, 1985.

Whipple E. C., Current collection from an unmagnetized plasma: a tutorial, Proceedings of
Workshop on Current Collection from Space Plasmas (NASA Conference Publication 3089),
1, 1990.

Wright Jr. K. H., N. H. Stone, J. D. Winningham, C. Gurgiolo, C. Bonifazi, B. Gilchrist, M.
Dobrowolny, F. Mariani, and D. Hardy, Satellite particle collection during active states of the
tetherd satellite system (TSS), 27th AIAA Plasmadynamics and Lasers Conference, 2298,
1996.

Figure Captions

Fig. 1. The Parker-Murphy (PM)current collection tube. Here a denotes the satellite radius and
 r_0 refers to the PM sheath radius. The current was shown to be mainly collected along the
magnetic field line.

Fig. 2. The current collection region for a moving satellite which is obtained by shifting the
satellite. The orientation of the motion is considered to have an arbitrary angle (θ) with
respect to the magnetic field line. Here the V_0 is the satellite velocity; δt (in the text we
use t_c) is the time of collection; and Z_{sh} is the sheath along the magnetic field. The plasma
velocity flow also contributes the current collection.

Fig. 3. Current collection with motion effect (the solid line) and the PM current (the dotted-
dashed line) vs. the satellite potentials. Parameters are chosen to be those measured
during TSS-1R. All currents are normalized by the thermal current.

Fig. 4. Current collection with the motion effect vs. the orientation angle of the motion (the solid line); the PM current is also drawn for comparison (the dotted-dashed line).

Fig. 5. The third set of IV survey (3IV24) on the TSS-1R data is plotted against the current predictions by both the present and PM models. The present model at $\gamma = 2.0$ fits the data shown in the first two IV scans and at $\gamma = 1.6$ fits the 4th and 5th IV scans. The data points shown in the third and 6th IV scans, however, fall between $\gamma = 1.6$ and $\gamma = 2.0$ curves.

Table 1: Plasma parameters in the 6 IV scans

IV Scan	Temperature (K)	Density ($\times 10^5 \text{ cm}^{-3}$)	B field (Gausses)
1	1500	8.0	0.319
2	1650	8.1	0.320
3	1000	6.5 - 8.0	0.321
4	2550	2.8	0.327
5	2800	3.0	0.326
6	2300	3.6	0.322

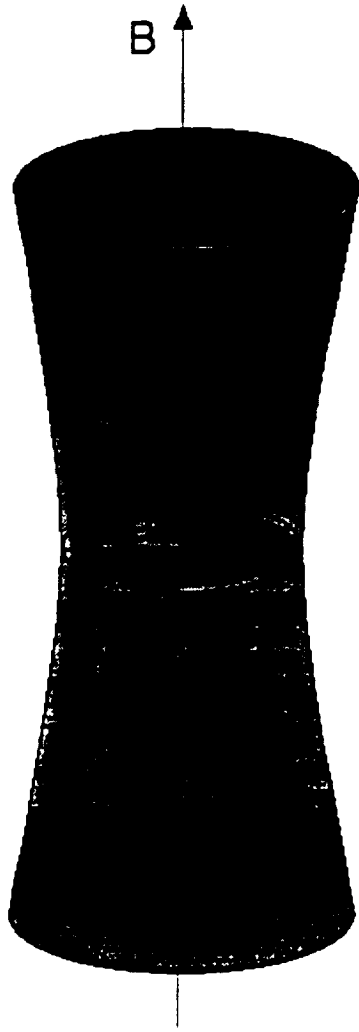


Figure 1

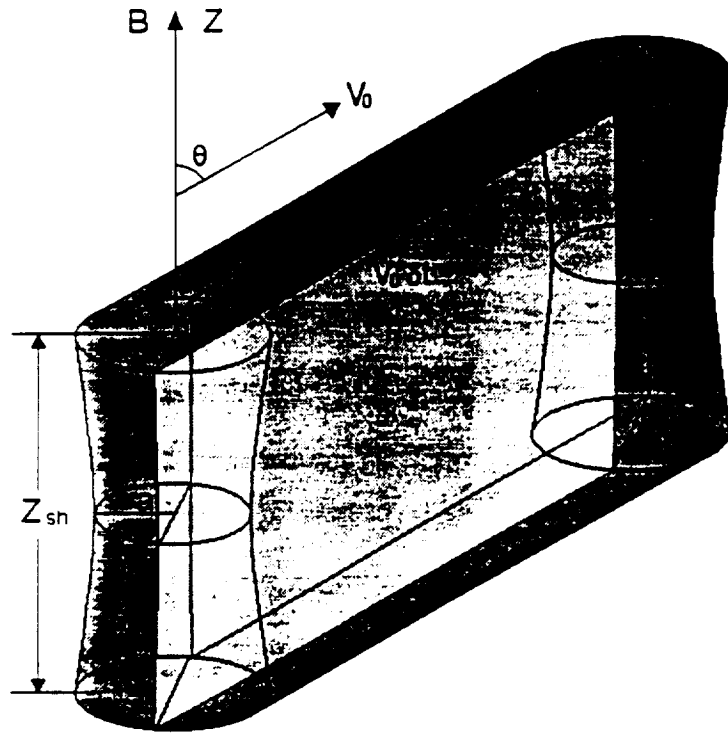
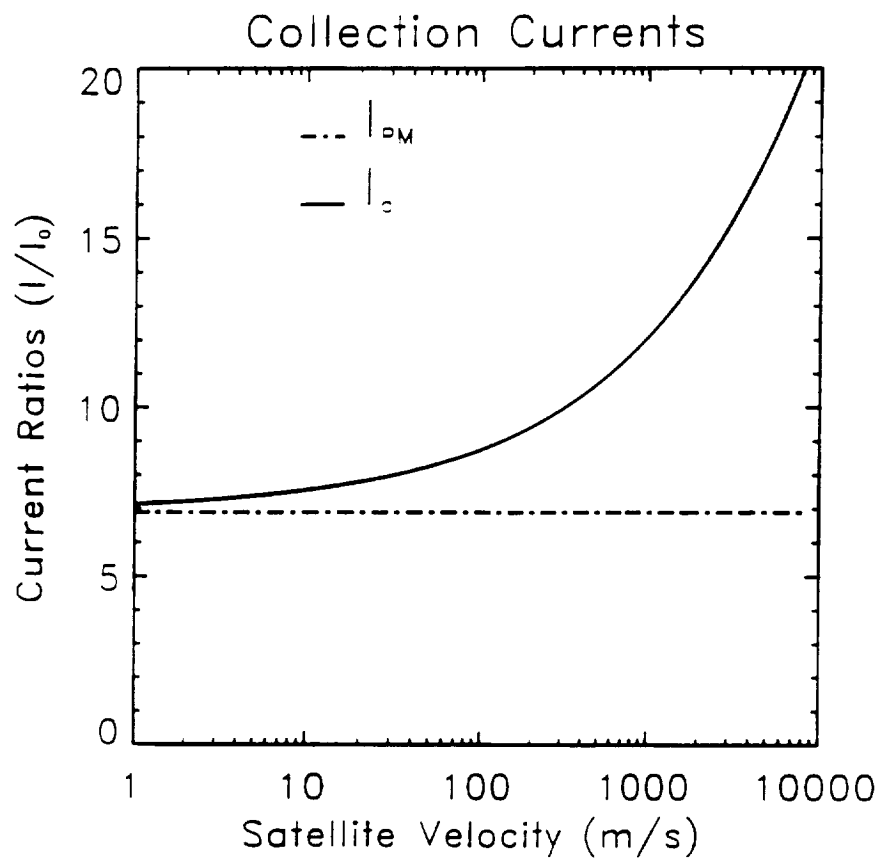
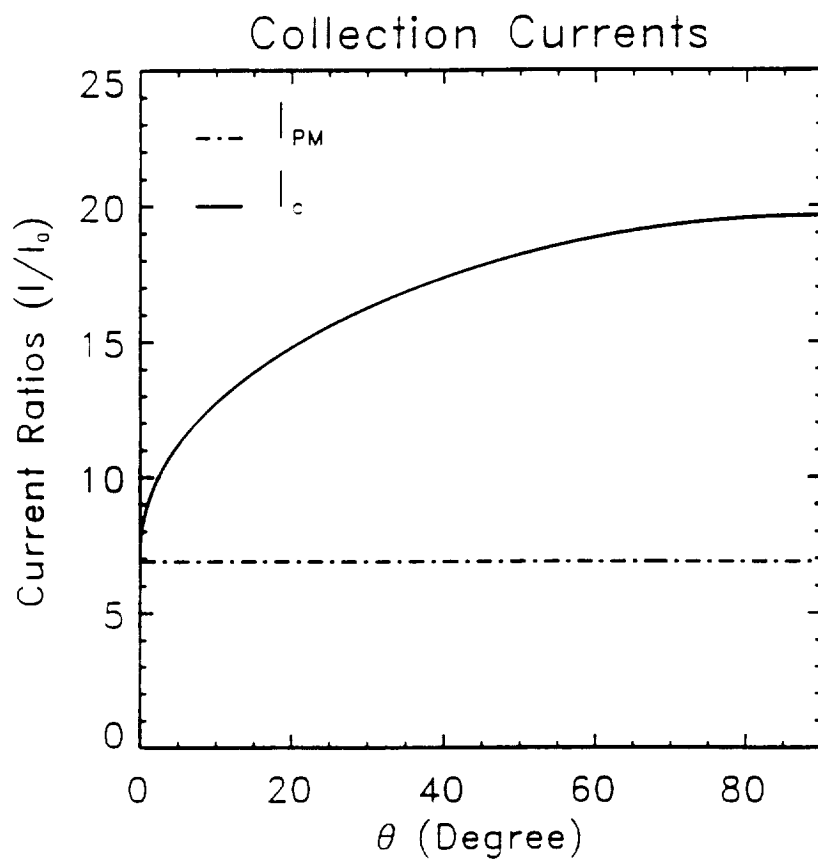
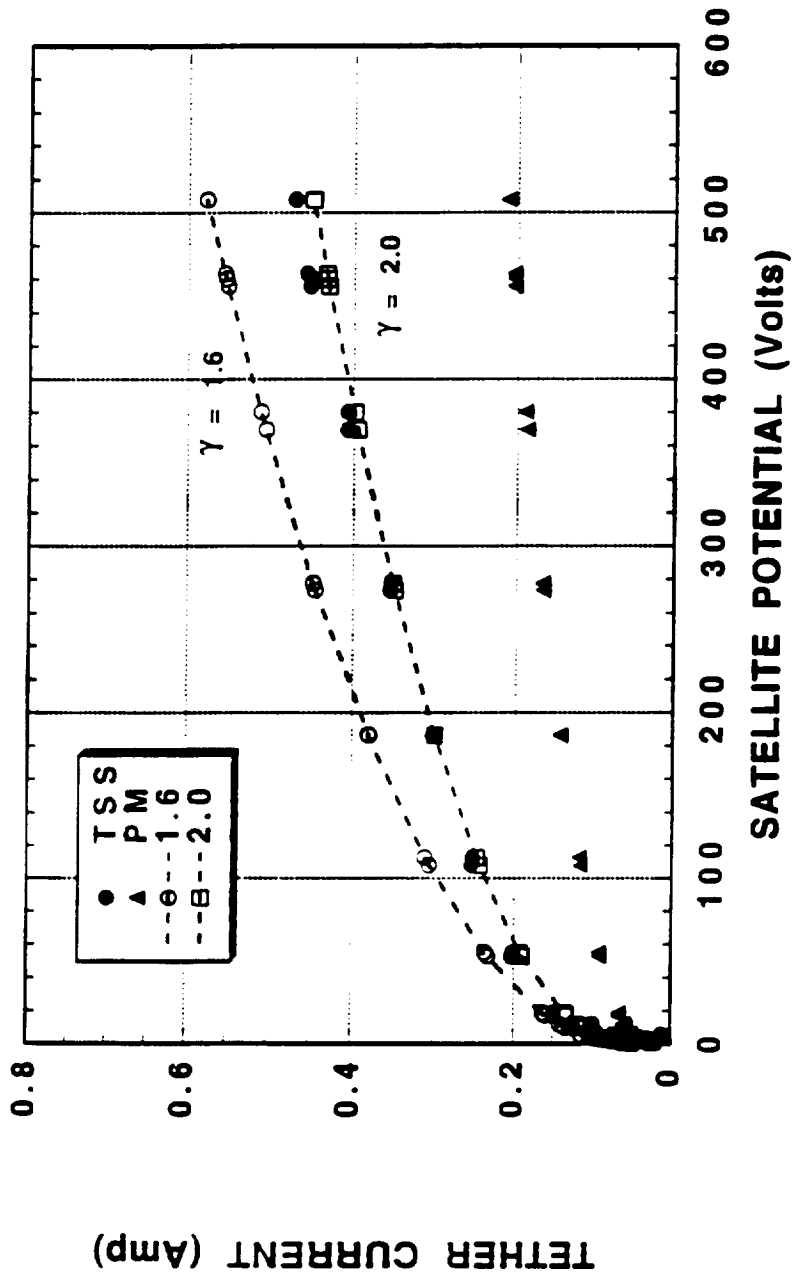


Figure 2

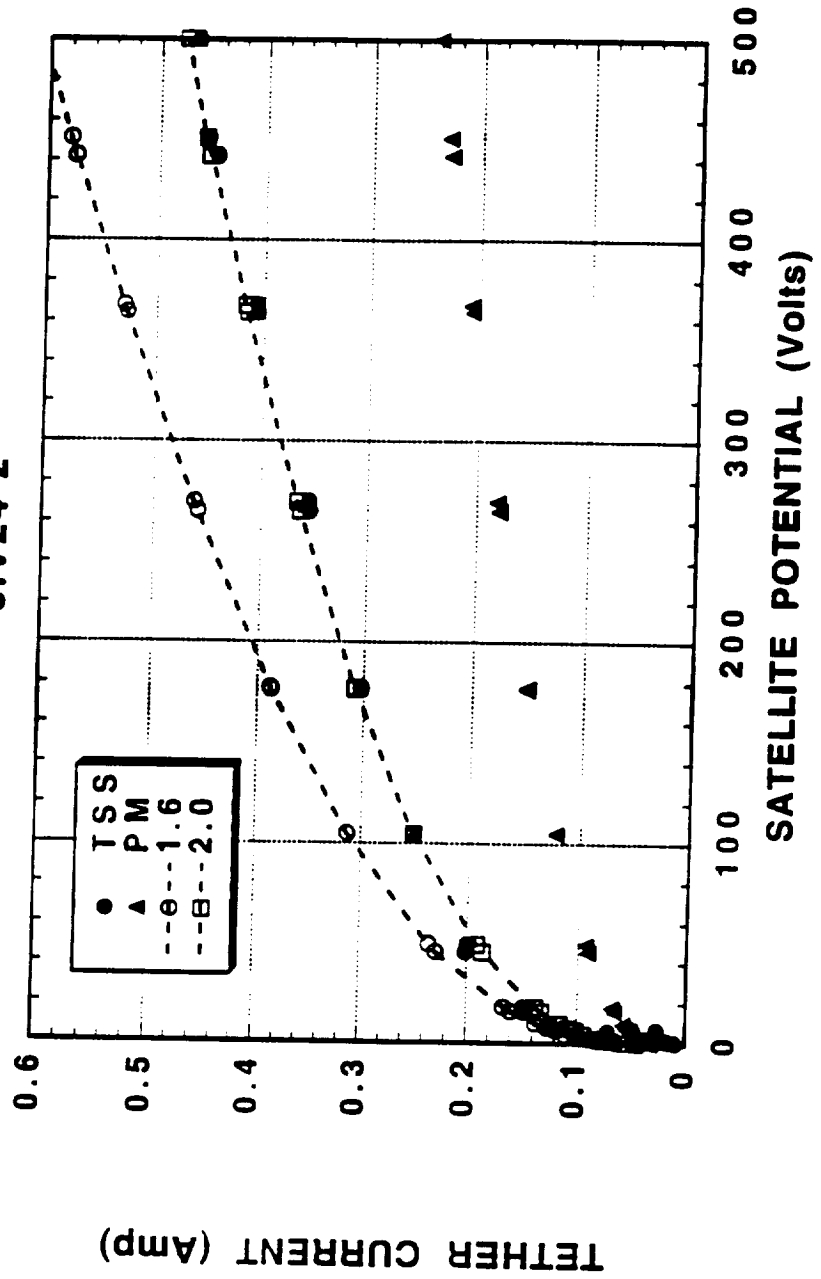




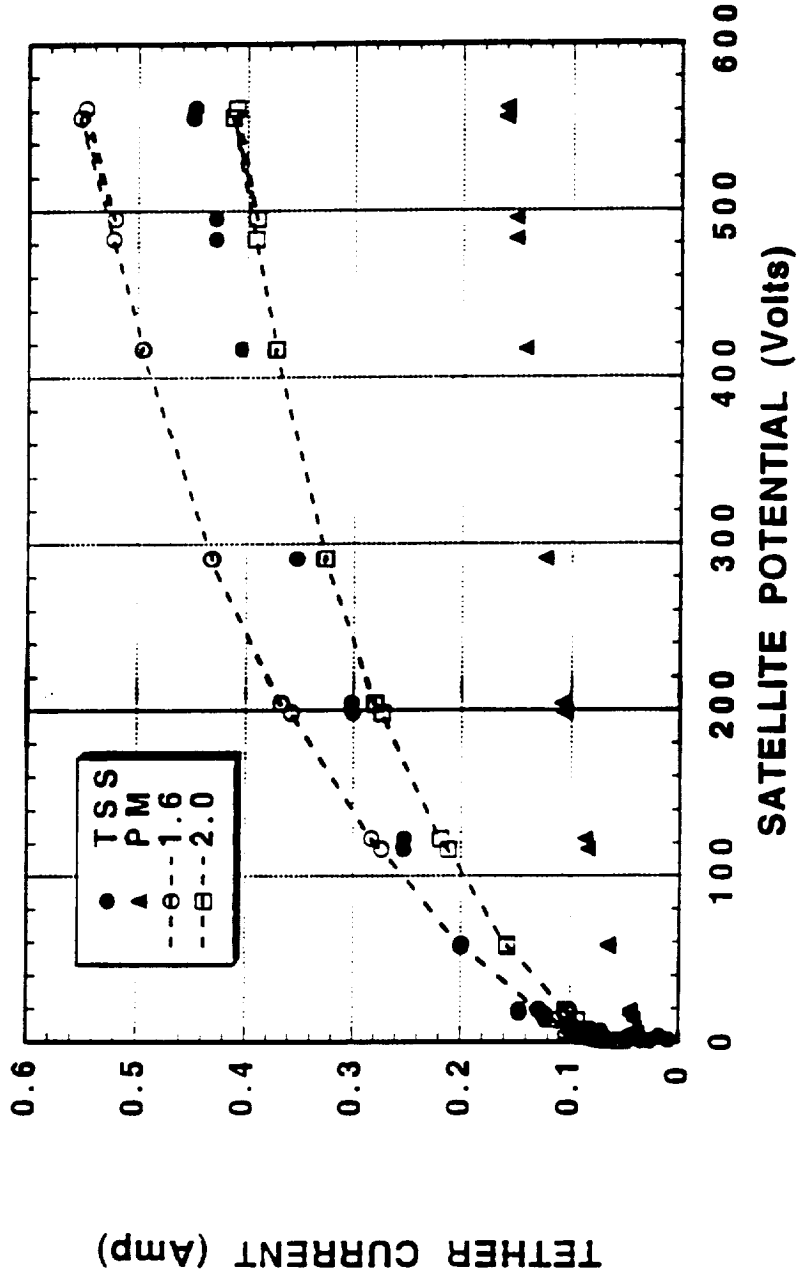
31V24-1



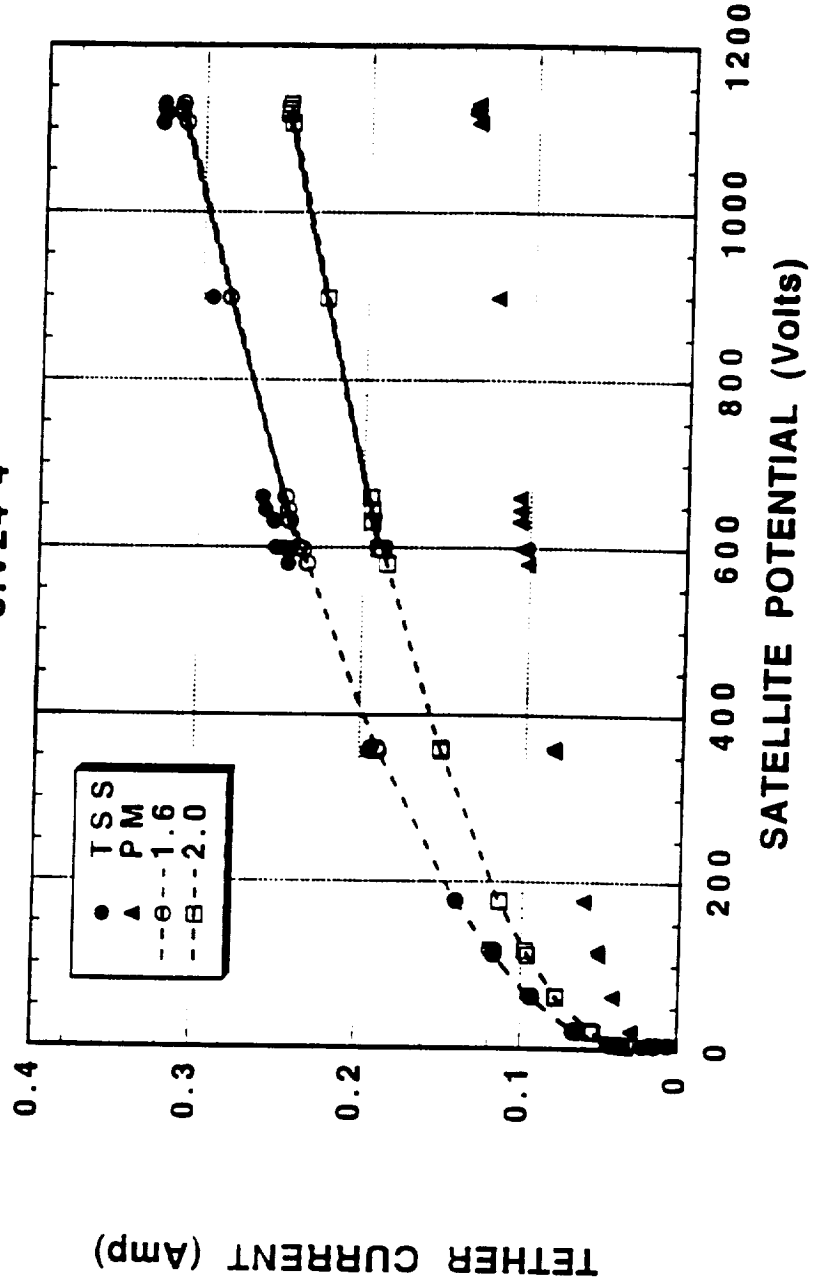
3IV24-2



3IV24-3

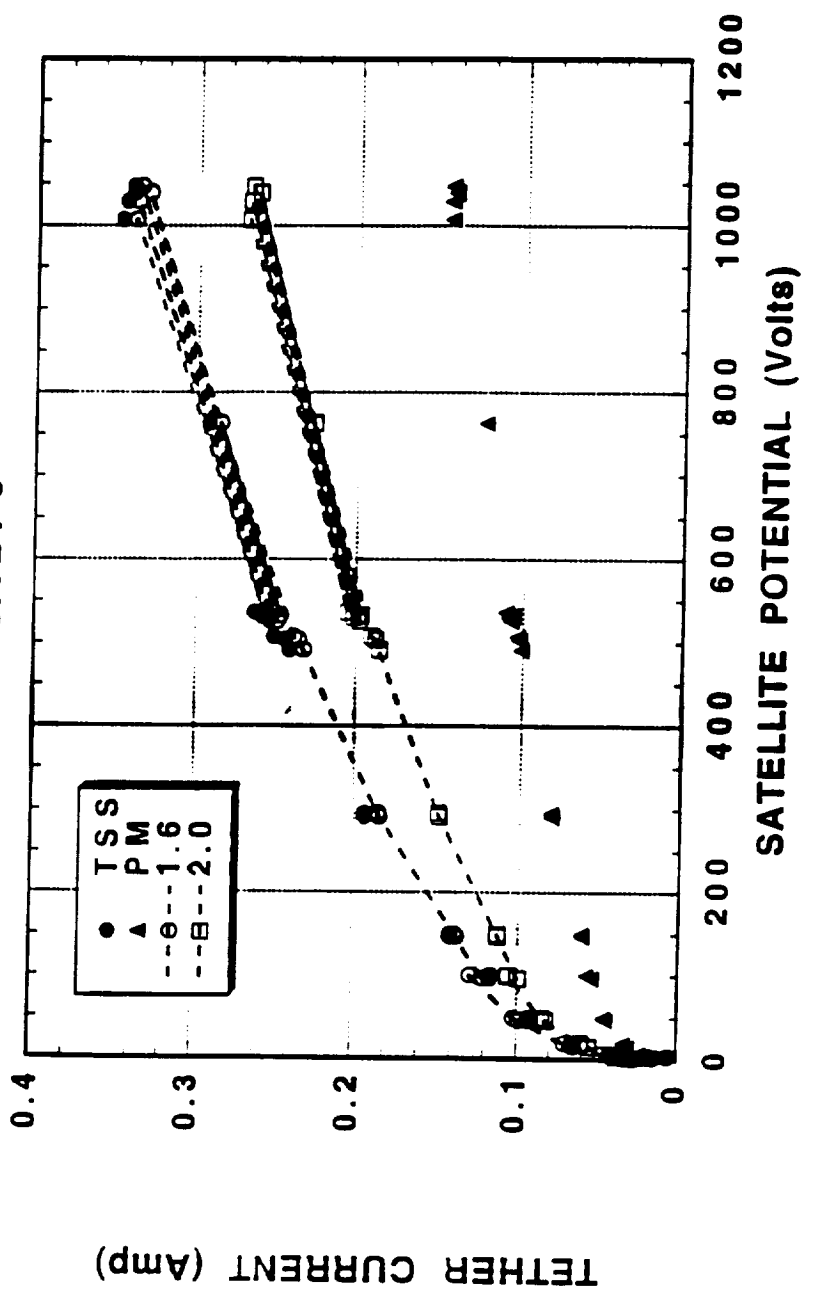


3IV24-4

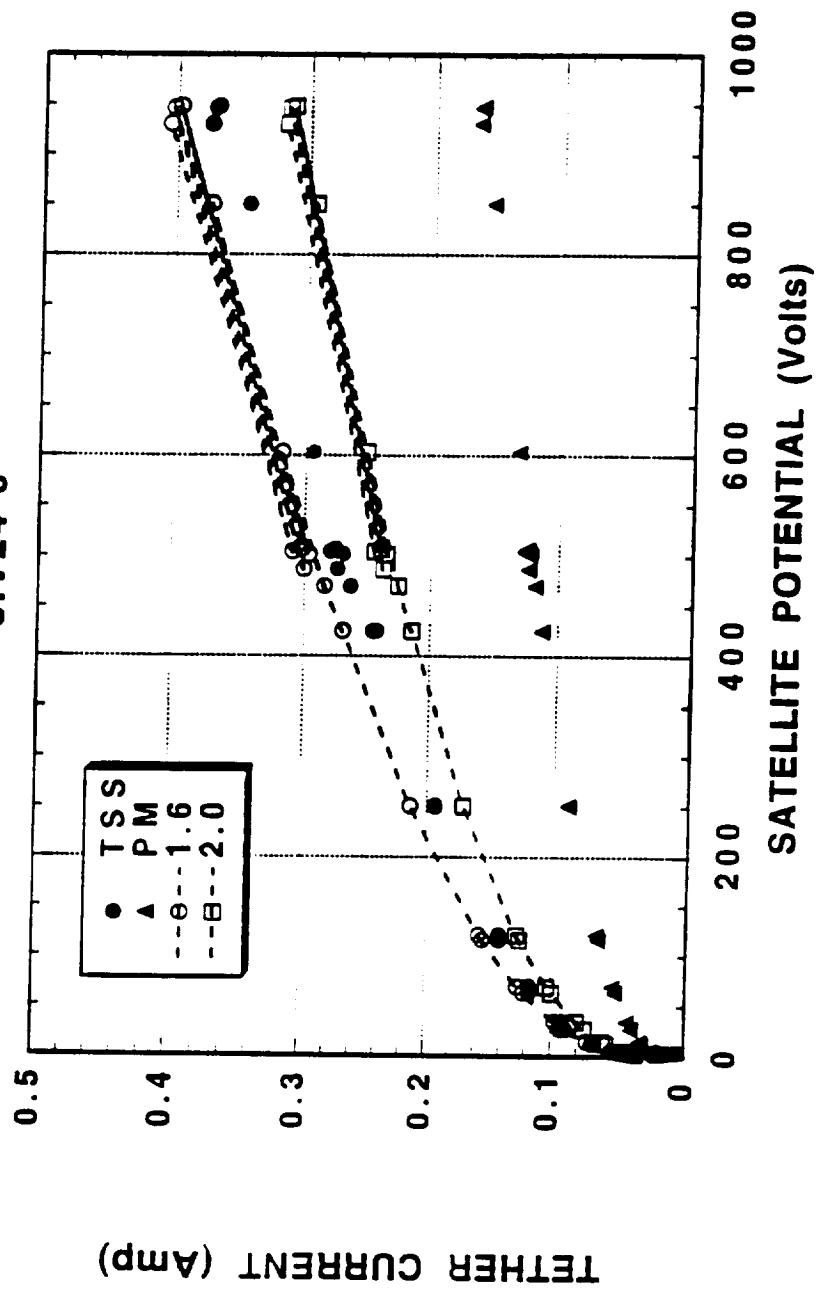


(1)

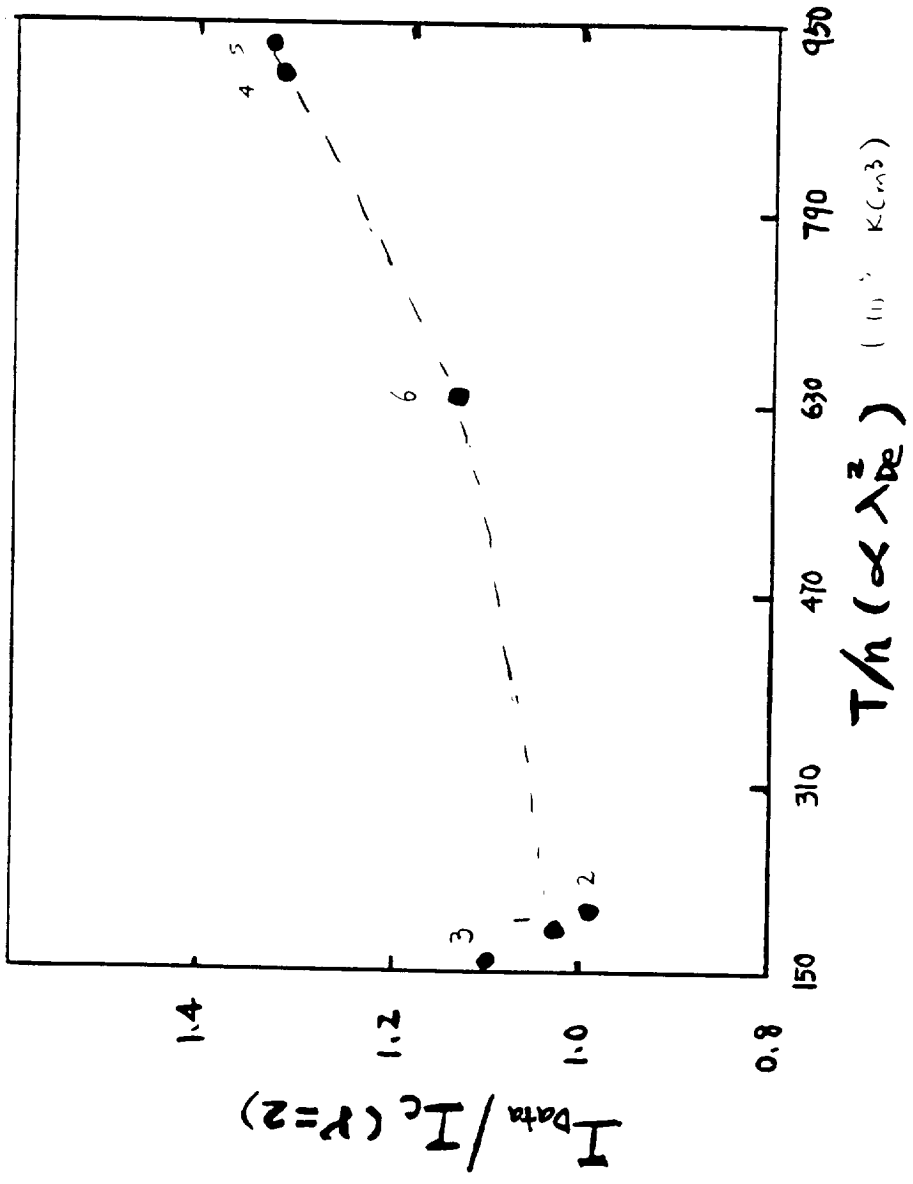
3IV24-5



3IV24-6



10000 Males



T. X. Zhang
Center for Space Plasma and
Aeronomic Research
Univ. of Alabama in Huntsville
Huntsville, AL 35899

June 23, 1998

Dear Dr. Chialie:

I was glad to talk to you on phone today. Now, I send you the paper.

I made some changes at the top of page 10 about the discussion for the case at $\gamma = 0$ according to your comments. Section 4 was rewritten, which needs your correction decision.

Best wishes.

Your sincerely



T. X.. Zhang

APPENDIX 18

Numerical Simulation of the SPES Instrument Operation Aboard TSS-1R – A Progress Report

S. Riyopoulos, D. P. Chernin, C. L. Chang, and A. T. Drobot
SAIC
1710 Goodridge Dr., McLean VA 22102

Abstract

Numerical simulations using the 2D PIC code MASK have been employed to evaluate the performance of the SPES spectrometer operation during the TSS-1R shuttle flight. We searched for possible pathways whereby false spectrometer energy readings are produced by spurious electrons, somehow originating inside the device, and not entering through collimator slit of the SPES instrument. By exhausting the plausible mechanisms involving secondary electron generation inside the instrument we have so far found no evidence that this is the cause of false readings.

I. Introduction

Determining the current-voltage characteristics was one of the primary goals of the Tethered Satellite System re-flight mission (TSS-1R) of the TSS satellite orbiting in the ionosphere. The current was measured directly with accuracy while the satellite potential was deduced from a circuit model involving the plasma sheaths between the satellite or the space shuttle and the ambient plasma ground. Energy spectrometers residing on the tethered satellite surface recorded the energy spectrum for the electrons accelerated through the sheath, thus providing a possible mean to measure the satellite potential.

The experimentally observed spectrometer energy fluxes as shown in Figs 1a-1c were taken during the first IV24 cycle by ROPE investigation. The peak in the energy distribution corresponds roughly to the anticipated value of the sheath voltage. However, a broad background of energy flux is observed to extend all the way up to energies higher than what sheath can provide. In fact, the energy flux of background electrons increases with the stepping current pulses to the point where the peak and the background merge into a broad band extended all the way up to about 200 eV. The

result is puzzling given that the estimated sheath potential at these current pulses is not expected to exceed 200 Volts.

In this report we investigate the possibility of spurious measurements caused by stray, low energy secondary electrons or other charged particles originating inside the instrument, reaching the spectrometer slit and register as high energy population. The primary goal of this report is to explore possible pathways of false spectrometer reading by spurious electrons, using numerical simulations employing the 2D PIC code MASK.

To put our investigation in proper context, a circuit equivalent of the shuttle-satellite system is shown in Fig. 2. Here V_{sat} and V_{shu} are, respectively, the voltage differences between the satellite or the shuttle surface, and the ambient plasma. Notice that the satellite and the shuttle surfaces serve as the capacitor plates surrounded by an electron and an ion sheath respectively (the other two "plates" correspond to the undisturbed plasma far away). The voltage source V_{ExB} corresponds to the potential induced across the wire (tether) of length L by moving through the earth's magnetic field, while R is the wire resistance. Voltage balance requires

$$V_{ExB} + I_0 R + V_{sat} + V_{shu} = 0 \quad (1)$$

An electron current I_e and an ion current I_i pass through the satellite and the shuttle sheaths. The upper limits for the electron/ion current densities are given by the Child-Langmuir law

$$\frac{V^{3/2}}{L^2} \frac{e^{1/2}}{m^{1/2}}, \quad \frac{V^{3/2}}{L^2} \frac{(Ze)^{1/2}}{M^{1/2}} \quad (2)$$

Because of the much higher ion mass $M \gg m$, the total ion current cannot match that of the electrons, as that would take an ion collection area orders of magnitude larger than the electron collection area and/or a shuttle sheath voltage much higher than the satellite voltage. Current conservation takes place by electron expulsion from the shuttle through the current I_g delivered by electron gun assembly (EGA) onboard shuttle so that

$$I_e = I_o = I_g + I_i \quad (3)$$

Current level delivered by EGA's is controlled in part by the temperature of the cathode emitter in operation. Changing the current level in IV24 pulses

affects the voltage distribution along the tether circuit. Therefore, current steppings in the IV24 cycle provide an effective current-voltage scan on the satellite side.

II. Numerical Simulation of the SPES Instrument

A series of numerical particle simulations using the code MASK was undertaken to uncover potential mechanisms of stray electrons arriving at the detector slit through paths other than the collimator slit. Those hypothetical electrons, generated inside the apparatus via either secondary emission, photo-ionization, or other unspecified process would not have the same energy as those passing through the collimator, thus yielding false readings.

The simulation area is shown in Fig. 3a-3b. The particles are orbiting in fixed externally applied fields (self-fields are negligible), including the earth's magnetic field of the order of 0.4 Gauss. Both a symmetric arrangement (with both the ion and electron collection slits) and an asymmetric one (only the electron collection slit) were tested. The corresponding equal potential surfaces are shown in Figs. 3a and 3b respectively. Typical electron trajectories inside the instrument are shown in Fig. 4. It was confirmed that there is hardly any observable difference in the numerical electron spectrometry between symmetric and non-symmetric configuration. Therefore, the arrangement of using only the electron collection slit was employed to reduce computation time. It was also confirmed that flipping the magnetic field direction did not produce any discernible difference in the particle orbits, provided that the injected energies exceed 0.5 eV.

A numerical calibration test was done by recording the flux at the detector slit of electrons injected with nearly constant energy and narrow velocity angle cone $\Delta\theta = 5^\circ$, as determined by the collimator specifications. The voltage at the deflection plates was held constant as the injection energy was swept through a range, and the collected current vs. injected energy was recorded, as plotted in Fig. 5. The ratio of the injected electron energy E_m , which corresponded to maximum collected current, to the deflection plate voltage V was compared with the experiment. This ratio is approximately constant and yields the calibration curve $E_m = A \times V$ of the instrument.

The numerical grid size was successively refined until the measured value of A converged. We found that going beyond a 200×200 mesh resolution lead to no significant change in A . The numerically measured value $A = 11$ is off from that of the SPES instrument (12.5) by about 10%. The difference is partly attributed to the stair-step surface boundaries, resulting by modeling a cylindrical surface with a rectangular mesh. This generates high field harmonics acting on the particles grazing the deflection plates.

In addressing the possibility of stray electrons it is easier to start with numerical electrons at the slit and march them backwards in time (i.e. negative time step dt in the code), taking advantage of the time-reversibility in the equations of motion. Such approach yields all the possible initial conditions and locations of electrons that can reach the detector slit. The parameter space subjected for search involves only the energy and angle spread of the impacting electrons entering the detector slit. It is therefore much easier to identify all the possible origins of electrons entering the detector slit.

For each of a typical backward trace runs, the initial conditions include a monochromatic energy electron bunch, with a uniform distribution of electron velocities within a cone of angle θ around the surface vertical. For fixed deflection plate voltage the run is repeated with different electron energies until an energy range is covered. The reliability of the backward integration involved first marching electrons forward from the collimator slit to the detector slit and registering their impact energy and velocity at the detector slit. A subsequent backward trace from the final conditions should then bring these electrons back to the collimator slit of the instrument.

Typical backward traces for electrons registered at the slit with impact angles between -45 and $+45$ degrees from surface vertical are shown in Figs. 6-7. Electron energy is coded in color. We are interested primarily in backward orbits intersecting some physical structures, such as the light trap surface or the deflection plate itself. Because such intersections imply that secondaries produced by particles impacting these surfaces at specific energies could actually reach the detector slit. From figures 6 and 7, we can see that electrons reaching the slit at impact energy E could originate from the light trap (Fig. 7) or the deflection plate (Figs. 6 and 7) with initial energies $E + 1$ eV and $E + 20$ eV, respectively. The second case is highly improbable, given that most of the secondaries are emitted with energies of a few eVs, regardless of the primary impact energy, and well below the 20

eV required to overcome the potential barrier between the deflection plate and the detection slit. The remote possibility is a small fraction of deflection plate secondaries, emitted at energy equal to that of the impacting primary through elastic backscattering, which could in principle overcome the potential gap. The first case involves low energy secondaries ejected from the light trap surface reaching the detection slit. However, since the surface of light trap is plated in gold, the yield for secondaries is too low for a substantial electron production if the primary particles are electrons energized in the sheaths. For instance, energies of primary electrons in Fig. 1 are in the range of 10-50 eV, well below the impact energy for secondary yield equal to 1 (the maximum yield for gold is 0.15 at impacting energy of 50 eV). Furthermore, at issue is the accessibility of the light trap surfaces to the primary electrons. Backward traces from the light trap surfaces were performed to determine the possible origins of primary electrons that are sufficiently energetic to produce secondaries. The result is shown in Fig. 8. It was found that such electrons do not come from the collimator slit. Instead, they are produced either at high initial energy from the tail end of the deflection plate, or behind the deflection plate, or at low energy from the surface of the detector plate (other than the slit). None of these scenarios are likely in reality.

It is therefore deemed that secondary electrons are not the cause of the high background energy flux registered by the SPES instrument. In particular, any attempt to identify the origin of the background should also explain, not only the origin and high values of the recorded energy flux in the background energy tail, but also (i) the exponential increase in the integrated background energy flux with the linear increase in the sheath voltage and (ii) the apparent uniformity in the energy flux with E , suggesting an $E^{-(3/2)}$ dependence of the background number density.

It is well known that, in a uniform field electrostatic spectrometer, the deflection angle depends only on the energy and the charge, regardless of the mass of the charged particle. Therefore, the possibility arises that negative ions passing through the collimator, such as H-, O-, and N-, reach the detection slit and register as electrons, creating the observed background. Test particle runs, such as in Figs. 9 and 10, confirmed this scenario. For a given deflection plate voltage, the energies of H-, O-, N- ions and electrons registering at the slit are approximately equal. So, practically speaking, there is no way to distinguish between electrons or single charge negative ions. There are several issues needing to be resolved

before proposing negative ions as the source for the enhanced background energy flux. The first issue is identifying the electron attachment mechanisms and the production rates of the negative ions, since they are not part of the ionospheric plasma at 300 km height. The second issue is explaining the enhanced reading in energy flux, considering one electron exchange for one negative ion. The third issue is relating the impinging negative ions to the exponential increase in the observed integrated flux with sheath potential.

III. Conclusions

The use of numerical simulations has excluded, by the process of elimination, most of the plausible scenarios that stray electrons, produced by secondary emission somewhere inside the instrument, yield false instrument readings and are responsible for the broad background energy flux and the high energetic tails recorded by the SPES instrument. The possibility of contributing negatively charged ions, created and energized in the sheaths outside the instrument, remains to be resolved.

Figure Captions

Fig. 1. Energy flux spectra produced during the TSS-1R flight for low circuit current / sheath voltages.

Fig 2. Schematic layout of the equivalent TSS circuit.

Fig 3. Illustration of the simulation geometry and the resulting equal potential contours employed for the SPES spectrometer (a) both ion and electron detectors present (b) electron detector only.

Fig 4. Electron trajectories inside the instrument for injected e-beam energy of 230 eV and deflection plate voltage of 20 V.

Fig 5. Calibration showing the fraction of electron beam current arriving at the detector slit as a function of the injected beam energy. The two different curves correspond to numerical spatial resolutions of 100x100 and 200x200 grid points covering the simulation area. The curves for symmetric and non-symmetric detector arrangements coincide.

Fig 6. Backward tracing of electrons that have arrived at the detector slit with energy 1 eV and a uniform velocity distribution within 45° angle from surface vertical. The color code indicates energy in eV.

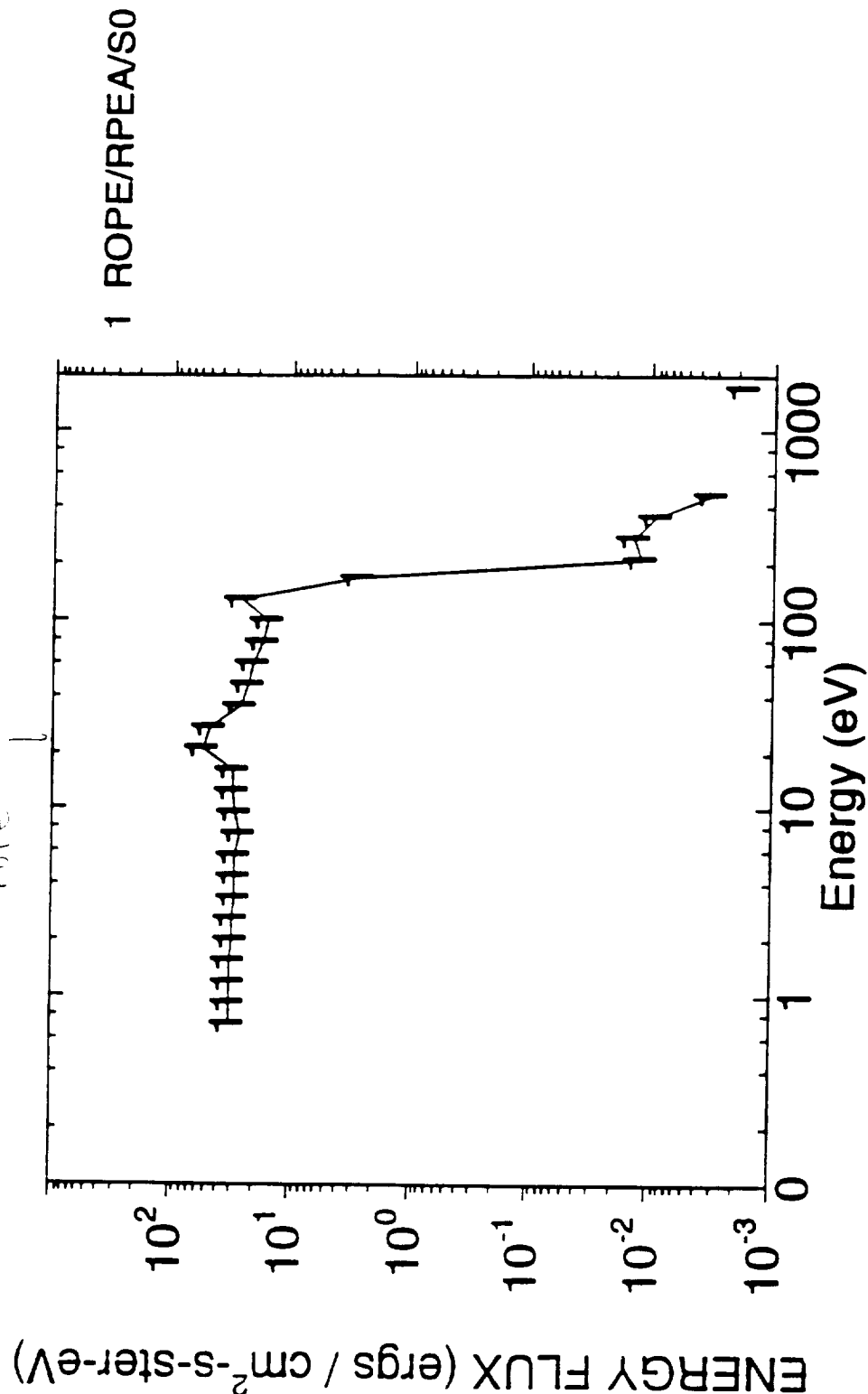
Fig 7. Same as Fig 5. for 25 eV electrons.

Fig 8. Backward tracing of electrons to determine possible origin of primaries that could hit the light trap. The electrons are uniformly distributed over the surface with gaussian velocity distribution and vertical impact energy of 1 eV.

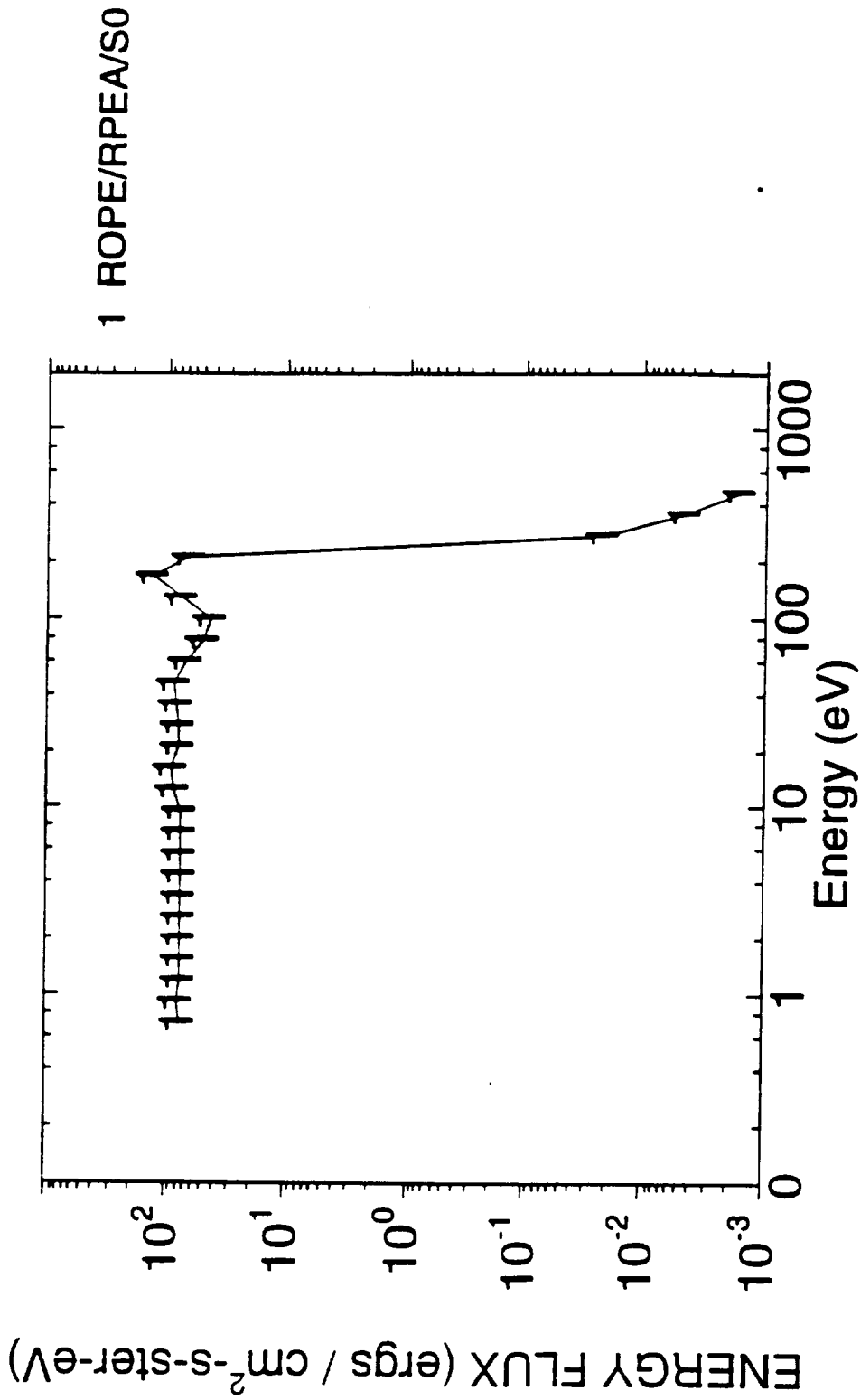
Fig 9. Trajectories of O⁻ ions injected through the spectrometer slit at 230 eV at 20 V deflection voltage. Note the similarity with the electron trajectories of the same parameters in Fig. 4.

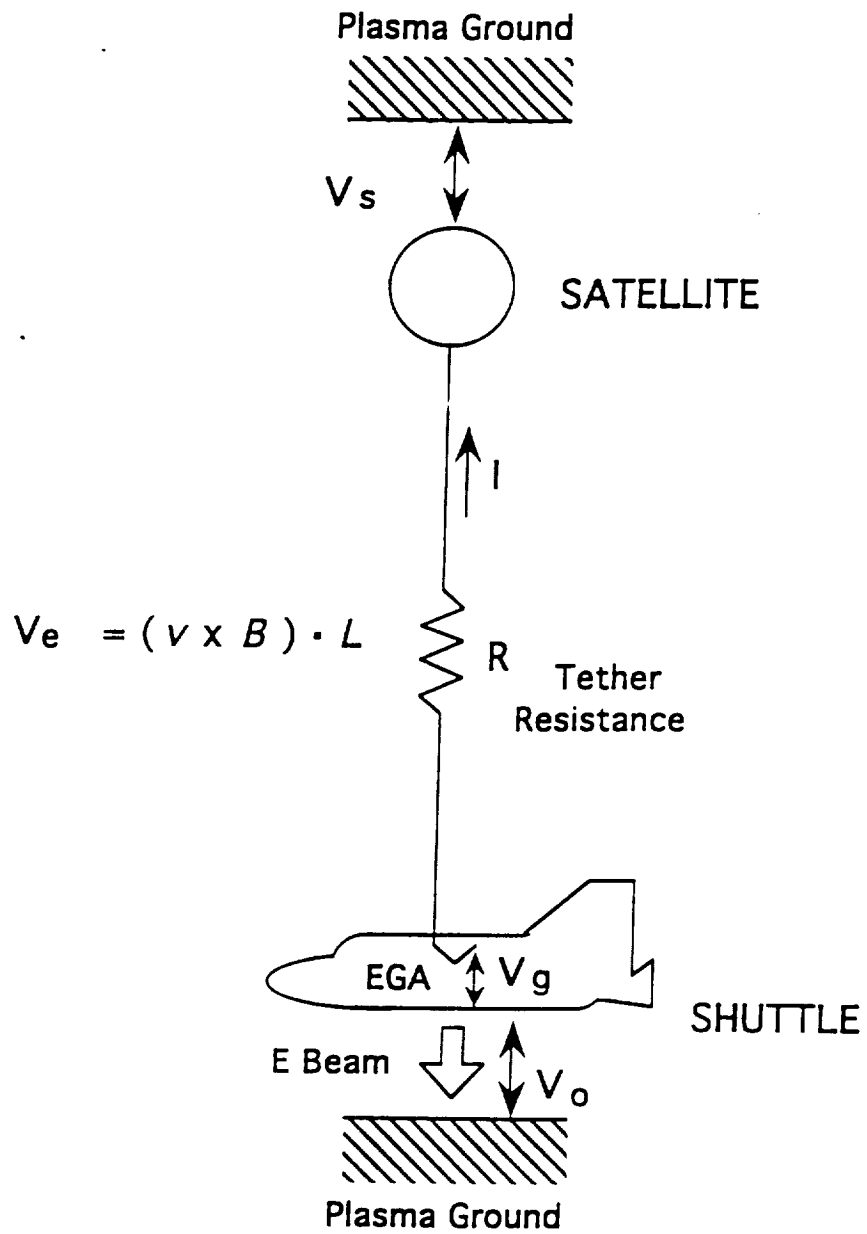
Fig 10. Spectrometry curve, fraction of injected current recorded at the slit for, electrons, H⁻ and O⁻ ions of injected energy of 230 eV and 20 V deflection plate voltage.

1996 056
 23:23:23 075 to 23:23:25 059



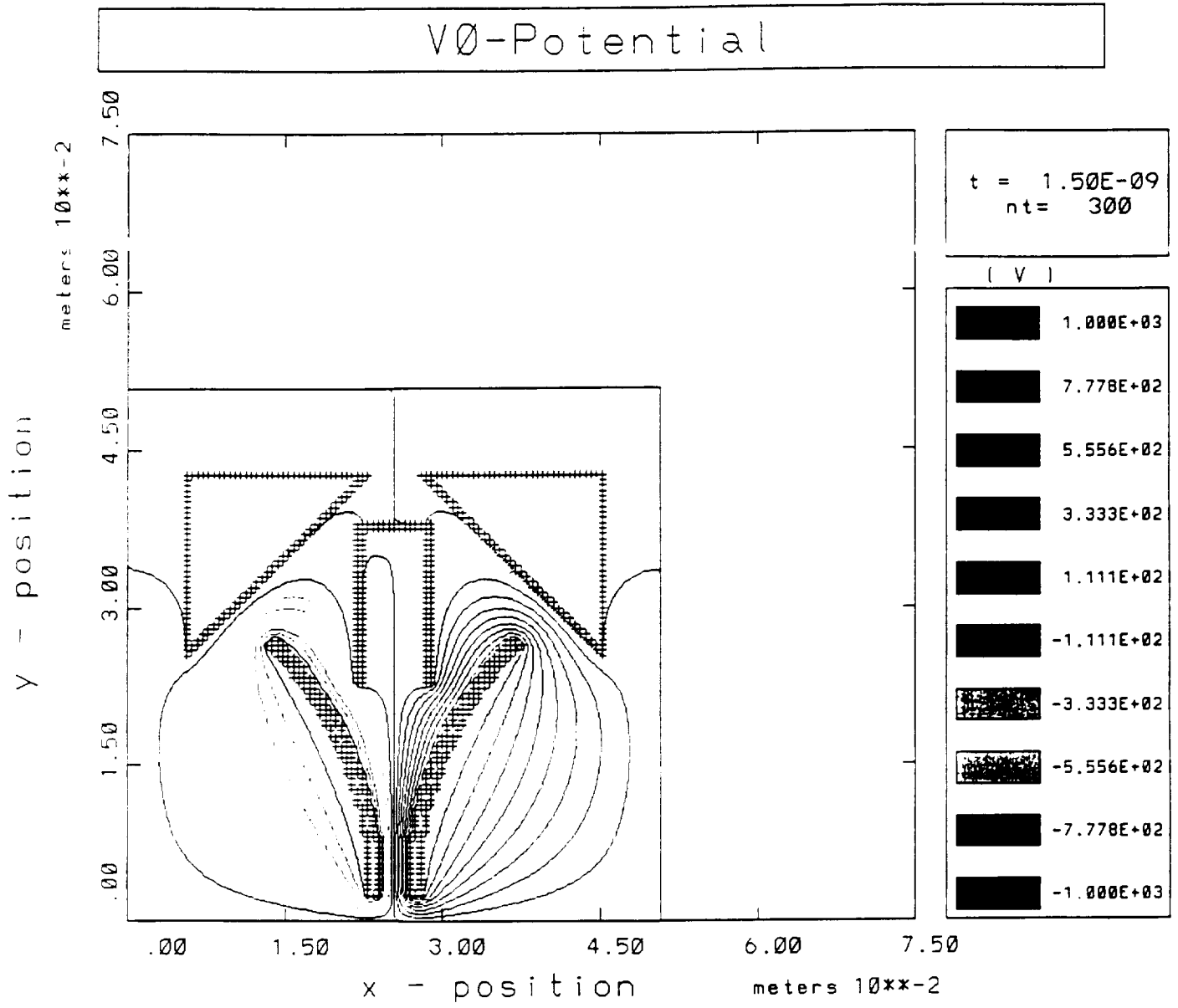
1996 056
23:23:27 171 to 23:23:29 155





$$V_e = V_s + I R + V_g + V_o$$

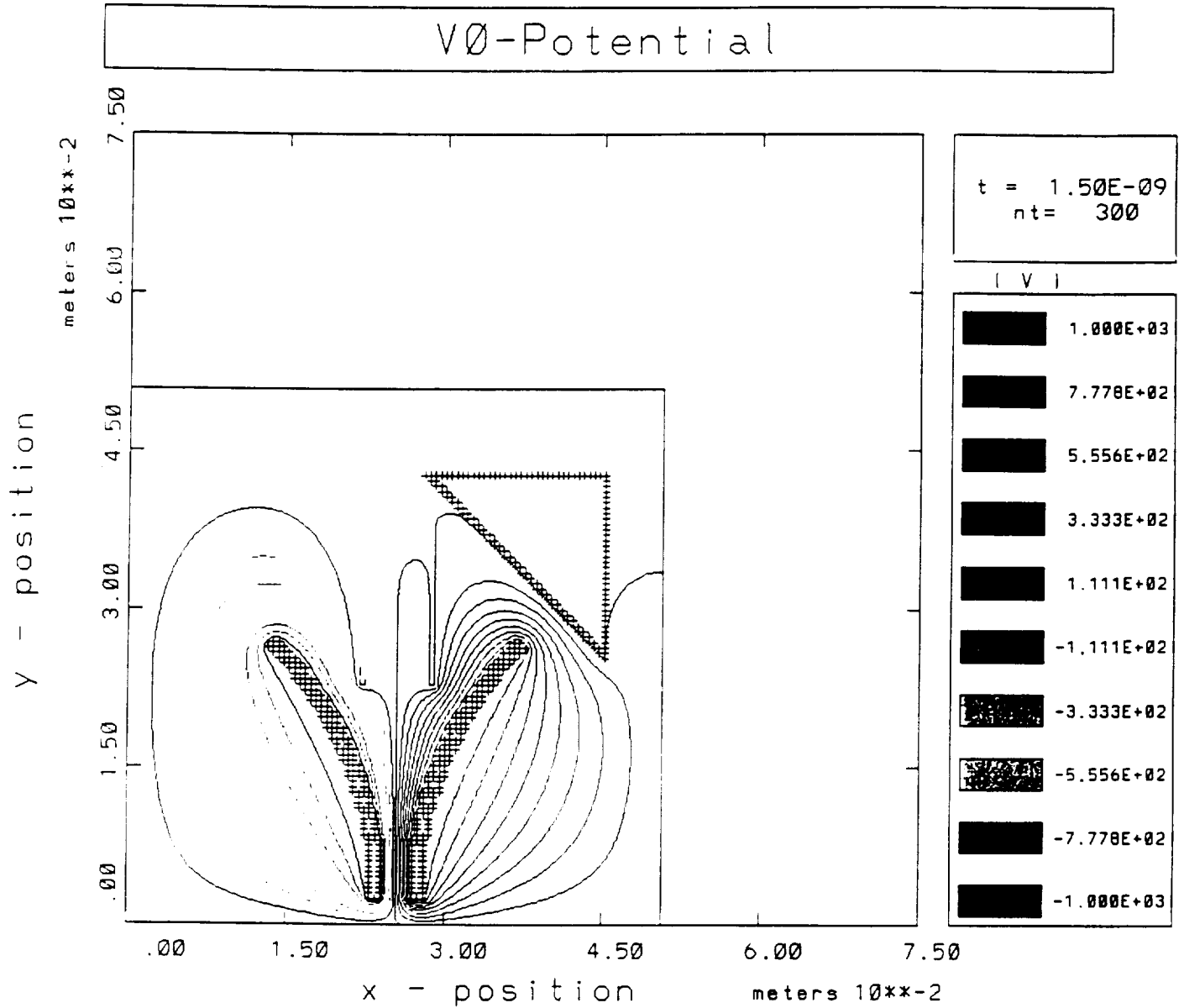
Figure 2



MASK	SIMULATION OF SPES DEFLECTOR - 100x100 grid defsm 19 May 97 15.31.23 tensor
------	---

Page 003

Fig. 3a

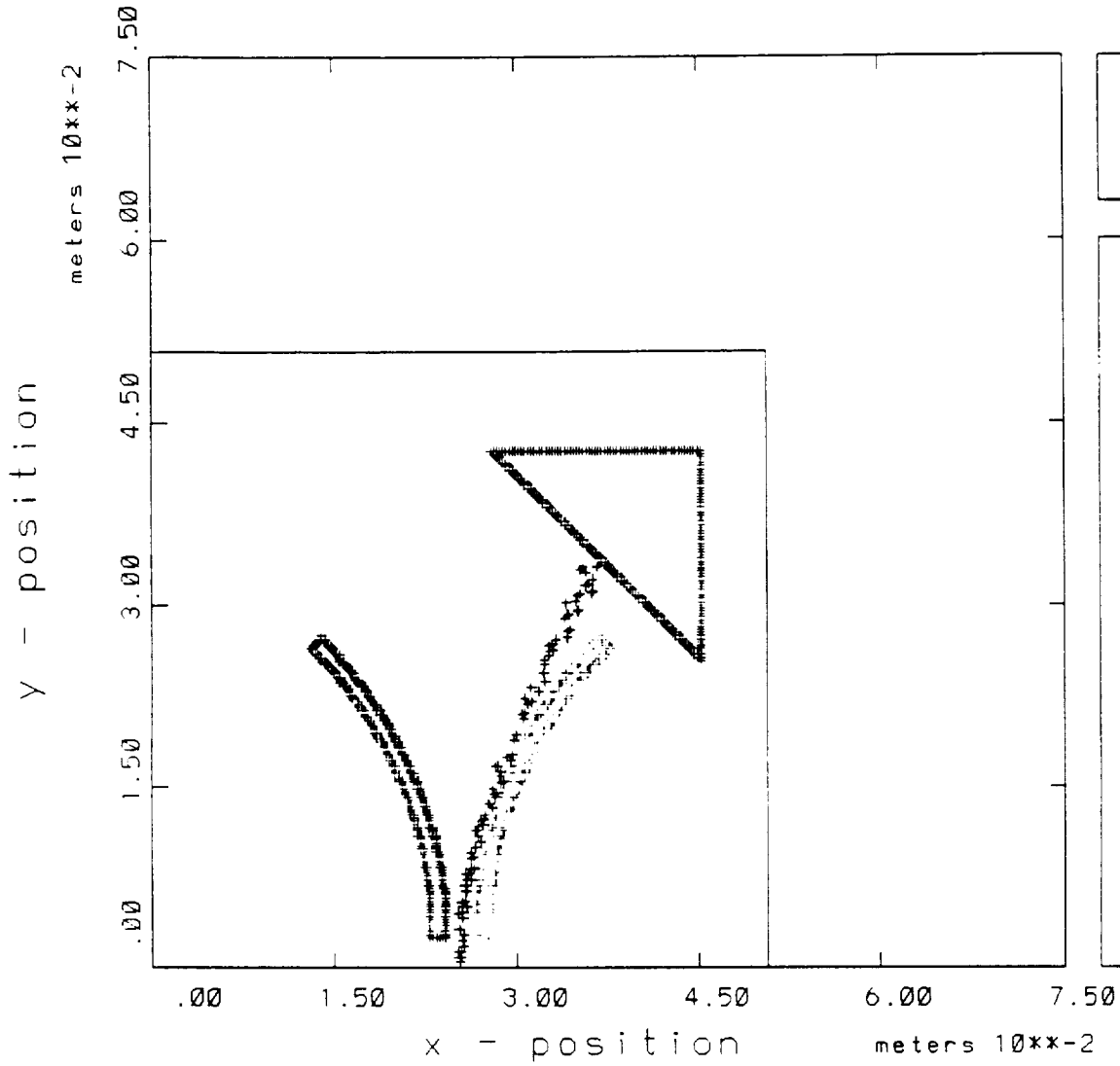


MASK	SIMULATION OF SPES DEFLECTOR - 100x100 grid def0z 18 Apr 97 15.54.30 tensor
------	---

Page 003

Fig. 3b

Particle Position Specie = 1



MASK

- SIMULATION OF SPES
- Vdef =20, V: E = 0.23 eV
0.23 19 May 97 18.38.46 tensor

Page
005

Fig. 4

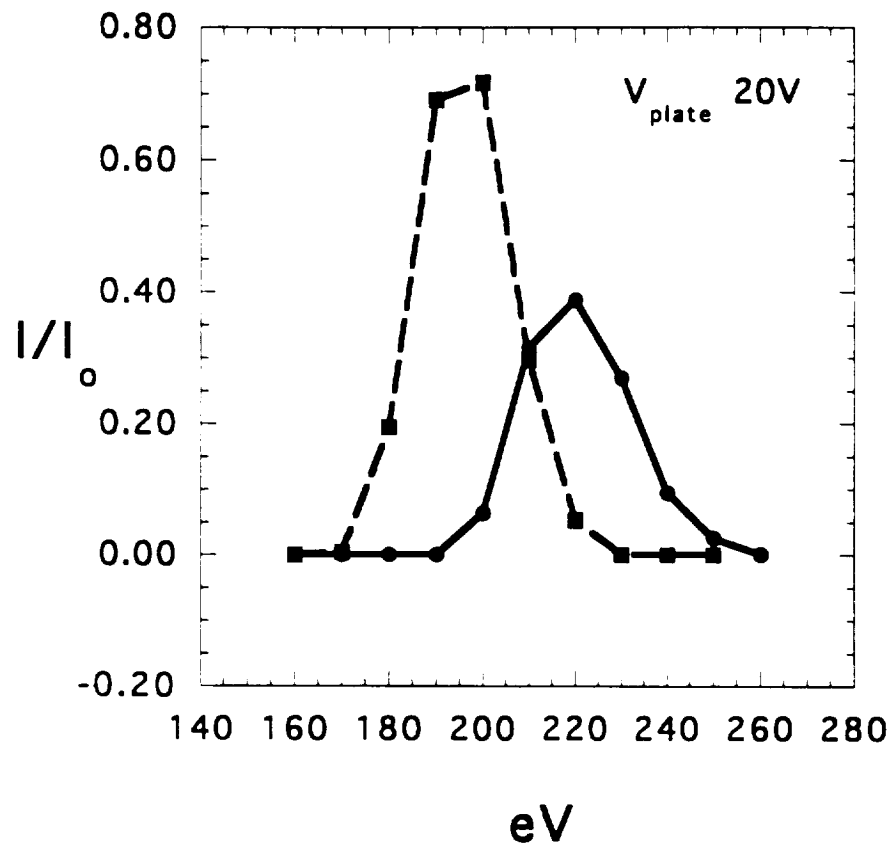
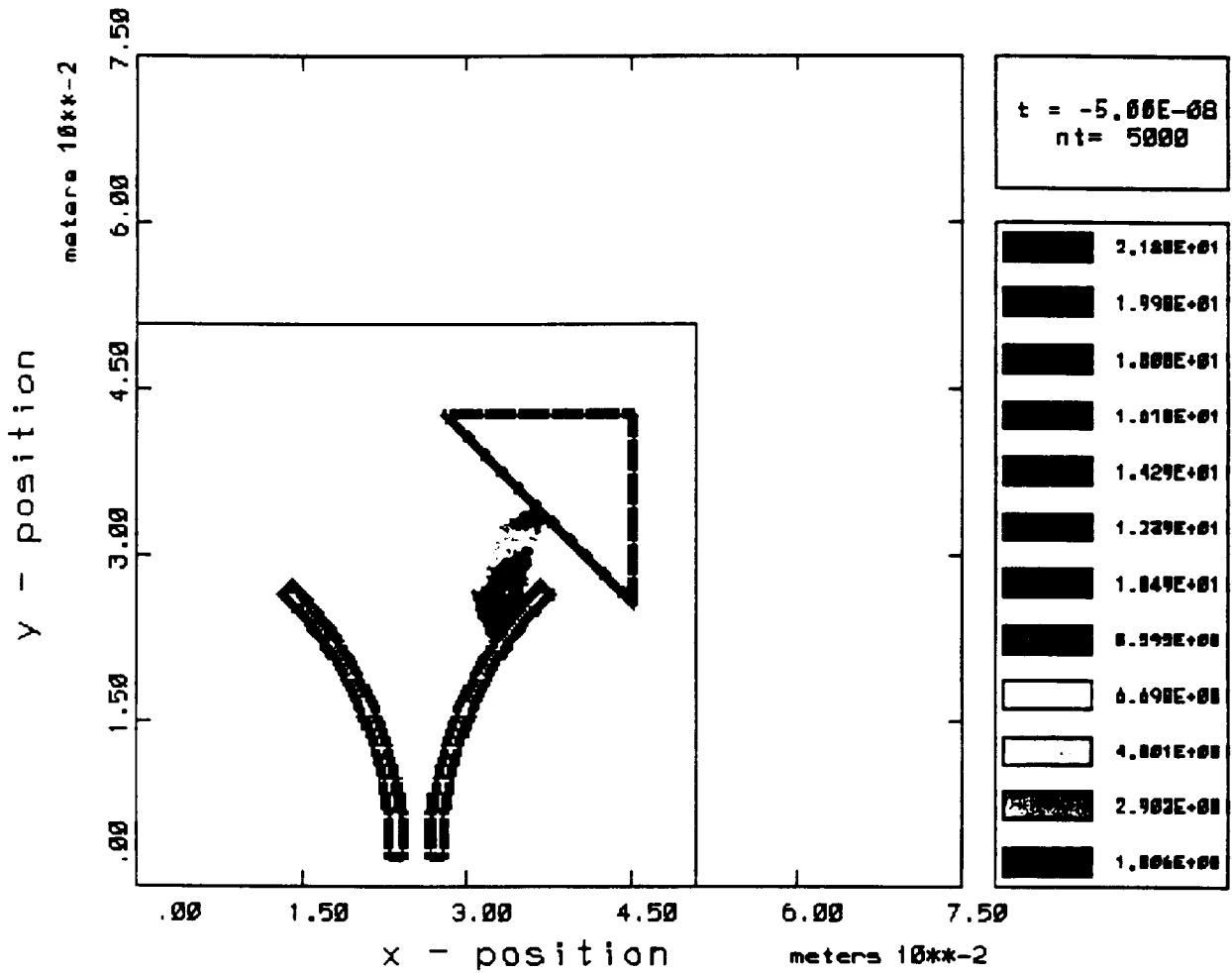


Fig. 5

Particle Position Specie = 1

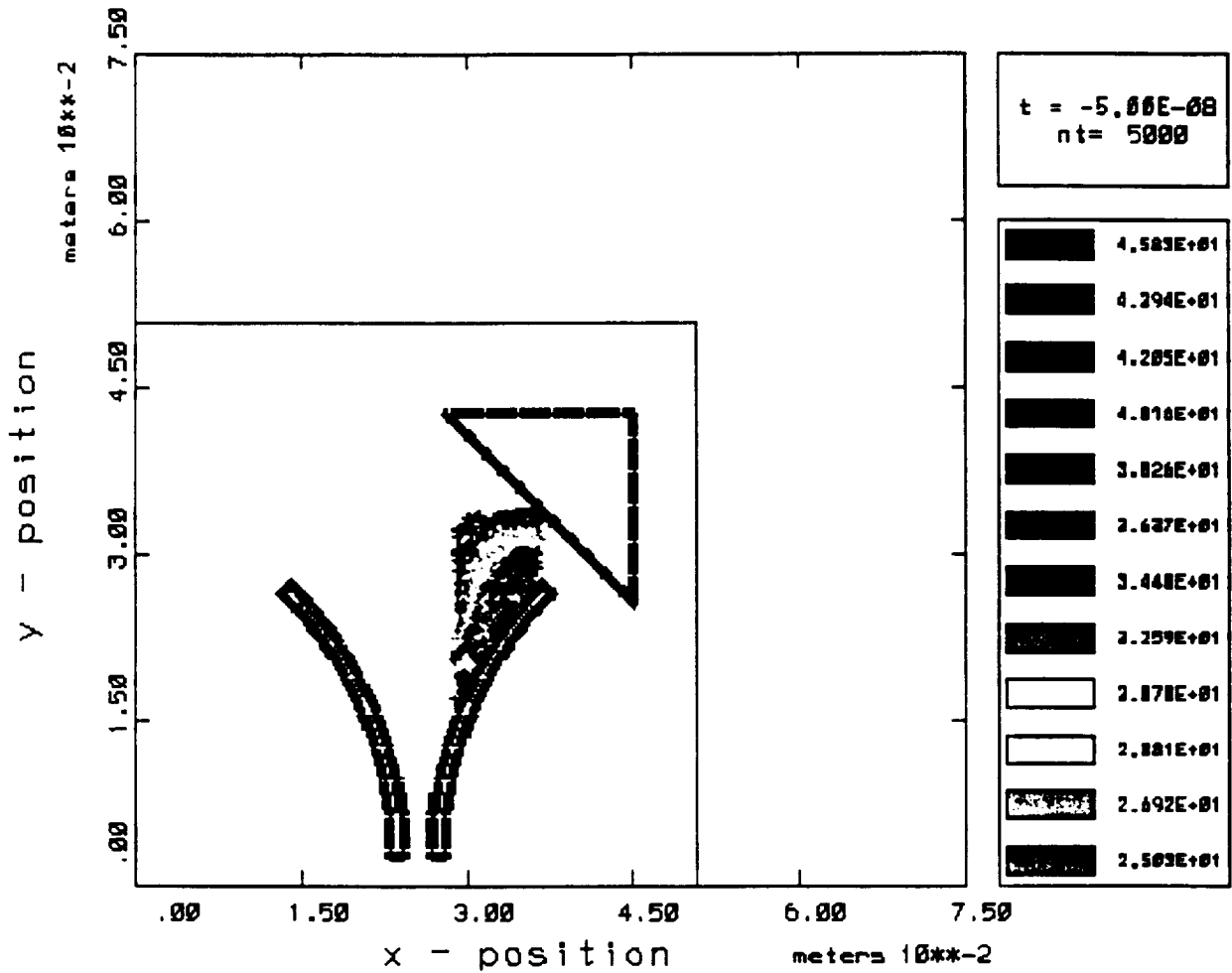


MASK	- SIMULATION OF SPES
	- Electron Energy Series I: E = 1.0 V
	1.0 23 Dec 97 15:06:21 teneer

Page
001

FIGURE 6

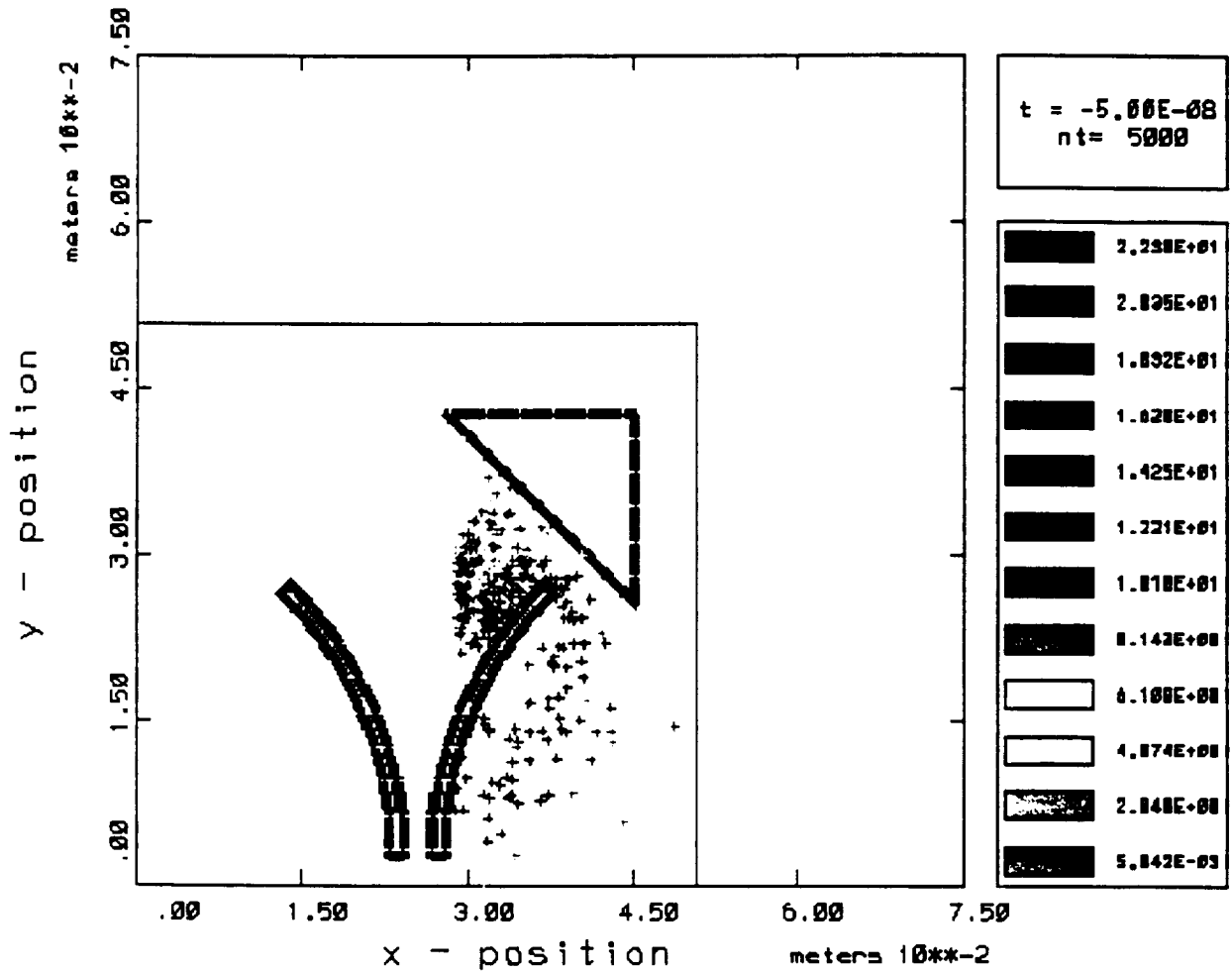
Particle Position Specie = 1



MASK - SIMULATION OF SPES
 - Electron Energy Series I, E = 25.0 V
 25.0 17 Dec 97 18:43:47 tanner

FIGURE 7

Particle Position Specie = 1



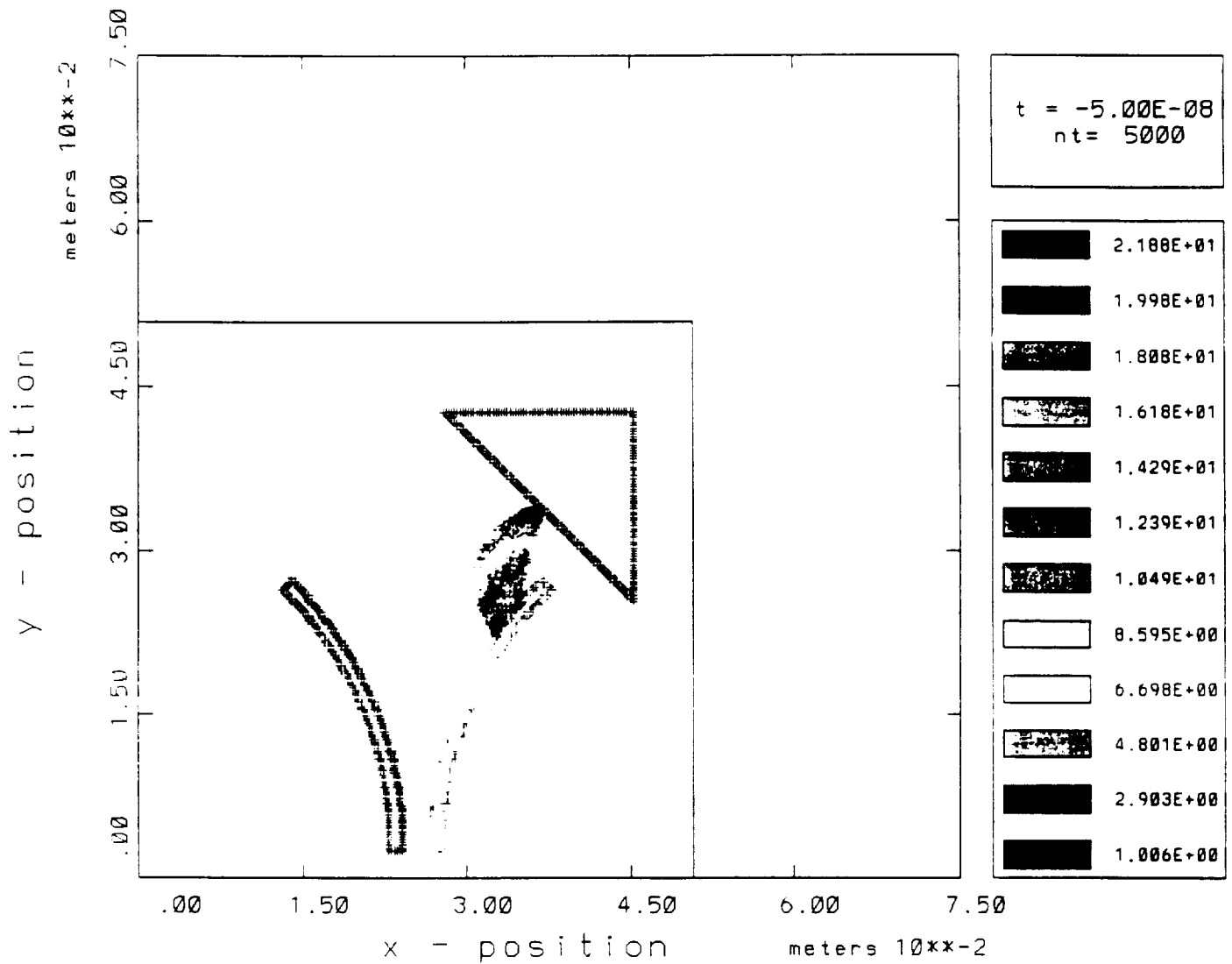
MASK

- SIMULATION OF SPES
 - Electron Energy Series I. E = 1.0 V
 1.0 8 Jan 98 12:52:01 tansar

Page
 001

FIGURE 8

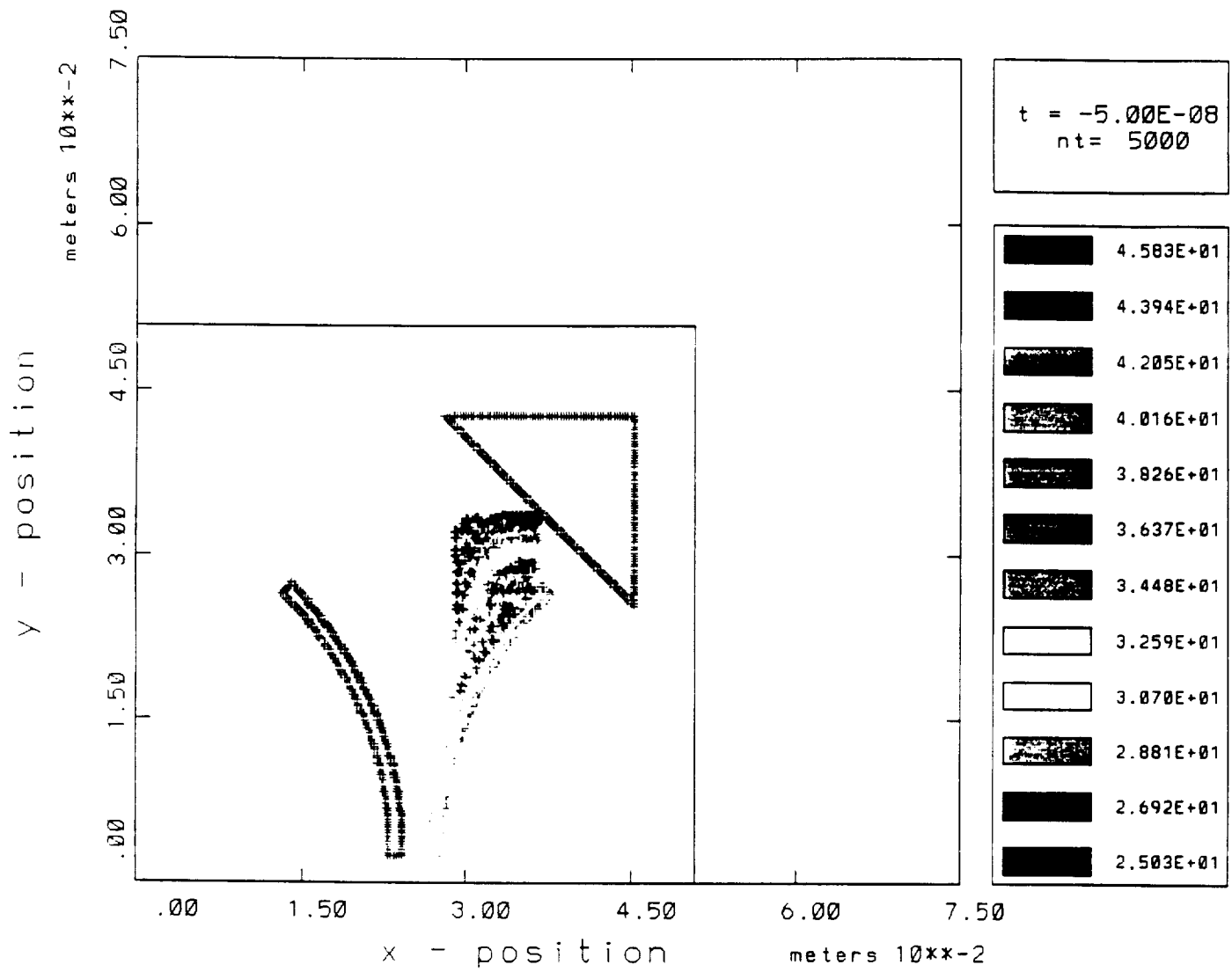
Particle Position Specie = 1



MASK - SIMULATION OF SPES
 - Electron Energy Series I: E = 1.0 V
 1.0 23 Dec 97 15:06:21 tensor

Fig. 6

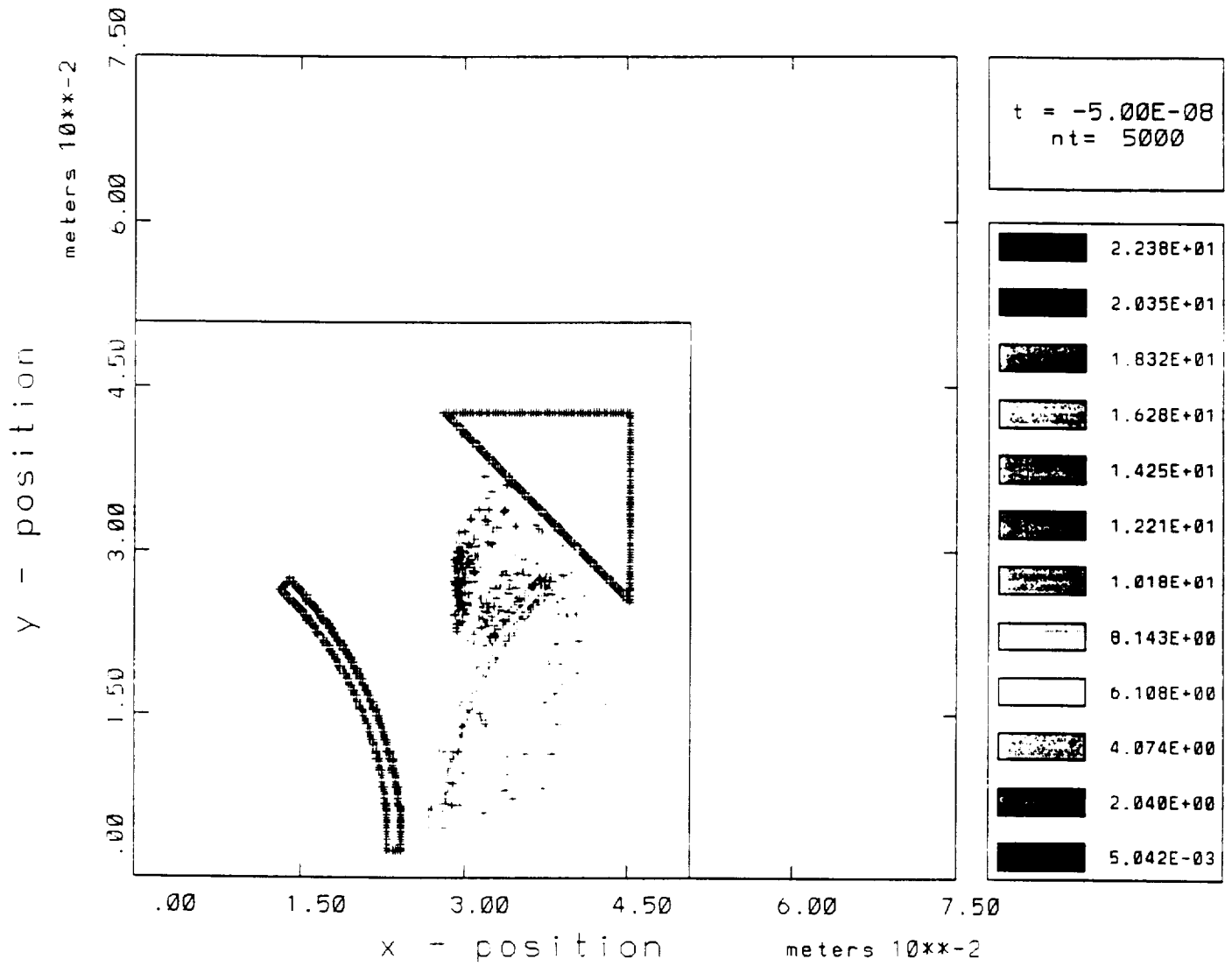
Particle Position Specie = 1



MASK	- SIMULATION OF SPES
	- Electron Energy Series I: E = 25.0 V 25.0 17 Dec 97 18.43.47 tensor

Fig. 7

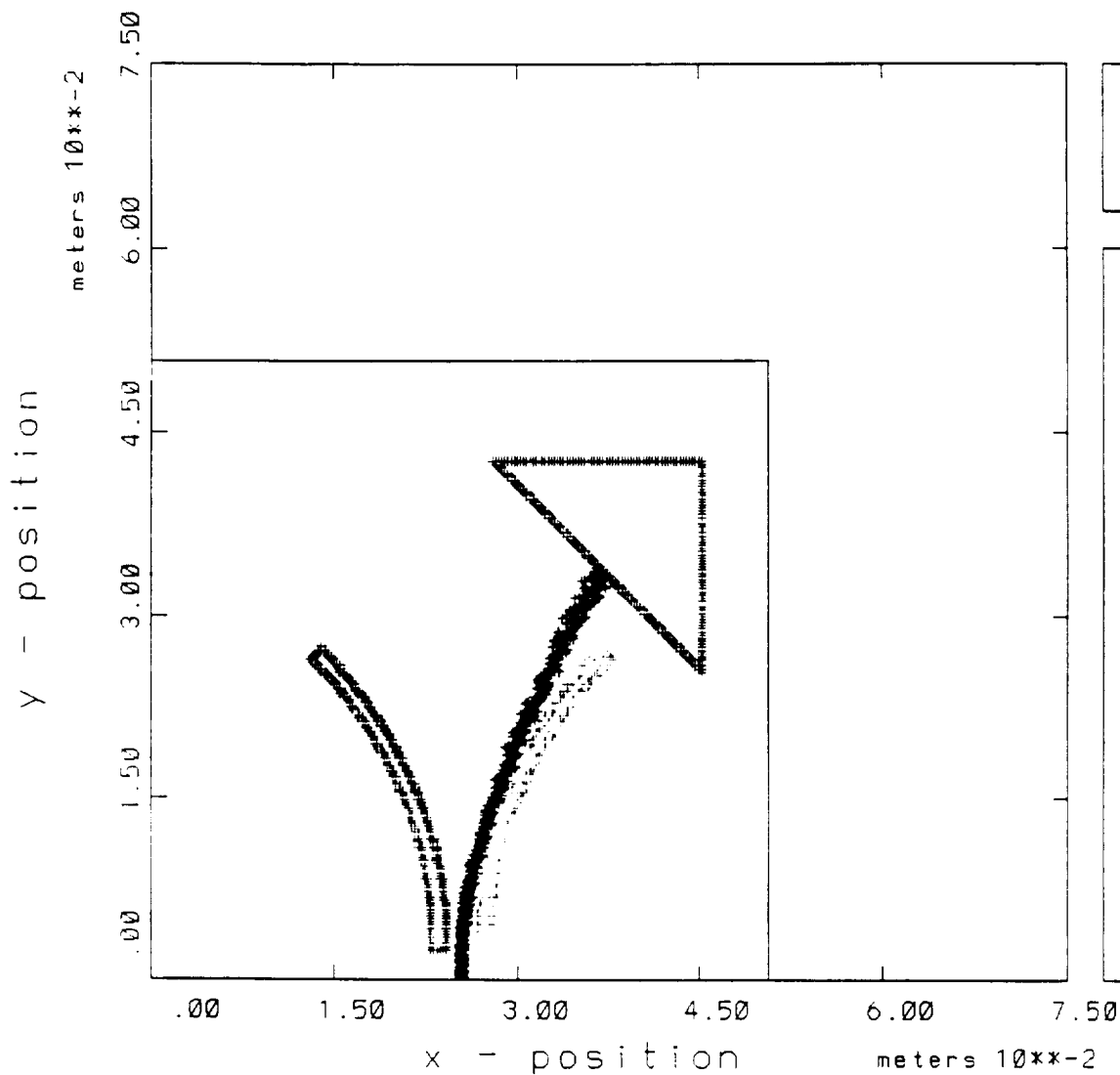
Particle Position Specie = 1



MASK - SIMULATION OF SPES
 - Electron Energy Series I: E = 1.0 V
 1.0 8 Jan 98 13:52:01 tensor

Fig. 8

Particle Position Specie = 1



t = 2.00E-06
nt = 1000

MASK

- SIMULATION OF SPES
- Electron Energy Series I: E = 0.23 V
0.23 9 Feb 98 18:31:59 tensor

Page
004

Fig. 2

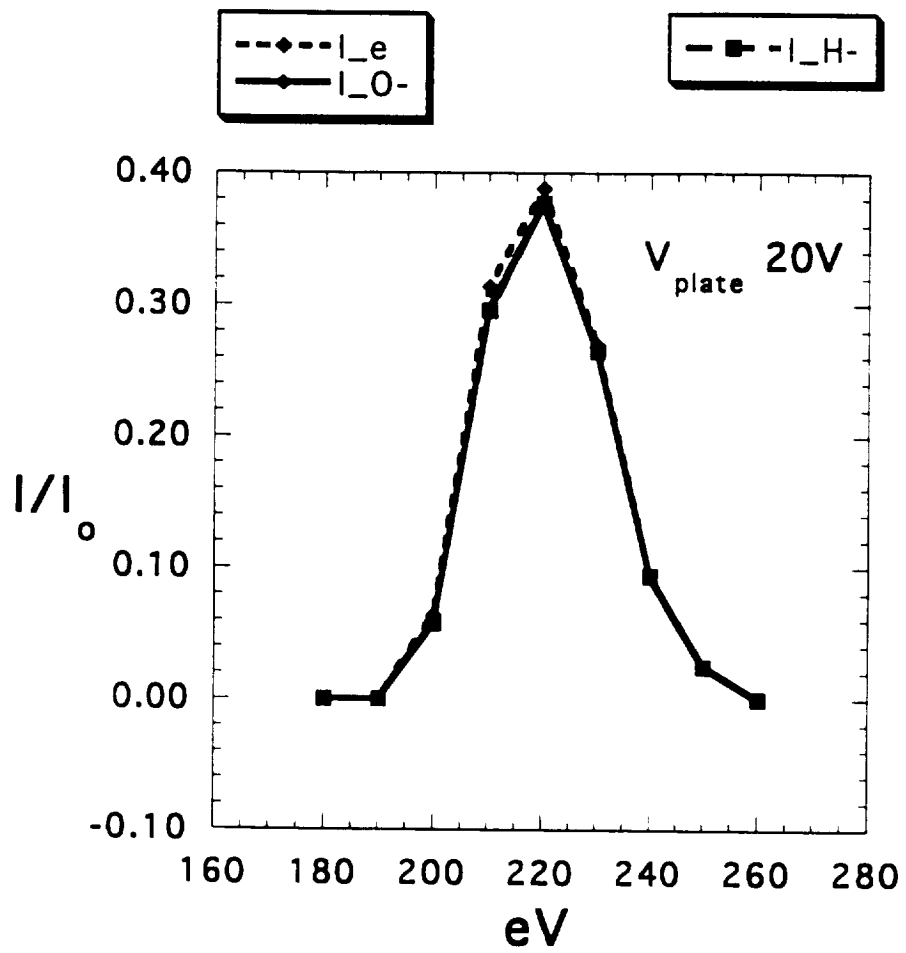


Fig. 10

APPENDIX 19

Satellite motion effects on current collection in LEO space

T. X. Zhang¹, K. S. Hwang², S. T. Wu¹,
N. H. Stone³, C. L. Chang⁴, A. Drobot⁴,
and K. H. Wright Jr¹,

¹ CSPAAR/UAH, Huntsville, Alabama 35899

² CSC/MSFC, Huntsville, Alabama 35812

³ SSL/MSFC, Huntsville, Alabama 35812

⁴ SAIC, Mclean, Virginia 22102

Contents

- 1. Introduction**
 - **Parker-Murphy model (1967)**
 - **TSS-1R data**
 - **Objective of present study**
- 2. New model**
 - **Motion effect on current collection**
 - **Sheath determination**
 - **Numerical results**
 - **TSS-1R data comparisons**
- 3. Summary**

1. Introduction

The Parker-Murphy (PM) model (1967) was developed for current collection in plasmas by a motionless and spherical probe with size greater than the Debye length, which is in good agreement with laboratory experiments and simulations (Quinn 1966; Shiah et al., 1997) and sounding rocket (SR) measurements (Myers et al., 1989).

However, the TSS missions indicated that mere currents were collected in comparison with the static PM model predicted (Dobrowolny et al., 1995; Thompson et al., 1997).

- Parker and Murphy (PM) model (1967)

In this model, the current collected by a body is given by:

$$I_{\text{PM}} = 2 \pi r_0^2 j_0,$$

j_0 : Thermal current density,

r_0 : Sheath radius defined as

$$\frac{r_0^2}{a^2} = 1 + \sqrt{\frac{8e\phi}{m_e a^2 \Omega_e^2}},$$

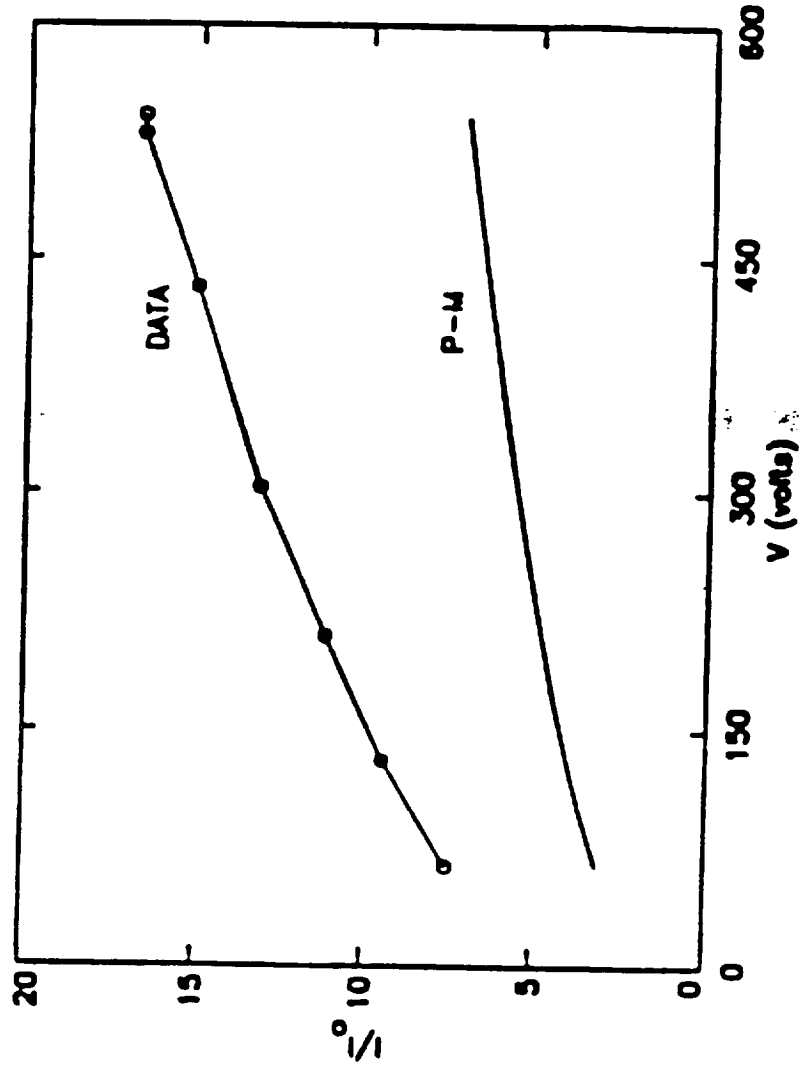
Note: The body should be spherical and motionless.



- TSS-1R data (Wright et al., 1996)

The TSS measured currents are greater than the PM model predicted.

$$I_{\text{TSS-1R}} \sim (2-4) I_{\text{PM}}$$



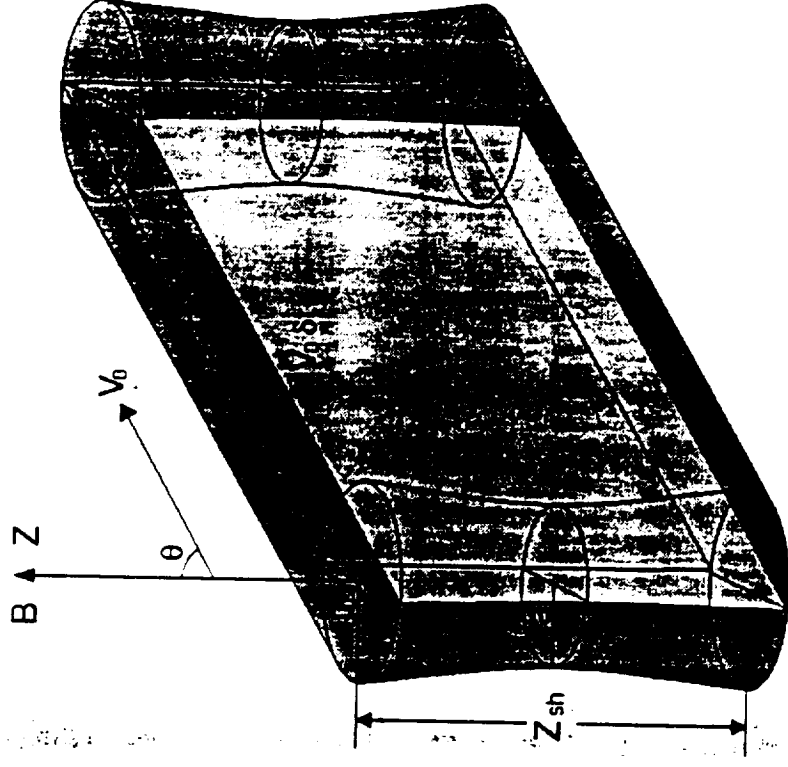
• **Objective of present study**

In order to reconcile this difference, we develop a current collection model by considering the satellite motion effects.

2. New model

- Motion effect on current collection

For a moving satellite, current collection is limited in the direction parallel to the magnetic field lines and extended along the moving direction. The collection region can be drawn as:



- Sheath determination

To study such motion effect, Thompson (1985) assumed a sheath, which was modified by including potential effect (Dobrowolny et al., 1995) as

$$Z_{\text{sh}} = \frac{2r_0 V_{\text{Te}}}{V_0}.$$

Substituting this sheath into the current formula, we obtain

$$I_c \approx \left[1 + \frac{4}{\pi} \left(1 + \frac{a}{r_0} \right) \right] I_{\text{PM}} \approx (2-4) I_{\text{PM}},$$

which is ~ 2-4 times greater than the PM current and hence in agreement with the TSS-1R measured data. However, this sheath leads to a current independent of the probe velocity, which may not be physical.

Now we solve the field aligned sheath from the electron motion equation,

$$m_e \frac{dv}{dt} = -e\nabla\phi + e \frac{\mathbf{v} \times \mathbf{B}}{c},$$

and obtain

$$Z_{\text{sh}} = 2 \left(\frac{(\gamma + 2)a}{2V_0 \sin\theta} \sqrt{\frac{2ea^\gamma \phi_s}{m_e}} \right)^{2/(\gamma+2)}.$$

Here the potential along the magnetic field line is chosen

$$\phi(Z) = \phi_s \left(\frac{a}{Z} \right)^\gamma.$$

Both theory and simulation indicate the parallel potential is not exponentially distributed.

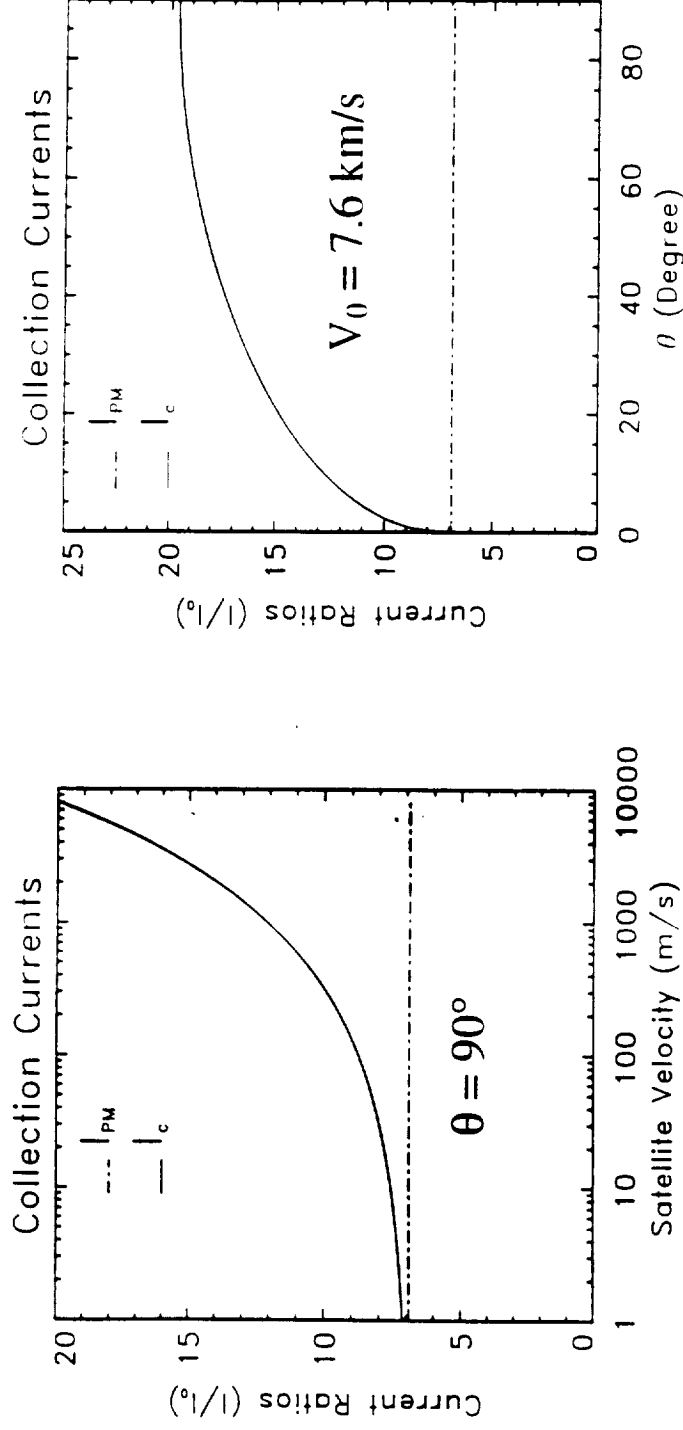
Substituting this new obtained sheath into the current formula, we have

$$I_c = I_{PM} + 2(a + r_0)(V_0 \sin \theta)^{\gamma/(\gamma+2)} n_{e0} e \left(\frac{3a}{2} \sqrt{\frac{2ea^\gamma \phi_s}{m_e}} \right)^{2/(\gamma+2)}$$

This current is dependent on both the velocity and the orientation of motion. When the velocity approaches to zero, it returns to PM current. However, in a typical orbit velocity, $I_c \sim (2-4) I_{PM}$, in agreement with TSS-1R data.

• Numerical Results

With the TSS-1R conditions, we plot current collection vs. velocity and orientation angle.



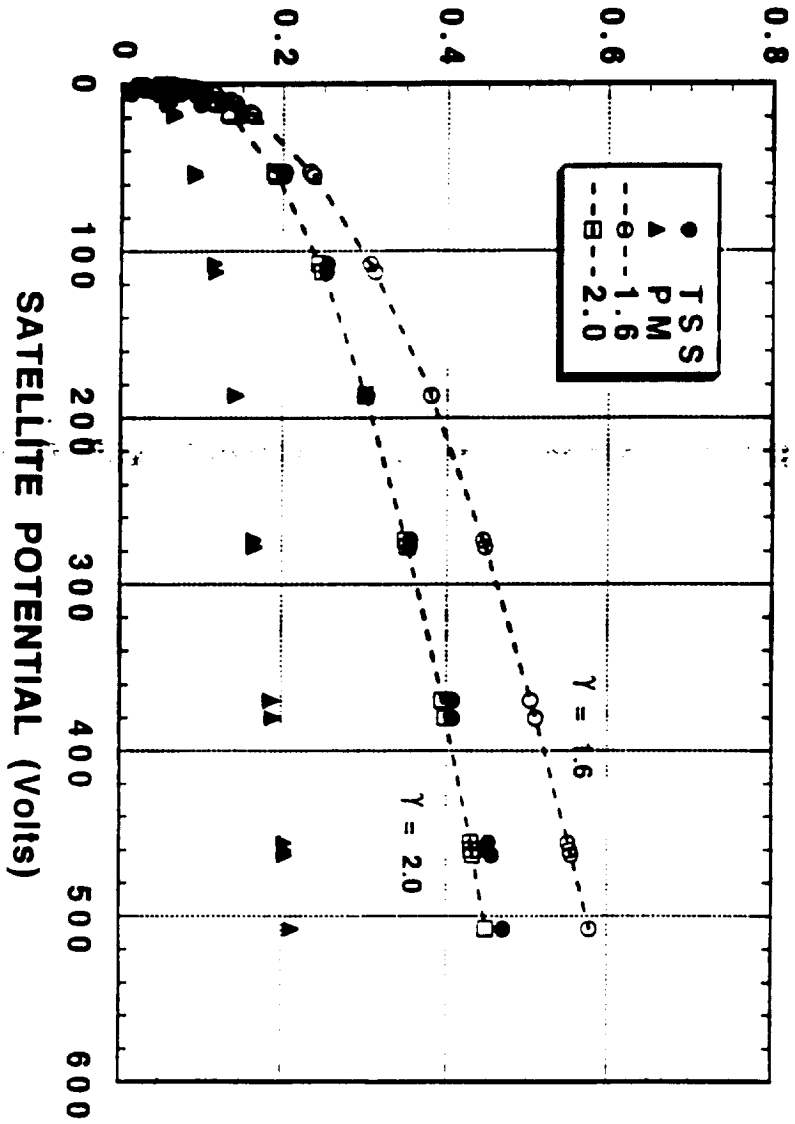
It is shown that current collection increases with the velocity and the angle θ . For a motionless probe, it is I_{PM} ; however, for a satellite with 8km/s, it is $\sim 2-4 I_{PM}$. A satellite moving \parallel to B field collects I_{PM} .

• TSS-1R data comparisons (6 IV Scans)

Table 1: Plasma parameters for the 6 IV scans which are deduced from Italian Langmuir probe dataset

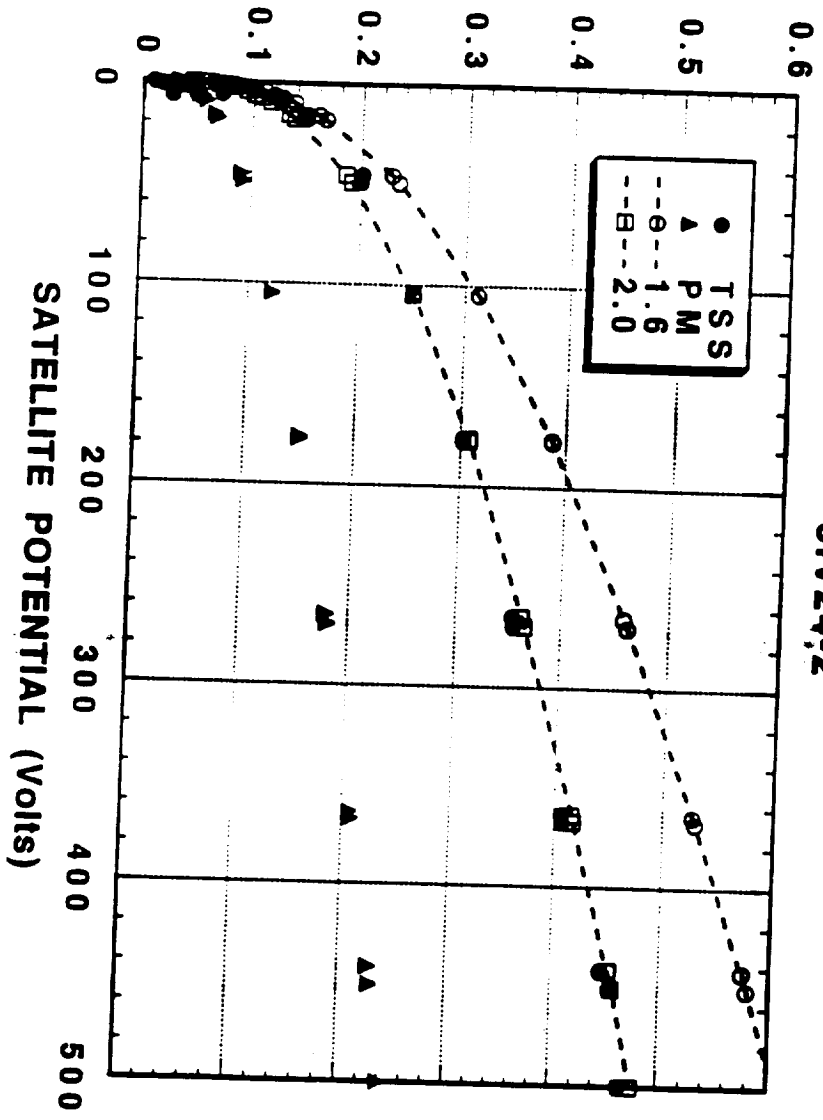
IV Scan	T_e (K)	n_e ($\times 10^{15}$ cm$^{-3}$)	B (Gausses)
1	1500	8.0	0.319
2	1650	8.1	0.320
3	1000	6.5 - 8.0	0.321
4	2550	2.8	0.327
5	2800	3.0	0.326
6	2300	3.6	0.322

TETHER CURRENT (Amp)

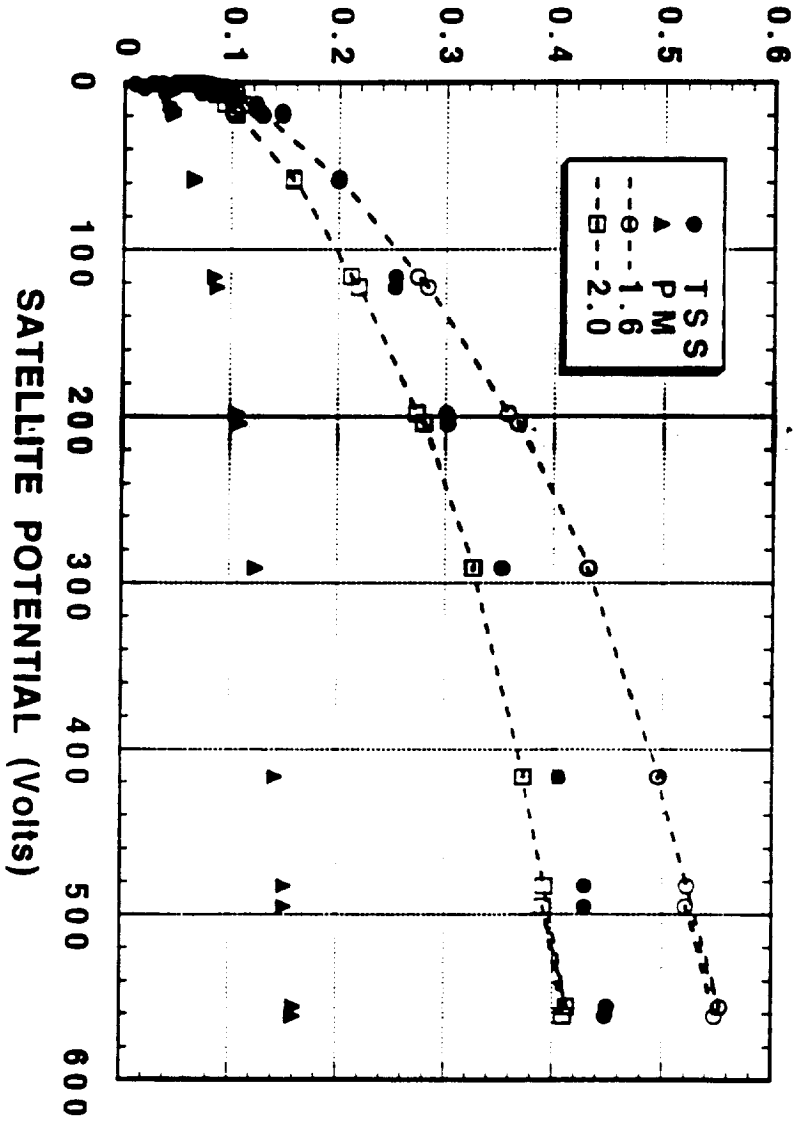


31V24-1

TETHER CURRENT (Amp)

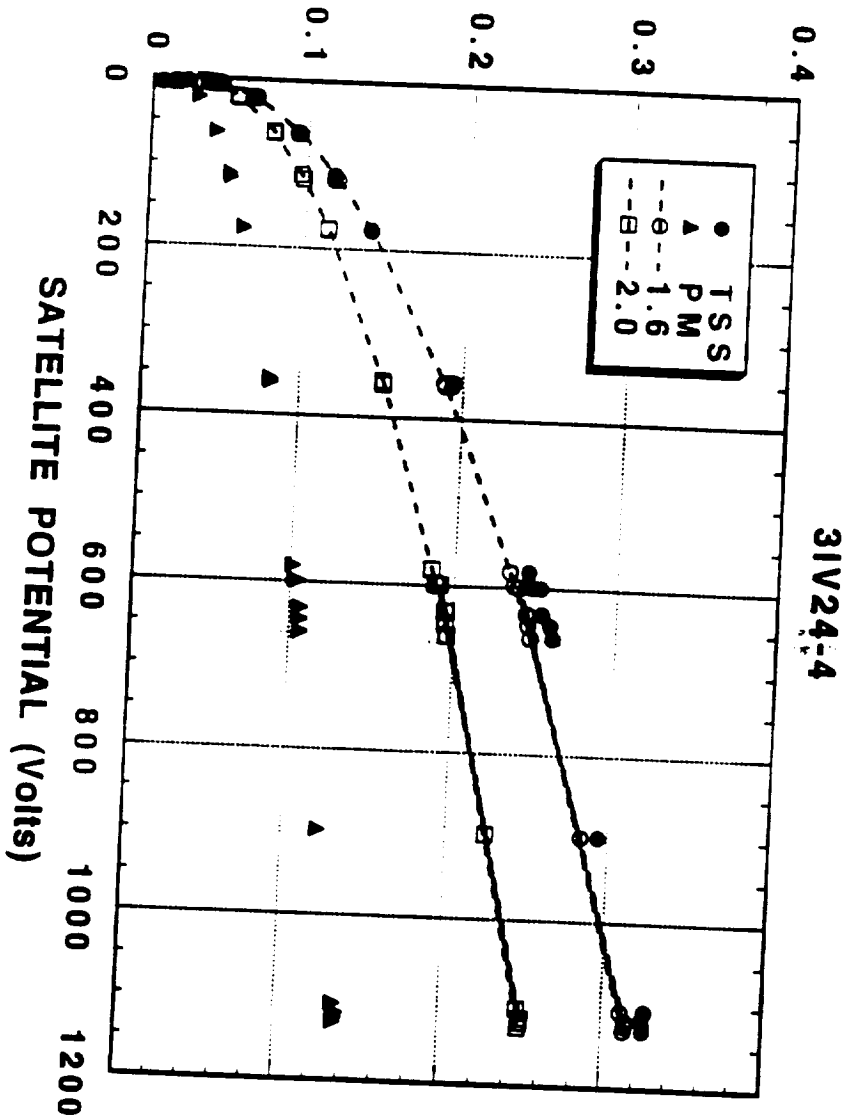


TETHER CURRENT (Amp)

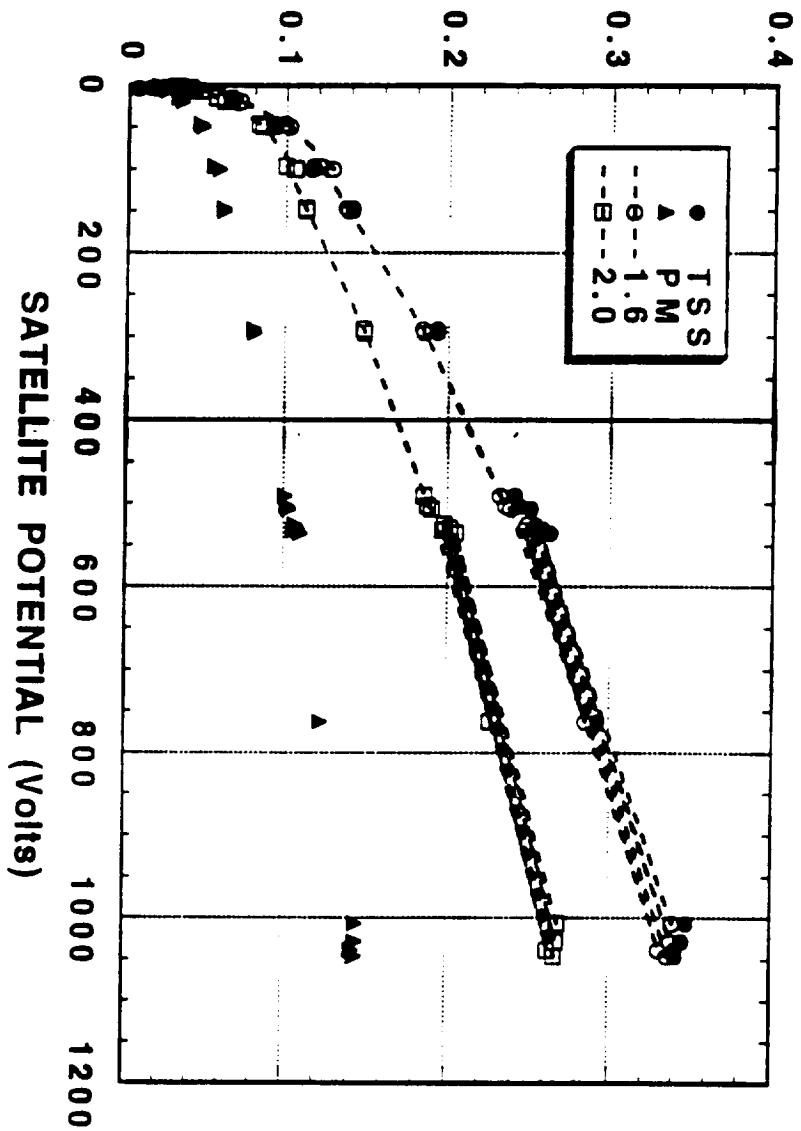


31V24-3

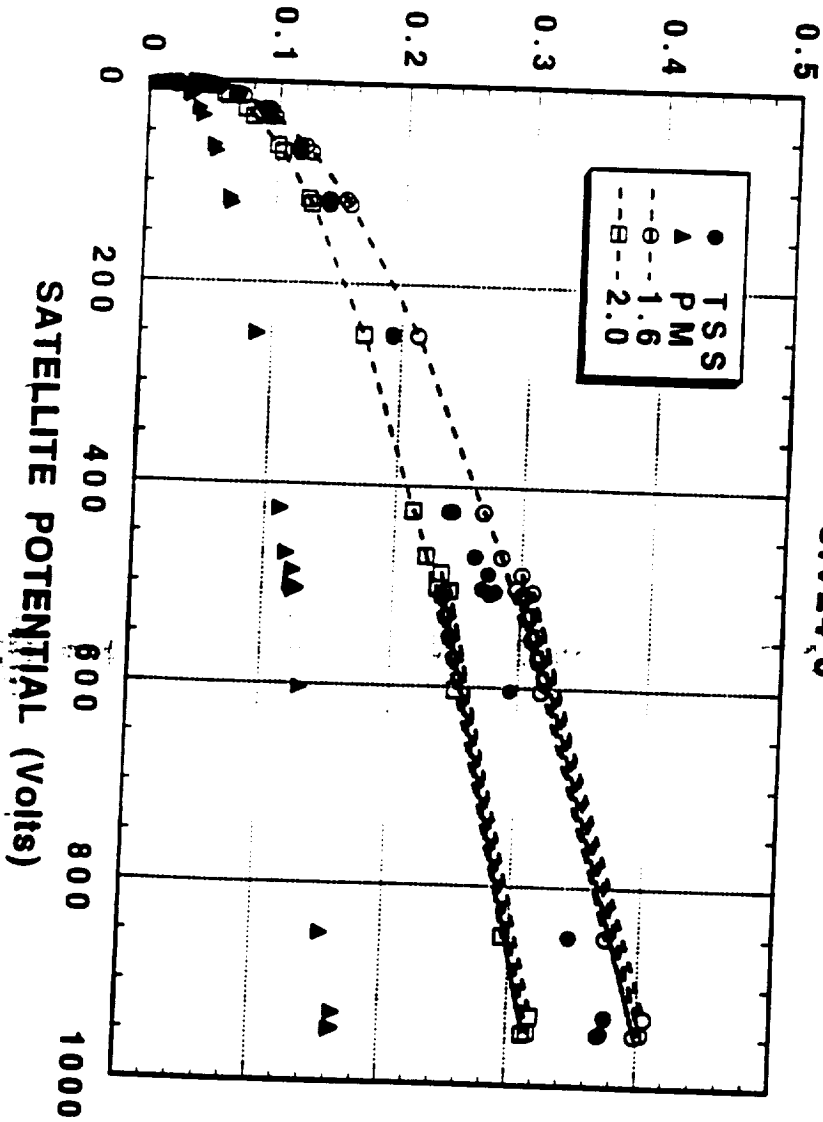
TETHER CURRENT (Amp)



TETHER CURRENT (Amp)



TETHER CURRENT (Amp)



4. Summary

- A current collection model with satellite motion effect is developed.
- A new field aligned sheath is obtained by solving the equation of motion of electron, which leads to current collection dependent on the velocity.
- The motion effect increases with the velocity. For a motionless probe, the predicted current reduces to PM current.
- For the TSS-1R, the present model at $\gamma = 2$ (or $\gamma = 1.6$) fits the data with low (or high) T_e and high (or low) n_e very well.
- Orientation of motion also affects current collection. A satellite moving parallel to the magnetic field line collects the least current ($= I_{PM}$).

APPENDIX 20

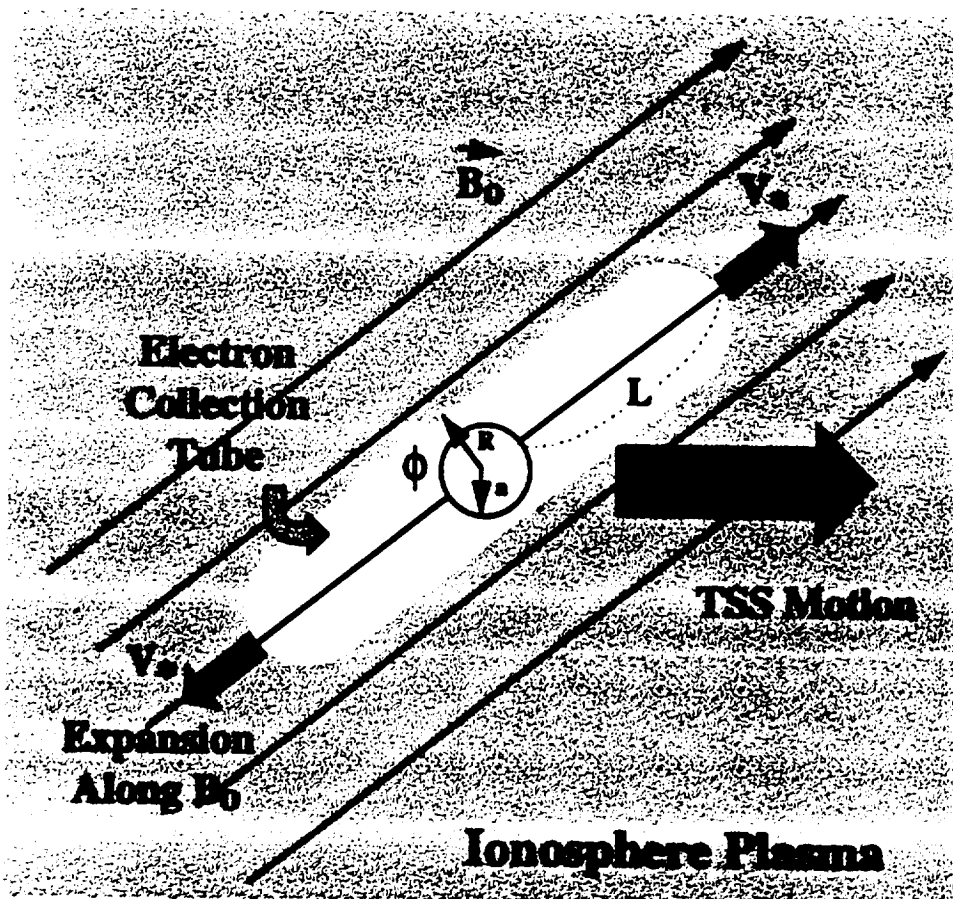
ELECTRON COLLECTION
BY THE
HIGH VOLTAGE TSS SATELLITE

Adam Drobot SAIC
Chia-Lie Chang SAIC

American Geophysical Union
Annual Spring Meeting at Boston, MA

May 26 , 1998

ELECTRON COLLECTION ALONG B



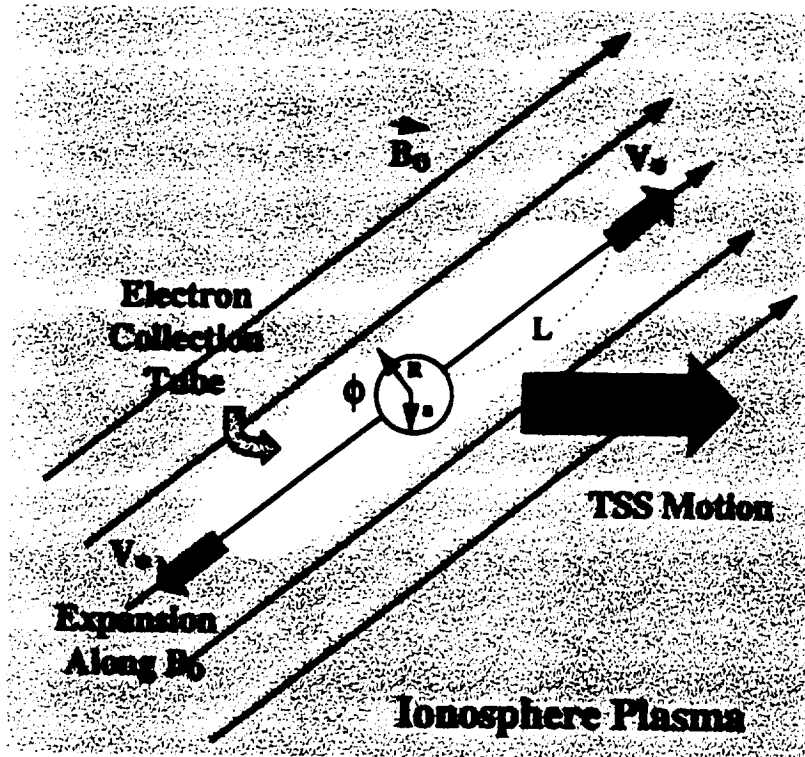
L - Length of the electron collection tube

T - Transit time of the TSS satellite on a field line

$$T = 2R / V_{tss\perp}$$

- Electron collection occurred on a transient basis.
- Length of the tube L is continuously increasing.

ELECTRON COLLECTION ALONG B



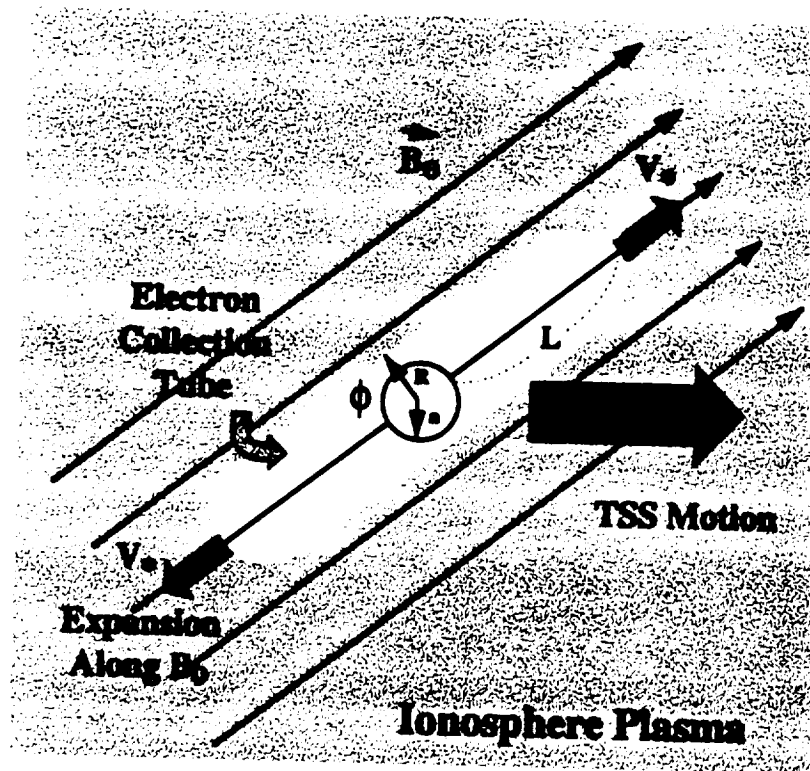
- Averaged tube expansion speed V^* within transit time T

$$V^* = L / T$$

- Total charge collected by the satellite within time T

$$Q = 2 e N_0 (\pi R^2) L$$

ELECTRON COLLECTION ALONG B



- Averaged current in time T

$$I = Q/T = 2 e N_0 (\pi R^2) V^*$$

- Collection radius R is defined by Parker-Murphy

$$R^2 = a^2 [1 + 2 (\phi / \phi_0)^{1/2}] ; \phi_0 = (e a^2 / 2 m_e c^2) B_0^2$$

- Averaged tube expansion speed can be written as

$$V^* = \frac{I}{2 e N_0 (\pi a^2) [1 + 2 (\phi / \phi_0)^{1/2}]}$$

EXPANSION SPEED FROM TSS DATA

- Averaged Tube Expansion Speed

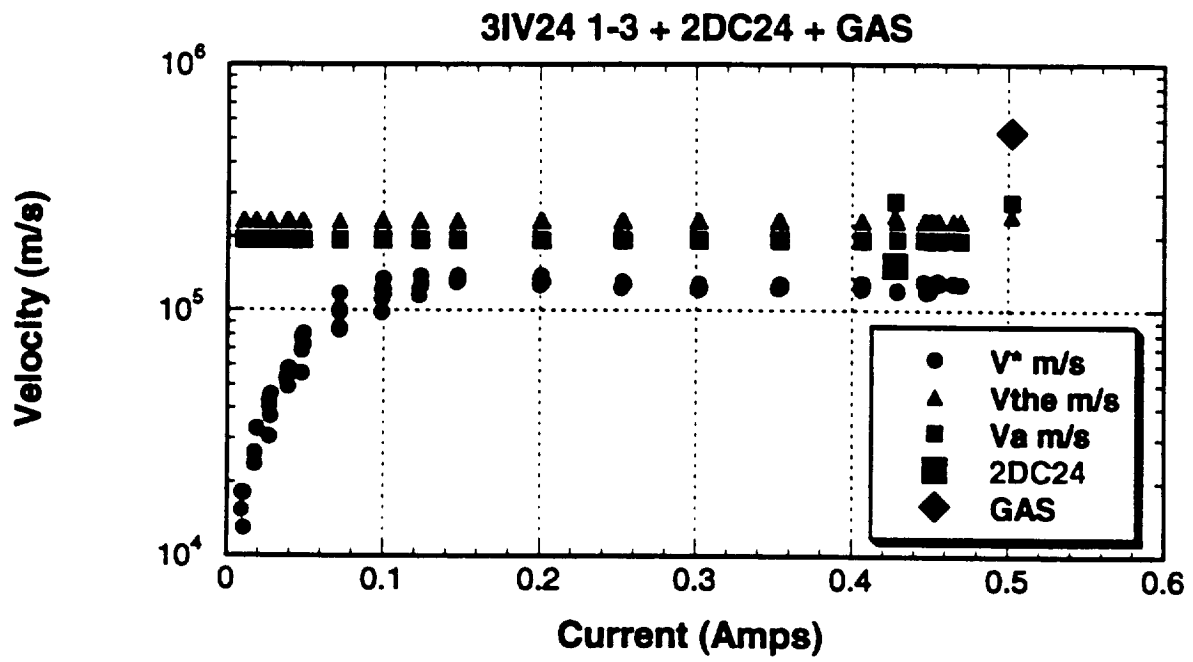
$$V^* = \frac{I}{2 e N_o (\pi a^2) [1 + 2 (\phi / \phi_o)^{1/2}]}$$

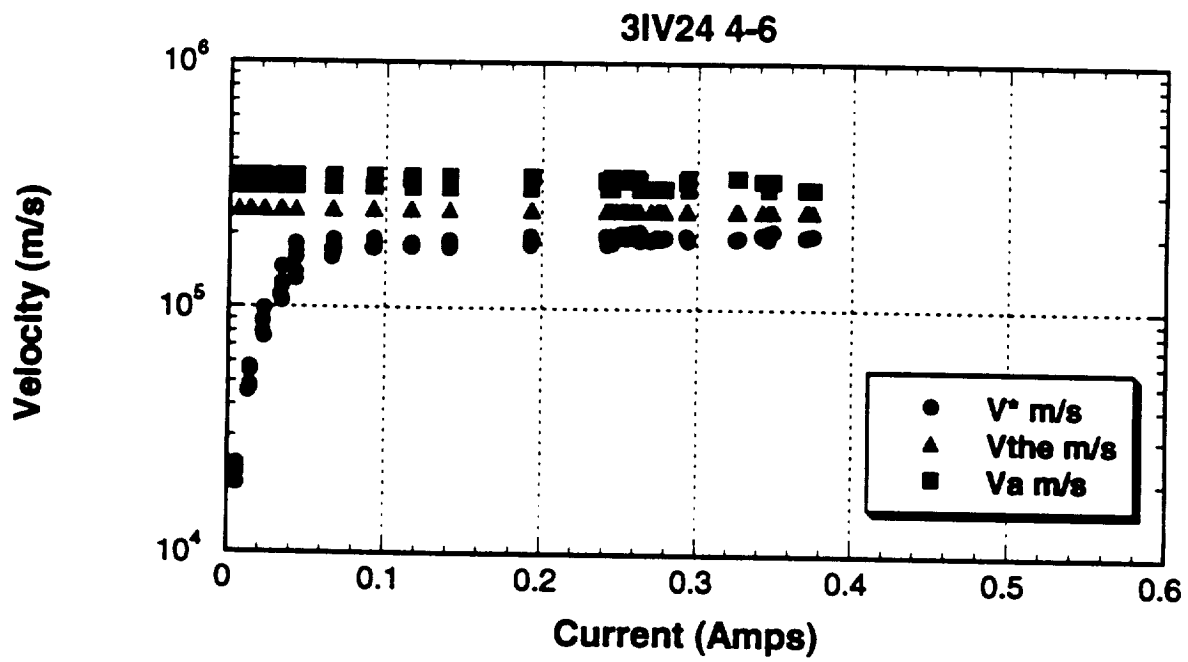
$$\phi_o = (e a^2 / 2 m_e c^2) B_o^2$$

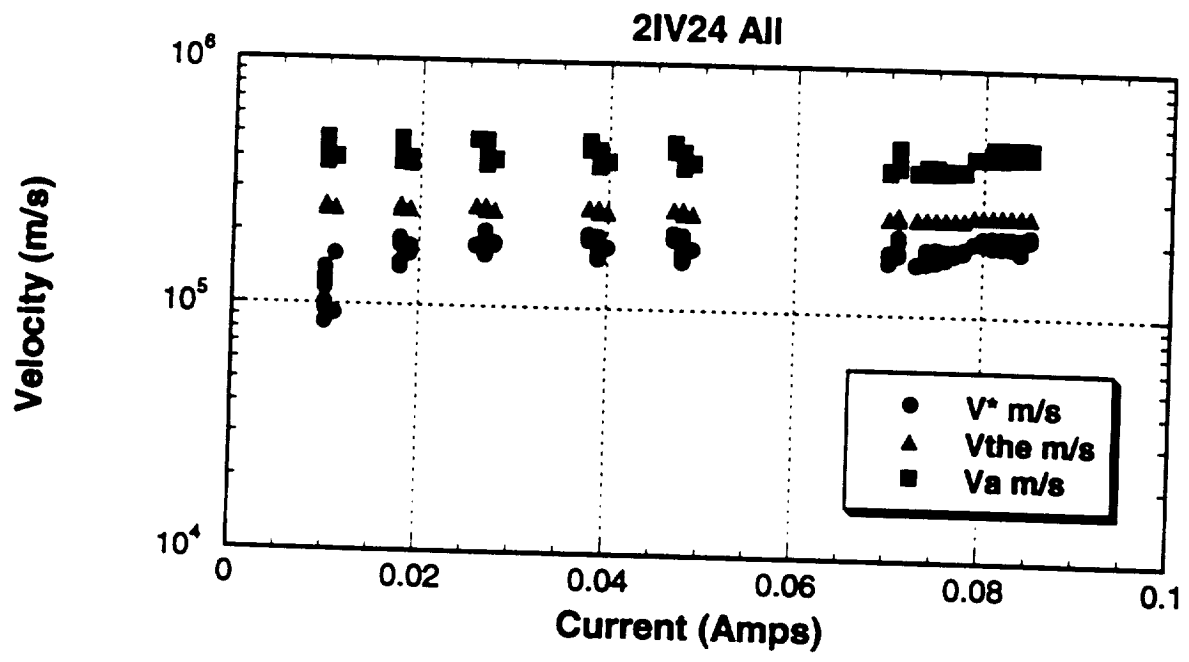
- TSS-1R provided measurements on I , N_o , B_o , and ϕ

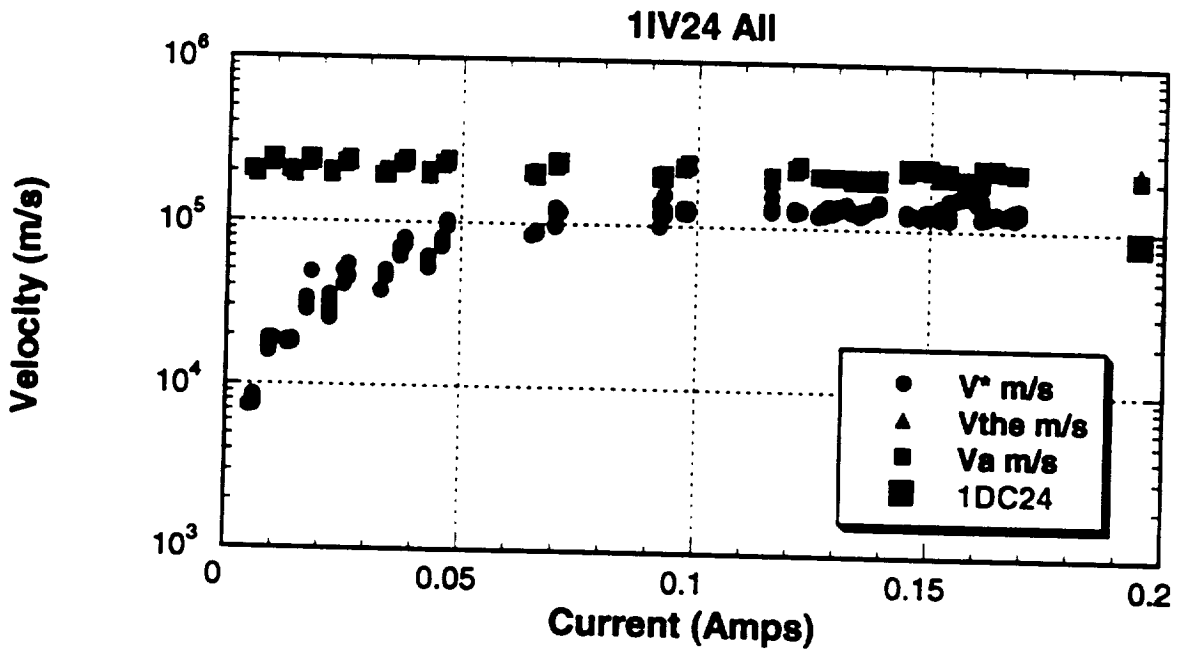
FO	GMT	N_o (/c.c.)	T_e (°K)	B_o (G)
1IV24 1-3 4-6	56/23:20:48 - 23:23:57	5.7×10^7	1400	0.32
	56/23:32:51 - 23:36:00	7.7×10^7	1100	0.32
1DC24	56/23:50:00	5.1×10^7	1400	0.35
2IV24 1-3 4-6	57/00:11:59 - 00:15:08	9.8×10^7	1600	0.22
	57/00:24:02 - 00:27:11	9.4×10^7	1700	0.25
2DC24 GAS	57/00:53:00	7.2×10^7	1500	0.345
	57/00:54:05	7.2×10^7	1500	0.345
3IV24 1-3 4-6	57/01:06:17 - 01:09:25	8.1×10^7 ←	1400	0.32
	57/01:18:20 - 01:21:28	2.9×10^7 ←	1650	0.32
Tether Break	57/01:30:20	1.1×10^8	2000	0.28

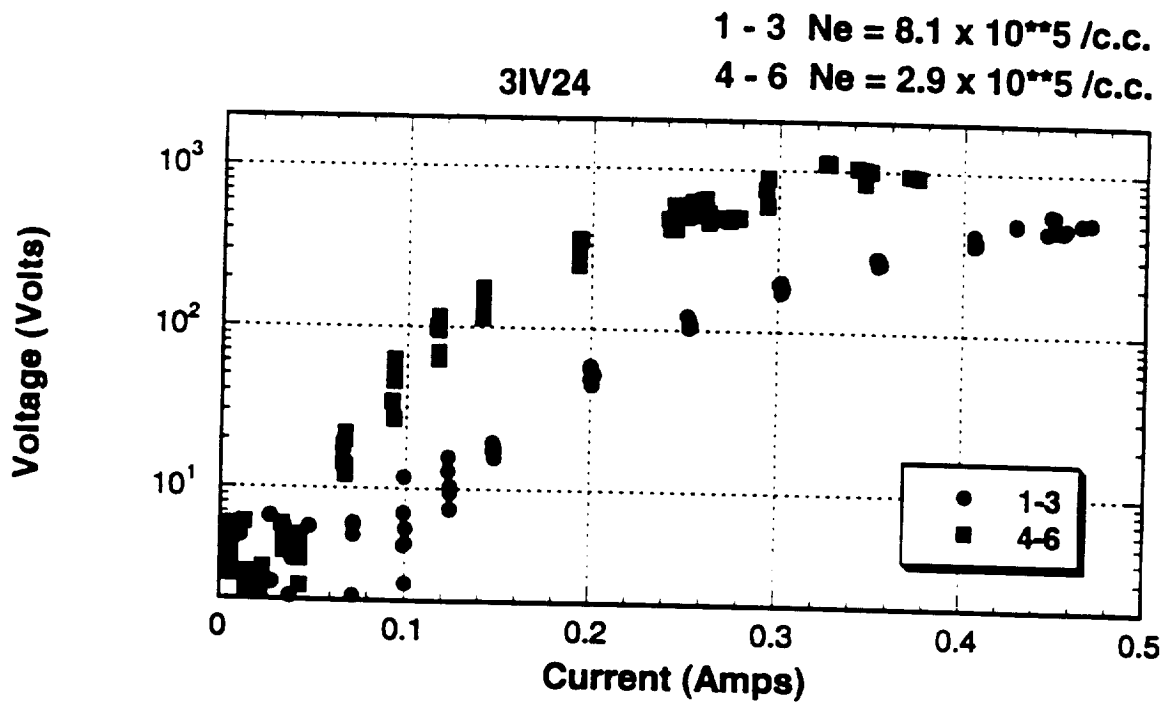
- What is the characteristic tube expansion speed V^* as suggested by TSS dataset ?







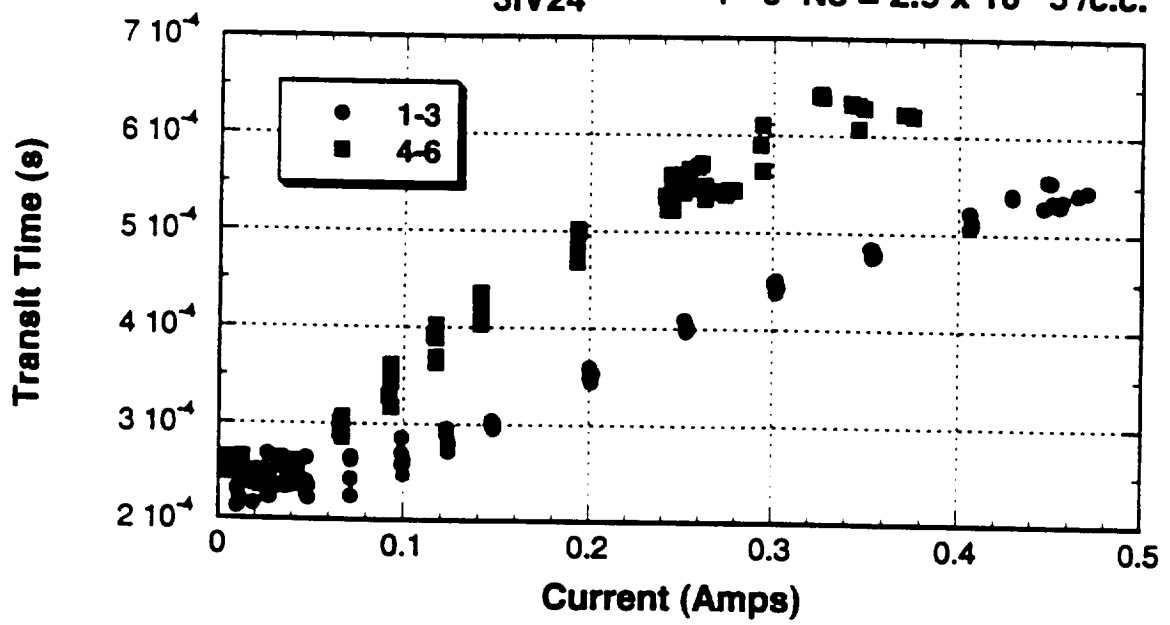




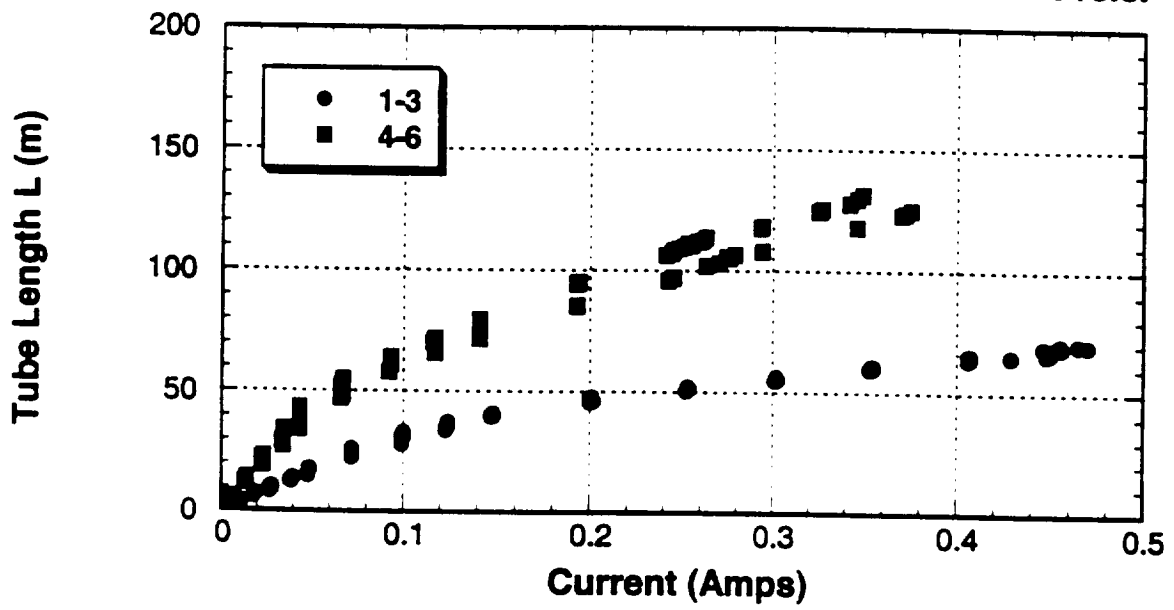
3IV24

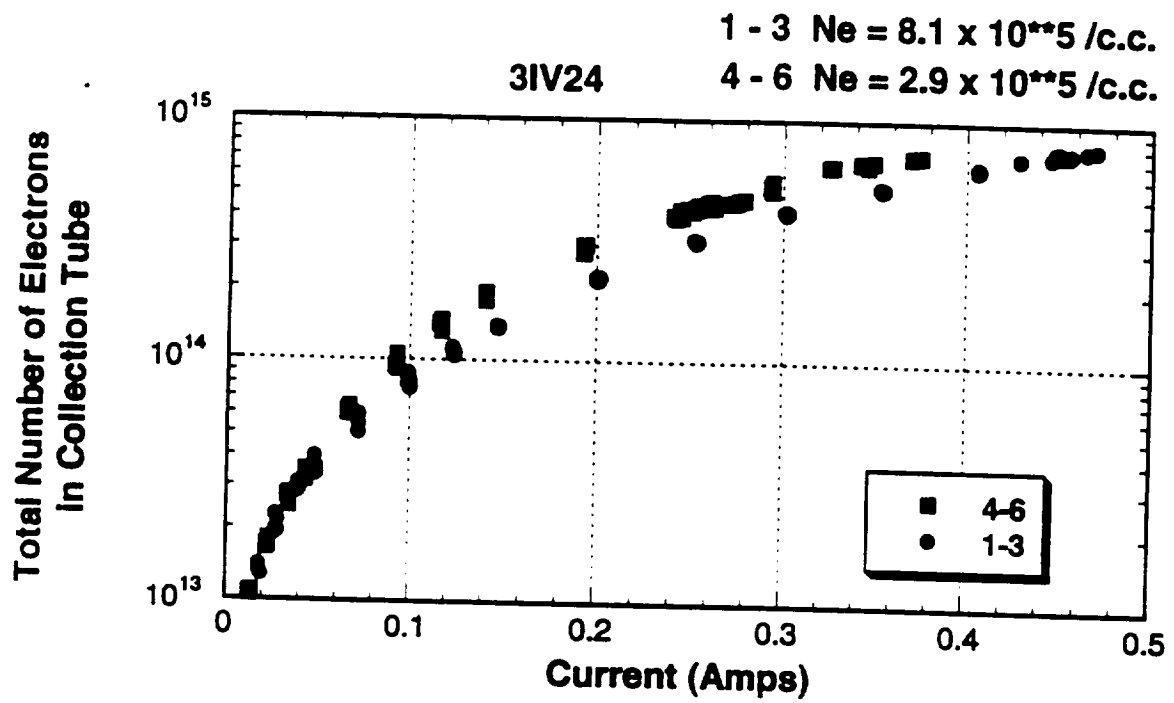
1 - 3 Ne = 8.1×10^{15} /c.c.

4 - 6 Ne = 2.9×10^{15} /c.c.



3IV24
1 - 3 Ne = $8.1 \times 10^{**5}$ /c.c.
4 - 6 Ne = $2.9 \times 10^{**5}$ /c.c.





SUMMARY

- Electron collection tube expands with roughly constant speed V^* at high satellite voltage.
- Constant V^* at high voltage \iff Parker-Murphy scaling

$$V^* = I / 2 e N_0 (\pi R^2) \iff I / I_0 = (R/a)^2$$

- The constant expansion speed is less than characteristic electron thermal speed or Alfvén speed

-> indicating more efficient electron collection processes

anomalous transport into collection tube ?

motional effects ?

- Tube volume is self-adjusted according to ambient density

APPENDIX 21

**NEUTRAL GAS RELEASE
FROM HIGH VOLTAGE TSS SATELLITE
AND ITS EFFECTS ON THE
CURRENT COLLECTION**

Chia-Lie Chang	SAIC
Dennis Papadopoulos	SAIC
Gennady Milikh	UMD
Adam Drobot	SAIC

**American Geophysical Union
Annual Spring Meeting at Boston, MA**

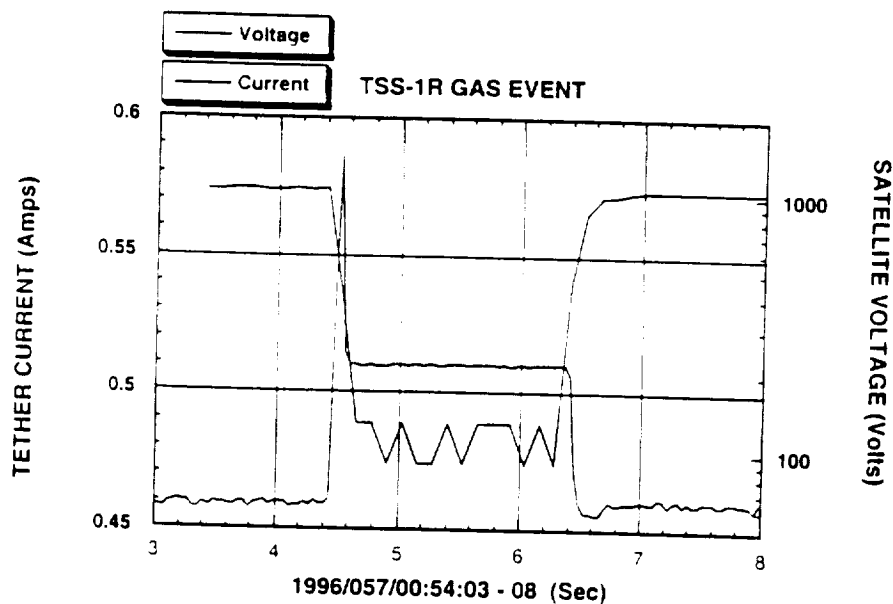
May 26 , 1998

TSS-1R GAS EVENT

- Gas was released from Yaw thrusters on the TSS satellite during 2DC24 operational cycle for about 2 seconds.
- There was an initial surge on the tether current:

0.46 A \rightarrow 0.59 A \rightarrow 0.51 A (EGA gun limited)

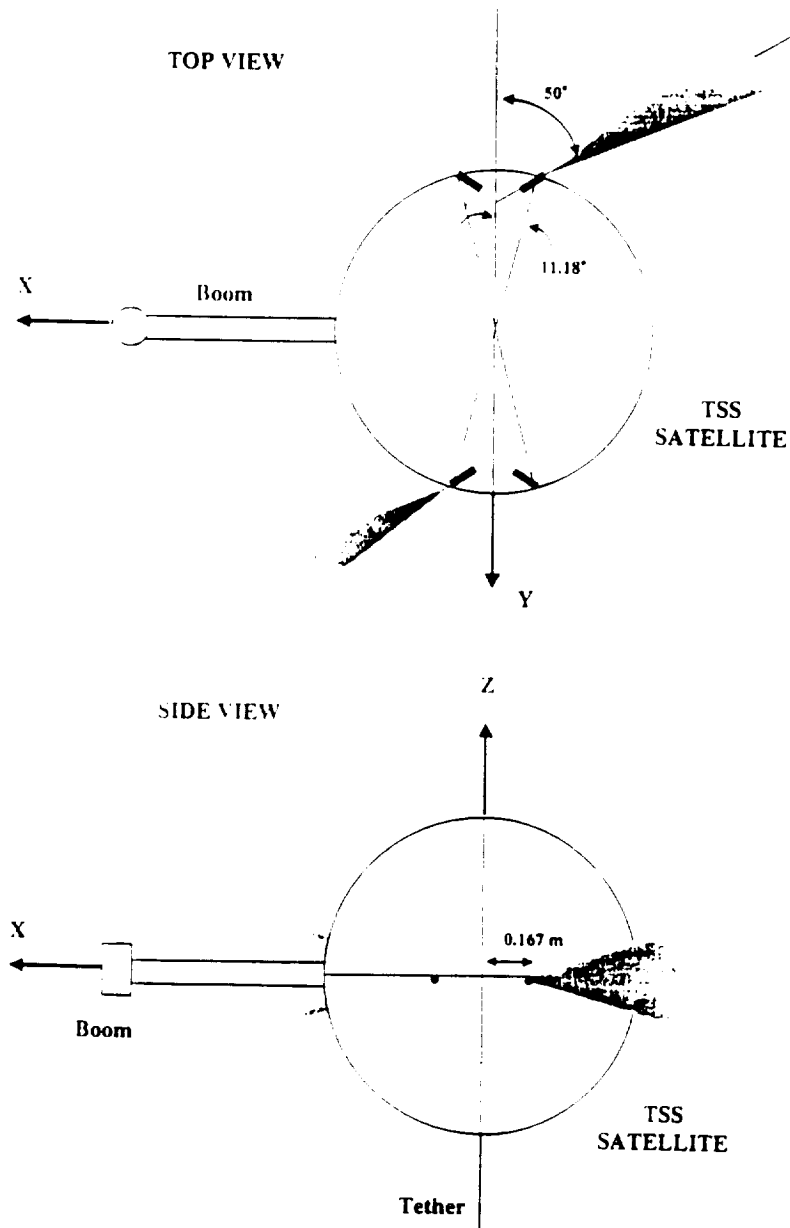
and a drop on the satellite voltage: 1000 V \rightarrow 100 V



- Electrons from neutral gas ionization (Townsend discharge) enhanced TSS current collection.
- Parameters: $T = 1700$ °K; $N = 5.8 \times 10^{11}$ /m³; $B = 0.35$ G; Parker-Murphy Radius: 2.4 m \rightarrow 1.5 m.

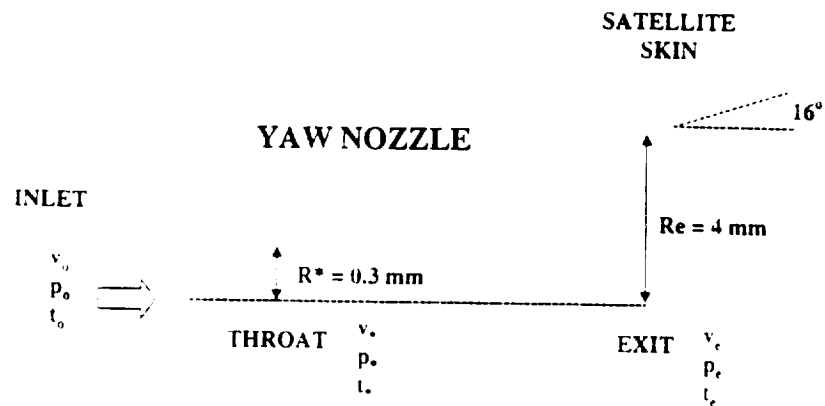
GAS RELEASE FROM YAW THRUSTERS

- 4 yaw thrusters are located on the equatorial plane of the satellite for spin control, operated in pair



GAS FLOW IN YAW THRUSTERS

- Yaw nozzle design:



- Inlet parameters: N_2 , $p_o = 10 \text{ atm}$, $t_o = 300 \text{ °K}$
- Isentropic Flow: (M is Mach Number)

$$\frac{p_o}{p} = \left(1 + \frac{\gamma-1}{2} M^2 \right)^{\frac{\gamma}{\gamma-1}}, \quad \frac{t_o}{t} = 1 + \frac{\gamma-1}{2} M^2, \quad \frac{\rho_o}{\rho} = \left(1 + \frac{\gamma-1}{2} M^2 \right)^{\frac{1}{\gamma-1}}, \quad c = \left(\frac{\gamma p}{\rho} \right)^{\frac{1}{2}}$$

$$\left(\frac{R_e}{R_*} \right)^2 = \frac{1}{M} \left[\left(\frac{2}{\gamma+1} \right) \left(1 + \frac{\gamma-1}{2} M^2 \right) \right]^{\frac{\gamma+1}{2(\gamma-1)}}$$

- At Throat: $M = 1$, $\gamma = 1.4$, $p_* / p_o = 0.5283$,
 $t_* / t_o = 0.8333$, $\rho_* / \rho_o = 0.634$, $v_* = 322 \text{ m/s}$
- At Exit: $M_e = 7.88$, $t_e = 22.35 \text{ °K}$, $v_e = 760 \text{ m/s}$,
 $p_e = 1.13 \times 10^{-3} \text{ atm}$, $\rho_e = 1.72 \times 10^{-2} \text{ kg/m}^3$,
 $n_e = 3.67 \times 10^{23} / \text{m}^3$

GAS DYNAMICS SIMULATIONS

- Continuum flow field near yaw nozzle exit

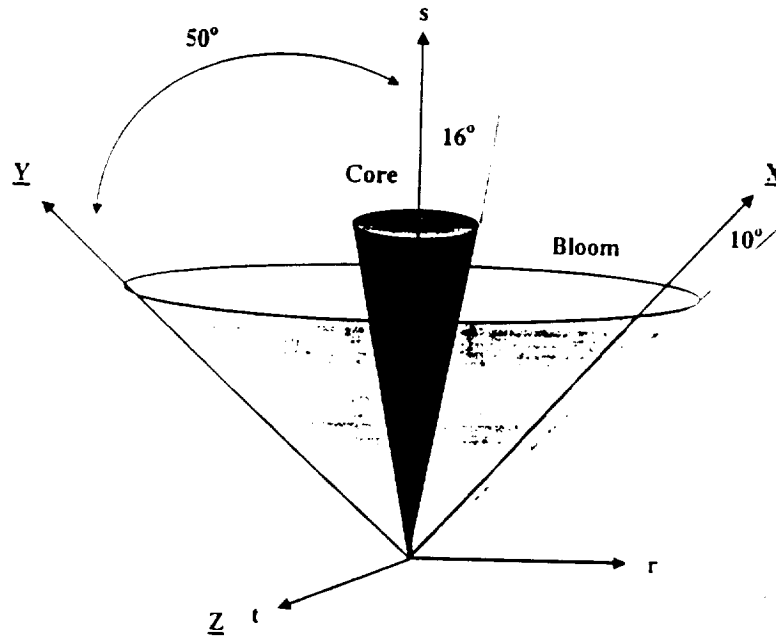
- Define breakdown surface

Scale Length / Mean Free Path = 0.05

- Beyond breakdown surface, collisionless DSMC flow

NEUTRAL DENSITY PROFILE

- Neutral density in Core and Bloom cones



- Core angle is 16° , bloom angle is the maximum expansion angle (Prandtl-Myer expansion) at 34°

$$r = \underline{X} \sin 40^\circ - \underline{Y} \sin 50^\circ, \quad \theta = \tan^{-1} \left(\frac{\sqrt{r^2 + t^2}}{s} \right)$$

$$s = \underline{X} \cos 40^\circ + \underline{Y} \cos 50^\circ, \quad t = \underline{Z}$$

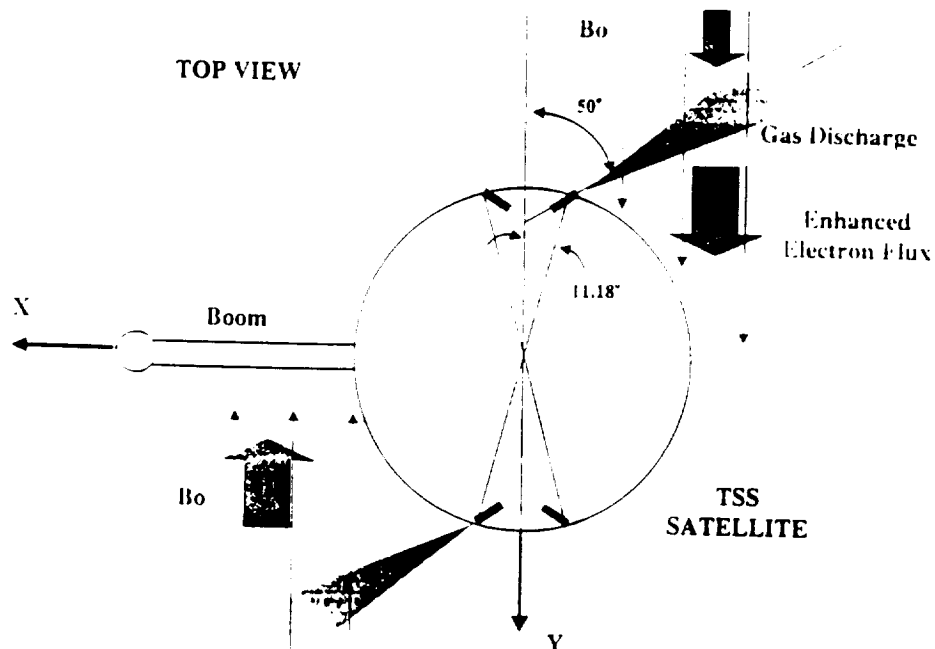
$$N_{\text{core}}(s) = N_{\text{exit}} \frac{R_{\text{exit}}^2}{(R_{\text{exit}} + s \tan 16^\circ)^2}$$

$$N_{\text{bloom}}(r, s, t) = N_{\text{core}}(s) \times 10^{\frac{\theta - 16^\circ}{4.25^\circ}}$$

$$N_{\text{core}}, N_{\text{bloom}} \geq N_{\text{ambient}} = 10^{15} \text{ m}^3$$

ENHANCED CURRENT COLLECTION DUE TO GAS DISCHARGE

- Measured ambient magnetic field is mainly along the Y axis
 $B_x = 0.038 \text{ G}$, $B_y = 0.325 \text{ G}$, $B_z = 0.109 \text{ G}$
- Electron collection is mainly along the B field (Y axis)
- Electron flux along B encounters neutral gas, causes discharge and enhanced collection by the TSS satellite.



DISCHARGE ALONG B FIELD

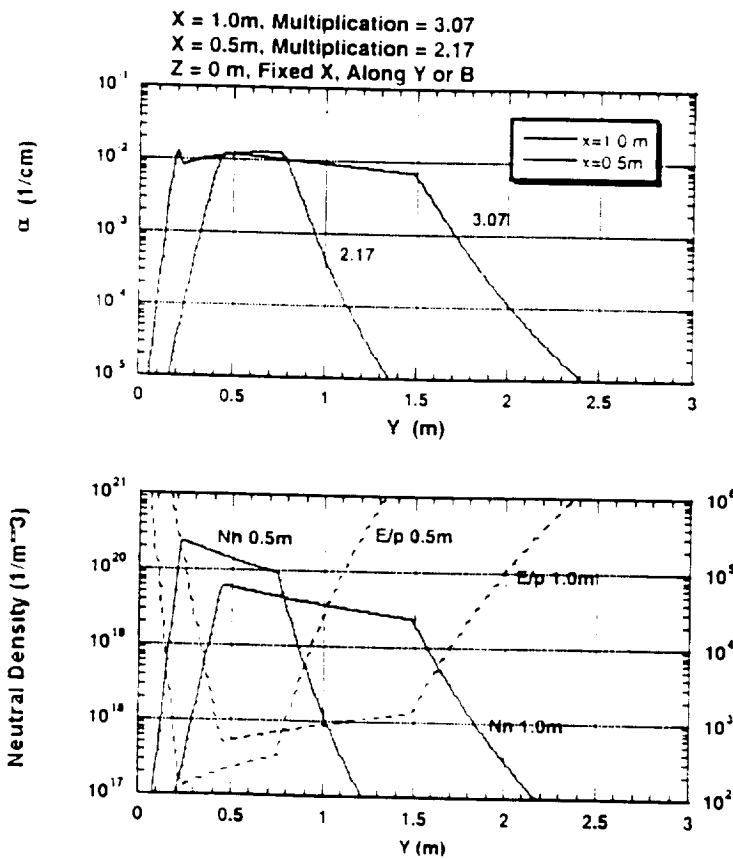
- Townsend Formula:

$$\alpha(Y) = A p(X, Y, Z) \exp(-B p(X, Y, Z) / E)$$

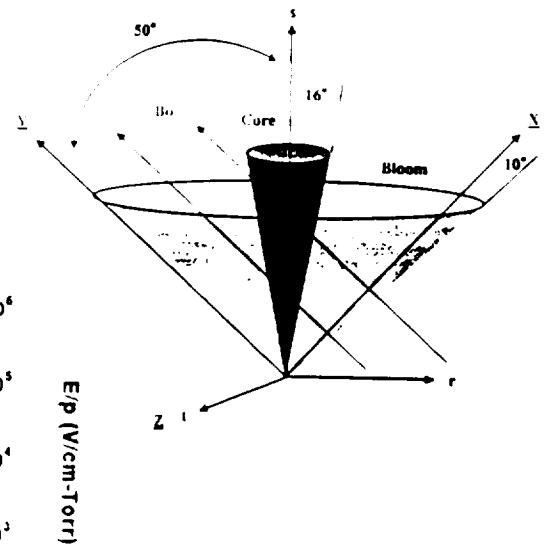
with α in 1/cm, p in Torr, E in V/cm, and

for E/p : 200 - 600 $A = 12, B = 342$
 for E/p : 27 - 200 $A = 8.8, B = 275$

- Electron multiplication factor along B:



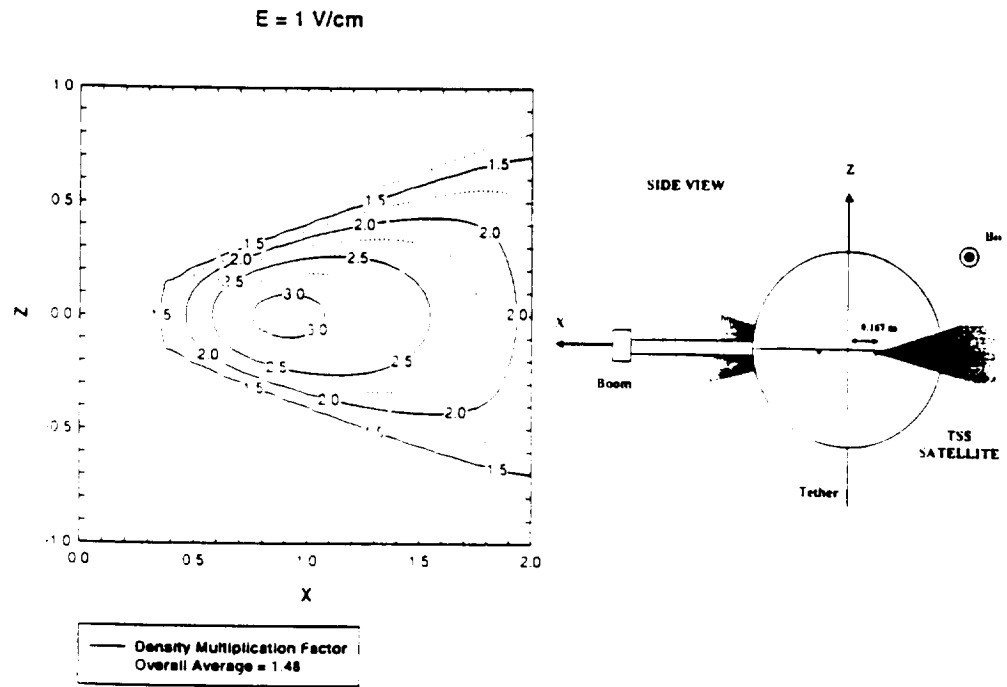
$$\frac{N_e(Y)}{N_{e0}} = \exp \int_0^Y \alpha(Y) dY$$



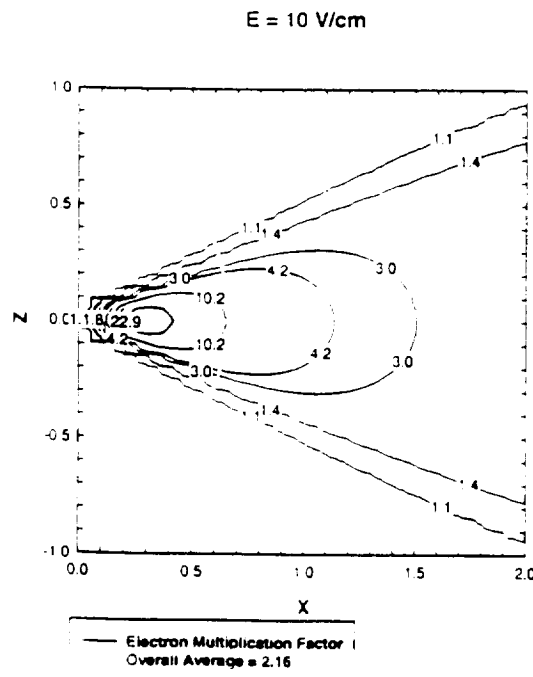
E/p (V/cm-Torr)

ELECTRON MULTIPLICATION BY GAS RELEASE

- Low Voltage (100 Volts, Rpm = 1.5 m)

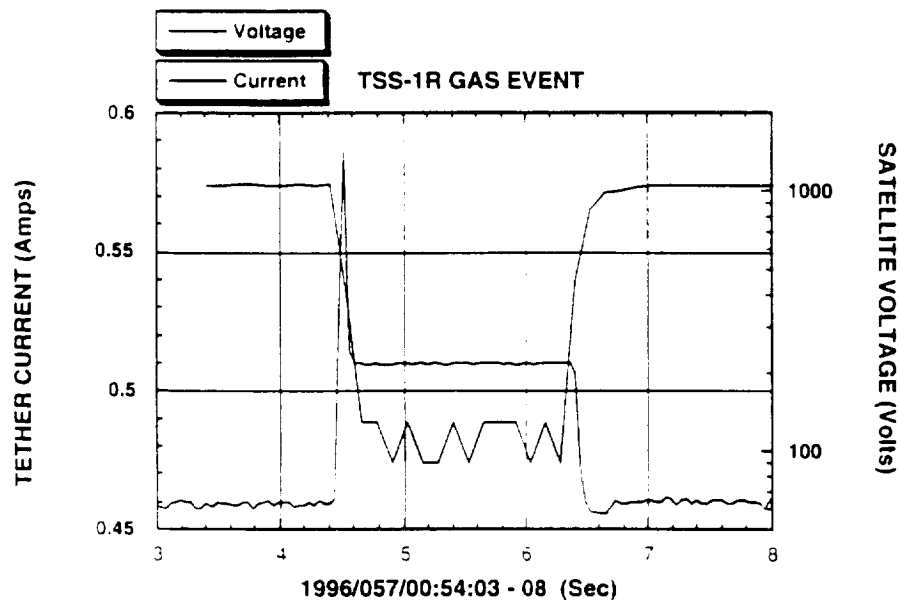


- High Voltage (1000 Volts, Rpm = 2.4 m)

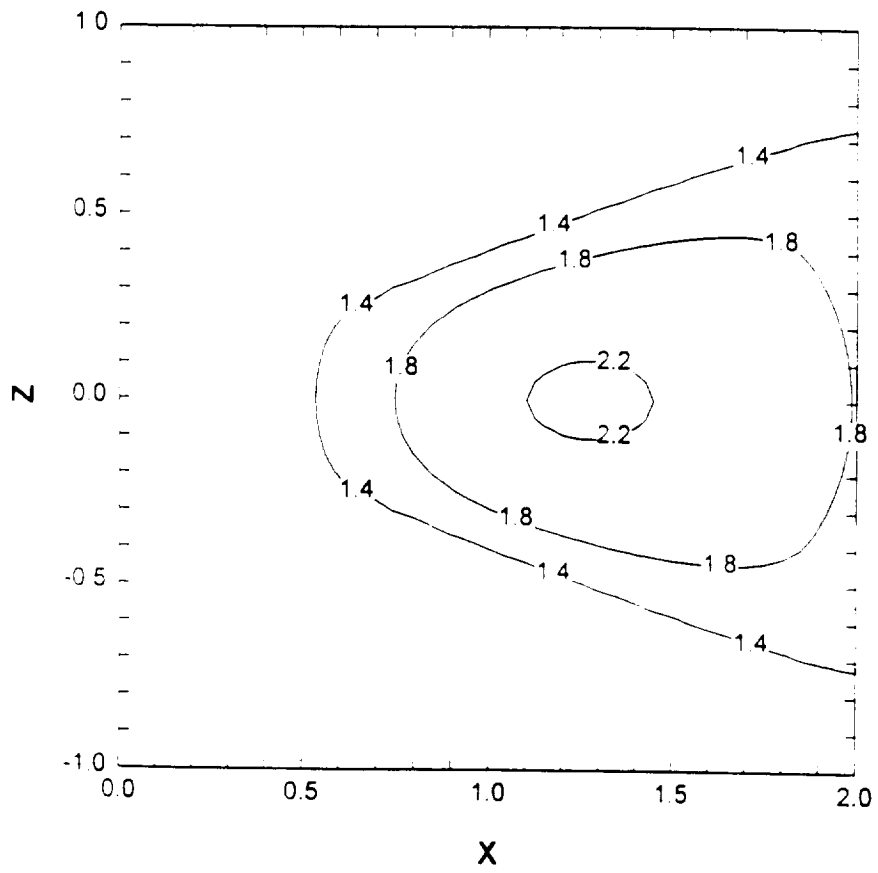


IMPLICATION ON CURRENT COLLECTION

- Initial surge of current due to discharge at high voltage (~ 1000 V), then the current decreased to the limit set by EGA gun at ~ 0.5 A, satellite voltage self-adjusted to ~100 V accordingly, and a lower level of discharge was maintained for 2 seconds.

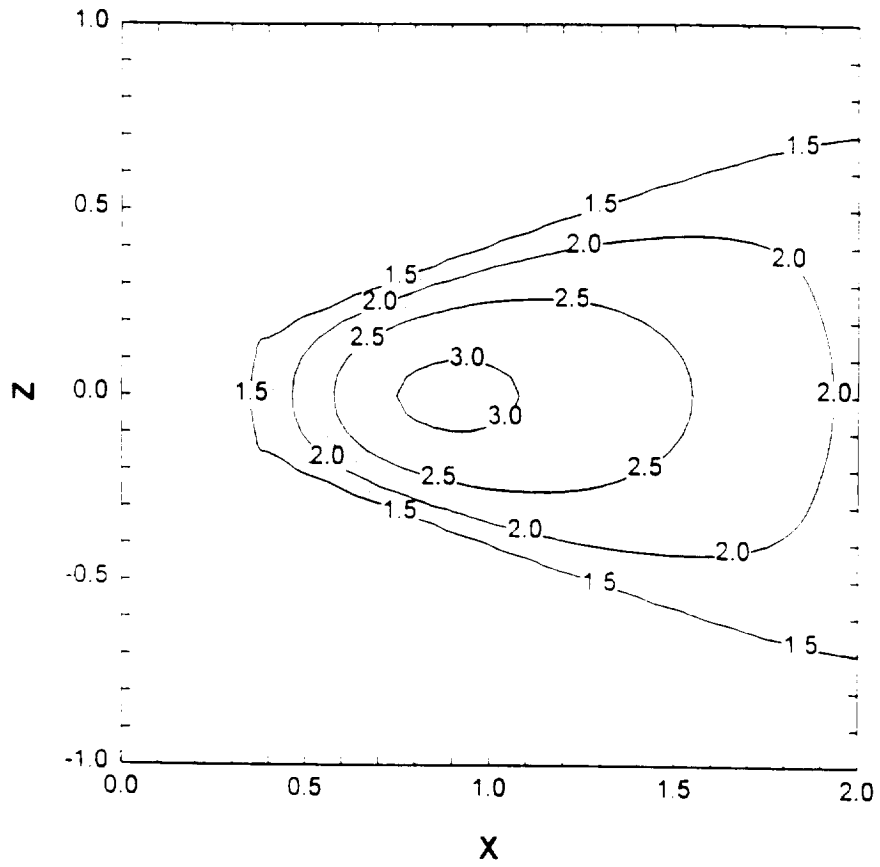


E = 0.5 V/cm



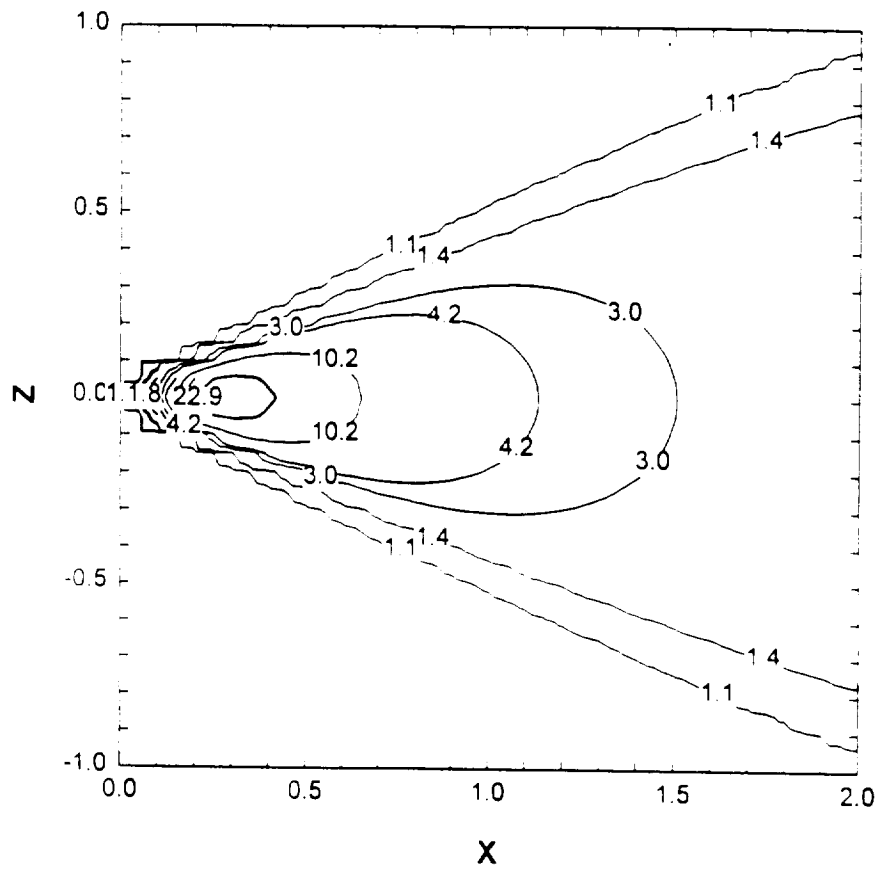
— Electron Multiplication Factor
Overall Average = 1.33

E = 1 V/cm



— Density Multiplication Factor
Overall Average = 1.48

E = 10 V/cm



— Electron Multiplication Factor
Overall Average = 2.16

APPENDIX 22

Post Mission Laboratory Tests

by

George Bergeron

Science Applications International Corporation

1. Laboratory Tests on Tether

Several "quick and dirty" experiments were performed on a short section of the tether in an effort to examine the possibility that plasma breakdown due to trapped air around the center conductor may have caused or contributed to the failure of the Tethered Satellite Experiment. These experiments were carried out in a small volume vacuum chamber, estimated at 5 liters, which was first characterized for pump-out speed while empty, then again with about 2 feet of the tether installed. The center conductor of the tether section was attached to a high-voltage feed-through to which voltages to 15kV could be applied. The power supply used in this experiment was a current-limited, 0-15 kV supply with a peak current output of 25 mA. The results of both pump-out speed tests and high-voltage breakdown test are presented here.

2. Vacuum Tests

The first item to note was the significant difference in pump-down speed between the empty vessel, and evacuating it once the tether section had been installed. The empty chamber could be evacuated from atmosphere to

1×10^{-3} Torr in about six minutes. Pump out to the same pressure with the tether in place took hours (see attached data sample). This indicates that there was indeed trapped gas (air) around the center conductor and that it was not easily removed due to the small gas conductance around the electrical conductor to the ends of the tether section.

3. Plasma Breakdown Tests

High voltage was applied to the tether section while it was held in a number of configurations, both near a ground plane and away from ground. In general, igniting a plasma within the chamber and along the surface of the tether proved easy, as was expected given the vacuum test results.

Depending on gas pressures and arrangement of the tether, breakdown was observed to occur over a range in intensities from a few sparks to igniting the whole chamber. At one point the whole outer sheath was observed to breakdown (Voltage -7.8 kv, Pressure (start) -9×10^{-4} , Pressure (end) -5×10^{-3} Torr) in random sections, jumping from one area to another. More typically, local discharges were observed in the form of "sparks" occurred on various locations of the tether.

4. Conclusions on the Laboratory Tests

These experiments cannot stand as definitive proof that the root cause of the tether break was plasma breakdown however; when taken in conjunction with other data and the observations of the technical crew on the mission indicate strongly that that this mode of failure is highly likely. However, no residual gas analyzer (RGA) was available at the time of the experiments to verify that the gas generated was air rather than other neutral constituents.